The NASA Ionospheric Connection Explorer : ICON

Calibration, Measurements and Algorithms Document

Version – 2 Draft
Date – November 20, 2024

Signature List

ICON Calibration and Measurement Algorithms Document
ICON CMAD

Thomas Immel – Principal Investigator Date

Scott England – Project Scientist Date

Ken Marr – MIGHTI Instrument Scientist Date

Rod Heelis – IVM Instrument Scientist Date

Harald Frey – FUV Instrument Scientist Date

Eric Korpela – EUV Instrument Scientist Date

By signing this document, signatories are certifying that the content herein is acceptable direction for managing the project's data and that they will ensure its implementation by those over whom they have authority.

Change History Log

Revision	Effective Date	Description of Changes
Baseline	10/05/2022	Original
Version 2 Draft	10/21/2024 11/20/2024	FUV O/N2 Limb Product and Algorithm added. MIGHTI Temperature and references updated.

		Re-titled - Calibration, Measurements and Algorithms Document

ICON CALIBRATION AND MEASUREMENT ALGORITHMS DOCUMENT

1. SCOPE

This document provides key information on instrument functionality, performance, ground and flight calibration for the four instruments constituting the science payload on the Ionospheric Connection Explorer, Launched October 19, 2019. Following a checkout period and initial flight calibrations, Science Operations were entered into on December 1, 2019.

2. RELATED DOCUMENTATIONS

Project Level Documents

Title	Document Number	Publication Date
ICON Science Requirements Document	ICN-SCI-003	28 Jul 2014 [Rev E]
ICON Project Requirements Document	ICN-SYS-001	15 Jan 2015 [Rev D]
ICON Science Data Processing Requirements Document	ICN-OPS-006	15 May 2015
ICON Performance Verification Plan	ICN-SYS-008	7 Apr 2014

3. DOCUMENT STRUCTURE

This document follows with four chapters, one for each instrument on the ICON Payload

Chapter 1. The ICON Michelson Interferometer for Global Heterodyne Thermospheric Imaging - MIGHTI

Chapter 2. The ICON Ion Velocity Meter - IVM

Chapter 3. The ICON EUV Spectrometer - EUV

Chapter 4. The ICON FUV Spectrographic Imager - FUV

1. Chapter 1: MIGHTI

This document describes the MIGHTI instrument function and those aspects of the on-orbit instrument performance that are dependent on calibration and ground processing algorithms. MIGHTI consists of two sensor elements used to derive horizontal thermospheric wind profiles and temperature profiles.

For the thermospheric winds, absolute radiometric measurements are not mandated by the science requirements, so key calibration procedures are focused on determining accurate phases for the interferograms resulting from observation of red and green line emissions. For temperature measurements the relative radiometric calibrations are key. MIGHTI calibrations include both ground-based pre-launch measurements and continuing on-orbit measurements.

2. Related Documentations

2.1 Applicable Documents

This section identifies any other project/mission documentation with higher-level guiding requirements or that provide more detail or context.

Title	Document Number	Publication Date
MIGHTI L4 Requirements Document	ICN-MTI-007	
MIGHTI Requirements Verification Matricies	**ICD:** MIGHTI RM Workbook ICN-ICD-002 Rev C **ERD:** MIGHTI RM Workbook ICN-SYS-003 Rev E **IRD:** MIGHTI RM Workbook SSD-RQT-MI001 Rev B	23 March 2016
MIGHTI Verification and Validation Plan	Included Above	
MIGHTI Calibration Plan	3.0.20 Calibration Test Procedure_As-run	11 Feb 2016
MIGHTI Instrument Design and Calibration	Space Science Reviews, 212, pp. 553–584 (2017)	20 Apr 2017
(MIGHTI) On-Orbit Wind Observations: Data Analysis and Instrument Performance.	Englert et al., 2023, https://doi.org/10.1007/s11214-023-00971-1	August 2023

Temperatures in the Upper Mesosphere and Lower Thermosphere from O_2 Atmospheric Band Emission Observed by ICON/MIGHTI	Stevens et al., 2022, https://doi.org/10.1007/s11214-022-00935-x	November 2022

3. Overview and Background Information

3.1 Science Objectives

The Michelson Interferometer for Global High-resolution Thermospheric Imaging (MIGHTI) instrument was designed to provide thermospheric wind and temperature measurements for the Ionospheric Connection (ICON) Explorer mission. The wind velocity observation is based on the Doppler shift measurement of the forbidden atomic oxygen red and green lines at the wavelengths of 630.0 nm (O(1D → 3P)) and 557.7 nm (O(1S → 1D)) respectively, imaging the limb of the Earth between 90 and 300 kilometers tangent point altitude during day and night. Wind directions are determined by combining observations of two fields of view that are directed nominally at an azimuth angle of 45 degrees and 135 degrees from the spacecraft ram direction, each providing line of sight wind components. This observational approach is described in Figure 1. To measure the Doppler shift, MIGHTI uses the Doppler Asymmetric Spatial Heterodyne (DASH) technique, which is a modified version of Spatial Heterodyne Spectroscopy (SHS).

The temperature observation is based on the radiometric measurement of three narrow band regions within the temperature dependent molecular oxygen Atmospheric band (A-band, O2(b1Σ → X3Σ (0,0))) around the wavelength of 762 nm. Two additional passbands on either side of the band are used to observe the background contribution while avoiding signal from the (1, 1) vibrational band. The A-band observations are performed utilizing the same optics and detector as the wind observations and cover an altitude region of about 90-140 km.

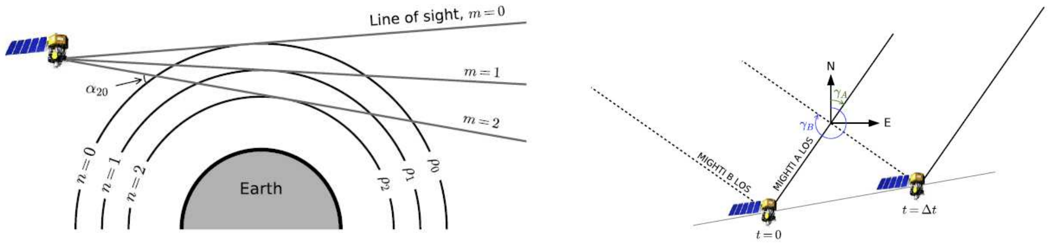

Fig. 1 Illustration of the MIGHTI viewing geometry, showing the altitude imaging (left) and the near-collocated and near-synchronous measurements of MIGHTI-A and MIGHTI-B along the path to derive the horizontal vector wind (right).

3.2 MIGHTI Instrument Requirements

The MIGHTI instrument design was driven by the ICON science requirements and the available spacecraft accommodations. The ICON science requirements flow down to measurement requirements for MIGHTI. One fundamental measurement requirement for MIGHTI is to measure the horizontal wind speed and direction. Since a Doppler shift measurement is sensitive only to the wind velocity component parallel to the viewing direction (line of sight), MIGHTI uses two perpendicular fields of view nominally pointing 45° and 135° in azimuth from the spacecraft velocity (MIGHTI-A and MIGHTI-B). This way, the two MIGHTI fields of view measure virtually the same atmospheric volume about 8 minutes apart, given the ICON orbit altitude of approximately 600 km. The combination of near-collocated measurements at the observation tangent point then allows for the determination of the horizontal wind speed and direction. This technique has been used successfully by previous satellite-based wind sensors [e.g. WINDII]. MIGHTI measurement requirements for a single field of view are given in Table 1 for wind and temperature.

To translate the MIGHTI measurement requirements to instrument component requirements, an instrument performance model was developed that simulates all major elements of the instrument and uses representative atmospheric volume emission rates (VER) and expected viewing geometries for observations at noon and midnight local solar time. The brightnesses for the atomic oxygen red and green lines were determined based on low and mid-latitude WINDII observations taken in 1996, during the solar activity minimum between solar cycle 22 and 23 and are shown in Figure 2 (left panel). The average brightnesses for the oxygen A-band are shown in Figure 2 (right panel).

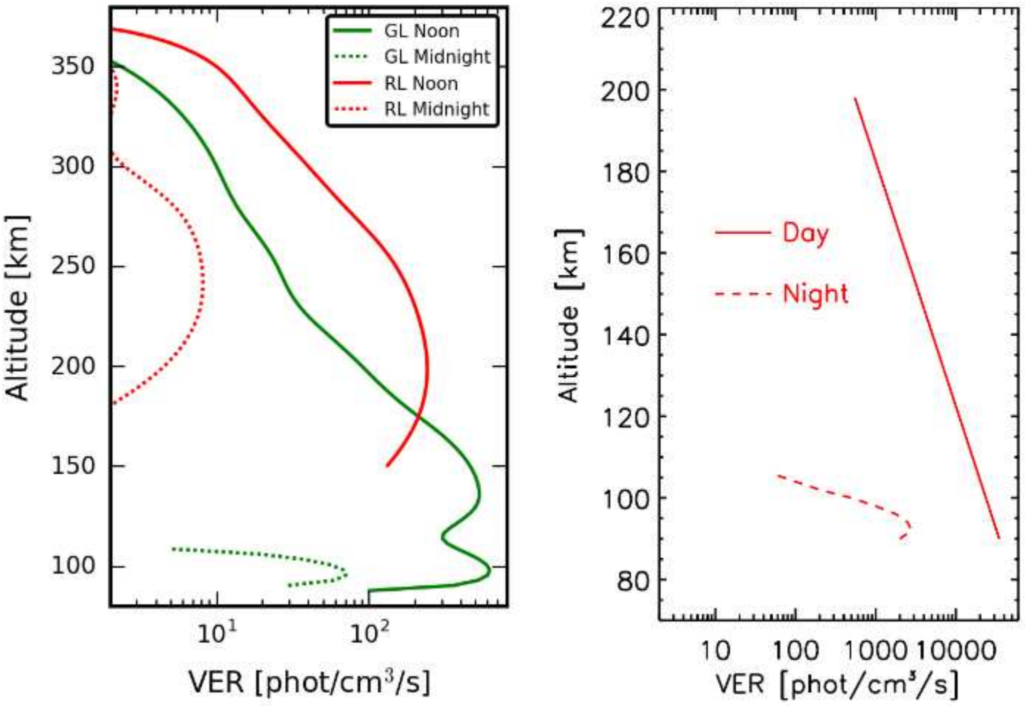

Fig. 2 The left panel shows the volume emission rates of the oxygen green (GL) and red (RL) line emissions used for the MIGHTI instrument model. The right panel shows the average volume emission rates of the oxygen A-band used for the MIGHTI instrument model.

The noon values for the A-band were determined using low and mid-latitude RAIDS observations taken in 2010, during the solar activity minimum between solar cycle 23 and 24. The average midnight brightnesses for the oxygen A-band were chosen to be consistently lower than the low and mid-latitude WINDII observations of 1992-1994, corresponding to the declining phase of solar cycle 22.

The driving instrument parameters and their associated requirements are listed in Table 1. The first four requirements in the table are determined by the design geometry of the optics and are met with minor variations resulting from alignments, slightly oversized optics, and manufacturing constraints. The other requirements were treated as minimal performance limits with the goal to exceed them to maximize the instrument capabilities. The last column of Table 1 lists the as-built instrument performance characteristics.

Parameter	**Minimum Success Requirements**	**Comprehensive Success Criteria**	**As-built Performance**
Field of View (vert × horiz)	5.36° ×3.22°	5.36° ×3.22°	> 5.36° ×3.22°
Total Etendue (AΩ) for 85–310 km limb scene (top 8 km are used for thermal tracking)	0.0495 cm^2 sr (Night) 0.0074 cm^2 sr (Day)	0.0495 cm^2 sr (Night) 0.0074 cm^2 sr (Day)	> 0.0495 cm^2 sr (Night) > 0.0074 cm^2 sr (Day)
Interferometer Optical Path ± Difference Interval	5.1±0.4cm	5.1±0.4cm	Red: 4.89±0.4cm (A), 4.94±0.4cm (B) Grn: 4.85±0.4cm (A), 4.90±0.4cm (B)
Interferometer Echelle Grating Groove Density	64 grooves/mm	64 grooves/mm	64.285 grooves/mm
Monochromatic Interferometer Fringe Contrast	Red Day: 66% Red Night: 57% Green Day: 43% Green Night: 43%	Red Day: 66% Red Night: 57% Green Day: 43% Green Night: 43%	Red Day: 78% (A), 78% (B) Red Night: 73% (A), 72% (B) Green Day: 78% (A), 85% (B) Green Night: 75% (A), 83% (B)
Optical Efficiency (incl. all optics, filters and CCD quantum efficiency)	Red: 15.8% Green: 11.5%	Red: 15.8% Green: 11.5%	Red: 18.7% Green: 14.7%
CCD Dark Current @-40°C	0.1 elec./sec./pix	0.1 elec./sec./pix	0.01 elec./sec./pix (at launch)
CCD Read Out Noise	16.8 (rms) e/binned pixel/read	16.8 (rms) e/binned pixel/read	<4.2 (rms) e/binned pixel/read
Stray Light Amount (day only)	35% of max. red line signal	35% of max. red line signal	<10% (by analysis)

Table 1: MIGHTI instrument requirements and performance.

3.3 Instrument Subsystem Descriptions

Figures 3 and 4 show the elements of the MIGHTI sensor, viewed from the outside of the instrument and the top of the optical bench with the cover removed, respectively.

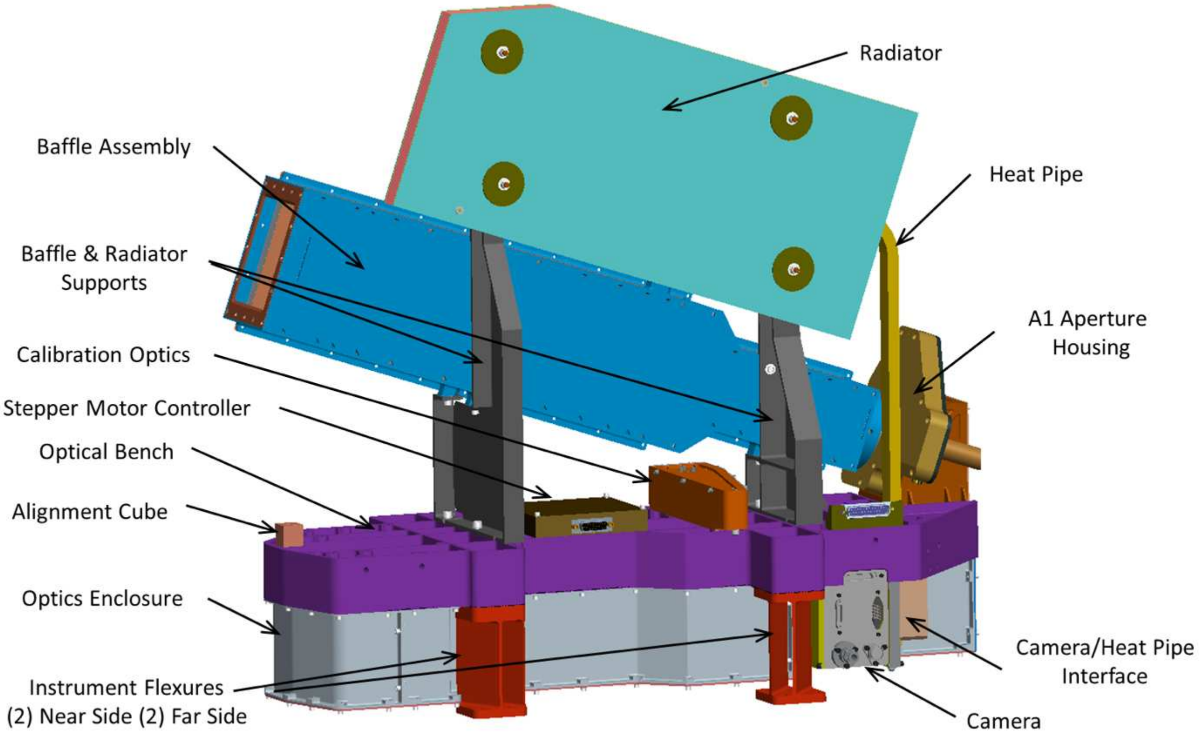

Fig 3: Single MIGHTI sensor unit

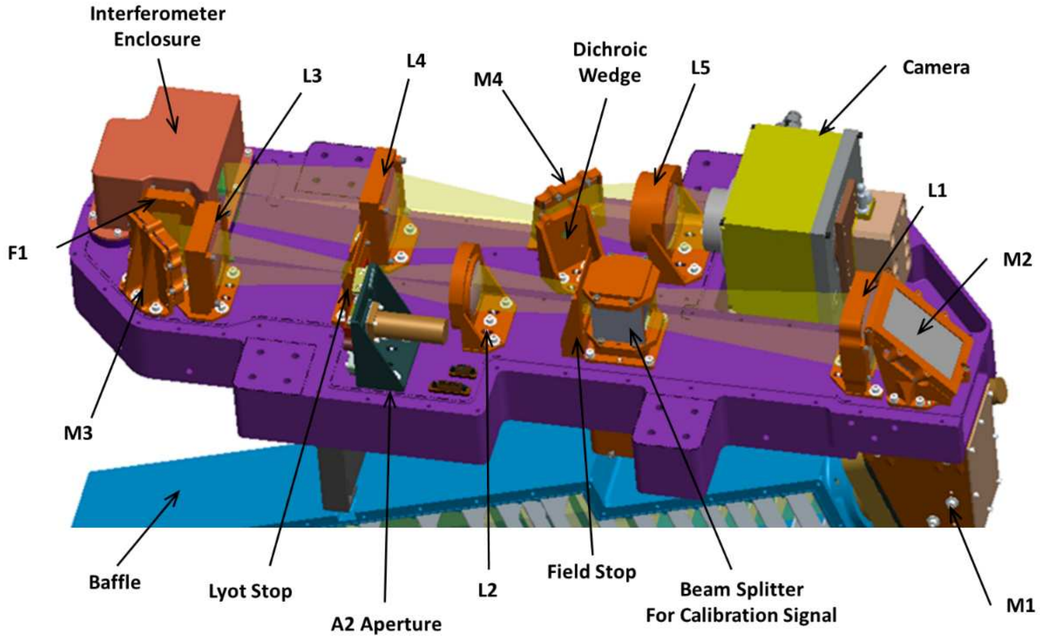

Fig 4: MIGHTI optical bench (purple) populated with all optical elements. L denotes lenses, M denotes mirrors, F denotes interference filters.

3.3.1 Baffle

Each MIGHTI sensor is equipped with a blackened baffle tube (see Figures 3, 4, and 5) that extends forward of the entrance pupil located at A1. The primary purpose of the MIGHTI baffle is the suppression of signal that originates from angles outside the field of view. This is of vital importance, since the illuminated Earth's disk and the sun represent light sources that are many orders of magnitude brighter than the targeted airglow emissions, and during the day, the bright Earth is always close to the MIGHTI fields of view. Due to the ICON orbit and MIGHTI limb pointing geometry, the sun can also get close to or even enter the MIGHTI fields of view during the mission. A secondary purpose of the baffle is to reduce contamination from particles that could reach the first optical element and create a scattering source.

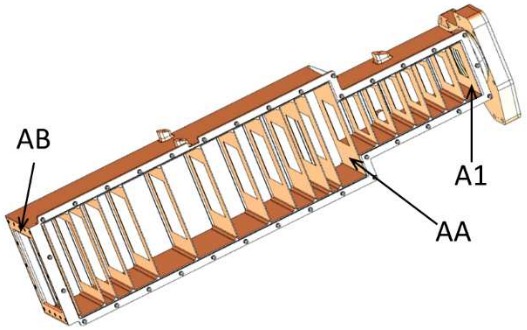

Fig 5: MIGHTI baffle with the sidewall removed. On the top right, the mechanism housing for the day/night aperture, A1, at the pupil is shown. The inside surfaces of the baffles are coated with black epoxy primer (Cytec Industries BR 127NC).

The design of the MIGHTI baffles adapted several features of the WINDII baffle, such as a two stage construction and the variable baffle exit aperture, A1. By design, the field stop and Lyot stop of the input optics (see Figure 4) limit the MIGHTI field of view (FOV) so that all of the baffle elements are outside the FOV. Light from outside the FOV can only enter the optical system by reflection off of baffle structures and then onto an optical surface. From there, it must be redirected into the FOV by scattering from the optical glass itself or from particulate contamination.

More details on the baffles can be found in Englert et al., doi: 10.1007/s11214-017-0358-4.

3.3.2 Entrance Optics

The MIGHTI entrance optics are shown in Figure 6 and include all optical elements between the first fold mirror (M1) and the interference filter (F1), located immediately in front of the interferometer. The purpose of the entrance optics is to (1) direct the beam from the baffle aperture (A1) onto the MIGHTI optical bench, (2) define the field of view for day and night aperture positions (note that the FOV is not defined by any baffle vanes), (3) superimpose signal from the calibration lamps onto the atmospheric signal, (4) eliminate signal from unwanted spectral regions between about 200-525 nm and 900-1100 nm, and (5) form an image of the limb at the fringe localization plane close to the gratings within the interferometer.

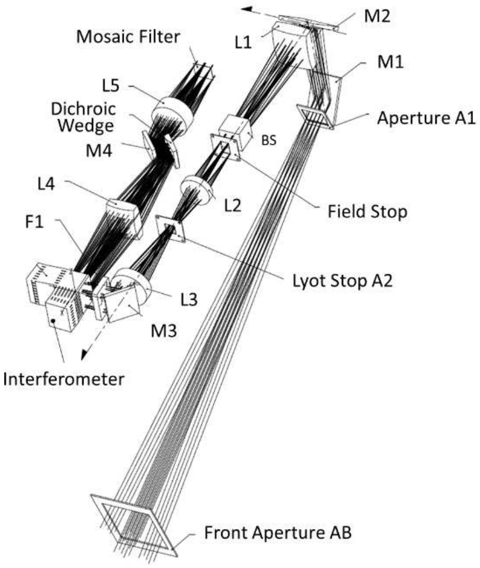

Fig 6: MIGHTI optical components shown with representative rays.

As shown in Figure 6, two flat mirrors (M1 and M2) are used to direct the beam onto the optical bench. The following lens, L1, simultaneously forms an image of the limb on the field stop and collimates light from the entrance pupil (A1). In front of the field stop is a cubic beam sampler which transmits 95% of the atmospheric signal and reflects into the beam 5% of the signal from the on-board calibration sources (see Section 3.3.3). Lens L2 collimates light from the field stop and images A1 onto the Lyot stop. The Lyot stop is slightly undersized with respect to the image of A1, so that the edges of A1 are blocked and the field of view is determined solely by the field stop and the Lyot stop. Immediately in front of the Lyot stop is a second adjustable aperture (A2). This aperture is equivalent to the adjustable aperture A1. In day mode, it also blocks about 85% of the rectangular Lyot stop by rotating a blackened vane into the beam. The vane is aligned so it blocks light originating from the edge of the daytime A1 aperture. Lens L3 collimates light from the Lyot stop and forms an image of the limb onto the fringe localization plane in the interferometer. The beam entering the interferometer is telecentric. The beam enters the interferometer enclosure after reflecting off a fold mirror (M3) and passing through a broad-band interference filter with a 525-900 nm passband. This filter reduces light going into the interferometer that is within the sensitivity range of the MIGHTI CCD detector, but outside any wavelengths of interest.

The optical bench and M1 enclosure are thermally stabilized using three separate zones comprised of strip heaters, temperature sensors and PID (Proportional-Integral-Derivative) controllers. The bench is thermally controlled to maintain a temperature of about 20°C on orbit.

3.3.3 Calibration Lamps

As with every interferometer, thermal effects are a potential concern. For MIGHTI, there are two different effects that need to be considered and mitigated. The first one is that thermal distortions of the structural hardware, such as the optical bench or the interferometer holder, could result in a shift of the image on the CCD detector. A lateral shift of the fringe image on the CCD is equivalent to a fringe phase shift and would therefore be interpreted as a Doppler shift. To detect and quantify lateral image shifts, a periodic notch pattern that is inscribed on one of the interferometer gratings is used. Using this notch pattern, sub-pixel scale movements can be detected and corrected.

The second effect is a phase change due to a change in the optical path difference in the interferometer which could be caused by a thermal change in index of refraction of the interferometer field widening prisms, the thermal expansion of the diffraction gratings, and/or stresses induced in the interferometer due the differences in the coefficient of thermal expansion of the interferometer elements. A proven approach to quantify interferometer thermal drifts is to measure the fringe drift of calibration lamp lines that are spectrally close to the atmospheric red and green line emissions. The measured calibration line phase drifts directly track the equivalent phase drifts of the atmospheric signal. Note that the thermal phase drift due to the drift in image location on the CCD is a function of the spatial frequency of the recorded fringe pattern, which can be significantly different for the atmospheric and calibration lines, whereas the phase drifts originating from the interferometer are a function of the wavelength of the emission lines, which is chosen to be virtually identical for the atmospheric and calibration lines. Therefore, both the grating notches and calibration lamp signals are needed to unambiguously quantify and correct for all thermal drifts in the data analysis.

The on-board calibration lamps at 630.48 nm (neon) and 557.03 nm (krypton) provide two spectrally narrow emission lines that are close in wavelength to the oxygen red and green lines respectively and are used on-orbit to track and quantify thermal drifts of the interferometer. Both of these lines have been used successfully in previous instruments such as WINDII and REDDI.

The MIGHTI calibration lamps are electrode free, radio frequency (RF) excited discharge lamps that are based on previous lamp designs for the NASA Gravity Probe B, Wind and Hubble missions. The two lamps are housed in one enclosure and each lamp requires 4 W of unregulated power. The lamp assembly is passively cooled via radiative coupling of the assembly walls to the environment. Signal from the bulbs is coupled into one fiber bundle per lamp via a focusing lens. The two fiber bundles each contain 60 individual, fused silica, 200-µm core diameter fibers. These bundles lead to a crossover assembly, where half of each fiber bundle is rerouted to each of the MIGHTI sensors (A and B). Each sensor then receives a fiber bundle containing 30 fibers guiding red and 30 fibers guiding green signal. These “bicolored” fiber bundles interface with the calibration optic assembly shown in Figure 3. This assembly includes a fold mirror, an off-axis parabolic mirror to collimate the signal out of the fiber, an interference filter with a bandpass from 540-650 nm and a holographic diffuser. The filter rejects any lamp signal that would contaminate the NIR channels of MIGHTI when the calibration lamps are on. The holographic, fused silica diffuser spreads the signal over approximately 20° in angle, overfilling the atmospheric beam angles, and is located near the beam splitter cube in the entrance optics shown in Figure 4. This beam splitter superimposes 5% of the calibration lamp signal onto the atmospheric signal. A false color image taken with the MIGHTI-A detector is shown in Figure 7. It shows the fringe patterns formed by the krypton and neon calibration lines and on the bottom right the locations of the five NIR filters.

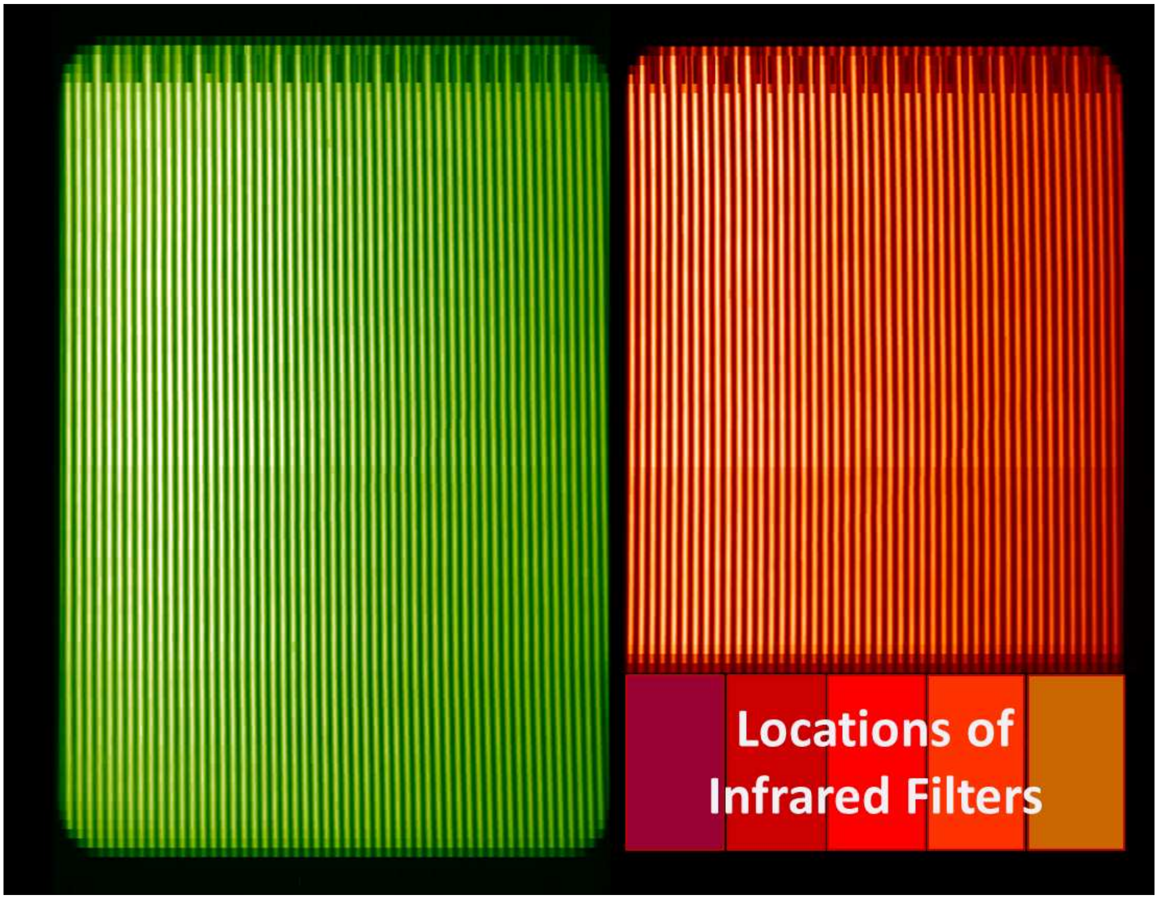

Fig 7: False color image of calibration lamp signal taken with MIGHTI-A. This image is binned by 2 pixels in the vertical and 2 pixels in the horizontal dimension. On orbit, the binning will be 16 × 2 (vertical × horizontal) and the vertical dimension will cover the tangent point altitudes between about 90-300 km. The top of both red and green images show the periodic notch pattern that is inscribed onto one of the gratings of each interferometer. This pattern is used to track any residual horizontal image shifts on the CCD detector. The locations of the NIR filters are shown on the bottom right using superimposed rectangles as they are not illuminated by the calibration lamps.

3.3.4 Interferometer

A schematic of the MIGHTI interferometer, shown in Figure 8, receives a telecentric incident beam from the entrance optics of square profile f/9.0 along an edge. The entrance optics forms a 27.0 mm x 15.5 mm image of the Earth's limb on the diffraction gratings located at the ends of the interferometer arms. The interferometer itself is a monolithic DASH design whereby a Fizeau fringe pattern is measured over a fixed path difference interval that is optimized for measuring the Doppler fringe phase shift associated with thermospheric winds. Although the spacer and prism angles are the same in both arms, the arm with the longer path utilizes a thicker field widening prism and thinner air spacer. In this way a DASH interferometer can be thought of as a conventional Spatial Heterodyne Spectrometer with an offset aperture.

Low order Echelle diffraction gratings enable the interferometer to simultaneously process light from spectral bands diffracted from multiple grating orders. Specifically, MIGHTI measures thermospheric winds using the Doppler shift of the atomic oxygen red (630.0 nm, 7th grating order) and green (557.7 nm, 8th order) lines. Within each of these spectral passbands, emission lines of Ne (630.5 nm) and Kr (557.0 nm) from on-board calibration sources can be measured simultaneously to track residual thermal instrument drifts. In addition, MIGHTI measures lower thermospheric O_2 A-band temperatures using a multi-channel photometer approach between 754 and 780 nm. Although interference fringes are not utilized for this temperature measurement, the NIR signal passes through the interferometer (in grating order 6) before reaching the photometer filters located at the detector (Figure 4).

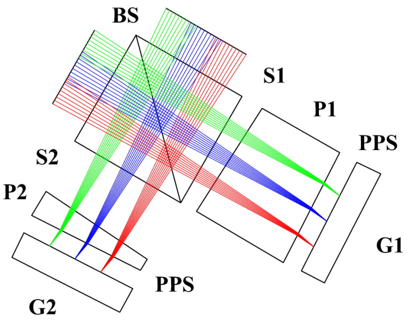

Fig 8: The MIGHTI Interferometer. The arms are terminated by identical low-order Echelle diffraction gratings G1 and G2. BS = N-BK7 cube beamsplitter, S1 = Fused Silica Spacer, S2 = CaF2 spacer, P1 and P2 are N-SF57 field widening prisms, PPS = Plane parallel fused silica spacer. The spacers (not shown) consist of hollow frames that are slotted to allow for differential thermal expansion between the elements they support.

Path difference At center of interferogram Interval	 5.1 cm ± 0.4 cm
Etendue	0.055 cm^2 steradian
Beamsplitter (BS) Material Size Beamsplitting coating	 Schott N-Bk7 42 x 32 x 32 mm 50-50 Hybrid metallic non-polarizing
Wedged Spacers (S1 & S2) Material (Hollow/Slotted) Wedge angle Thickness @ center	 CaF_2 (S2), Fused Silica (S1) 3.402 degrees 16.116 mm (S2), 5.573 mm (S1)
Prisms (P1 & P2) Material Wedge angle Thickness @ center	 Schott N-SF57 6.280 degrees 5.554 mm (P2), 25.103 mm (P1)
Parallel Spacers (PPS) Material (Hollow/Slotted) Thickness	 Fused Silica 5.0 mm nominal
Grating (G1 & G2) Blank material Groove density Blaze angle Material/coating	 Fused Silica 64.285 lines/mm 8.2 degrees Gold on epoxy replica
Cement	Norland 61

Table 2. Interferometer Design Parameters

The interferometer design parameters are shown in Table 2. N-SF57 was chosen as the prism material for its negative dn/dT at 630 nm which compensates for the change in grating groove spacing due to thermal expansion of the fused silica grating substrates. If not compensated, the grating expansion would result in a fringe frequency change with temperature. The materials and thicknesses of the spacers S1 (Fused Silica) and S2 (CaF2) were chosen to compensate the phase shift of the fringes as the arms expand and contract with temperature along their lengths.

N-SF57 is a high dispersion glass for which the optimum thicknesses and angles of the field widening prisms are slightly different for red and green bands. Multi-element prism designs that mitigate the dispersive effects of a single prism were considered but rejected because they were difficult to thermally compensate and more difficult to fabricate. The single prism parameters chosen, shown in Table 2, are a compromise between the red and green optimum values.

3.3.5 Exit Optics

The exit optics are all the optical elements between the interferometer and the CCD detector, which is located immediately behind a mosaic filter, as shown in Figure 4. The purpose of the exit optics is to spatially separate the signal of the green line from the red and infrared components to form two separate images of the fringe localization plane on the CCD focal plane array. Lens L4 collimates the light from the fringe localization plane within the interferometer and forms an image of the Lyot stop on the dichroic mirror. The dichroic mirror is a wedge-shaped element that introduces an angular separation between the red/IR and green beams. Its first surface reflects the red beam components (red line and A-band) and transmits the green line signal. Its second surface, which is slightly tilted with respect to the first, reflects the green line signal. The first surface is plane and acts as a simple mirror. The second surface has a weak cylindrical shape to correct for the astigmatism introduced into the green beam by the thickness of the dichroic wedge. Mirror M4 redirects the beams toward the CCD. Lens L5 forms two images of the limb/fringe scene, one green and one red, on the focal plane array. The imaging is accomplished by collimating the signal from the dichroic wedge, which is an image of the entrance pupil and the Lyot stop. Thus, the beam onto the CCD is telecentric. Telecentricity makes the recorded fringe phase less sensitive to temperature drifts of the optical bench, since the first order effect of a camera misalignment in the direction of the beam does not change the fringe spacing (i.e., focus shift is not coupled to image magnification).

A mosaic filter containing seven narrow band interference filters, as shown schematically in Figure 9, is located immediately in front of the CCD. Two filter elements provide narrow spectral filtering for the green and red line images, and the other five elements are for the determination of the A-band shape and the broad band near infrared (NIR) background signal. Three of the NIR channels are located within the spectral region of the A-band while two channels are at slightly shorter and slightly longer wavelengths. Key filter specifications are given in Table 3. The exit optics were designed such that the green signal, which is reflected from the back side of the dichroic wedge is entirely transmitted by the green filter of the mosaic before it forms an image of the fringe/limb scene on one side of the CCD immediately behind the filter. The red line signal and the A-band signal, both of which are reflected by the front side of the dichroic wedge, are transmitted on the other half of the mosaic filter. Since the vertical direction in Figure 9 corresponds to the tangent point altitudes on the limb (perpendicular to the horizon), the signal originating from tangent point altitudes between about 90 km and 140 km passes through the A-band filters, while the signal originating between about 150 km and 300 km is transmitted by the red line filter. Using this geometry, the wind and temperature measurements can be accomplished simultaneously for these two different altitude regions using only one detector array for each MIGHTI field of view. To ensure that the signal levels from the red, green and A-band signals are compatible with the dynamic range of the CCD, the A-band filter peak transmittances were deliberately lowered to about 45%. In addition, the in-band reflection of the A-band filters was minimized by an indium-tin-oxide (ITO) coating to minimize multiple reflections between the filters and the interferometer. The mosaic filter was assembled from individual filters using opaque epoxy resin to avoid cross contamination by angled rays that would otherwise pass through substrate boundaries between filters.

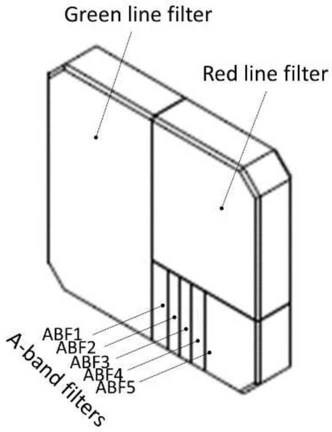

Fig 9: Mosaic filter geometry.

	Red line filter	Green line filter	A-band Filter 1	A-band Filter 2	A-band Filter 3	A-band Filter 4	A-band Filter 5
CWL day [nm]	630.17	557.99	754.22	760.23	762.87	765.28	780.29
Width day [nm]	1.97	1.91	1.92	1.95	1.92	1.93	2.07
CWL night [nm]	630.31	558.02	754.51	760.54	763.17	765.57	780.59
Width night [nm]	1.99	1.90	2.05	2.09	2.05	2.06	2.18

Table 3: Median filter passband center wavelengths (CWL) and spectral widths (full width half maximum) as measured at the CCD pixels with the day and night aperture positions for MIGHTI-A. The values for day and night are different because of the different illumination of the filter. The data for MIGHTI-B filters is similar.

The MIGHTI entrance and exit optics components are made from fused silica, BK7G18, and n-SF6, all of which are radiation hard glasses that show little darkening when exposed to the on-orbit radiation environment.

3.3.6 Camera

MIGHTI uses two actively cooled CCD cameras based on the e2v CCD42-80 back illuminated detector chip. The CCD features a multiband antireflection coating to maximize quantum efficiency and is cooled to -40°C or below to minimize dark current. The 2048 × 4096 pixel format sensor has a pixel pitch of 13.5 μm and is used in frame transfer mode to avoid a mechanical shutter.

Figure 10 shows a cut-away of the camera head as designed by Space Dynamics Laboratory (SDL) in Logan, UT.

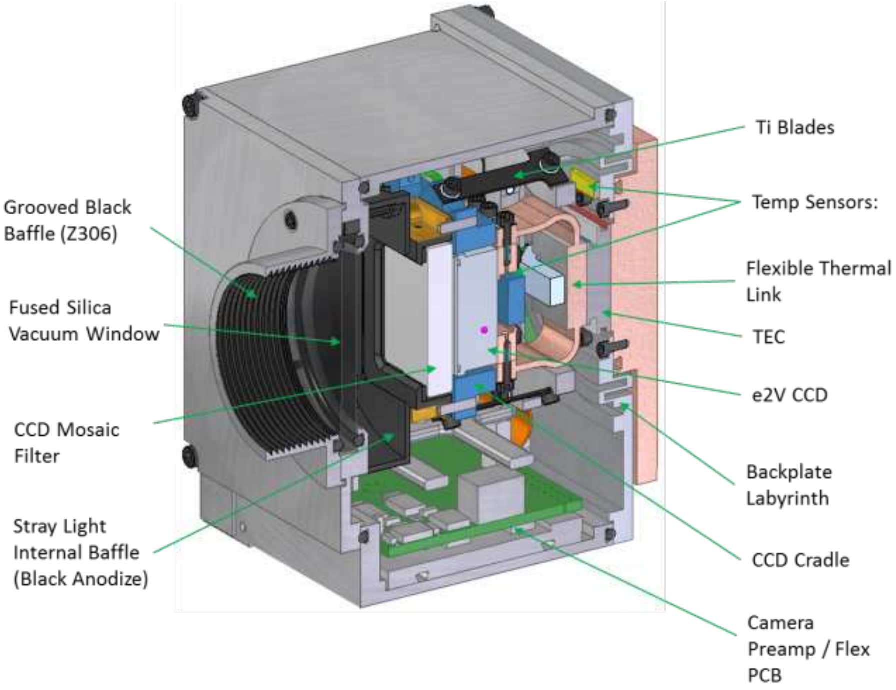

Fig 10: MIGHTI camera head cut-away.

Each MIGHTI sensor uses an identical camera head. The two camera heads are controlled by a single camera electronics assembly also designed and built at SDL.

The CCD is oriented so that the frame transfer direction is parallel to the limb, which minimizes the transfer of pixels with low signal, e.g., at the top of the airglow layer, through areas of high signal, e.g., the maximum of the path integrated airglow layer. The main, as-built performance specifications of the MIGHTI cameras are given in Table 4.

Camera Parameter	Parameter Value
Dark current @ -40°C [electrons/pixel/s]	0.01 (beginning of life)
Read out noise [RMS electrons]	<4.2 (for gain of ~1.65 electrons/digital number)
Gain [electrons/digital number]	~1.65 (two more gains available via command)
Power consumption [W]	11.0 to 12.9 depending on mode and bus voltage
Frame transfer time [ms]	307.5
On chip pixel binning	commandable (on-orbit: 1×1 or 16×2)

Table 4: As-built MIGHTI camera performance

CCD cooling is achieved using a thermoelectric cooler (TEC). The excess heat from the hot side of the TEC is conducted to a double-sided radiator via an ammonia filled heat pipe, as shown in Figure 3.

The camera heads are fitted with vacuum windows so they can be evacuated in the laboratory and cooled to -40°C. This feature allows flight like test conditions on the ground without placing the entire instrument into a vacuum chamber. In addition, the polarity of the TEC can be reversed to heat the CCD to remove condensed contaminants on its surface on-orbit, or to anneal the CCD.

Laboratory measurements showed that the two MIGHTI flight CCDs show a measurable amount of persistence, i.e., increased dark current for pixels that were previously illuminated. A detailed investigation of the persistence at a CCD temperature of -40° C showed that (1) the persistence effect is not present in the dark current after the CCD is cooled from room temperature in darkness; (2) the maximum persistence, or dark current increase, achieved with preceding saturated exposures, is equivalent to about 47 DN (Digital Number output of the analog digital converter) per 60-second exposure which, with a gain of about 1.65 DN per electron, is equivalent to about 1.3 electrons per second per binned pixel (16×2) for MIGHTI-B and about 0.2 electrons per second per binned pixel for MIGHTI-A; (3) after maximizing the persistence effect, this additional dark current decays by about a factor of two after approximately two hours of reading out dark images once every minute; (4) the persistence effect is cumulative, i.e. a dark image taken after one exposure with a non-saturated count rate (e.g. 30,000 DN, with saturation occurring at 2^{16} DN) shows less persistence than a dark image taken after two of the same non-saturated exposures; (5) the difference in persistence between the two detectors is an inherent property of the individual CCDs, not the read out electronics, so that the root cause might be small differences in the manufacturing process that are, for example, dependent on the chip position on the wafer. In summary, the persistence effect in MIGHTI-B, which is about 6 times higher than in MIGHTI-A, is a small fraction of the expected signal levels. Moreover, dark current corrections using dark exposures, taken on-orbit, will provide a partial elimination of this effect due to its long decay time, which is more than the time it takes to complete one orbit. Also, periodic dark exposures will serve as a continuous verification that the persistence effect is not changing on orbit. Changes with mission duration are not expected since persistence has been traced to a constant characteristic of the individual CCD, caused by electron trapping or charge diffusion.

3.4 MIGHTI Heritage

3.4.1 Instrument Heritage

The main heritage of MIGHTI is SHIMMER (Spatial Heterodyne Imager for Mesospheric Radicals), the primary payload of the DoD Space Test Program Satellite STPSat-1. The instrument was designed and built at the Naval Research Laboratory under the direction of its Principal Investigator, Dr. Englert. The SHIMMER team also included the ICON Co-I Dr. Harlander whose main responsibilities included the design of the SHIMMER interferometer and imaging optics, and the support of instrument integration and testing.

The SHIMMER mission was baselined for 1 year and successfully completed 2.5 years of operation in October 2009, when the STPSat-1 mission was terminated for programmatic reasons. At that time the SHIMMER instrument was still working properly and all nominal and extended mission objectives were met. This highly successful instrument measured mesospheric OH and polar mesospheric clouds with high spectral resolution in the near UV. The SHIMMER interferometer is a Michelson interferometer with two fixed gratings terminating the interferometer arms. This modification of the widely used Michelson technique is also known as Spatial Heterodyne Spectroscopy (SHS) and is identical to what is used in the ICON MIGHTI instrument.

Just like the MIGHTI instrument, SHIMMER consisted of an optics assembly including a baffle, entrance optics, interferometer, exit optics, and a TEC-cooled CCD camera. The camera structure was designed by Term Engineering under the direction of Dr. Englert. It allowed operating the

CCD at -40°C in the laboratory by evacuating the camera enclosure and dispersing the heat from the TEC with a second external TEC and a fin/fan assembly.

3.4.2 Algorithm and Calibration Heritage

The algorithm and calibration heritage of MIGHTI is based on SHIMMER and the ground based REDDI instrument (doi:10.1029/2010JD014398, doi:10.1016/j.jastp.2012.07.002). The SHIMMER and REDDI Level 0 to 1 calibration software was developed by Dr. Englert. Heritage algorithms were modified and used for SHIMMER Level-2 and Level-3 data processing to derive geophysical propertied from the observations. SHIMMER Level-2 and Level-3 data processing did not require an inversion, so that the observed wind speed is a simple conversion from the measured and zero-wind corrected fringe phase.

4 MIGHTI Calibration Plan

4.1 Overall Calibration Scheme

4.1.1 Wind Data Calibration

The main steps of the MIGHTI wind data calibration are shown schematically in Figure 11.

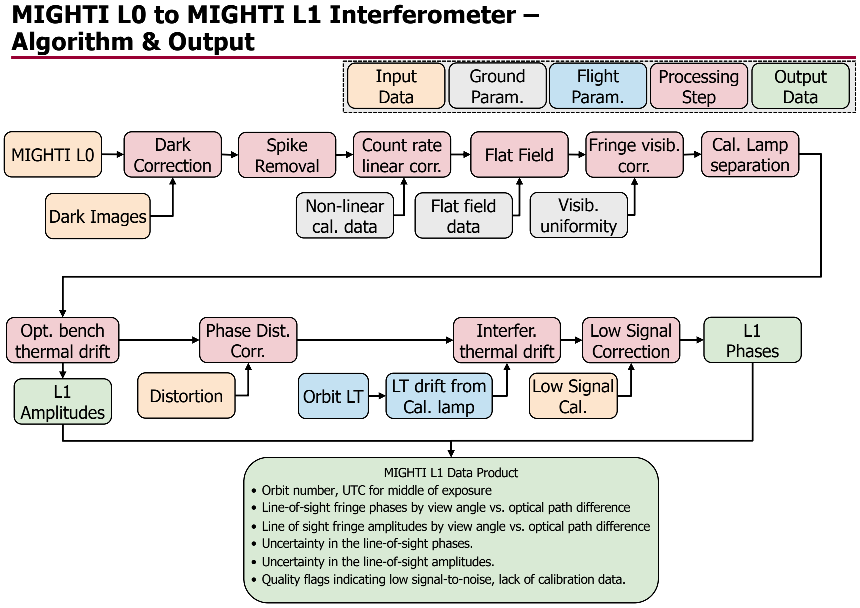

MIGHTI L1 Data Product

- Orbit number, UTC for middle of exposure
- Line-of-sight fringe phases by view angle vs. optical path difference
- Line of sight fringe amplitudes by view angle vs. optical path difference
- Uncertainty in the line-of-sight phases.
- Uncertainty in the line-of-sight amplitudes.
- Quality flags indicating low signal-to-noise, lack of calibration data.

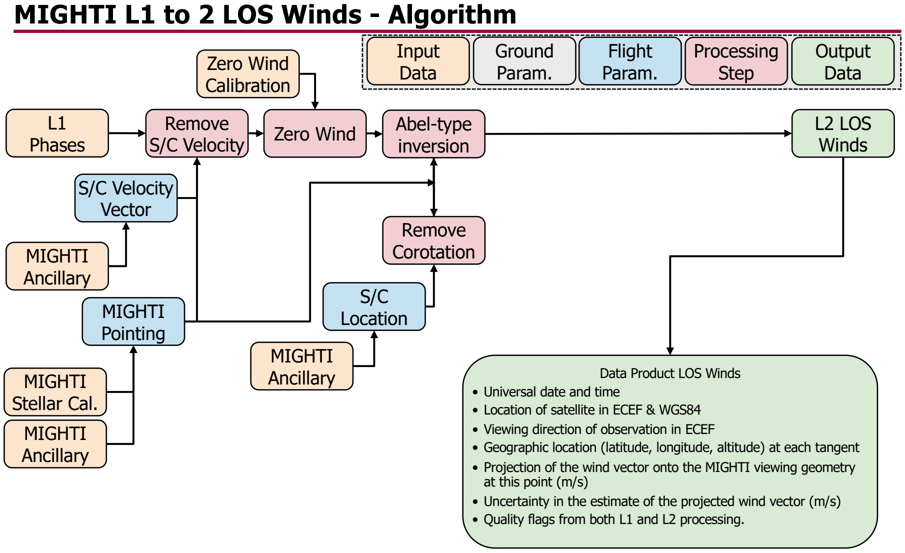

Data Product LOS Winds

- Universal date and time
- Location of satellite in ECEF & WGS84
- Viewing direction of observation in ECEF
- Geographic location (latitude, longitude, altitude) at each tangent
- Projection of the wind vector onto the MIGHTI viewing geometry at this point (m/s)
- Uncertainty in the estimate of the projected wind vector (m/s)
- Quality flags from both L1 and L2 processing.

Fig 11: Overview of MIGHTI L0 to L1 and L1 to L2 wind data processing steps.

Raw MIGHTI wind data is dark current corrected using dark exposures taken close in time. Several dark images are used to identify and remove cosmic ray induced spikes in any individual dark observation. A spike removal algorithm is used to identify and remove cosmic ray induced spikes and spikes in the fringe patterns that result from stars in the field of view, utilizing fringe image interpolation techniques similar to the ones used for the SHIMMER data. After a small count rate non-linearity correction, ground-based flat field data, measured in the laboratory using a spatially homogeneous source is used to perform a flat field correction and pre-launch observations of spectrally narrow sources are used to correct for instrument related fringe visibility variation, which alters the fringe amplitude as a function of optical path difference. For observations that include calibration lamp signal, in addition to the atmospheric signal (periodic calibration orbits), the calibration lamp signal is separated using standard Fourier techniques. The next step is the correction of the fringe image drift (horizontal displacement of the image on the CCD) using the signature of the periodic notch pattern that is inscribed on one of the interferometer gratings. At this point, the L1 fringe amplitude versus tangent altitude is created.

In order to obtain the fringe phases, a phase distortion correction is applied, which is based on the fringe distortion of the calibration lamp fringes. These calibration data are measured routinely on orbit and show a slight variation in time, which is why this correction is time dependent. The effect of the thermal drift of the interferometer is corrected using routine on-orbit measurements of the calibration lamp signal, because this effect depends on the thermal profile along the orbit, which changes with beta angle, season, etc. Finally, a “low-signal” correction is performed, before determining the L1 fringe phase, which contain the Doppler shift information. The low-signal effect is a behavior that was unexpected, but recognized and characterized using on-orbit data. In short, an increasing fringe phase shift was observed for decreasing airglow signal from the limb, which is most likely a result of an imperfect CCD readout. Special observations with different integration times are now performed regularly to track this effect and enable its accurate correction.

The L1 fringe phases versus altitude are subsequently used to obtain line of sight wind speeds. As a first step, the spacecraft (S/C) velocity is removed, which requires the S/C velocity vector and the MIGHTI pointing angles. The MIGHTI pointing is traced back to an early-orbit observation of the Pleiades star cluster, which provided accurate, post-launch information on the pointing information of all parts of the field of view with respect to the ICON star trackers, which are used together with the GPS data to continuously determine the S/C orientation with respect to the earth. Next is the zero-wind calibration, which calibrates the wind data to an absolute scale, by defining the phase differential that corresponds to zero atmospheric motion. The original plan for this calibration was to point MIGHTI into the ram and wake, observing the same atmospheric region within about 10 min, under the assumption that the wind does not change in that time period. The MIGHTI team found, however, that the accuracy of this relatively short measurement, in addition to the uncertainty arising from the operation with different attitudes, including the associated thermal changes, was not satisfactory. Thus, for the first versions of the Level 2 wind products, zero wind was determined by matching averaged winds to the HWM empirical wind model data. Starting with Version 5 of the Level 2 wind products, the zero-wind correction no longer uses any *a priori* reference, but a self-consistent zero wind that is determined using the fact that, averaged over one precession cycle, the wind measurement for the ascending nodes and descending nodes should be the same. This is fundamentally similar to the use of ram and wake observations, because the viewing direction of the MIGHTI sensors is “rotating” with respect to the equator for the two nodes, and the large averaging time (~48 days) together with the spatial averaging removes any short term or localized, geophysical variations. Finally, an Abel-type inversion is performed to retrieve the altitude dependent line of sight (LOS) wind speeds. Combining collocated and near simultaneous observations of MIGHTI-A and MIGHTI-B yields wind vector profiles and ultimately the cardinal winds versus altitude.

4.1.2 Temperature Data Calibration

The main steps of the MIGHTI temperature data calibration are shown schematically in Figure 12.

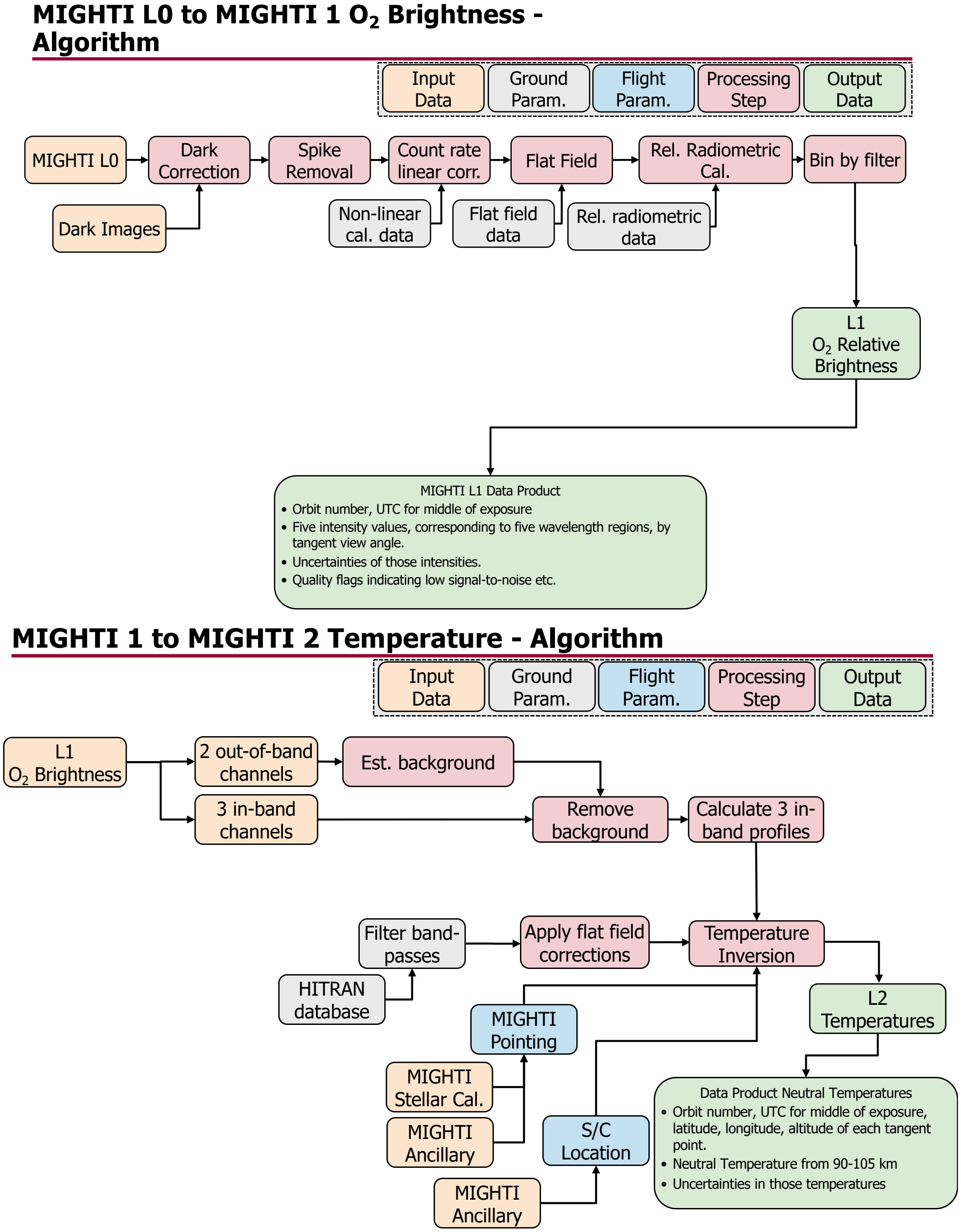

Fig 12: Overview of MIGHTI L0 to L1 and L1 to L2 temperature data processing steps.

The steps to obtain calibrated radiances to inform the temperature retrieval are described in the first table of Figure 12 data. First, the raw MIGHTI data is dark and spike corrected and a small count rate non-linearity is corrected, as described above for the wind data. An initial flat field and relative radiometric calibration is performed using laboratory measurements and a relative sensitivity factor between MIGHTI-A and MIGHTI-B, which was determined on orbit, taking advantage of the fact that the sensors are routinely viewing the same tangent point regions about 7 minutes apart. The final multi-channel emission brightnesses are determined by averaging detector pixels for each channel behind the respective filter elements (see Figures 7, 9). The temperature retrieval follows, as shown in the second diagram of Figure 12. In the first step in this retrieval, the background contributions to the on-band channels are estimated using the two of-band channels and are subsequently removed. This technique was put in place due to pre-launch concerns about stray light from the bright disk of the earth, but this effect turned out to be small when compared to other airglow emissions (see Stevens et al., Space Science Reviews, 2022). However, the MIGHTI team noticed significant post-launch changes in the flat field relative to the pre-launch characterization, which might be a result of the long (~2 year) storage time of the ICON observatory. To quantify these changes, observations of the Rayleigh-scattered solar spectrum were performed below the typical tangent heights of the MIGHTI field of view and the insights gained from these special observations were used to determine a modified flat field correction. Finally, an Abel-type temperature inversion is performed using temperature dependent band data from the HITRAN data base. Corresponding altitude data for the temperature profiles are determined similar to the wind data, as described above.

4.2 Pre-flight Calibration Plans

4.2.1 MIGHTI Pre-flight Calibrations

The main MIGHTI pre-flight calibration data was gathered during a laboratory campaign at the Space Dynamics Laboratory, for which the sensors were installed in a T/Vac chamber, so they could be operated as close as possible to flight conditions. During these laboratory measurements, the sensors could be illuminated using an integrating sphere, through one of the chamber windows. This set-up allowed for the illumination with spectrally narrow sources, such as neon and krypton lamps, or the MIGHTI sensors could be used as detectors of a conventional Fourier transform spectrometer, which allowed the full spectral calibration of the sensors. All measurements were conducted in the main operating modes, “Day”, and “Night” which have different aperture settings (A1 and A2), resulting in different sensitivity and spectral characteristics. The absolute spectral calibration was performed using a NIST traceable SRM-2065 transmission standard. It is worth noting that MIGHTI had no requirement to perform absolute radiometric calibration, because neither wind nor temperature retrievals are depending on such absolute sensitivity knowledge.

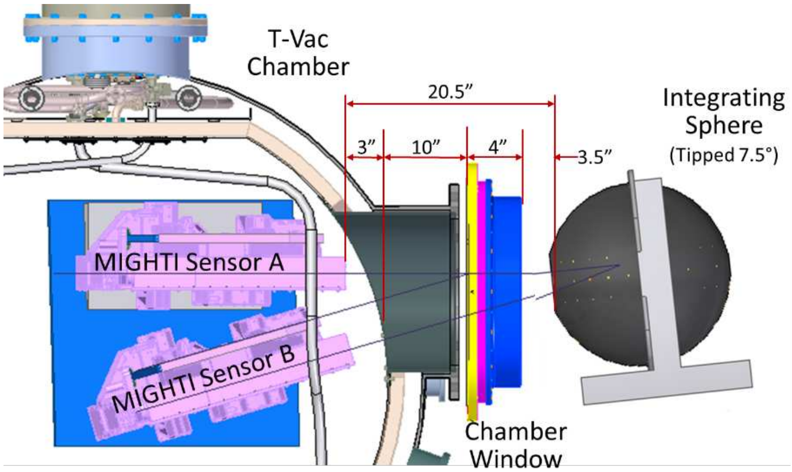

Fig 13: Schematic of calibration set-up

Using the set-up shown in Figure 13, the spectrally dependent flat fields (incl. CCD row-to-row sensitivity cross calibration) were determined. All other calibration data is obtained on orbit, either at the beginning of the mission (star calibration for the pointing), periodically during normal science mode (e.g. dark, phase distortion, thermal drift), or during special operations (e.g. small signal correction, temperature channel flat field corrections).

4.2.2 Instrument Description

The instrument configuration and subsystems are described in detail above in Section 3.3. (Instrument Subsystem Descriptions). In short, MIGHTI images the earth’s limb and makes three fundamental observations: the Doppler shift of the atomic red-line airglow, the Doppler shift of the atomic green-line airglow, and the multispectral sampling of the molecular oxygen A-band. These observations are subsequently used to determine thermospheric line of sight (LOS) wind profiles and temperature profiles. Given that a single sensor can only determine LOS wind speeds, two sensors are deployed on ICON with perpendicular viewing directions, so that the combination of the measurements can be used to derive vector wind profiles and ultimately cardinal winds.

MIGHTI does not use consumables, so that there is no lifetime limitation from a limited supply of fuel, coolant or the like. The aging of calibration data is also not an issue, because most of the calibration data is determined regularly on-orbit and absolute radiometric calibration is not required. One issue that could impact the long-term data quality is the radiation induced dark current and hot pixel increase of the CCD focal plane arrays. This issue was anticipated and MIGHTI has the ability to reverse the polarization of the thermoelectric coolers that normally cool the CCDs. This way, the coolers can heat the CCD in order to “anneal” its pixels. This is a process where the thermal energy in the crystals allow the lattice structure to “heal” from damage inflicted by the on-orbit radiation environment. Once the CCD performance deteriorates to the point that Level 2 wind retrieval uncertainties approach levels that exceed requirements, the project will consider annealing the CCDs.

4.3 In-flight Tracking of Short-Term Changes

The most important short-term change of the MIGHTI instruments is the thermal drift that occurs during every orbit. The thermal drift is caused by the changing solar illumination conditions along the orbit and is highly periodic. There are two main components to the drift. The first is the shift of the image on the CCD, which can be mistaken for a fringe phase change and therefore a Doppler shift. This effect is tracked by locating the notches that are inscribed on one of the gratings in the interferometer and which are imaged on the CCD. The second drift is the thermal change in Littrow frequency of the interferometer. This effect is tracked every day using a so-called "calibration orbit," during which the calibration lamps are turned on. The stable frequency of the stationary calibration lamps allows the quantification and correction of this thermal drift effect.

4.4 Long-term Absolute Calibration Tracking (Re-Calibration)

There are several long-term calibration aspects that are tracked for MIGHTI, most importantly the long-term temporal variations of the small-signal correction, the long-term changes in the phase distortion and any drift in the zero wind. All these effects are routinely tracked, quantified and adjusted in the data analysis that is executed in the ICON science data center, to ensure that the calibration is up to date. MIGHTI does not require any absolute radiometric calibration and so effects such as glass darkening or performance drift of optical coatings that would affect overall optical efficiency of the instrument are not independently tracked.

4.5 Validation

Validation of MIGHTI wind and temperature data is performed using independent ground-based and space-based instrumentation. Successful validations of the wind product, showing their high quality, were performed using ground-based Fabry-Perot interferometers (see doi: 10.1029/2020JA028726) and specular meteor radars (doi: 10.1029/2020JA028947), followed by the space-based Fabry-Perot interferometer on the NASA TIMED mission (TIDI) (doi: 10.1029/2021JA029904). A thorough validation of the MIGHTI temperature product using ground-based sodium LIDAR data and the temperature product of the SABER instrument on the NASA TIMED mission has also yielded good agreement and is published by Stevens et al., Space Science Reviews, in press, 2022. Independent validations of the MIGHTI data products are performed by the wider domestic and international science community, using the publicly available data.

5 MIGHTI Measurement Algorithm Description

5.1 Theoretical basis

The theoretical basis, or physical phenomenon, that is exploited for the MIGHTI wind measurement is the Doppler Effect, affecting two specific, thermospheric airglow emission lines, namely the quasi-monochromatic, atomic oxygen red- and green-lines at λ=630 nm (O(1D → 3P)) and λ=557.7 nm (O(1S → 1D)). These lines are produced following multiple excitation mechanisms that depend on both altitude and local solar time. Details on excitation mechanisms of these airglow emissions can be found in the literature, e.g. in publications by Frederick et al. [1976], Solomon and Abreu [1989], or Bates [1990, 1992], and references therein.

The bulk motion of the atmosphere, or wind, contributes to the relative speed of the emitting atoms with respect to the ICON satellite. Thus, the detected wavelength of the airglow emissions is Doppler-shifted by $\Delta\lambda=\lambda_0 \cdot v/c$, where λ_0 is the rest wavelength of the emission line (relative speed of zero between the emitter and the detector), v is the relative speed between the emitter and the sensor along the direction of the line of sight of the instrument, and c is the speed of light in vacuum (doi: 10.1364/ao.46.007297). After correction for the satellite velocity, the wind speed can be retrieved from this Doppler shift (doi: 10.1007/s11214-017-0359-3).

The raw MIGHTI wind observations, that are used to retrieve this Doppler shift, are based on a two-path Michelson-type interferometer that images a range of optical path differences in one dimension and the tangent point altitude in the second dimension of a 2D focal plane detector. The Doppler shift information of the observed, quasi-monochromatic atmospheric emission source is contained in the phase of the Fizeaux fringe pattern that is detected along the optical path difference interval (doi: 10.1007/s11214-017-0358-4, see also Section 5.1.1).

The theoretical basis, or physical phenomenon, that is exploited for the MIGHTI temperature measurement is the temperature-dependent change of the ro-vibrational spectral band shape of the molecular oxygen (O_2 b $^1\Sigma_g^+(0)$ — X $^3\Sigma_g^-(0)$) A-band near 760 nm [Noxon, 1968]. Figure 14 shows this temperature dependence. The band is excited through collision with O(1D), resonance fluorescence, or a 2-step chemical reaction involving atomic oxygen called the Barth process [Bucholtz et al., 1986; Sheese et al., 2010]. Because molecular oxygen is in thermal equilibrium at the lower-thermospheric altitudes that are observed by MIGHTI, the spectral band shape carries the information on the atmospheric temperature, which determines the population of the ro-vibrational states, and therefore the line strengths within the band (doi: 10.1007/s11214-017-0434-9).

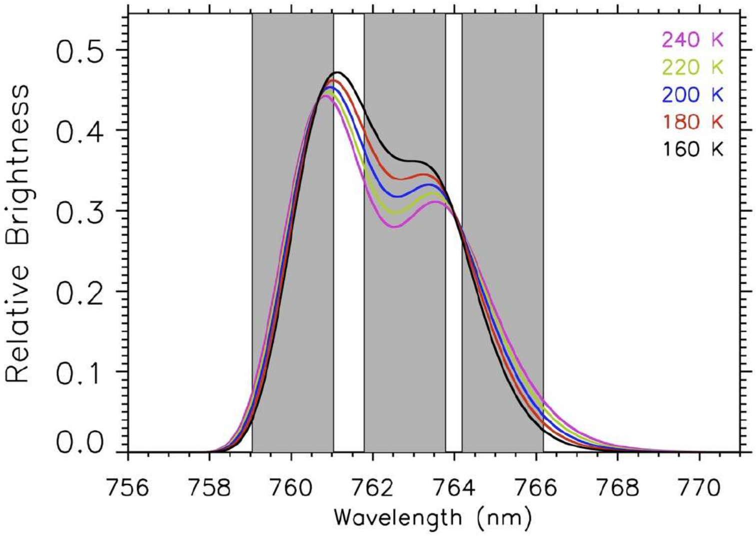

Fig 14: Curves illustrate the temperature dependence of the oxygen A-band. The gray areas indicate the MIGHTI on-band filter positions (doi: 10.1007/s11214-017-0434-9).

The MIGHTI temperature observations are based on a simple, narrow-filter-based multispectral observation of the molecular oxygen A-Band, as illustrated in Figure 14. The relative brightnesses in the filter channels are used to retrieve the vertical temperature profiles using an Abel-type inversion (doi: 10.1007/s11214-017-0434-9, see also Section 5.1.1).

5.1.1 Conversion of Instrument Signals to meters/second (wind) and Kelvin (temperature) and corresponding Measurement Equations

For the wind observation, the measured monochromatic interferogram signal can be written as a function of pixel row and column, I(x, y)

$$I(x,y) = \underbrace{\int_0^\infty B(\kappa)\left(t_A^2(\kappa,x,y) + t_B^2(\kappa,x,y)\right)d\kappa}_{\text{Non-Modulated Term}} + \underbrace{\int_0^\infty 2B(\kappa)\varepsilon(\kappa,x,y)t_A(\kappa,x,y)t_B(\kappa,x,y)\cos\left[2\pi\kappa x + \Theta(\kappa,x,y)\right]d\kappa}_{\text{Modulated Term}}$$

Eq. 1

In this equation, B(κ) is the fringe frequency dependent spectral density, [t_A(κ, x, y)t_B(κ, x, y)] accounts for the spectral and spatial dependence of the signal transmission through the instrument optics via the two interferometer arms (A & B) as well as the quantum efficiency of the detector pixels, ε(κ, x, y) is the fringe modulation efficiency, and Θ(κ, x, y) is a phase distortion term. For a small wavelength change in the quasi-monochromatic source B(κ) (=Doppler shift), the recorded fringe frequency will change, which, in turn, causes a cumulative phase change at a larger optical path offset, which is where MIGHTI makes its observations.

The relationship between the fringe phase and the wind speed is simply determined by:

$$\Delta\phi = \frac{2\pi d}{\lambda c} v$$

Eq. 2

where $\Delta\Phi$ is the phase shift in [rad], v is the corresponding wind speed in [m/s], defined as positive towards MIGHTI, c is the speed of light in [m/s], λ is the rest wavelength of the emission in [m], and d is the optical path difference in [m], which is "frozen" into the monolithic interferometer.

The line-of-sight, limb-sounding-geometry observations are subsequently inverted using an Abel-type inversion.

For the temperature measurements, a forward model is created, which fundamentally consists of a temperature profile, a volume emission rate profile and a path length matrix that is consistent with the limb-sounding geometry. The multi-spectral, on-band emission brightness measurements allow a least-squares fit algorithm to find the best fit of the temperature and brightness profile, yielding the temperature data in Kelvin, based in the band shape data published in the HITRAN data base (doi: 10.1007/s11214-017-0434-9).

5.1.2 Determination of Atmospheric Tides from MIGHTI Winds and Temperatures

The atmospheric tides are determined by fitting a set of functions to a set of MIGHTI winds and temperatures retrieved over a particular length of time. That time is determined by the precession of the orbit, during the period of which MIGHTI visits all combinations of local-time, latitude and longitude available to it from its orbit.

5.1.2.1 Determination of Tides

Solar tidal variations in atmospheric variables such as winds, temperature and pressure at a given height and latitude are commonly expressed in the form

$$A_{n,s} \cos(n\Omega t + s\lambda - \varphi_{n,s}) \qquad \text{Eq. 3}$$

where $A_{n,s}$ is the amplitude; n = 1, 2, 3 refers to diurnal, semidiurnal and terdiurnal periods, respectively; $\Omega = 2\pi\ d^{-1}$; s is the zonal wavenumber; λ is longitude; and $\varphi_{n,s}$ is the phase (time of amplitude maximum at $\lambda = 0$, or longitude of maximum at t = 0). Setting the quantity in parentheses equal to a constant and differentiating yields the zonal phase speed of the tide, $C_{ph} = -n\Omega/s$. A solar-synchronous tide that follows the westward motion of the Sun to a ground-based observer ($-\Omega$, i.e., s = n), is traditionally referred to as a migrating tide; otherwise it is solar-asynchronous and is said to be non-migrating (Chapman and Lindzen, 1970). By accumulating MIGHTI winds and temperature data for ~35-45 days, tidal phases and amplitudes can be estimated for each tidal component from 94 km to 106 km and ~250 km [Cullens et al., 2020 and Forbes et al., 2022].

5.1.2.2 Determination of Hough Mode Extension (HME) fits to tides

Hough's original work in 1898 presented a critical mathematical representation of oscillations on a rotating earth as an eigenfunction-eigenvalue problem. The eigenfunctions are solutions to Laplace's tidal equation and provide the latitudinal structures, whereas the eigenvalues are related to the depth of the oscillating fluid. The eigenvalues comprise an orthogonal set of functions that can be fit through a least-squares method to any appropriate dataset (Hough, 1898). However, it is not physically meaningful to fit Hough functions to winds. To enable fits that include self-consistent relationships between perturbation fields in temperature, zonal, meridional and vertical wind, and density (T, u, v, w, ρ), the Hough Mode Extension (HME) into the dissipative thermosphere was developed by Lindzen et al. (1977) and Forbes and Hagan (1982). The HMEs are computed using the GSWM with zero-velocity background winds and global mean vertical temperature and density profiles derived from the MSISE90 empirical model (Hedin, 1991). Each HME maintains a self-consistent amplitude and phase relationship for the perturbation fields in temperature, zonal, meridional and vertical wind, and density (T, u, v, w, ρ). HMEs are arbitrarily calibrated in amplitude to yield a maximum perturbation horizontal wind speed of 10 m/s (either zonal or meridional, whichever is larger) at 93 km. Absolute values of phases are also arbitrary. HME fitting involves finding a single complex normalizing factor for the HMEs that determines absolute amplitudes and phases for all variables that best fit the input data in a least-squares sense. Figure 15 shows structures of amplitude and phase in zonal wind tides for the DW1, SW2, and DE3 HMEs. These also show the first symmetric and first antisymmetric HMEs, respectively. For antisymmetric HMEs, antisymmetry enters through the phases.

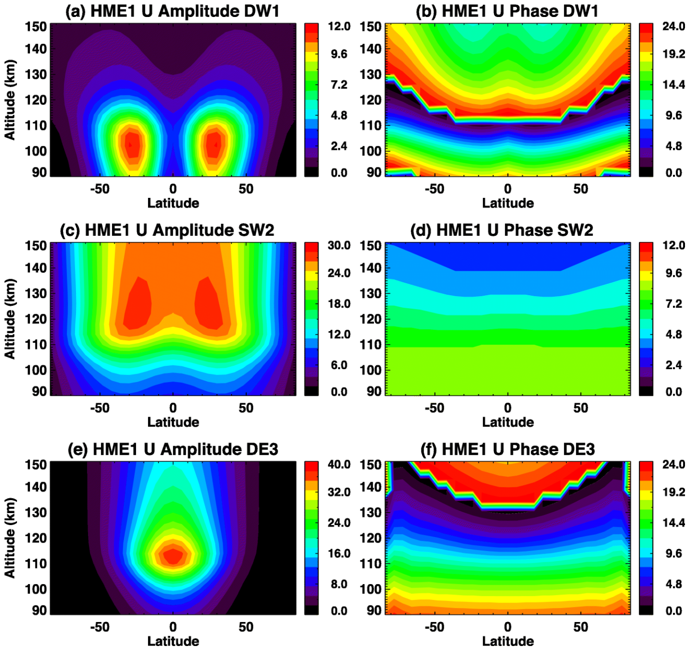

Fig 15: First symmetric HME amplitudes and phases for zonal wind (U) for a, b DW1; c, d SW2; and e, f DE3. HMEs are arbitrarily calibrated in amplitude to yield a maximum perturbation horizontal wind speed of 10 m/s (either zonal or meridional, whichever is larger) at 93 km. Absolute values of phases are also arbitrary.

Figure 16 shows sample results of DE3 tidal amplitudes in V05 temperature and V05 zonal winds. Using MIGHTI tidal measurements (Fig. 16a and c) in 10ºS to 40ºN, global DE3 tides are estimated based on HME. HME results are shown in Fig. 16b and 16d. For this sampled result, winds and temperature data are accumulated over 45-day window for HME fits.

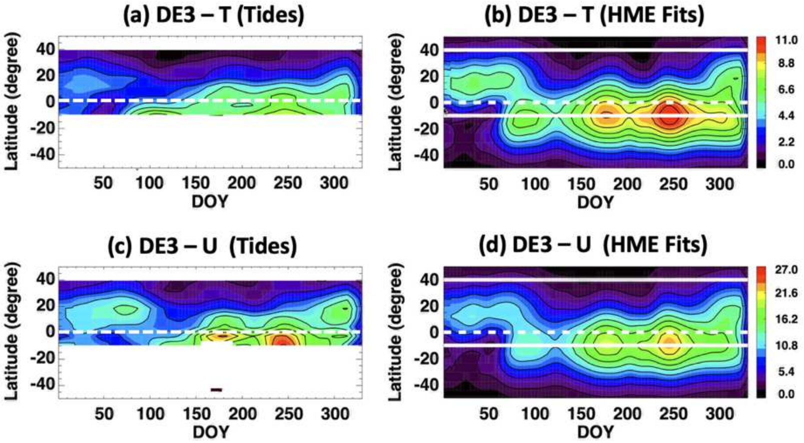

Fig 16: MIGHTI DE3 amplitudes in (a) temperature and (c) zonal wind at 98 km in 2021. Amplitudes of DE3 HME fits in (b) temperature and (d) zonal winds at 98 km in 2021.

5.2 Signal Estimates and Error Analyses for Subsystems

5.2.1 MIGHTI Wind Signal Estimates and Error Analysis

Before launch, volume emission rates (VER) for the oxygen red and green lines were determined using independent measurements from WINDII, at solar minimum conditions. These rates, for noon and midnight are shown in Figure 17 (doi: 10.1007/s11214-017-0358-4). These volume emission rates, which are based on solar minimum conditions, provided the baseline that guided the instrument design, testing and verification.

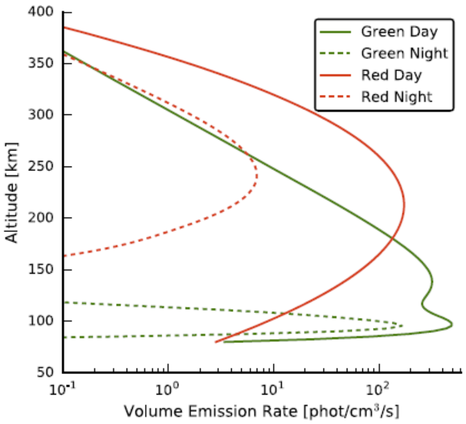

Fig 17: Representative solar-minimum airglow volume emission rate profiles used for the pre-launch design and testing efforts.

Post-launch, on-orbit wind measurement uncertainty estimates are reported for each profile individually as part of the data product. The uncertainties are, in part, depending on the atmospheric signal strength, so that in regions of low airglow volume emission rate, such as at the edges of the airglow layers or at the terminator, larger errors are encountered.

Given the measurement technique, the Abel-type inversion, the calibration approach, and the combination of MIGHTI-A and MIGHTI-B data to obtain altitude profiles of cardinal winds, several uncertainties, with different correlation times are intrinsic to the MIGHTI wind product. The values for each are included in each wind profile and the relevant explanations of the uncertainties are included in the published netCDF files. In the following, we reproduce the explanation of the 1-sample, 1-day, and total precision for the line-of-sight wind product.

- The **"1 sample"** error variable quantifies errors that are uncorrelated from one exposure to the next, dominated by shot noise and dark noise in the detectors. The correlation time of this error source is 30-60 seconds (i.e., the measurement cadence). The reported error is estimated from the fringe intensity and background. This is the recommended variable to use for analyses of wind fluctuations within a single day and a single altitude (e.g., gravity waves). Because the Level 2.2 data (cardinal winds) include interpolation of Level 2.1 data (line of sight winds), some correlation remains between consecutive samples. Errors are slightly correlated across small altitude gaps as a result of the inversion.
- The **"1 Day"** error variable quantifies the error introduced by daily calibrations, which is correlated for an entire 24-hour period (00:00 - 23:59 UT). This is estimated from the magnitude of fluctuations in the daily-averaged fringe phase, propagated through the inversion. Errors in day mode and night mode are nearly uncorrelated. For studies pertaining to atmospheric tidal modes that combine data from many days, this error can be treated as uncorrelated across time.
- For robust error propagation, users are encouraged to consider the individual error variables: "Precision_1_Sample," "Precision_1_Day," and "Accuracy." The "Wind_Error" or **“total precision”** variable is included for backwards compatibility and is equal to the quadrature sum of the "1 Sample" error and the "1 Day" error. This is the recommended uncertainty to use for analyses that collect data from several weeks and compute perturbations from the mean (e.g., for estimating tides and planetary waves). This error is uncorrelated across time lags larger than 24 hours. Errors are slightly correlated across small altitude gaps. Errors in day mode and night mode are nearly uncorrelated.

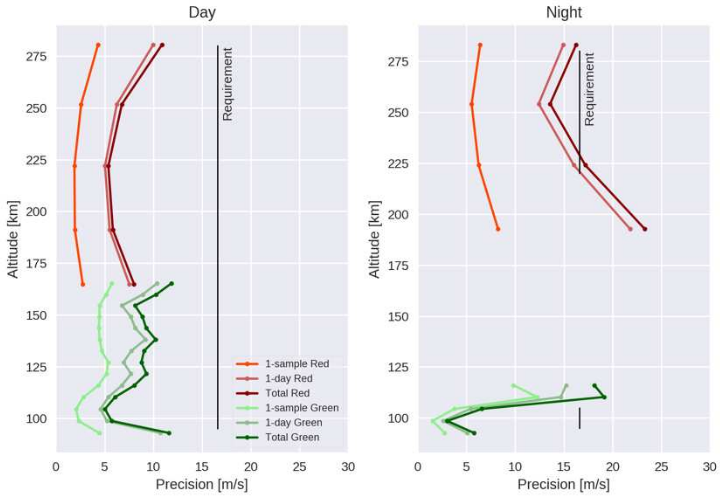

Fig 18: MIGHTI-A and MIGHTI-B averaged precision numbers for 24 days in early 2021. The vertical line indicates the ICON wind precision requirements and corresponding altitude regions. Values are determined for a horizontal resolution of <500 km and the vertical resolutions of 30 km (5 km) for the middle (lower) thermosphere, corresponding to the ICON mission requirements.

Figure 18 shows average wind uncertainties determined using 24 days of data in early 2021, including all local times, i.e. including low and high airglow signal cases. The illustration shows that, on average, the mission requirements are being met, with the exception of a ~1 m/s violation in total precision at the bottom of the nighttime red line requirement (z=225 km).

Going forward, the evolution of the wind uncertainties is expected to be influenced predominantly by two effects, namely the increasing airglow signal, expected from the increase in solar activity, and the deterioration of the MIGHTI focal planes, due to the on-orbit radiation environment. The second effect can be mitigated by annealing the CCD, which is a capability that MIGHTI was specifically designed for. In particular, the MIGHTI CCD coolers can be used to heat the CCD on orbit, a technique that has been used on previous missions with similar CCD detectors, such as the Hubble Space Telescope and the NRL EIS instrument (EUV Imaging Spectrometer on HINODE).

5.2.2 MIGHTI Temperature Signal Estimates and Error Analysis

Similar to the wind product, conservative VER estimates were used for the temperature observation to guide instrument design and pre-launch performance verification. These estimates are shown in Figure 19 and are based on previous observations from flight experiments (Stevens et al., 2018).

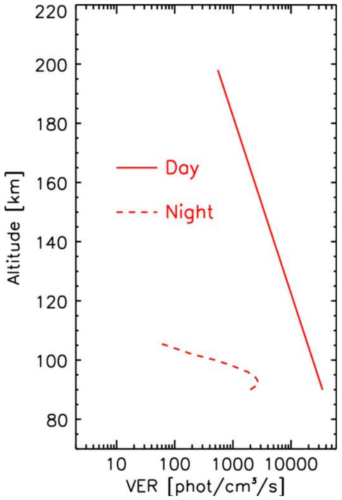

Fig 19: Average volume emission rates of the oxygen A-band used for the MIGHTI instrument design and pre-launch requirements verification.

In-flight performance has been evaluated and representative results are shown in Figure 20 (or Figure 23 from Stevens et al., 2023). The uncertainties are split into the statistical uncertainties (precision) and bias, or systematic uncertainties (accuracy). For comparison, the ICON required precision is 12 K. While there is no explicit accuracy requirement leveraged on MIGHTI temperatures, the systematic uncertainty can be different between day and night, so that scientific investigations that use both day and night data require knowledge of the accuracy estimate shown in Figure 20. MIGHTI measures A-band emission to 140 km and daytime temperature retrievals from the MIGHTI-A detector were extended from 127 km to 135 km in Version 06 (v06) of that product.

Temperature retrievals near the solar terminator pose a unique challenge for MIGHTI primarily because the instrument switches from “nighttime” mode when the aperture is fully opened to “daytime” mode when the aperture is only open 15%. These temperature data near the solar terminator are often unreliable and it was empirically determined that daytime images with solar zenith angles less than 90 degrees be removed from processing and nighttime images with solar zenith angles greater than 100 degrees be removed in v06.

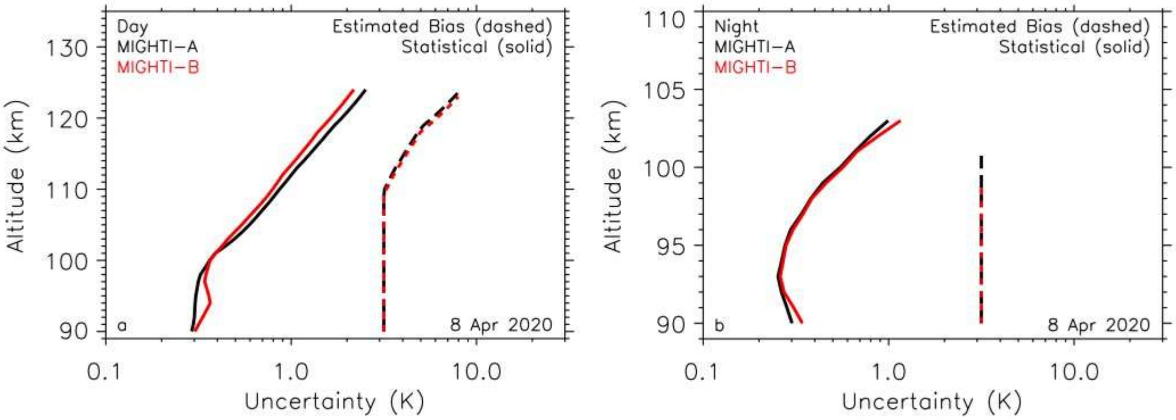

Fig 20: (left panel) Average statistical (solid) and estimated bias or systematic (dashed) uncertainties for daytime MIGHTI-A and MIGHTI-B temperature observations. The estimated systematic uncertainty is due to uncertainty in MIGHTI flat fields (all altitudes) as well as the uncertainty in the contributions from above the top layer of the retrievals (above ~110 km), which start near 140 km. The uncertainties are averaged over the indicated day. (right panel) Same as left panel, except for nighttime observations.

5.3 Preflight Calibration Algorithms

There are no pre-flight calibration algorithms that are different from the calibration that is performed routinely with the flight data. As described above, critical calibration data was gathered pre-launch, such as the spectral flat fields and the interferometer optical path difference (variable "d" in equation 2, above). These data are used in the calibration activities described earlier.

The preflight calibration of the IR channels from which we infer temperature was revised with data obtained during special operations on orbit. The re-calibration of these five channels is discussed in the paper describing the v05 temperature product (Stevens et al., 2023).

References

Bates D.R., Excitation and quenching of the oxygen bands in the nightglow, Planet. and Space Sci., 36, 9, 875-881, doi: 10.1016/0032-0633(88)90093-1, 1988.

Bates D.R., Oxygen green and red line emission and O_2^+ dissociative recombination, Planet. Space Sci., 38, 7, 889-902, 1990.

Bates D.R., Nightglow emissions from oxygen in the lower thermosphere, Planet. Space Sci., 40, 2/3, 211-221, 1992.

Bucholtz A. W.R. Skinner, V.J. Abreu, P.B. Hays, The dayglow of the O_2 atmospheric band system, Planet. Space Sci., 34, 11, 1031, doi: 10.1016/0032-0633(86)90013-9, 1986.

Englert, C.R., Harlander, J.M., Marr, K.D., Harding, B.J., Makela, J.J., Fae, T., Brown, C.M., Ratnam, M.V., Rao, S.V.B. and Immel, T.J., 2023. Michelson Interferometer for Global High-Resolution Thermospheric Imaging (MIGHTI) On-Orbit Wind Observations: Data Analysis and Instrument Performance. *Space Science Reviews, 219(3)*, p.27. DOI: 10.1007/s11214-023-00971-1

Forbes J. M., M.E. Hagan, Thermospheric extensions of the classical expansion functions for semidiurnal tides. J. Geophys. Res. 87, 5253–5259, 10.1029/JA087iA07p05253,1982.

Frederick, J.E., D.W. Rusch, G.A. Victor, W.E. Sharp, P.B. Hays, and H.C. Brinton, The OI (λ5577Å) airglow: observations and excitation mechanisms, J. Geophys. Res. 81, 3923, 1976.

Hedin A.E., Extension of the MSIS thermosphere model into the middle and lower atmosphere. J. Geophys. Res. 96, 1159–1172, 1991.

Hough, S.S., On the Application of Harmonic Analysis to the Dynamical Theory of the Tides. Part II: On the General Integration of Laplace's Dynamical Equations, Philosophical Transactions of the Royal Society of London. Series A, Containing Papers of a Mathematical or Physical Character, Volume 191, pp. 139-185., 1898.

Lindzen RS, Hong S-S, Forbes JM, Semidiurnal Hough mode extensions in the thermosphere and their application. Memo Rept. Nav. Res. Lab 3442:69, 1977.

McDade, I.C. and E.J. Llewellyn, The excitation of O(1S) and O2 bands in the nightglow: A brief review and preview, Canad. J. of Phy., 64, 12, 1626-1630, doi: 10.1139/p86-287, 2011.

Noxon J.F., Day Airglow, Space Sci. Rev., 8, 92, 1968.

Solomon S.C., V.J Abreu, The 630nm airglow, Journal of Geophys. Res., 94, A6, 6817-6824, 1989.

Stevens, M.H., Englert, C.R., Harlander, J.M., England, S.L., Marr, K.D., Brown, C.M., and Immel, T.J., 2018. Retrieval of Lower Thermospheric Temperatures from O2 A Band Emission: The MIGHTI Experiment on ICON. Space Science Reviews, 214:4 (9pp.). Public access. DOI: 10.1007/s11214-017-0434-9

Stevens, M.H., Englert, C.R., Harlander, J.M., Marr, K.D., Harding, B.J., Triplett, C.C., Mlynczak, M.G., Yuan, T., Evans, J.S., Mende, S.B. and Immel, T.J., 2022. Temperatures in the Upper Mesosphere and Lower Thermosphere from O2 Atmospheric Band Emission Observed by

ICON/MIGHTI. *Space Science Reviews, 218(8)*, pp.1-32. Public access. DOI: 10.1007/s11214-022-00935-x

1. Chapter 2 : IVM

This document describes the IVM instrument function and those aspects of the on-orbit instrument performance that are dependent on calibration and ground processing algorithms.

The IVM consists of two sensor elements used to derive the properties of the thermal ion population at the satellite altitude.

Derivation of the key parameters of ion drift and ion temperature do not require an absolute conversion of ion current to ion number flux. Thus, key calibration procedures are limited to those required to accurately convert electrometer voltage to current and current ratio.

The key operating principles are described, leading to the calibration requirements and the methodology employed in ground processing to retrieve geophysical parameters.

2. Related Documents

2.1 Applicable Documents

Title	Document Number	Publication Date
ICON IVM Calibration and Measurement Algorithms Document (this document)	ICN-IVM-xxxxx-xxxx	TBD
IVM L4 Requirements Document	UTD 206-011	3 December 2014
IVM Requirements Verification Matrix	UTD 206-046 (A,B,C,D)	27 Jan 2016
IVM Verification and Validation Plan	UTD 206-017	24 Nov 2015
IVM Calibration Plan (Master Integration and Test Plan)	UTD 206-012	24 Nov 2014
Ion Velocity Measurements for the Ionospheric Connections Explorer	Space Science Reviews, 212, pp. 615-629 (2017)	20 Jul 2017
In-flight performance of the ICON Ion Velocity Meter	Space Sciences Reviews, 217, (2022)	November 2022

3. Overview and Background Information

3.1 Science Objectives

Plasma motions in the ionosphere arise from currents driven internally by neutral winds, gravity and plasma pressure gradients, and externally from interactions between the magnetosphere, the solar wind and the ionosphere-thermosphere system. Descriptions of the plasma drifts that accompany the state of the solar wind and the prevailing neutral winds are essential to understanding the behavior of geospace as a coupled system. The IVM is a compact and elegantly simple instrument that utilizes the supersonic velocity of a low earth orbiting vehicle to determine the ambient ion drift vector at the location of the spacecraft. Coupled with contemporaneous measurements of the solar wind and the neutral atmosphere dynamics it is possible to determine the relative influence of changes in these drivers on the motion of the plasma and the subsequent distribution of charged particles. This information is a fundamental contribution to all SMD missions examining the behavior of the ionosphere and thermosphere as a coupled system.

3.2 IVM Instrument Requirements

3.2.1 Measurement Concept

The IVM consists of two sensors. A retarding potential analyzer (RPA) measures the kinetic energy of the ion species along the direction of motion of the satellite as it moves supersonically through the medium. Measurement of the energy distribution is used to determine the potential of the sensor with respect to the plasma, the bulk flow of the ions along the sensor look direction, and the ion temperature defined by a Maxwellian distribution function. The RPA measures the ion energy distribution by measuring the ion current behind a planar retarding grid as a function of the retarding grid potential. A 32-point integral energy distribution function is obtained every second. Given the major ion masses that are present, the current voltage characteristic is fit to determine the ion drift and ion temperature. An ion drift meter (IDM) presents a square aperture to the supersonic plasma flow with respect to the satellite. By determining the displacement of the ion beam from normal incidence behind the aperture, it measures the angle of arrival of the ion beam behind the aperture in two mutually perpendicular directions that are nominally in the local horizontal and the local vertical. The associated cross-track ion drifts are related to the bulk ion flow measured by the RPA through a simple trigonometric relationship.

The IDM presents a segmented collector behind a square aperture so that the currents to adjacent collector halves can be measured. The ratio of currents to adjacent halves is directly proportional to the tangent of the arrival angle, which is subsequently multiplied by the RPA derived ion drift to produce the cross-track ion drifts. Table 1 summarizes the instrument performance capability.

Parameter	Range	Precision
Cross Track Ion Drift	-750 to 750 ms^{-1}	4.5 ms^{-1}
Ram Ion Drift	-500 to 500 ms^{-1}	19 ms^{-1}
Vertical Ion Drift perp to B	-500 to 500 ms^{-1}	8 ms^{-1}
Total Ion Number Density	$1.5x10^3$ to $5x10^6$ cm^{-3}	$1x10^3$ cm^{-3}

Major Ion Constituents	0.0 – 1.0	0.02
Ion Temperature	400 to 8000 K	100 K
Sensor Plane Potential wrt Plasma	-3 to +2 V	0.01V

Table 1. IVM Derived Geophysical Parameters

3.2.2 Instrument Subsystems

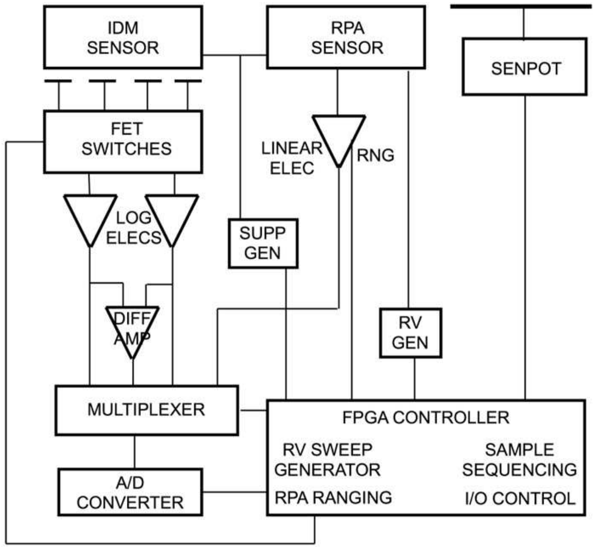

Fig 1. IVM Block Diagram indicating major subsystems.

Figure 1 shows the key sub-systems that make up the IVM. The collector current at the RPA is measured with a ranging linear electrometer, while FET switches are used to configure the IDM collector into half-segments that are alternately oriented on the local horizontal and local vertical. The current to each collector-half is measured with a logarithmic electrometer, allowing the ratio of the currents to be determined using a linear difference amplifier. Planar grids within the IDM and RPA are biased to produce uniform fields that repel thermal electrons, limiting their access to the sensor collectors, and suppress direct electron photoemission from the collector. In the IDM, a planar grid is biased at a fixed positive potential to remove the signal from H+. Internal planar grids in the RPA have programmed voltage steps applied to allow the current or ion flux, as a function of voltage to be determined.

The IVM sensor is electrically isolated from the spacecraft and establishes an independent reference ground from a conducting plate that is floating with respect to the plasma. The potential between the plate and the spacecraft ground, called SENPOT, provides a bias from the sensor reference ground that is near the plasma potential, independent of the behavior of the spacecraft ground with respect to the plasma.

3.3 IVM Heritage

3.3.1 Instrument Heritage

The ICON IVM instrument is based on successful designs for similar instruments most recently deployed on ROCSAT-1, C/NOFS and COSMIC-2. The design also benefits from a long history of successful operation on the DMSP satellites.

3.3.2 Algorithm and Calibration Heritage

The IVM requires a simple and robust calibration procedure executed in the laboratory for the production of the L1 data products. Derivation of the key geophysical parameters of ion drift and ion temperature is independent of the procedures required to convert ion flux (current) to ion number density. However, previous studies that have examined other error sources have shown that conversion process utilizing the geometric size of the sensor aperture and the optical transparency of the planar grids has an error of less than 10%. The maximum and minimum observable currents are primarily determined by the geometry of the sensor and the range of number density. Laboratory calibration using standard current sources applied directly to the collector is used to determine the transfer function and noise levels of the electrometer response and its sensitivity to the system temperature. Previous instrumentation, calibrated in the laboratory and operated in low-earth orbit, show little sensitivity to the range of operating temperatures and no change over many years of operation.

Ground processing algorithms have been continuously improved to provide as much adaptation to the changing geospace environment as possible. Refinements in RPA least-squares fitting procedures include adaptive selection of the I-V curve segments, geophysical constraints on the least-squares variables and adaptive modeling of variations around the orbit to accommodate changes in ionospheric composition.

4. IVM Calibration Plan

4.1 Mechanical Sensor Dimensions

The sensor aperture dimensions contribute to the effective collection area of the instrument. They are specified in precision mechanical parts and verified by physical measurement before and during assembly.

The IVM depth from knife-edge entrance aperture to the collector surface is determined by precision assembly of the grid stack between the entrance aperture and the collector. This is accomplished by using precision machined ceramic spacers between each grid holder, which are subsequently bolted between the entrance aperture and the collector. Each grid holder is likewise precision machined to enclose the grid within a flat plane with tolerances less than 0.001”. The dimensions of all mechanical parts are verified by precision measurement before and during assembly.

4.2 Grid Stack Transparency

A series of grids within the instrument are used to provide planar potentials that control the access of charged particles through the grid stack and confine applied potentials to fixed regions inside the sensor. Grids are constructed from gold-plated tungsten wire of diameter 0.001”, that is uniformly woven with a density of 50 or 100 wires per inch. Laboratory testing verifies that an electrically grounded grid presents a transparency to ions that can be closely approximated using the optical transparency. During assembly grid holders are rotated to ensure that no wires in adjacent grid planes are aligned.

4.3 Electrometer Sensitivity

The gain and sensitivity of the RPA linear ranging electrometer is determined by directly stimulating the collector with a current calibration source with accuracy traceable to NIST. The current is varied over the entire range expected in flight to determine the offset and the gain at each sensitivity level. The values for each sensitivity level are recorded at the expected range of operating temperatures and used by the ground processing software to convert voltage to current and ion flux.

The logarithmic electrometers in the IDM are likewise calibrated in the laboratory by directly stimulating the collector segments with current calibration sources with accuracy traceable to NIST . In addition, the standard current sources are used to inject a known current ratio to segment halves, while the output of the difference amplifier is recorded. This procedure provides a direct measure of the difference amplifier output as a function of the arrival angle of an ion beam. We note that since the IVM functions in an environment where the ions are moving supersonically with respect to the sensor, no calibration using an ion beam is required. Laboratory calibration is robustly performed using the direct injection of known currents.

Table 2 shows the performance required to produce the geophysical parameters at the specified levels and the measured performance as a function of temperature obtained from laboratory calibration.

Parameter	Analysis #	Room Temp	+45C	-10C
RPA Min Cur (nA)	0.475 (max)	0.050	0.050	0.050
RPA Max Cur (nA)	2371 (min)	3929	3909	3954
RPA Elec Slope Error	0.12% (max)	0.007%	0.013%	0.007%
RPA Elec Offset Error (counts)	5 (max)	0.32	0.60	0.31
RPA Elec Noise Floor (pA)	5.0 (max)	1.6	3.0	2.2
RPA RV uncertainty	3 mV (max)	2	2	2
IDM Min Curr (nA)	0.473 (max)	0.25	0.25	0.25
IDM Max Curr (nA)	834 (min)	9500	9500	9500
IDM Angle Error (deg)	0.02 (max)	0.0003	0.00024	0.00041

Table 2. IVM Calibration Properties

4.4 Instrument Operations

Operation of the IVM is accomplished by optimizing the retarding voltage sequence used to determine the energy of the incoming ions and optimizing the repeller grid voltage for the IDM that removes the signal from H+ ions that do not move supersonically with respect to the sensor.

These instrument parameters require adjustment during the mission to accommodate the changing operating environment produced by changes in the solar flux. In the presence of such periodic changes, the instrument operates continuously and provides data whenever the sensors are facing the ram directions. Two IVM sensors mounted in the ram and anti-ram direction, allow data to be gathered when the spacecraft is oriented in the local vertical/local horizontal (LVLH) or reverse LVLH.

During routine operations, the RPA retarding grid steps through a series 32 discrete voltages. An automatically ranging linear electrometer measures the ion current after the retarding grid is stepped to a discrete potential. The electrometer has 8 sensitivity ranges, differing by approximately the square-root of ten, allowing currents between 50 pA and 3.9 µA to be measured. At each step the RPA output consists of the memory location that provides the retarding voltage, the current recorded with 14-bit accuracy and accompanied by 3 bits that designate the electrometer sensitivity level.

In the IDM, low leakage JFET switches allow the collector segments to be combined to provide a current from collector halves that are aligned either along the local horizontal or the local vertical axis. For a designated axis the current from each collector half is measured by a logarithmic electrometer having a dynamic range from 250 pA to 9.5 µA, which is subsequently registered with 14-bit accuracy for transmission to the ground. The outputs from each logarithmic electrometer are sampled at 16 Hz. The outputs from each logarithmic electrometer also provide the inputs to a linear difference amplifier that delivers the ratio of the ion currents to be used in the expression described in Section 5.2.1 to derive the ion arrival angle. The output of the difference amplifier is recorded with 14-bit accuracy and accompanied by one bit (axis) that describes the collector halves orientation (horizontal or vertical) and one bit (polarity) designating which collector half is connected to which logarithmic electrometer. The difference amplifier outputs and configuration indicators are sampled at 32 Hz. The instrument may be configured by ground command to alternate between horizontal and vertical arrival angles with a 16 Hz or 8 Hz cadence or to remain measuring a fixed axis arrival angle (horizontal or vertical). In both cases biases in the logarithmic electrometers are determined by periodically changing the polarity of the inputs. The rejection of thermal electrons and the suppression of photoemission currents are accomplished with the suppressor grid, which precedes the collector and may be biased between 0 and -10.5 volts in 1.5-volt steps. In addition, the repeller grid may be biased with a potential between 0 and 3.5 volts, in 0.5-volt steps, to reject the admission of H+ ions.

4.5 Long-Term Electrometer Offsets

For the RPA, changes in the electrometer gains and sensitivity are monitored continuously by comparing the outputs when currents are increasing and decreasing across a level that causes a change in sensitivity. These transitions occur naturally during the course of a day as the spacecraft crosses all local times. Long-term biases in the drift meter outputs are determined by trend analysis following the constraint that the ion drift vector must conform to a curl-free electric field. This allows the data gathered at a fixed location over all local times to be averaged in longitude and set to zero. The satellite precession period of about 50 days enables accurate specification of the offsets that can be applied to the L-1 outputs for ion drifts to be corrected.

4.6 Short-Term Electrometer Offsets

Short-term biases in the IDM outputs may be produced by variations in the electrostatic environment of the spacecraft, that result in asymmetric acceleration of the ions through the sheath. The relatively large offsets produced with time periods less that one day are easily recognized by the unreasonably large ion drifts that are derived from anomalous ion arrival angles. Removal of absolute values is possible by imposing a curl-free electric field from the average of data taken at all magnetic apex heights. However, it should be noted that the influence of planetary waves is attenuated by this procedure.

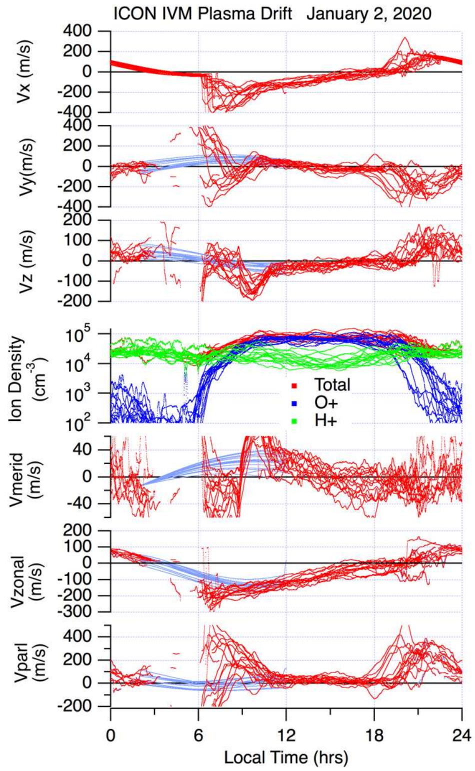

Fig. 2: Daily ion drifts show expected behaviors during solar minimum. See text for details.

4.7 Validation

The outputs from the IVM may be validated in an absolute way using comparison with simultaneous measurement s made from ground-based radar. Additionally, fully coupled models of ionosphere-thermosphere coupling may be used to compare waveforms in local time and longitude for consistency with the requirements of a curl-free electric field.

Environmental conditions in the initial ICON orbit were not consistent with optimum operation of the IVM. Extremely low solar activity levels with 10.7 cm solar flux levels near 70 x 10^{-22} Wm^{-2} Hz^{-1}, produce regions during the nighttime where the O+ number density falls below 5x103 cm-3. In the pre-noon sector, low O+ densities persist, leading to high noise levels and the inability of the ambient ion flux entering the sensor to overcome the emission of photoelectrons from internal surfaces.

Figure 2 shows a typical day of native and derived parameters and derived parameters from the IVM. The top three panels show the ion drifts derived from the RPA (Vx) and from the IDM (Vy and Vz). Local time is the strongest organizer of the data and results for all orbits for one day are shown. Areas where blue lines connect the data indicate where poor signal levels and contamination form photoemission exists and first order corrections to the signal have been made. The fourth panel show the ion composition, indicating the dominance of H+ during the nighttime and the residence of the satellite near the O+/H+ transition height during the daytime. The lower three panels show the ion drifts in magnetic coordinates. Vertical (meridional) ExB drifts are in accord with previous expectations of behavior at solar minimum, with a semi-diurnal component to the drift present during the daytime. The zonal drift is westward by day and eastward at night as expected, while field aligned flows are week except near dawn and dusk when the ionosphere expands and contracts in response to solar illumination.

Despite the limitations in IVM performance due to environmental, conditions, a continuous supply of data in the afternoon and evening sectors has allowed the ICON mission to meet the science goals.

4.8 Offset Determination

Following the preparation of an IVM geophysical data set for a period exceeding a year, the appearance of systematic offsets in the ion drift components parallel and perpendicular to the magnetic field can be detected. Over significantly long periods, each location in latitude, longitude and local time is sampled by northbound and southbound passes. For these different configurations the contributions of the native components of the drift (Vx,Vy,Vz) contribute with directions to the magnetic drift components, as indicated in figure e Long-term systematic offsets, regardless of their source can be estimated by imposing fundamental physical constraints that must be met simultaneously at all relevant locations.

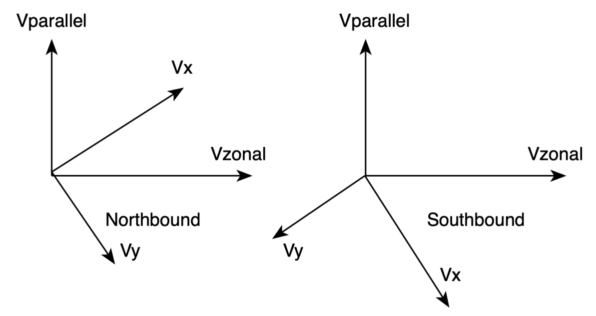

Figure 3. Pointing directions for northbound and southbound passes.

Regarding drifts perpendicular to the magnetic field, we impose the condition that the local-time and longitude average of the meridional drift must be zero. At the magnetic equator, this imposes only an offset in Vz, since this direction is itself perpendicular to the magnetic field. At locations away from the magnetic equator both Vx and Vy contribute to the vertical drift, but the weighting is very small. In addition, there is requirement for magnetic conjugacy and inspection of figure 3 shows that an offset in Vy has the opposite sign imposed on the meridional drift in each hemisphere and cannot therefore contribute to an offset in the meridional drift. An offset in Vx has the same sign imposed on the meridional drift in each hemisphere and must compensate for the difference between the vertical drift at the magnetic equator and at the off-equator location assuming the meridional drift is independent of magnetic apex height (magnetic latitude).

For the zonal ion drift, we impose the condition that the local-time and longitude average of the drift be zero. This enforces the condition the ionosphere does not significantly sub-rotate. The ICON orbit inclination is ~27° and thus this condition applies principally to the Vx, which contributes to the zonal drift with high weighting and the same sign at all locations. Offsets in Vx originate principally from inadequate specification of the sensor aperture potential with respect to the plasma. In some circumstances, where sufficient concentrations of O+ and H+ exist, this parameter can be derived with reasonably high confidence. In other circumstances, where the plasma density is low or dominated by O+, an estimate of the aperture potential must be utilized. The aperture plane potential with respect to the plasma has a significant impact on the zonal ion drift determination with an uncertainty of 0.1V translating to an uncertainty in Vx excess of 70 m/s.

Inspection of Figure 3 shows that an offset in Vy applies to the zonal drift in the opposite sense for northbound and southbound passes, while it contributes in a dc manner to the parallel drift. Thus, it is not permissible to apply and offset in Vx that produces an asymmetry in the northbound and southbound derivations of the drift parallel to the magnetic field. Similarly, it is not permissible to apply an offset to Vy that produces an asymmetry in the northbound and southbound derivations of the zonal drift. In order to resolve this difficulty, we additionally determine an offset in Vy that varies around the orbit, being an extremum at the northbound and southbound crossings of the equator, where there is a contribution to the zonal drift, and being zero at the latitude extremes of the orbit, where there is no contribution to the zonal drift. Such an offset also allows for small differences in the angle between the magnetic meridian and sensor look direction, that are not specified in the model magnetic field. In addition, it compensates for variations in Vy produced by changes in the aperture potential that are interpreted as offsets in Vx.

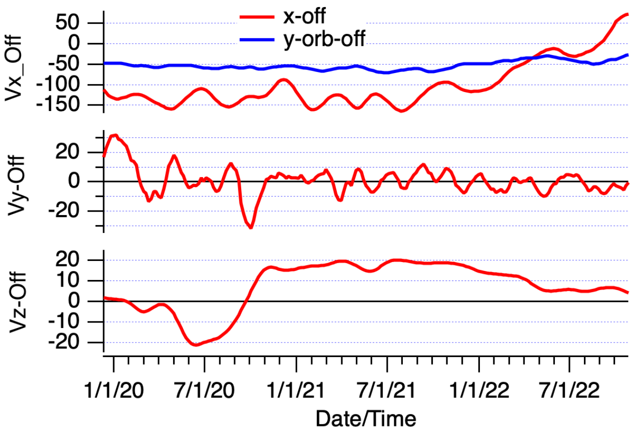

Figure 4. Component offsets applied to native drifts prior to rotation into magnetic coordinates.

Regarding the ion drift parallel to the magnetic field, we recognize a seasonal variation reflecting the interhemispheric transport of plasma and thus demand only that northbound and southbound passes through the same location show the same seasonal variations. All these constraints can only be satisfied in a least-squares fashion and thus the derived drifts cannot satisfy the conditions exactly. However, a description of the long-term variations in the offsets can be obtained. Figure 4 shows the evolution of the offsets derived in the manner described above. It can be quickly seen that the orbit-constant offset in Vy (middle panel) is negligibly small. The offset in Vz is small, but comparable in magnitude to the meridional drifts in the equatorial ionosphere. Long-term variations in the offset could be consistent with very small changes in the aperture plane potential with respect to the plasma, but there is no unambiguous verification of this effect. The largest offset is in Vx, the component of ion drift approximately parallel to the spacecraft velocity. This is likely due to inadequate specification of the spacecraft ground potential with respect to the plasma, which can be corrected by a corresponding offset in Vx. In addition a correction for the component of drift along the y-axis will be present due to the plasma acceleration through the potential sheath. This will cause the ion drift, which is dominated by atmospheric corotation to be underestimated, which is likely the cause of the Vy offset that varies around the orbit as described above. While physically reasonable explanations for the offsets can be described, it is not possible to independently verify their source. Nevertheless, when applied they provide physically sensible constraints on the ion drifts parallel and perpendicular to the magnetic field.

5 IVM Measurement Algorithm Description

5.1 Theoretical basis

The IVM functions by utilizing the supersonic velocity of an orbiting vehicle to extract the bulk flow and the temperature of the ambient ions assuming a flowing Maxwellian distribution. With this assumption an aperture normally incident to the satellite velocity produces an ion beam behind it from which the ion drift and temperature can be derived from the incident energy and the arrival angle can be derived from the deviation of the beam from normal incidence.

5.2 Conversion of Instrument Signals Ion Flux and Ion Arrival Angle

5.2.1 Measurement Equations

For the RPA the current at the collector is determined from the integral of the flowing Maxwellian velocity distribution function and the effective collection area determined by the aperture size and the griod-stack transparency.

$$I(\phi) = qA_{eff}\frac{N_i}{2}V_r\left[1+erf(\beta f)+\frac{1}{\sqrt{\pi}\beta V_r}\exp\left(-\beta^2 f^2\right)\right]$$

where A_{eff} is the effective area of the collector, $f = V_r - \left(2q\phi/m\right)^{1/2}$, with q the electron charge, represents the average velocity of the ions that have access to the collector and $\beta = \left(m/2kT_i\right)^{1/2}$, is the reciprocal of the thermal velocity of the ions. Here, $V_r = \left(\vec{V}_d + \vec{V}_s\right)\cdot\hat{n}$ is the total velocity of the ions given by the sum of the ambient ion drift $\vec{V}_d$ and the spacecraft velocity $\vec{V}_s$ and $\hat{n}$ is the unit vector along the sensor look direction. $\phi = R_v + \psi_s$, is the potential on the grid as seen by the plasma and is thus the sum of the retarding potential R_v with respect to the sensor ground and the sensor ground potential with respect to the plasma ψ_s. A least-squares fitting procedure determines the most probable values for $\vec{V}_d$, β and ψ_s.

For the IDM the linear difference amplifier measures a signal directly proportional to the ratio of currents to the collector-halves. That ratio provides the ion arrival angle in terms of the sensor dimensions, as

$$\frac{I1}{I2} = \frac{W/2 + D\tan\alpha}{W/2 - D\tan\alpha}$$

where W is the length of the square aperture and D is the depth from the external aperture face to the collector. The corresponding transverse drift velocity is given by

$$\left(\vec{V}_d + \vec{V}_s\right)\cdot\hat{t} = \left[V_r^2 - 2q\psi_s/m\right]^{1/2}\tan\alpha$$

5.2.2 IVM Signal Error Analysis

Uncertainties in the retrieved ion current and ion arrival angle arise from uncertainties in the laboratory calibration, the electrometer noise levels and the minimum digitization level of the output voltages. These errors are summarized in Table 2.

5.2.3 IVM Parameter Uncertainties

Uncertainties in the derived parameters arise from specification of the gain, offset and noise floor of the linear electrometer, in the specification of the retarding voltage and in the discretization of the output by the analog to digital converter. Uncertainties in deriving the transverse ion drift arise principally from the angular sensitivity of the device itself, which translates to an uncertainty in the derived ion arrival angle. This angle is then used with the ram ion drift derived from the RPA to determine the transverse ion drift. Thus, given an uncertainty in the ram ion drift, the uncertainty

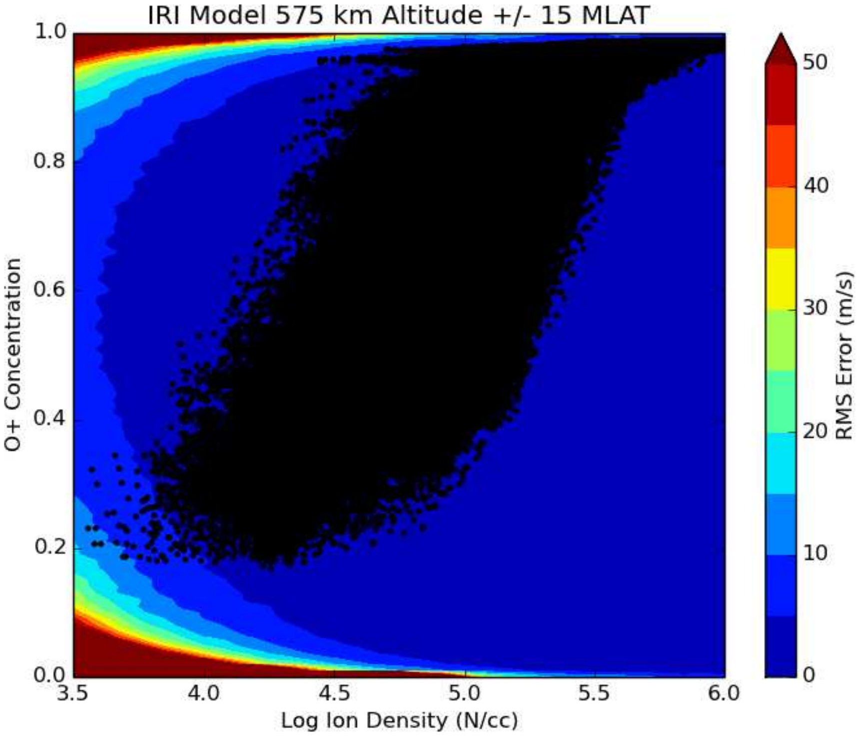

Fig 3: The RMS error in derived drift velocity over a range of plasma density and O+ relative composition. For a given density and fractional population the average uncertainty is obtained over the temperature range from 400 K to 8000 K and aperture potential range from +2 V to -3V.

in the transverse ion drift can be easily specified. For the RPA, geophysical parameters are derived in a least square analysis procedure. It is therefore not possible to distribute uncertainties in the derived ion drift velocity to separate uncertainties in subsystem parameters or variability in geophysical conditions. The uncertainties in geophysical parameters from the RPA can only be determined from controlled least-squares fitting of simulated data for which the real result is known. Thus, the instrument performance is simulated with the uncertainties in the instrument parameters specified by the analysis values given in table 2. Simulated I-V curves are produced by randomly selecting geophysical parameters in the range specified in table 4. Each curve is then fit utilizing the ICON ground software to derive the ram ion drift, the ion temperature, the fractional ion composition and the aperture plane potential. The total plasma density is also derived from the RPA saturation current at low retarding voltages. Figure 3 shows the derived accuracy of the ram ion drift as a function of total ion density and fractional composition. This figure is constructed by calculating the deviation between the derived ion drift and the input ion drift for more than one thousand curves for which the temperature, the ion drift and the aperture potential are randomly chosen. Each curve is fit multiple times to improve the statistical representation of the uncertainty. The black dots indicate the predicted total plasma density and fractional composition encountered during the ICON mission from the IRI model. The expected operating range, the anticipated uncertainty in the derived ram ion drift is less that 15 ms^{-1}.

1. CHAPTER 3: EUV

This section provides a brief description of the specific aspects of instrument calibration covered by this plan

2. RELATED DOCUMENTATIONS

EUV Instrument Documents

Title	Document Number	Publication Date
ICON EUV Calibration And Measurement Algorithms Document (this document)	ICN-EUV-54063-0015	09 Jun 2022
EUV L4 Requirements Document	ICN-EUV-54021-001A	15 Jan 2015 [Rev A]
EUV Requirements Verification Matrix	ICN-EUV-54021-002	15 Jan 2015
EUV Verification and Validation Plan	ICN-EUV-54021-004	04 Feb 2015
EUV Calibration Plan	ICN-EUV-54063-001	
Design and Performance of the ICON EUV Spectrograph	Space Science Reviews, 212, pp. 631–643 (2017)	20 Jul 2017
In-flight performance of the ICON EUV spectrograph	Space Science Reviews (2022), submitted.	28 Apr 2022

3. OVERVIEW AND BACKGROUND INFORMATION

3.1 SCIENCE OBJECTIVES

The existence of EUV emission from singly ionized oxygen (O^+) in the ionosphere of the Earth has long been known and is a useful diagnostic of the ionization state and density of the lower ionosphere. The brightest of the OII dayglow line complexes in the EUV is the 83.4 nm resonance triplet resulting from transition from the $2p^4\ ^4P$ excited states to the $2p^3\ ^4S^0$ ground state. The population of ions in the ground state typically peaks at densities on the order of 10^4 10^6 cm^{-3}, enhancing the probability that an emitted photon from this transition will be reabsorbed and resulting in an optical depth to the ICON EUV on the order of 1-10 in this transition. This can make it difficult to disentangle optical depth effects from illumination and ion density effects when attempting to determine density of the O^+ ion. The nearby triplet at 61.6 nm from the $3s\ ^2P$ state to the $2p^3\ ^2D^0$ state is optically thin. The two taken together can be used to more directly obtain the ion density and illumination source function than the 83.4 nm emission alone. Similar transitions at 53.8 nm , 67.3 nm and 71.8 nm could theoretically be used to supplement this analysis.

(plus 0.76 degree caused by 12s of spacecraft motion). Height of the atmosphere is exaggerated by 5x.

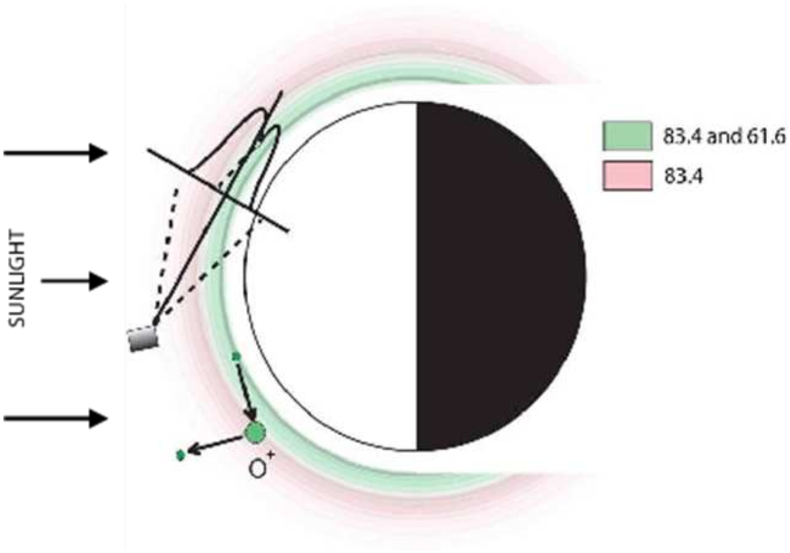

Fig 1. Illustration of the *ICON EUV* observing geometry. Spacecraft motion is towards the reader. Vertical (imaging) field of view is 17°.3 and is demarcated by dashed lines. Horizontal (spectral) field of view is 12.1 degree

3.2 EUV INSTRUMENT REQUIREMENTS

3.2.1 MEASUREMENT CONCEPT

The ICON EUV spectrometer is designed to perform wide field altitude profiles of the region surrounding the peak O^+ densities in the lower ionosphere, at tangent altitudes between 100 and 500 km with a vertical resolution of 20 km, and a horizontal resolution of 500 km (Figure 1. See also Figure 16 of Immel et al. (2018)). In normal observing mode, the ICON EUV field of view faces perpendicular to the spacecraft velocity vector and downward to cover this targeted altitude range. Each 12 second exposure images a 12° wide (spectral) by 17° high (imaging) wedge of the atmosphere from which daytime ion density altitude profiles are determined. The spacecraft velocity along the orbital track during 12 s results in a spacecraft motion of about 100 km, which is small compared to the 500 km range of the 12° field of view at the tangent point. In effect each exposure is a snapshot taken at a specific spacecraft position and time. The required sensitivity (3σ Minimum Measurable Flux (MMF)) of 7.4 Rayleigh at 61.6 nm and 30 Rayleigh at 83.4 nm were determined based on simulated model inversions of the altitude profiles to derive the O^+ density versus altitude. This minimum sensitivity is 10% of the maximum ionospheric density emission. The primary design requirements relate to obtaining the sensitivity and angular resolution necessary to determine the maximum ion density of the F2 layer and the altitude of the maximum density using the 61.6 nm and 83.4 nm emission, while rejecting interference from scattered HI Lyα and the nearby HeI 58.4 nm line. End of life requirements are based upon pre-flight calculations of the worst case sensitivity losses in the microchannel plate detector and continuous low-rate deposition of hydrocarbon contamination on the instrument diffraction grating. Total end of life efficiency loss under these assumptions was 60% from "pristine" conditions on receipt of the optics and microchannel plates. Actual degradation has been tracked through on-orbit calibration activities.

Parameter	**Minimum Success Requirements**	**Comprehensive Success Criteria**	**Performance**
Wavelengths	OII 83.4 nm, OII 61.7nm	OII 83.4 nm, OII 61.7nm	OII 83.4, OII 61.7, HeI 584, OII 67.3, OII 74.1, OI,NII 71.8
Wavelength Resolution	4.2 nm $FEW_{90\%}$	4.2 nm $FEW_{90\%}$	2.4 nm $FEW_{90\%}$
Imaging Resolution	0.45° $FEW_{78\%}$	0.45° $FEW_{78\%}$	0.25° $FEW_{78\%}$
Time Cadence	<= 60 sec	<= 60 sec	12 sec
Vertical FOV	>14°	>14°	17.3°
Absolute Calibration	< factor of 2	< factor of 2	50%
Relative Calibration	5% pixel to pixel	5% pixel to pixel	1.7% pixel to pixel
Mission Life	2 years	>2 years	?
3σ Minimum Measurable Flux	7.4R (61.7 nm) 30R (83.4 nm)	7.4R (61.7 nm) 30R (83.4 nm)	4.0R (61.7 nm) 16.2R (83.4 nm) (Measured following 12/21 HV increase)

Table 1. EUV subsystem design and performance specifications.

3.2.2 INSTRUMENT SUBSYSTEM DESCRIPTIONS

3.2.2.1 ENTRANCE SLIT

The entrance slit defines the geometric area that allows light to pass into the instrument. As such its size is carefully calibrated on the ground.

3.2.2.2 DIFFRACTION GRATING

The EUV instrument is a single optical element design, which is necessary for high efficiency. The grating is a modified profile (lamilar groove) holographic design manufactured by Horiba-Jobin Yvon which results in high efficiency at the design wavelengths as exceptionally low scattering. The grating was coated with a multilayer of Boron Carbide over Iridium over Chromium, for optimal EUV efficiency. The grating efficiency was measured by the vendor and by us in and out of the instrument. Values determined in instrument in combination with the flight detector are used in our analyses.

3.2.2.3 MICROCHANNEL PLATE DETECTOR

The instrument utilizes a 19x54mm cross delay line microchannel plate (MCP) detector with a time to digital conversion system. We chose to use an uncoated MCP because bare MCPs are relatively insensitive to long wavelengths such as Lyα 121.5 nm airglow. The spatial resolution of the detector system is 90 μm in the spectral direction and 160 μm in the imaging direction. Any discussion of imaging or spectral resolution in this document includes these resolutions as a factor. The quantum efficiency of the detector was measured both separately and within the instrument, any measurement of responsivity includes the detector efficiency. Microchannel plates do have potential issues with sensitivity changes due to contamination or excessive charge extraction from regions of the plates where bright sources or lines are images, hence in-flight calibration is necessary.

3.2.3 EUV HERITAGE

3.2.3.1 INSTRUMENT HERITAGE

The ICON EUV instrument is based upon the successful EURD and SPEAR spectrographs. To maintain high optical throughput in the EUV, the spectrograph uses a single reflective optic, a toroidal diffraction grating that acts as both imager and spectral disperser. Light passing through the entrance slit strikes the diffraction grating and is dispersed onto an imaging microchannel plate (MCP) detector. The MCP detector electronics use a cross delay line anode and time-to-digital converter electronics based upon the Cosmic Origins Spectrograph (COS) and JUNO designs.

3.2.3.2 RETRIEVAL ALGORITHM AND CALIBRATION HERITAGE

The core of the ICON inversion algorithm to derive the daytime ionospheric parameters was originally developed and described by Picone et al. (1997a, 1997b). The concept adapts the approach used by Meier and Picone (1994) to measure O, N_2, and O_2 in the thermosphere using far-ultraviolet airglow, and most recently implemented to successfully invert measurements from the Global Ultraviolet Imager (GUVI) instrument on the NASA Thermosphere Ionosphere Mesosphere Energetics and Dynamics (TIMED) Explorer mission (Meier, et al., 2015). The daytime ionospheric algorithm described here for the ICON mission has most recently been applied to analyze measurements from the Special Sensor Ultraviolet Limb Imager (SSULI) instruments on the Defense Meteorological Satellite Program (DMSP) F18 and F19 satellites (see Stephan, 2016). More recent measurements from the Remote Atmospheric and Ionospheric Detection System (RAIDS) and Limb-imaging Ionospheric and Thermospheric EUV Spectrograph (LITES) that both were flown on the International Space Station in 2009 and 2017, respectively, have provided supplemental advancements to the algorithm and data analysis approach, most specifically regarding the specifics of pairing of the emission at 61.7 to the centrally-focused 83.4 nm emission (Stephan et al., 2012; Stephan, 2016; Stephan et al., 2019).

The heritage of the calibration methods and facilities used in the laboratory calibration of ICON EUV are straightforward and have been used on essentially every UV mission in which the Space Science Laboratory has been involved, including EUVE, FUSE, FAUST, DUVE, FUVCR, CHIPS, IMAGE, SPEAR/FIMS, EURD, etc. The basics are to measure components individually (as a check on system performance) and as a full system, under vacuum using the science wavelengths (or as close as can be achieved). This is supplemented with in-flight calibrations if astronomical or internal calibration sources are available. *As described in the next section, ICON implemented lunar observations to achieve absolute flight calibration in coordination with SDO EUV observations of the solar spectrum, and noon-time nadir observations for relative pixel-to-pixel (flatfield) calibration.*

4. PAYLOAD CALIBRATION PLAN

4.1 EUV CALIBRATION PLAN

4.1.1 OVERALL CALIBRATION SCHEME

The single aperture, optic, and detector simplicity of the instrument inspired this calibration strategy:

1. Separately characterize the performance of the diffraction grating (coating efficiency, order efficiencies) and the detector quantum efficiency (QE) at discrete wavelengths.
2. For the integrated instrument determine the absolute throughput, wavelength scale, resolution, field of view, and in-, and out-of-band scattering levels at discrete wavelengths.
3. Use efficiency models provided by the diffraction grating and optical coating manufactures that are scaled to SSL measurements to predict performance at other wavelengths.
4. On–orbit, use Moon pointings of reflected Solar EUV light to verify optical alignment, focus, and throughput. Use downward-looking (nadir) pointings to make flat field maps.

4.1.2 PRE-FLIGHT CALIBRATIONS

4.1.2.1 ENTRANCE SLIT AREA

The slit dimensions were measured with a microscope on a fine micrometer stage and are 0.904 mm wide, and 40.0 mm long. The geometrical area is 0.3616 ± 0.0016 cm^2.

4.1.2.2 ANGULAR FIELD OF VIEW

The angular field of view was determined by shining a pencil beam of 83.4 nm EUV light at 3 different positions along the slit while rotating the instrument in both pitch and yaw by known amounts. The field of view measured at FWHM is $17^\circ.31 \pm 0^\circ.1$ and $12^\circ.12 \pm 0^\circ.05$ in the imaging and spectral directions, respectively. These values correspond to a full solid angle of 0.06391 ± 0.00045 sr. Each vertical pixel sees a subdivided fraction of this corresponding to 27 arcminutes of vertical acceptance. The value determined for the imaging direction is for the center of the slit. Off-axis rays may experience vignetting and are calibrated in orbit using time-averaged nadir pointings as part of the flat field correction.

4.1.2.3 ABSOLUTE PHOTOMETRIC THROUGHPUT/RESPONSIVITY

The throughput determinations required several steps. First, absolute measurements were performed for the central ray at three wavelengths (58.4, 61.6, and 83.4 nm) by alternately directing pencil beams into the instrument and onto a photodiode calibrated by NIST. To ensure full capture of the EUV pencil beams by the grating, the entrance slit was removed from the instrument during photometric calibrations. These measurements provide the absolute photometric sensitivity for on-axis light incident at the center of the grating.

Second, measurements were made relative to the central ray by rotating and translating the instrument to illuminate the grating at approximately flight-like conditions. The average value of each of these images (excluding regions beyond the measured field of view) gives sensitivities relative to the central ray of 97.8% and 105% at 58.4 nm and 83.4 nm, respectively. The displacement of peak sensitivity towards positive angles is an expected consequence of the MCP pore bias angle which is tilted 13° parallel to the spectral direction. Rays strike the MCP detector at up to 8.6° from normal along this dimension.

The third step is to determine the sensitivity at other wavelengths. This requires knowing the wavelength dependent efficiencies of the diffraction grating, the B4C/Ir/Cr coating, and the flight detector. Measurements were performed for each of these components at discrete wavelengths at SSL. Linear interpolation for intermediate values of detector QE proved adequate. For the coating efficiency and the diffraction grating relative order efficiency we use the theoretical performance (based on the measured groove profile) provided by the manufacturers, multiply them, and scale the resulting curve to match the Berkeley measurements. The product of these curves gives the predicted throughput which we compare to the Berkeley measurements of instrument efficiency, which gives an estimate of the efficiency curve between our measurement wavelengths. (In orbit lunar measurements give a much higher number of wavelength points.) Our ground based efficiency measurements have a total error of 11% at the measured wavelengths, and 12% at interpolated wavelengths.

4.1.2.4 SPECTRAL AND IMAGING RESOLUTION

To quantify the focusing properties of the spectrograph required fully illuminating the grating as well as the entrance slit. The optical simulator fully illuminates the grating, but produces a line-image only 1/3 (0.3 mm) as wide as the slit. Hence, small lateral motions of the simulator spherical mirror (slit scans) were required to create synthetic images of a fully illuminated entrance aperture. A set of slit scans obtained at different imaging angles and then added together provides our best proxy for flight-like illumination. Small changes in line shape and position are evident. Combining the synthetic O spectrum with a similar one obtained with He-Ne we find a resolution in the imaging direction of 0°.26 at FWHM. In the spectral dimension the resolution is slit-limited—emission features appear somewhat flat-topped. We find a typical line-width of 2.4 nm at 90% enclosed energy width which corresponds to R ~25.

We also obtained spectra during thermal vacuum testing to verify optical stability. Temperature excursions ranged from 10 C to 40 C. No significant shifts in position of spectral features was observed, nor any degradation of the spectral and imaging resolutions.

4.1.2.5 SCATTERED AND STRAY LIGHT

Most spectrographs are compromised to some degree by unwanted light typically caused by the diffraction grating scattering both in-, and out-of-band light, light from orders other than those of interest, and stray light that bounces off one or more interior surfaces and ultimately lands on the detector. When EUV light within the field of view is directed through the *ICON EUV* entrance aperture the holographically ruled gratings with square-wave groove profile shows insignificant (< 0.025%) scattering in-band at 83.4 nm, and out-of-band at 121.6 nm (Lyα). However, when Lyα light from beyond the field of view is directed through the aperture it can scatter from one or more baffles directly, or reflect off the grating in several different orders and then scatter from baffles. We measured significant scatter counts at the detector (19 cm^{-2} per 1.5x10^{6} Lyα input photons) from off-axis light in both the spectral and imaging planes. We define scatter counts as the count rate above dark background integrated over the entire detector surface.

Several modifications were required to reduce the scattered light to acceptable levels. In the spectral direction, baffle edges were sharpened to knife-edges to prevent glints. Outside of the slit, one baffle was extended slightly to prevent direct illumination of a baffle facet close to the grating. In the imaging direction additional baffles were fabricated to fully shadow existing baffles where knife-edging was insufficient. Figure 2 is a top-down view into the *ICON EUV* housing showing the baffle placement.

The measured scattering level was reduced by more than a factor of 13 (1.4 cm^{-2} per 1.5 10^{6} Lyα input photons) to a level which will not compromise science observations. In addition our detector includes a background region that allows scattered light to be subtracted from the science images.

4.2 INSTRUMENT DESCRIPTION

The ICON EUV instrument will observe O^{+} 61.7 nm and O^{+} 83.4 nm extreme-ultraviolet emission above the daytime limb of the earth. These observations will be used to determine the peak O^{+} ion density and the altitude of that peak.

The ICON EUV instrument is based upon the successful EURD and SPEAR spectrographs. To maintain high optical throughput in the EUV, the spectrograph uses a single reflective optic, a toroidal diffraction grating that acts as both imager and spectral disperser. Light passing through the entrance slit strikes the diffraction grating and is dispersed onto an imaging microchannel plate (MCP) detector.

The unique optical design combines imaging and spectral capabilities in a single optic. In the spectral dimension, the diffraction grating focuses an image of the slit onto the detector. In the perpendicular direction, the grating focuses parallel rays to a spot on the detector. In this design, the size of the grating determines the overall field of view, while the size of the slit determines the collecting area and the spectral resolution of the instrument. Optical aberrations and detector imaging characteristics set maxima to the effective angular and spectral resolution.

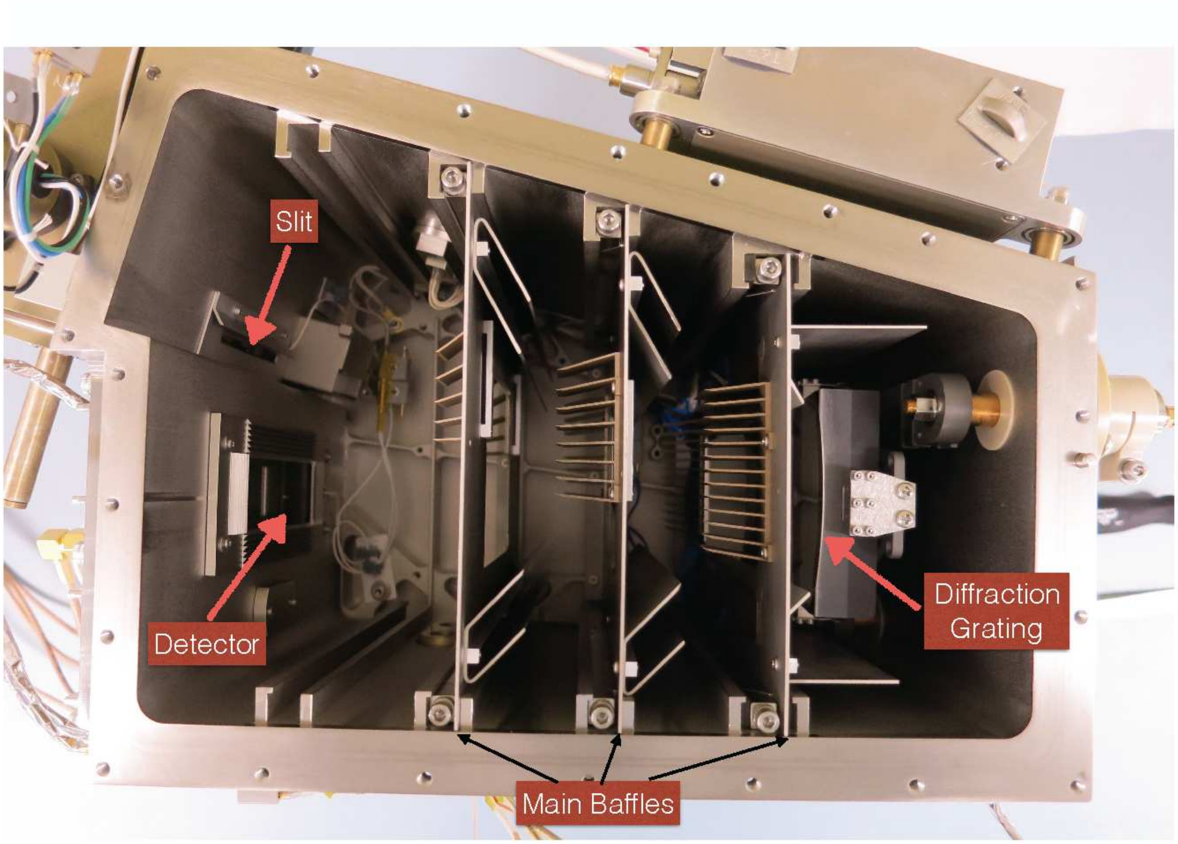

Fig 2: A top down view of the ICON spectral imager showing the locations of the slit, diffraction grating and MCP detector.

The detector electronics transmit X and Y position as well as charge amplitude of each event to the instrument control package (ICP). The ICP bins the events into a 169 by 108 image. These images are accumulated for an exposure time of 12 seconds. Ground software divides the image into 13 altitude profile regions for different wavelengths, including a background region. The regions corresponding to the O$^+$ 61.7, O$^+$ 83.4 after background subtraction and flux calculation are utilized in the Level 2 inversion discussed in Section 5.

Because contamination is a significant concern for EUV instruments, the entire instrument housing was built as a vacuum cavity. A sealed door in front of the instrument was opened on orbit and in a vacuum chamber to allow light to enter for calibration. Once assembled, the instrument was maintained at high vacuum by attaching a vacuum pump to the instrument's pumping port. During operations for which pumping was not possible, the instrument was purged with clean dry nitrogen through the purge port. During purge gas escaped through 1 psi poppet valves that were also used to release pressure during ascent. For short operations where purge was not possible, the instrument was backfilled with dry nitrogen and sealed to prevent contamination.

4.3 IN-FLIGHT TRACKING OF SHORT-TERM CHANGES

In part because of the contamination and charge depletion concerns, it is necessary that the EUV instrument is also calibrated after launch. Absolute and time relative calibration are accomplished through observations of the full moon each month. Pixel-to-pixel variations are calibrated through observations of airglow during nadir pointings. Changes in the gain of the detector are measured for each pixel in weekly engineering observations (starting in March 2022).

4.4 LONG-TERM ABSOLUTE CALIBRATION TRACKING (RE-CALIBRATION)

To determine our absolute photometric response at the science wavelengths we perform a monthly recalibration against the full moon. The EUV field of view is swept across the full moon at seven evenly spaced imaging angles at a rate of 0.25° s^{-1}. Using the initial pre-flight calibration of the spectrometer, and the lunar albedo of Flynn et al. (1998) as our starting points, and near-concurrent EUV solar measurements from the EVE instrument aboard SDO (Pesnell et al. 2012), a lunar phase function derived from 24 EUV lunar calibrations (Sirk, Korpela, and Stephan, in prep), and the pre-flight spectral response in regions of the detector that are unaffected by high-rate related charge depletion, we determine the geometric EUV albedo for the moon (which does not change from month to month) and calculate the spectral response in the science regions, $\epsilon(\lambda,t)$, so as to track in response changes over time. These changes could be due to contamination from off-gassing material on the spacecraft or due to charge depletion in the microchannel plates, with in orbit charge depletion being the largest contributor to degradation. Uncertainty in the absolute response at launch was 12%. Absolute uncertainty determination through use of SDO EVE spectra is higher as the absolute calibration determination of EVE is ~ 30% (P. Chamberlin 2020, private communication) over our passband, therefore we reference our initial in orbit responsivity calibration to our ground calibration. Any changes in field of view, pointing, or angular scale can also be tracked with these calibrations. No changes in those parameters from values determined on the ground have been found. Figure 3 is an example of a lunar calibration spectrum (red) compared to the contemporaneous SDO EVE spectrum (black). Figure 4 shows the ratio of the EUV to EVE flux for four different emission features.

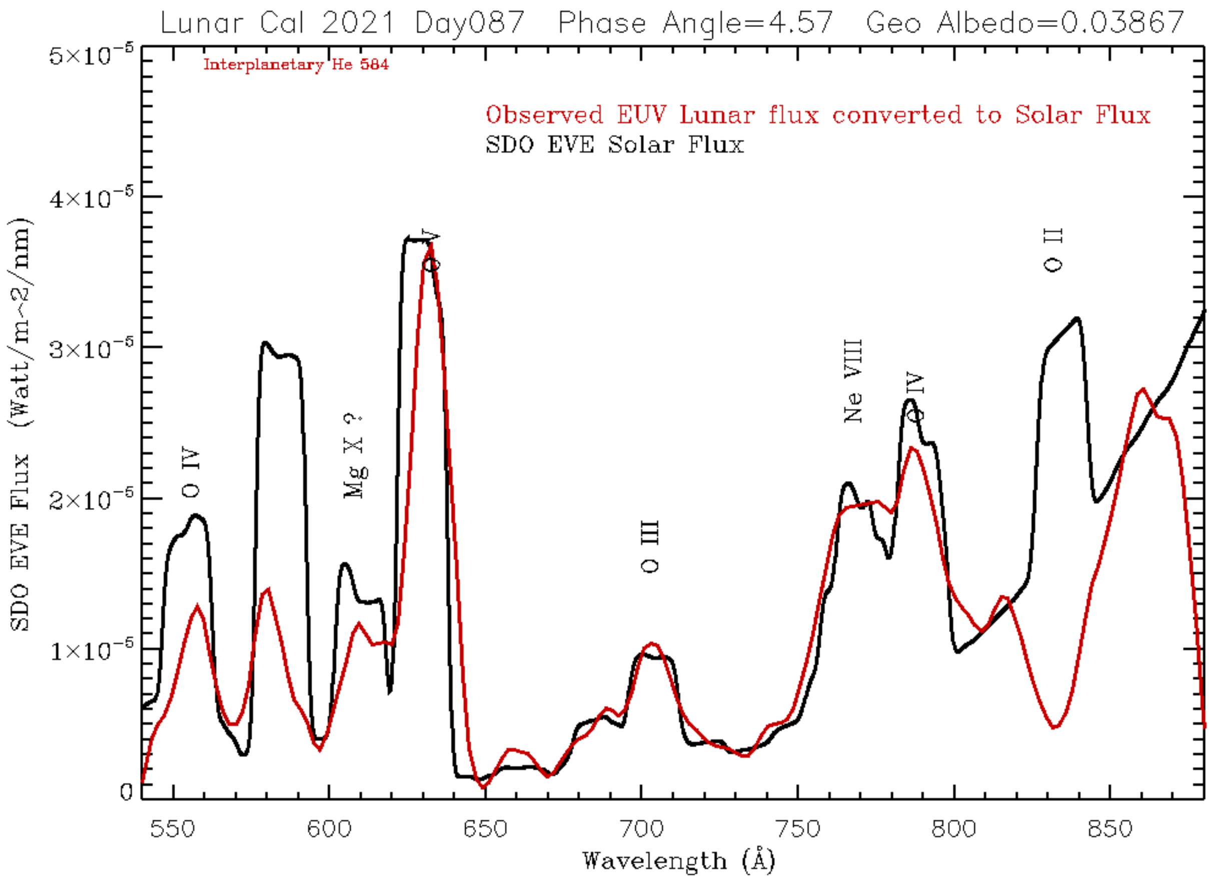

Fig 3: Comparison of ICON EUV Lunar and SDO EVE Solar spectra. Between 62.0 and 82.0 nm the agreement between the two instruments is excellent. The differences at 58.4 and 83.4 nm are direct measurements of gain loss of the EUV detector. The differences at 55.5 and 61.7 nm are most likely caused by known lower lunar albedo at these shorter wavelengths (Flynn et al., 1998).

Because the charge depletion depends upon the received intensity it is important to do a flat field calibration to measure pixel to pixel variations. In essence each vertical pixel has a different absolute calibration value and this can only be determined through flat field calibration. For these calibrations the spacecraft is oriented so that the EUV instrument boresight is pointing towards nadir with the slit oriented parallel to the spacecraft velocity vector. In this configuration any variation in the atmospheric intensity will quickly traverse along the slit. After a several hundred second exposure, each pixel will have seen essentially the same emitting regions and the resulting image can be used to determine a flat field correction at each of the science wavelengths and imaging angles. The primary purpose of the flat field calibration is to correct for sensitivity variations in the imaging directions that could distort the determination of the altitude profile of the emission. Figure 5 shows a comparison of raw O 83.4 nm profiles, averaged over 100 days (two full precision cycles), for time periods early in the mission, and about a year later.

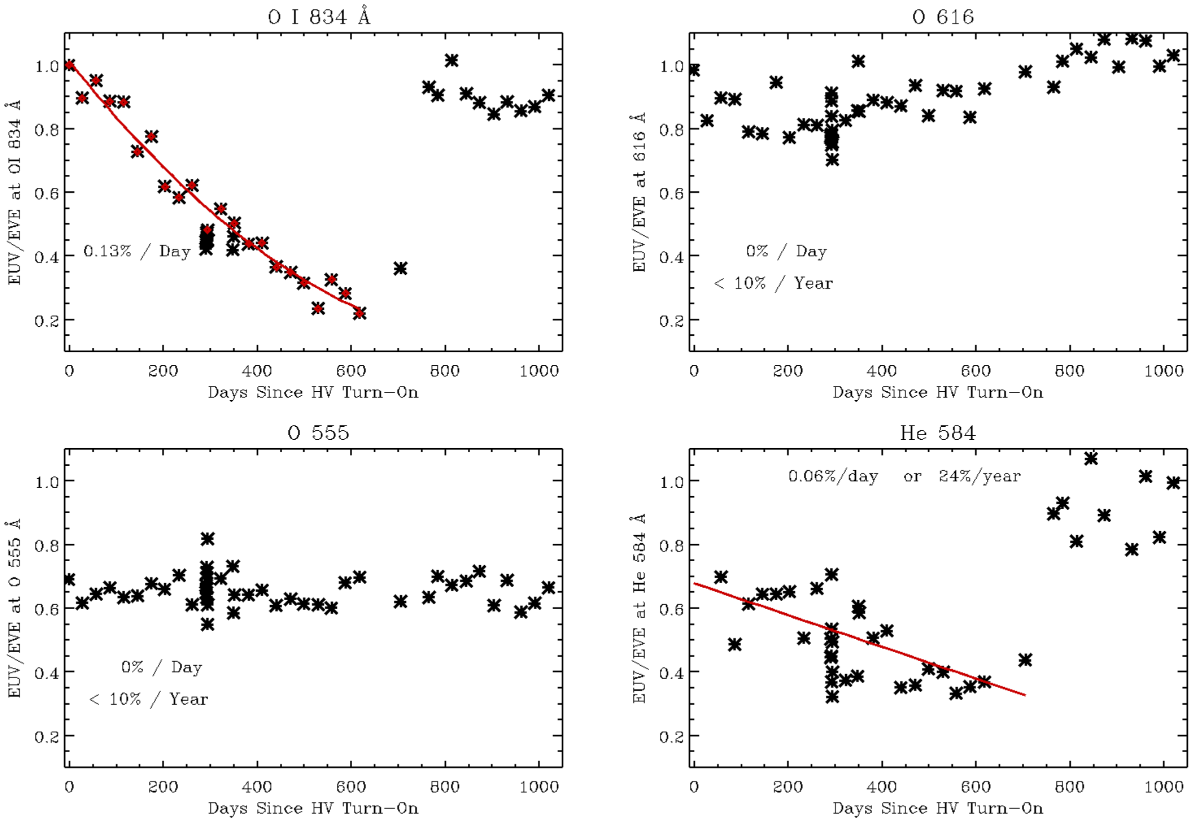

Fig 4: EUV to EVE flux ratios for four different wavelengths from Lunar spectra spanning nearly three years. Decreasing ratios for the O 834 and He 584 emission lines is indicative of detector gain loss, but is negligible at all other wavelengths. Detector voltage was increased by 250 V around day-of-mission 750 to restore sensitivity in the O 834 line to pre-flight levels.

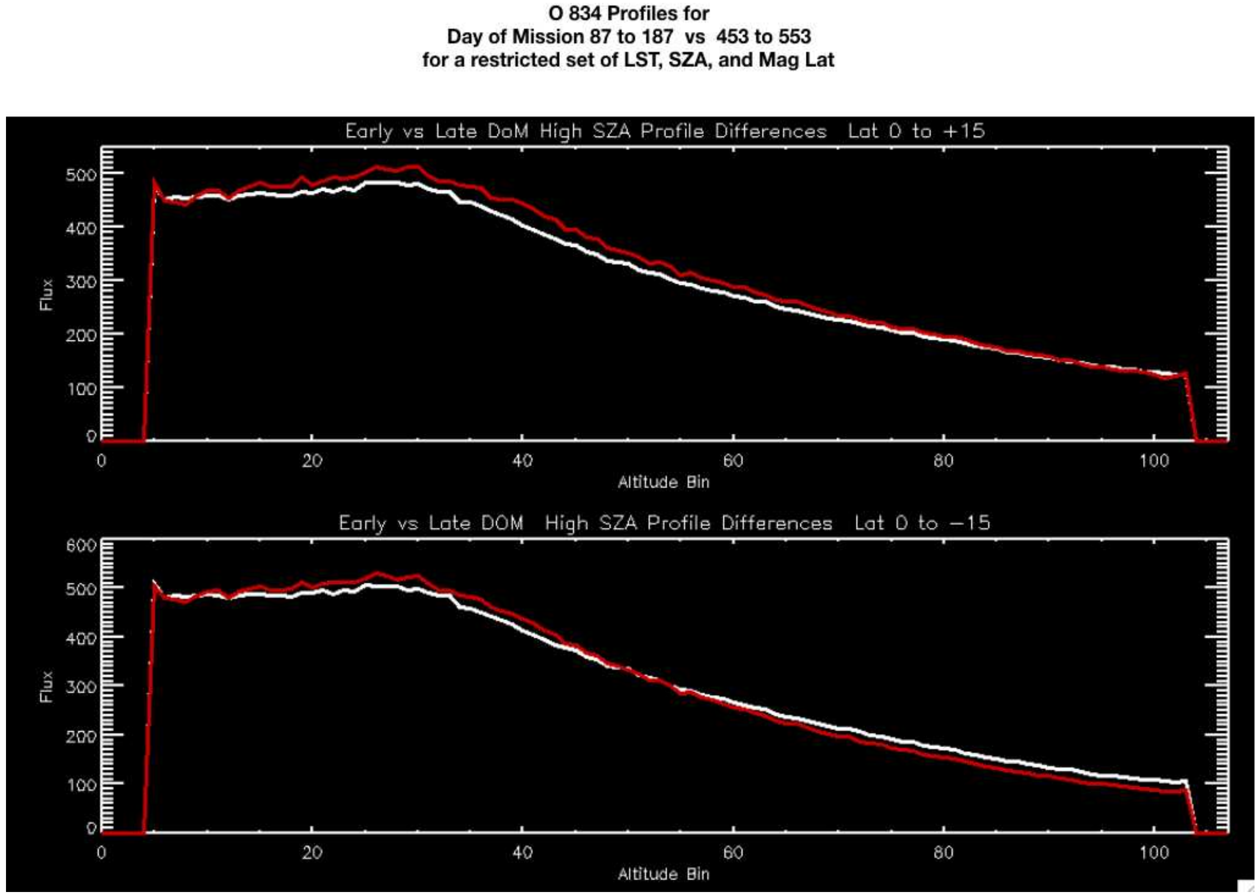

Fig 5: O 83.4 nm profile comparisons. The white curves are from early in the mission where gain loss was minimal while the red curves are from a year later. The upper and lower panels depict data within 15 degrees north, and south of the Earth's magnetic equator, respectively. Changes in the profile shape are minimal despite large changes in detector gain along the profile.

The locations and boundaries of spectral features in these flat field images are used to define altitude profile extraction regions. We determine this flat field, $F_{line}(\phi,t)$, on a "per spectral line" basis. The spectral line region is extracted using the region mask, the emission is summed along the spectral direction, and normalized to an average value of 1.0 to arrive at the flat field correction. Because the same image mask is used for the flat field determination and for the altitude profile extraction, changes in the width of the mask at differing imaging angles are automatically corrected. Flat field calibrations are performed about every six weeks.

4.5 VALIDATION

Further validation of the sensor performance is completed through analysis of the retrieved forward model scalings and propagated measurement uncertainties into ionospheric data product uncertainties that have the potential to identify systematic errors in the Level 1 data products.

Ionospheric data products retrieved from the measurement algorithm are validated primarily through comparison to near-coincident ground-based ionosonde and incoherent scatter radar measurements, and to space-based Global Navigation Satellite Systems (GNSS) radio-occultation measurements. In particular, the ionosonde data require manual processing to ensure the quality of such a comparison. Incoherent scatter radar facilities such as those at Millstone Hill and Jicamarca must operate in campaign modes during overflight of the ICON satellite to ensure proper data are collected for comparison. Additionally, it is noted that the ICON EUV senses O^+ density profiles while all other validation data collect electron density measurements, requiring approximations to the near-complete contribution of O^+ to the ionospheric density profile at F-region altitudes. No routine measurements of O^+ density profiles are made by other sensors or sources for such a direct validation of the ICON EUV data products.

5 EUV MEASUREMENT ALGORITHM DESCRIPTION

5.1 THEORETICAL BASIS

The overarching mission goals of the ICON mission include the need to measure the peak ion density of the F-layer (or its corollary in electron density, commonly referred to as NmF2) and the altitude of that layer peak (hmF2). The method chosen to meet this requirement during the daytime segments of its orbit uses the measurement of naturally-occurring airglow emissions of singly-ionized atomic oxygen (O^+) at 83.4 nm, along with a complementary emission at 61.7 nm, that are used to infer the concentration altitude profile of this species. The ion concentration of the F-layer is approximately 95% O^+ and because of charge neutrality the measurement serves as a proxy for electron density in this layer, and thus hmF2, and NmF2.

The concept for using limb-viewing altitude profiles of the OII 83.4 nm emission feature to infer the concentration profile of the sunlit O^+ was first developed by McCoy et al. (1985). The main source of this emission is photoionization of an inner shell electron of atomic oxygen by either solar EUV ($\lambda < 43.6$ nm) or a photoelectron, followed by the ($2p^4$ 4P $2p^3$ 4S) transition from the triplet exited-state to its singlet ground state along with the emission of a photon. These excitation processes peak in the lower thermosphere, below 200 km, but the photons that are generated undergo multiple resonant scattering by O^+ in the ionosphere that peaks in density at higher altitudes. The altitude profile of the 83.4 nm emission that is measured by ICON when viewed toward the limb thus depends on both the brightness of the original excitation sources in the lower thermosphere and the O^+ ion density in the F-region of the ionosphere.

To resolve the ambiguity between changes in the initial photoemission source in the lower thermosphere and the ionospheric scattering effects of the 83.4 nm emission, ICON will additionally measure the OII 61.7 nm triplet emission feature (3s 2P $\Rightarrow$ 2p3 2D) that derives from the same ionization processes in the lower thermosphere, but is optically thin to the ionosphere. As suggested by McCoy et al. (1985) and Picone (2008), and more fully developed by Stephan et al. (2012) and Stephan (2016) using data from the Remote Atmospheric and Ionospheric Detection System (RAIDS), the 61.7 nm emission solely reflects changes in the brightness of the photoionization source in the lower thermosphere. Pairing measurements of these two emissions allows the analysis to isolate changes in two environmental conditions and therefore more accurately infer the ionospheric profile that only affects the 83.4 nm emission.

A flow chart depicting the main algorithm sequence is shown in Figure 5, and is described in more detail in the following paragraphs. This represents the current as-implemented algorithm, as updated from the original design (Stephan et al., 2017).

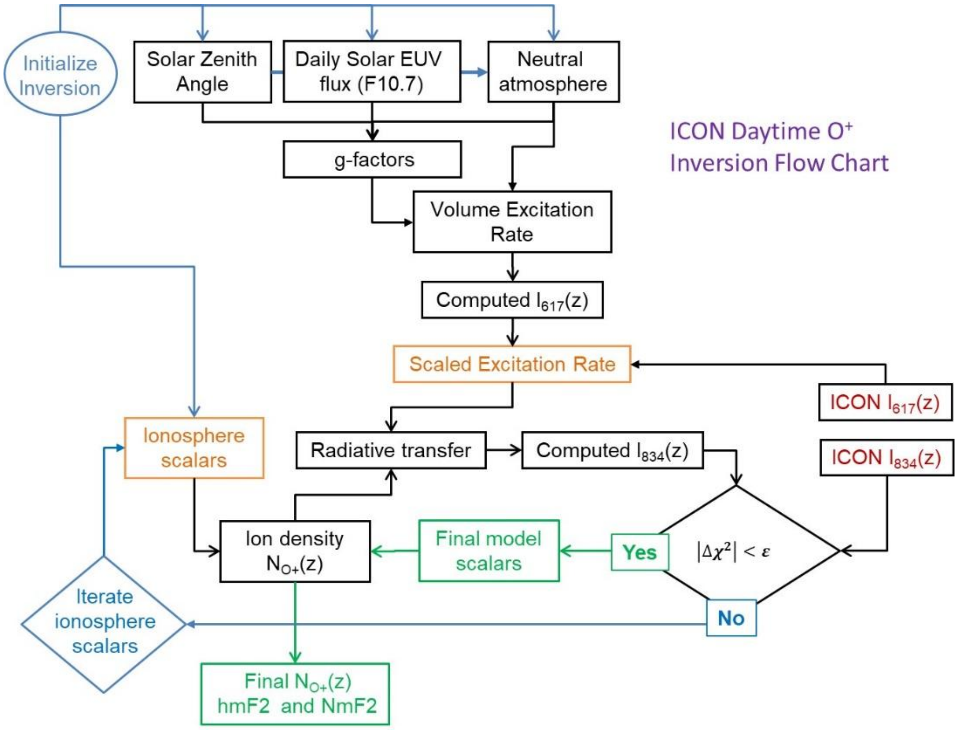

Fig 5. This flow chart shows the general sequence of steps in the forward model to obtain daytime ionospheric parameters using measurements from the ICON EUV instrument, including adjustments made to improve computational speed. Starting from the initialization point in the upper left, the algorithm uses a two-phase process. The algorithm first evaluates a scalar on the 61.7 nm emission to correct for systematic errors in the neutral atmosphere and other inputs to the volume excitation rate from photoionization of atomic oxygen in the lower thermosphere. Then the iterative fitting is completed on the 83.4 nm emission, modifying only the ionosphere parameters to adjust the forward model to best match the measured altitude profile. Measurement uncertainties are fully propagated through the forward model to calculate uncertainties in the precision of the ionosphere products.

A forward model is used to calculate the expected emission intensities as a function of look angle for direct comparison to the ICON EUV measurements. The model includes a calculation of the initial volume excitation of photons in the lower thermosphere, a representation of the ion density, and a calculation of the resonant scattering by O^+ ions as well as the absorption by O^+ ions and neutrals. Although the ionosphere can be most simply represented within the forward model by a Chapman parameterization, the ICON algorithm preferentially implements the 2007 International Reference Ionosphere (IRI) (Bilitza, 2001; Bilitza and Reinisch, 2008) to define the O^+ profile in order to enable a higher-accuracy and more complete representation of the ionospheric density profile by providing additional framework to an inherently underdetermined problem, particularly for ionospheres where hmF2 is low. It is important to note that the algorithm does not require the IRI model to produce an accurate ionosphere for a given time or set of conditions, but only that it is able to quickly generate different ionospheric profiles that can be tested to obtain the best fit to the EUV emissions. Because of the successful heritage of the algorithm with SSULI and the testing completed in preparation for ICON, newer versions of IRI have not been evaluated for use.

The forward model is iteratively adjusted using a set of parameters, $\boldsymbol{m}$, until the output produces the best match to the ICON EUV measurements. These model parameters are selected to be the necessary and sufficient set of model inputs and/or outputs that enable the model to describe the most comprehensive set of possible airglow measurements, and thus ionospheric profiles. For the ICON mission, based on experience developing this algorithm concept for the SSULI program (see Stephan, 2016), the model employs three model parameters (not counting the scalar on the excitation rate described above): two to adjust the profiles of the IRI model that describe the O^+ density using the 12-month running mean of sunspot number (Rz12) and the ionosonde-based 12-month running mean of the ionospheric global (IG12) index, and one to scale the entirety of the ion density profile. Testing with SSULI data and through the first two years of the ICON prime mission has found these to be sufficient to present a solution for most ionospheric conditions.

5.2 CONVERSION OF INSTRUMENT SIGNALS TO RAYLEIGHS

5.2.1 MEASUREMENT EQUATIONS

To determine the flux in Rayleighs at any vertical pixel, we use the equation:

$$I(\phi)[R] = \frac{4\pi}{10^6}\frac{F(\phi,t)}{\epsilon(\lambda,t)\ A_{\text{slit}}\ \Omega(\phi)}\left(\frac{n(\phi,t)-b(\phi,t)\frac{F_b(\phi,t)}{F(\phi,t)}}{t_{\text{exp}}\ d(t)}\right)$$

where

- $\epsilon(\lambda,t)$ is the instrument responsivity or efficiency terms of detector counts generated per incoming photon determined through the combination of ground calibrations and the lunar calibrations and interpolated to the time of the observations.
- A_{slit} is the geometric area of the instrument input slit (determined in ground calibrations)
- $\Omega(\phi)$ is the quantity of solid angle viewed by the specific angular pixel being calculated, also determined during ground calibration.
- $F(\phi,t)$ is the flat field correction value for the pixel, interpolated to the time of the exposure.
- $n(\phi,t)$ is the number of counts detected in the pixel
- $b(\phi,t)\ F_b(\phi,t)/F(\phi,t)$ is the number of counts in the same altitude pixel of the background region corrected for relative flat field effects.
- t_{exp} is the exposure time recorded by the Instrument Control Package (typically 12.000 seconds)
- $d(t)$ is the detector deadtime correction.

5.3 SIGNAL ESTIMATES AND ERROR ANALYSES FOR SUBSYSTEMS

The intensity of 83.4nm and 61.7 nm dayglow are fairly well known, and are typically of the order 800R and 70R respectively. However the goal of ICON EUV is to be able to invert the altitude profiles in order to determine the peak density and the altitude of the peak. We determine the necessary sensitivity by creating example profiles with various instrument sensitivities and finding which profiles could be correctly inverted. The allowed value of the relative and absolute errors are determined by the ability to perform the inversions on the profile to obtain the required nmF2 and hmF2 values (as discussed in the section on the ICON 2.6 data product.) Preflight simulations showed that a full field 3σ Minimum Measurable Flux of 7.2R in the 61.7nm OII line and 30R in the 83.4nm line would be sufficient to provide accurate inversions. The tables below describe the imaging, sensitivity, and error budgets necessary to achieve this result.

5.3.1 EUV SIGNAL ESTIMATES AND ERROR ANALYSIS

5.3.1.1 Spectral Imaging Budget

	Measured	Margin	Required Value
RLD	0.00195 nm/micron		
Slit Width	904 microns (FW)		
Spectral Focus	195 microns (FWHM)		
Detector X imaging	90 microns (FWHM)		
Electronic Pixel	2048		
X Imaging	2.36nm	78%	4.20nm

Total Margin	78%

5.3.1.2 Angular Imaging Budget

	Measured Value	Margin	Required Value
Vertical FOV	17.3 degrees		
Focal Length	17.11 cm		
Imaging Focus	200 microns (FWHM)		
Detector Y imaging	160 microns (FWHM)		
Reported Pixels	108		
Y Imaging	0.17degrees (FWHM)	171%	0.45degrees

Total Margin	171%

5.3.1.3 EUV COMPONENT EFFICIENCY BUDGET

	Current Estimate	Margin	Required Value
Slit Width	0.904 mm		
Slit Length	40 mm		
Horizontal FOV	12.12 degree		
Science Pixel (Req)	0.45 degree		
Detector QE	11.7 %		
Grating Coating	24.8 %		
Grating Ruling	33.6 %		
$A_{eff}*\Omega$	5.86×10^{-6} cm^2 sr^{-1}	90%	0.57×10^{-6} cm^2 sr^{-1}

Total Margin	90%

5.3.1.4 SENSITIVITY

Sensitivity Budget

	OII 61.7 nm	OII 83.4 nm
Aeff*Ω	6.61x10^{-6} cm^{2} sr	5.86x10^{-6} cm^{2} sr
Required MDF	7.4 R	30.0 R
Exposure Time	12.0 s	12.0 s
Line counts in exposure	46.7 counts	167.9 counts
Detector Background	8.9 counts	8.9 counts
Scattered Light	6.3 counts	6.3 counts
58.4nm contamination	1.2 counts	0.0 counts
Total counts	63.0 counts	183.0 counts
Background	16.3 counts	15.1 counts
Foreground Uncertainty	7.9 counts	13.5 counts
Background Uncertainty	5.1 counts	3.9 counts
Total uncertainty	9.4 counts	14.1 counts
Measurement significance	5.0 σ	11.9 σ
Margin	65.1%	297.5%

5.3.1.5 ABSOLUTE CALIBRATION ERROR BUDGET

Ground Calibration

Per Pixel Statistical Uncertainty	1 %
NIST Photodiode Uncertainty	10 %
Source Stability	5 %*
Total	15 %

Flight Calibration

Per Pixel Statistical Uncertainty	3 %
Solar Spectrum Knowledge	30 %
Lunar Albedo Knowledge	8 %
Lunar Albedo Systematic Uncertainty	2 %*
Lunar Phase vs Albedo Uncertainty	5 %
Total	34 %

* Contributes linearly, remaining values contribute in quadrature

5.3.1.6 RELATIVE CALIBRATION ERROR BUDGET

Pixel to Pixel (Nadir Pointing)

Airglow Uncertainty integrated over track	1 %
Effect of Variability over exposure	<1 %
Per Pixel Statistical Uncertainty	1 %
Total	2 %

Over time (Lunar and Nadir Pointing)

Per Pixel Statistical Uncertainty	1-3 %
Solar Spectrum /Airglow Variability Uncertainty	10 %
Lunar Phase Albedo Uncertainty	5 %
Total	12 %

5.4 PREFLIGHT CALIBRATION ALGORITHMS

Preflight Calibration Algorithms are described completely in the above section 5.2

5.5 RETRIEVAL ALGORITHM – CONVERSION OF RADIANCES TO IONOSPHERIC O^+ PROFILES

The initial volume excitation of the 83.4 and 61.7 nm emissions by solar photoionization of atomic oxygen in the lower thermosphere, the number of excitations per second per atom, is calculated using the g-factor $g(\boldsymbol{r})$ at position $\boldsymbol{r}$ in the atmosphere that is given by:

$$g(r) = \int_{\nu_0}^{\infty} \sigma(\nu) F(r,\nu) d\nu, \tag{1}$$

where F is the attenuated solar flux of wavelength ν at atmospheric position $\boldsymbol{r}$, and σ is the excitation cross section to the excited state for each emission feature ($2p^4\ {}^4P$ for 83.4 nm, and $3s\ {}^2P$ for 61.7 nm). The algorithm uses a parameterized representation of the g-factors derived from the Atmospheric Ultraviolet Radiance Integrated Code (AURIC) (Strickland et al., 1999) that enables a rapid computation of the g-factors as a function of the solar zenith angle, solar F10.7 index, and the total vertical column density of neutral species above location $\boldsymbol{r}$. A calculation of the solar 83.4 nm source contribution based on the solar flux model of Hinteregger, et al. (1981) is included in the ICON algorithm for completeness. As described in extensive mathematical detail in the appendix to Picone et al. (1997b), the forward model calculates this excitation at a discrete set of altitudes, z_i, that are then used to complete the radiative transfer and absorption calculations, and the integration along the line of sight. The key algorithm steps from Picone et al. (1997a, 1997b) are summarized here. With the approximation that horizontal transport is effectively zero due to spherical symmetry, $\boldsymbol{r}$ translates directly to z. Then the volume excitation rate $j_k(z)$ of line k in each emission feature, at altitude z, is given by:

$$j_k(z) = j_{0k}(z) + \sigma_{0k} N_{O^+}(z) \int_{z_0}^{\infty} j_k(z') H(|\tau_k' - \tau_k|, |t_k' - t_k|)\, dz', \tag{2}$$

which includes the production source from the initial photoionization of atomic oxygen in the lower thermosphere, j_{0k}, that is calculated from the appropriate photoionization g-factor from (1) and the number density of atomic oxygen, N_o, using

$$j_{0k}(z) = g(z) N_O(z). \tag{3}$$

The contribution from scattering by the population of O$^+$ (N_{o^+}) at all other altitudes into the altitude z is given by the Holstein probability function, H, which describes the probability that a photon will resonantly scatter from altitude z' to the altitude z (Holstein, 1947), and the scattering cross section σ_{0k}. This volume emission rate field is then used to integrate along the line of sight and calculate the measured emission intensity, $4\pi I$, in Rayleighs which, if I is the radiance in megaphotons cm^{-2} s^{-1} ster^{-1}, is then given by:

$$4\pi I(r, \hat{e}) = 10^{-6} \int \sum_k j_k[r'(s)]\, T_k(r', r)\, ds, \tag{3}$$

where T_k is the transmission probability that a photon emitted from region $\boldsymbol{r'}$ along the line of sight $\hat{e}$, will reach the sensor located at $\boldsymbol{r}$.

The algorithm first evaluates the 61.7 nm emission, which does not require the ionospheric scattering calculation, to determine a multiplicative bias term as described by Picone (2008) and Stephan (2016). This scalar term is a necessary component of the forward model to mitigate potential systematic errors in not only the absolute intensity of the EUV measurements but also in the physics of the forward model itself, as shown in the upper half of Figure 5. Systematic uncertainties in the forward model are most likely to stem from the specification of the production of photons in the lower thermosphere, also referred to as the “initial source” (Picone, 2008). However, the manifestation of these sources in the data are expected to be significantly different, with instrument calibration errors steady or slowly changing over time, and physics-based errors governed more by solar and global thermospheric conditions that change and alter the generation of airglow profiles with scales on the order of a day (Stephan, 2016). It is noted that this approach does not compensate for an additive bias created by an inappropriate background subtraction, or an altitude-dependent bias caused, for example, by non-uniform background contributions across the passband due to out-of-band light that unknowingly changes the shape of the emission brightness with respect to altitude.

The algorithm then uses the Levenberg-Marquardt scheme to minimize χ^2 between the measured 83.4 nm emission data and the model, with convergence determined by evaluating a threshold in change in the χ^2 between successive results. The resulting best fit is determined to be the most probable values for the model parameters, and a covariance matrix for the model parameter vector is calculated. The variances in the ionospheric density profile and the hmF2 and NmF2 values are calculated at each altitude using standard error propagation equations with the covariance matrix, the retrieved model parameters, and the partial derivatives of the density with respect to the model parameters.

The Level 2 data product for the EUV measurement will include the retrieved O^+ density profile and the correlated hmF2 and NmF2 values along with uncertainties in each. Random uncertainties are a product of the photon-counting nature of the measurement and are handled directly by the inversion algorithm. While systematic uncertainties can be included as part of the inversion process, they are best handled by the inclusion of the bias term as described. However, even using a state-of-the-art, best-practices approach for calibration of the EUV sensor, the systematic uncertainty in instrument response, and thus absolute intensity of the ICON EUV L1 data products is on the order of 13% (Sirk, et al., 2017; Korpela, et al., 2022). On-orbit characterization will be used throughout the mission to identify these factors and define the best approach to handle these within the inversion algorithm.

Data quality flags and metrics from the Level 1 data will be passed through to the Level 2 data, as well as new flags to identify the quality of the fit from the algorithm, along with other data quality and metrics from the fitting process (e.g. convergence issues, model parameters driven to functional limits) that users should consider when conducting an analysis with the ICON EUV data products.

6 REFERENCES

1. Bilitza, D. (2001) International Reference Ionosphere 2000, Radio Sci. 36(2), 261–275. https://doi.org/10.1029/2000RS002432
2. Bilitza, D., & Reinisch, B.W. (2008) International Reference Ionosphere 2007: improvements and new parameters, Adv. Space Res. 42, 599–609. https://doi.org/10.1016/j.asr.2007.07.048
3. Flynn, B.C., Vallerga, J.D., Gladstone, G.R., and Edelstein, J. (1998), Geophys. Res. Let. 25, 3253, http://dx.doi.org/10.1029/98GL02483
4. Hinteregger, H. E., K. Fukui, and B. R. Gilson (1981), Observational, reference and model data on solar EUV, from measurements on AE-E, Geophys. Res. Lett., 8, 1147–1150. https://doi.org/10.1029/GL008i011p01147
5. Holstein, T. (1947), Imprisonment of resonance radiation in gases. Phys. Rev. 72, 1212–1233. https://doi.org/10.1103/PhysRev.72.1212
6. Immel, T.J., S. L. England, S. B. Mende, R.A. Heelis, C.R. Englert, J. Edelstein, et al. (2018), The Ionospheric Connection Explorer mission: Mission goals and design, Space Sci. Rev., 214: 13. https://doi.org/10.1007/s11214-017-0449-2
7. Korpela, E.J., Sirk, M. M., Edelstein, J., McPhate, J. B., Tuminello, R. M., Stephan, A. W., et al. (2022). In-flight performance of the ICON EUV spectrograph, Space Science Reviews, submitted May 2022.
8. McCoy, R. P., D. E. Anderson Jr., and S. Chakrabarti (1985), F2 region ion densities from analysis of O^+ 834-A airglow: A parametric study and comparisons with satellite data, J. Geophys. Res., 90(A12), 12,257. https://doi.org/10.1029/JA090iA12p12257

9. Meier, R. R., and J. M. Picone (1994), Retrieval of absolute thermospheric concentrations from the far UV dayglow: An application of discrete inverse theory, J. Geophys. Res., 99(A4), 6307–6320. https://doi.org/10.1029/93JA02775
10. Meier, R. R., J. M. Picone, D. Drob, J. Bishop, J. T. Emmert, J. L. Lean, A. W. Stephan, et al. (2015), Remote Sensing of Earth's Limb by TIMED/GUVI: Retrieval of thermospheric composition and temperature, Earth and Space Science, 2, 1-37. https://doi.org/10.1002/2014EA000035
11. Picone, J., R. Meier, O. Kelley, D. Melendez-Alvira, K. Dymond, R. McCoy, and M. Buonsanto (1997a), Discrete inverse theory for 834-Å ionospheric remote sensing, Radio Sci., 32(5), 1973–1984. https://doi.org/10.1029/97RS01028
12. Picone, J., R. Meier, O. Kelley, K. Dymond, R. Thomas, D. Melendez-Alvira, and R. McCoy (1997b), Investigation of ionospheric remote sensing using the 834-Å airglow, J. Geophys. Res., 102(A2), 2441–2456. https://doi.org/10.1029/96JA03314
13. Picone, J. M. (2008), Influence of systematic error on least squares retrieval of upper atmospheric parameters from the ultraviolet airglow, J. Geophys. Res., 113, A09306. https://doi.org/10.1029/2007JA012831
14. Sirk, M. M., E. J. Korpela, Y. Ishikawa, J. Edelstein, E. H. Wishnow, C. Smith, et al. (2017), Design and Performance of the ICON EUV Spectrograph, Space Sci Rev., 212:631–643. https://doi.org/10.1007/s11214-017-0384-2
15. Stephan, A. W. (2016), Advances in remote sensing of the daytime ionosphere with EUV airglow, J. Geophys. Res. Space Physics, 121, 9284–9292. https://doi.org/10.1002/2016JA022629
16. Stephan, A. W., J. M. Picone, S. A. Budzien, R. L. Bishop, A. B. Christensen, and J. H. Hecht (2012), Measurement and application of the OII 61.7 nm airglow, J. Geophys. Res., 117, A01316. https://doi.org/10.1029/2011JA016897
17. Stephan, A. W., Korpela, E. J., Sirk, M. M., England, S. L., and Immel, T. J. (2017), Daytime Ionosphere Retrieval Algorithm for the Ionospheric Connection Explorer (ICON), Space Sci Rev., 212: 645. https://doi.org/10.1007/s11214-017-0385-1
18. Strickland, D. E., J. Bishop, J. S. Evans, T. Majeed, P. M. Shen, R. J. Cox, R. Link, and R. E. Huffman (1999), Atmospheric Ultraviolet Radiance Integrated Code (AURIC): Theory, software architecture, inputs, and selected results, J. Quant. Spect. Rad. Trans., 62(6), 689–742. https://doi.org/10.1016/S0022-4073(98)00098-3

1. Chapter 4 : ICON FUV

This document describes the FUV instrument function, ground calibration, and those aspects of the on-orbit instrument performance that affect or are dependent upon calibration and ground processing algorithms. The key operating principles are described, leading to the calibration requirements and the methodology employed in ground processing to retrieve geophysical parameters.

2. Related Documentations

2.1 Applicable Documents

Title	Document Number	Publication Date
FUV L4 Requirements Document	ICN-SYS-017-PSR	
FUV Requirements Verification Matrix		
FUV Verification and Validation Plan		
FUV Calibration Plans		
	ICN-FUV-077_distortion	9/17/2015
	ICN-FUV-078_turret	9/16/2016
	ICN-FUV-079_sensitivity	9/17/2015
	ICN-FUV-080_flatfield	9/17/2015
	ICN-FUV-081_stray-light	9/17/2015
Design and Performance of the ICON FUV Spectrograph	Space Science Reviews, 212, 10.1007/s11214-017-0384-2 (2017)	20 Jul 2017
In-flight performance of the ICON FUV spectrograph	Space Science Reviews, 219, (2022), 10.1007/s11214-023-00969-9	9 May 2022

3. Overview and Background Information

3.1 Science Objectives

ICON Far UltraViolet (FUV) imager contributes to the ICON science objectives by providing remote sensing measurements of the daytime and nighttime atmosphere/ionosphere. During sunlit atmospheric conditions, ICON FUV images the limb altitude profile in the shortwave (SW) band at 135.6 nm and the longwave (LW) band at 157 nm perpendicular to the satellite motion to retrieve the atmospheric O/N_2 ratio. In conditions of atmospheric darkness, ICON FUV measures the 135.6 nm recombination emission of O+ ions used to compute the nighttime ionospheric altitude distribution. ICON Far Ultra-Violet (FUV) imager is a Czerny–Turner design Spectrographic Imager with two exit slits and corresponding back imager cameras that produce two independent images in separate wavelength bands on two detectors. All observations are processed as limb altitude profiles. In addition, the ionospheric 135.6 nm data are processed as longitude and latitude spatial maps to obtain images of ion distributions around regions of equatorial spread F. The ICON FUV optic axis is pointed 20 degrees below local horizontal and has a steering mirror that allows the field of view to be steered up to 30 degrees forward and aft, to keep the local magnetic meridian in the field of view. The detectors are micro channel plate (MCP) intensified FUV tubes with the phosphor fiber-optically coupled to Charge Coupled Devices (CCDs). The dual stack MCP-s amplify the photoelectron signals to overcome the CCD noise and the rapidly scanned frames are co-added to digitally create 12-second integrated images. Digital on-board signal processing is used to compensate for geometric distortion and satellite motion and to achieve data compression.

3.2 FUV Instrument Description

3.2.1 Measurement Concept

The spectrum of the dayglow of the upper atmosphere is illustrated in Figure 3.2 below. Lines of the LBH band system are illustrated in black while the 135.6 nm O emission is in green. ICON FUV was designed to pick up parts of the LBH bands to measure the daytime N2 component of atmospheric density while the O component is measured via the 135.6 O atomic line. The same 135.6 line is used at night for the ionospheric ion density measurement. Three undesirable emission features are shown in orange color and they represent the optically thick 130.4 nm O line, the 149.3 nm N line, and the 164.1 nm O line. Including these lines into the FUV instrumental passband would make the data analysis more difficult and it was a specific requirement to avoid these features. ICON FUV spectral regions are labeled as Long Wave (LW) and Short Wave (SW) bands. The requirement of transmitting the 135.6 nm line and rejecting the 130.4 dictated the most stringent spectral resolution requirement. Lyman alpha (121.6 nm) is the brightest emission reaching almost several tens of kR near the limb. Suppressing Lyman alpha therefore is of paramount importance. The same goes for the 130.4 nm OI feature, as it is also very bright, and being optically thick cannot be used for direct inversion of the limb emission profiles.

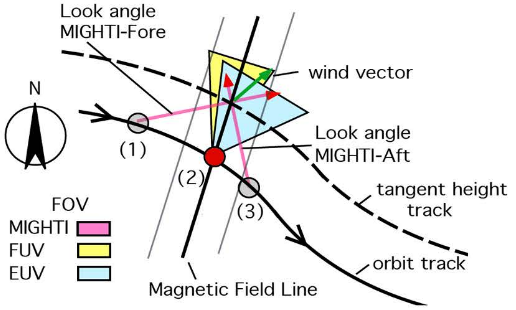

Fig. 4 Top view of the ICON observing scenario with the S/C at three positions along the orbit track. The EUV fixed FOV is illustrated in *blue* while the horizontally steered FUV is illustrated in *yellow* (Color figure online)

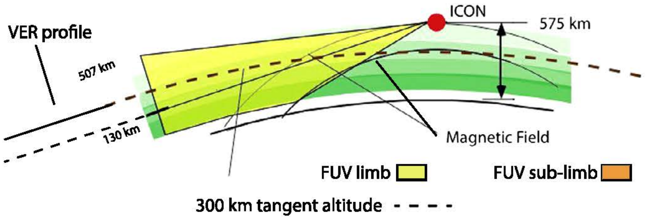

Fig 3.1: Side view of ICON FUV viewing geometry (not to scale). ICON S/C is shown travelling into the page (eastward) on the magnetic equator at 575 km altitude with FUV viewing on the port side with the central ray observing at 20 degrees below local horizontal. Volume Emission Rate (VER) profile with altitude for nighttime 135.6 nm emission shown on left

A top view of the ICON FUV observing scenario is shown with three positions of the S/C along the orbit track. First from position (1) and then about seven minutes later from position (3) the fore- and aft-viewing ICON Michelson interferometer (MIGHTI-Fore and MIGHTI-Aft) measure the Doppler shift of the line of sight components of the airglow emitted by the neutral wind driven atmosphere. From the two Doppler measurements the actual vector direction and magnitude of the wind can be derived at locations labeled as “tangent height track”. The ICON ion drift meter measures the ion velocity at the S/C on the same field line at position (2) where the wind is also measured, therefore the measured ion drift and corresponding electric field at the spacecraft can be mapped along the magnetic field to the wind altitude profile measurements. At position (2), the FUV and the Extreme-UV (EUV) instruments take a set of limb view images of the atmosphere and ionosphere also near the footprint of ICON’s magnetic field line. The horizontally steered FUV field of view is illustrated in yellow. At night time the equatorial ionosphere is structured and the structures are aligned along the magnetic field therefore it is advantageous to observe them in a direction parallel to the magnetic field. There is a requirement that on the night side the FUV field of view is steered to be parallel with the local magnetic field at ICON. The ICON FUV nighttime viewing geometry is illustrated as a side view. The 24◦ vertical FOV covers a region nominally from −8 to −32 degree elevation. Two arched equatorial magnetic field lines are also illustrated.

The observed intensity is limited at the bottom by the O_2 FUV extinction at about 130 km altitude. The figure shows the nighttime ionospheric emissions peaking around 300 km. The 300 km altitude line is indicated by a dashed curve. If all the emissions were generated at this altitude then ICON FUV would view them as a two dimensional scene observed at a slant view from above in the view angle region of tangent height of 300 km and below, shown in orange. This viewing scenario is designated as “FUV sub-limb” region. Emissions above the 300 km tangent height are mapped according to their tangent altitude. This viewing scenario is illustrated as “FUV limb” and is shown in yellow color. Processing the two dimensional FUV imaging data and compensating for satellite motion involves estimating the range distance of the object from the observer which is calculated from the assumed emission height. This process is described in detail in (Wilkins et al. 2017).

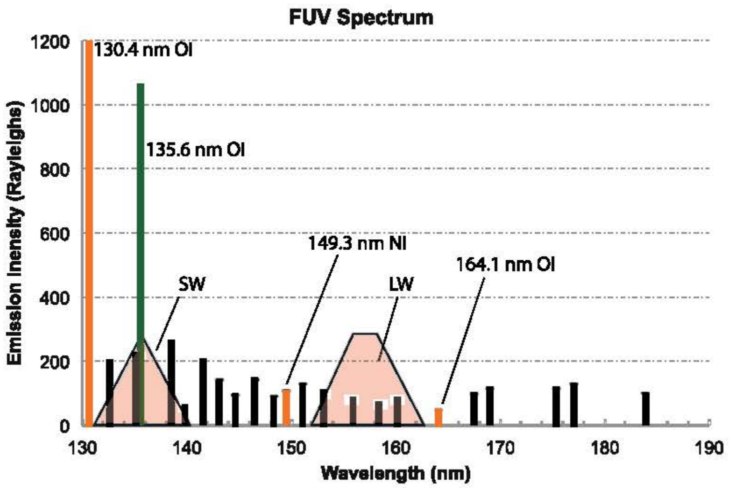

Fig 3.2: FUV dayglow spectrum. LBH band (black), OI 135.6 nm (green), and undesirable OI and NI lines in orange

Parameter	Minimum Success Requirements	Comprehensive Success Criteria	Performance
Wavelength	OI 135.6 nm and N2-LBH 157 nm	OI 135.6 nm and N2-LBH 157 nm	OI 135.6 nm and N2-LBH 157 nm
Wavelength suppression	Suppress 130.4 nm and 163 nm	Suppress 130.4 nm <1% and 163 nm <1%	Suppress 130.4 nm <0.1% and 163 nm <0.1%
Time Cadence	60 sec	< 20 sec	12 sec
Field of view	>15°	>15°	24° vertical, 18° horizontal
Imaging resolution	<10 km vertical	<10 km vertical	4 km vertical
Mission Life	2 years	2 years	>2.5 years

Table 3.1: Requirements and performance of ICON FUV instrument

3.2.2 Instrument Subsystem Descriptions

3.2.2.1 The FUV Spectrographic Imager

Two concepts are commonly used in FUV aeronomy: (1) Imaging Spectrometers (IS) and (2) Spectrographic Imagers (SI) (Mende, 2016). In both instrument types the dispersing element, the grating operates in combination with a slit to select the wavelength pass-band. The slit can be regarded as a mask, selecting only certain angles to pass. However, the image is formed at the slit in the IS while the image is formed at the grating in the SI. In the IS spatial imaging at the output is a convolution of the image and the instrumental wavelength profile. This is contrary to the SI where the spectral dispersion and the imaging properties are in "quadrature", i.e. they are separate and independent of each other.

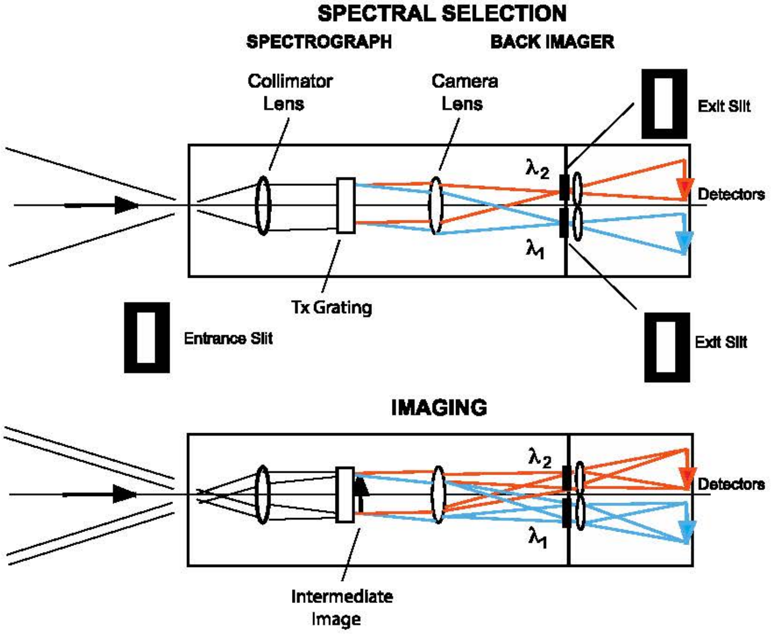

Fig 3.3: Schematic of the optical principle of a spectrographic imager designed to accept two wavelength channels using lenses

Here we present a schematic illustration of a dual wavelength SI concept using refractive optical elements. The diagram provides two illustrations of the ray-paths through the same instrument. The top is the ray path shown for spectral selection. Light enters at the slit and is collimated by the collimator optics that are placed one focal distance behind the entrance slit. This collimating optics has two basic functions, first it produces parallel light from the slit and second, it focuses the viewed object on the grating. The parallel light is dispersed by the grating according to wavelength. By having two separate exit slits it is possible to have two separate wavelength channels in a single instrument. The wavelength $\lambda 2$ illustrated in red is dispersed upward and the other wavelength $\lambda 1$ illustrated in blue is dispersed downward. After passing the grating, the camera lens focuses the parallel blue light of wavelength $\lambda 1$ into the lower exit slit, while the red light of wavelength $\lambda 2$ is focused into the upper slit. The blue and red light reach separate detectors in our scheme. In terms of the upper diagram, the instrument can be regarded as a conventional monochromator with two exit slits and without imaging.

The lower illustration of the figure represents the same optical train, but shows how two dimensional imaging takes place. From each distant object point in the scene, parallel light enters the entrance slit. The collimator lens, which is placed one focal distance in front of the grating, focuses the parallel light on the grating, thus forming an intermediate image at the grating. The “camera lens”, following the grating in combination with the small lens placed behind each exit slit re-images the intermediate image on the detector. This instrument therefore produces two-dimensional spectrally filtered images of the same scene on two detectors simultaneously. These instruments were introduced in the ultraviolet for space use where narrowband filtering with multi-layer filters would have been otherwise problematic (Mende et al., 2000c).

Fig. 8 A view of the ICON FUV instrument on the bench

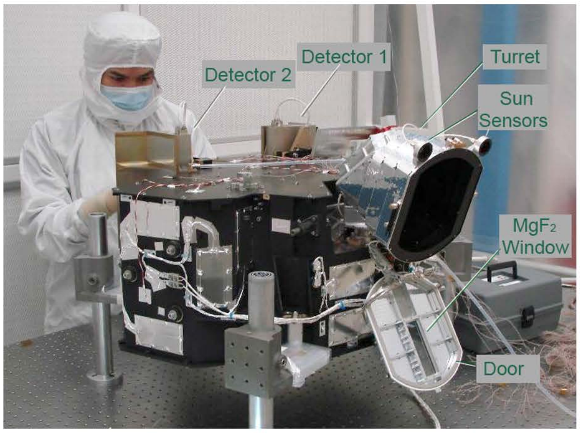

Fig 3.4: A photo of the ICON-FUV on the bench with a person for size comparison

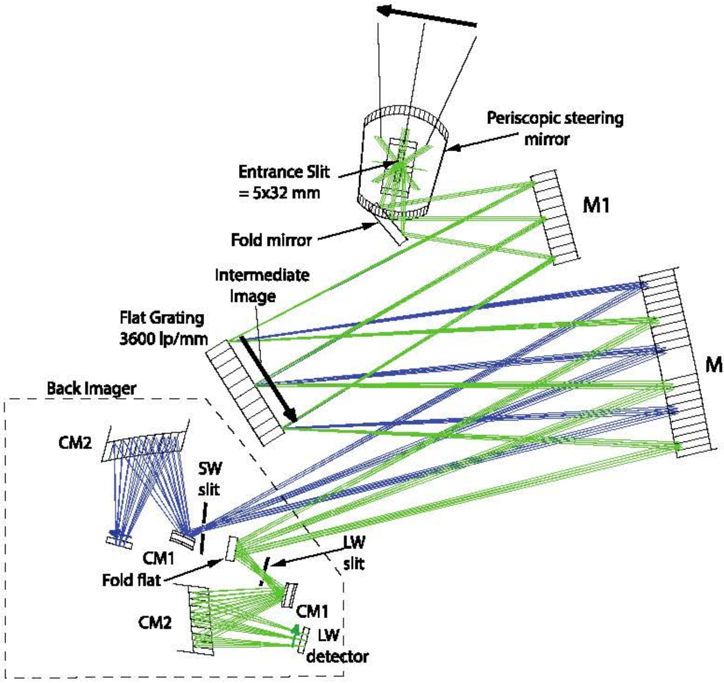

Fig 3.5: Top schematic view of the ICON-FUV

The first example of a Spectrographic Imager was flown on the NASA IMAGE mission. In this instrument the grating spectrometer was a Wadsworth configuration instrument with a concave grating and with a hole in the grating center where the entrance slit was placed. This allowed the use of an axial collimator for improved spectral performance. However, this hole appeared as an obscured region at the center of the final image. For ICON it was considered highly desirable to remove the obscuration and a Czerny–Turner (CZT) (Czerny and Turner, 1930) spectrograph configuration was selected instead. With the ICON resolving requirements, this optical arrangement permitted the use of off-axis mirrors and eliminated the requirement for the central obscuration of the IMAGE Wadsworth type instrument. A disadvantage of the Czerny Turner-based instrument is that it requires an additional mirror with the associated reflective losses and mass and cost penalties. Considerable progress has been made in producing highly-efficient UV mirrors since the IMAGE program and the additional reflection loss became a less crucial issue (Quijada et al. 2012).

A photograph of the ICON Spectrographic Imager is shown above together with a top view of the optical model. The viewed object is schematically illustrated by an arrow on the top. Light enters the instrument at the top of the illustration and is reflected by the steering mirror. The periscopic steering mirror points the direction of the optic axis by rotating around a vertical (perpendicular to the page) axis. There are two small 45◦mirrors behind the entrance slit, one of them is to provide the second periscope mirror and the other to turn the image to ensure that the horizon is perpendicular to the slit when the turret is in its normal (turret angle = 0) position. These two mirrors are not shown on the schematics. The spectrograph slits, grating and detectors are fixed in the instrument frame but if the scan mirror is not in its normal position the projection of the slit on the outside view will appear to be rotated. Thus effectively the spectral slit will be superposed on the outside atmosphere at an angle with respect to the vertical depending on the position of the steering mirror.

All optical elements are reflective with the exception of the detector windows, which are MgF2. The spectrograph mirrors M1 and M2 are both spherical. M1 acts as a spectroscopic collimator as well as a camera mirror to create the intermediate image of the scene at the grating acting the same as the collimating lens. M2 is the spectrograph's "camera mirror," focusing the image of the input slit at the output slits. Depending on the wavelength, the grating dispersion and the location of the output slits, light of the appropriate wavelength band is selected. One can regard M2 as a collimator for the imaging operation, creating near parallel light for each image point on the grating to be re-focused on the detectors by the back imager aspheric mirrors CM1 and CM2. There is a separate set of back imager optics for each of the two wavelength channels (SW and LW) including the exit slits shown in black. In order to allow more room and accommodate the configuration, the LW channel has a turning flat mirror, which allows placing the LW channel out of the way of the other channel.

3.2.2.2 ICON FUV Detectors, Electronics, and Data Handling

The ICON FUV detectors consist of image tubes that are fiber-optically coupled to CCDs. The image tubes have MgF2 windows and FUV photocathodes evaporated directly on to the microchannel plate (MCP). A stack of two MCPs are used, which arrangement provides sufficient charge multiplication gain to overcome readout or dark current noise downstream in the CCD. The CCDs operate in a fast scan mode at 8.33 frames per second (fps). 100 video frames are co-added digitally in memory in the ICON Instrument Control Processor (ICP) to produce images of 12-second integration. The data from the 12-second exposures are downlinked to the ground.

3.2.2.3 ICON FUV Data Handling

Because the satellite moves substantially during 12 seconds, two types of motion compensation schemes are used. In type one, six horizontally co-added vertical altitude profiles are generated for the measurements of the altitude distribution of the emission intensity, as illustrated below. In this figure the image of the limb is shown to be projected on the detector between tangent heights of about 150 and 507 km. The data is co-added horizontally into six strips as shown in blue. These strips represent the primary data source for taking vertical profiles of the thermosphere/ionosphere. The image can be regarded as having "rescells" of 4×4 km at the tangent height of 155 km representing an angular region of 0.093×0.093 degrees. Approximately 32 of these rescells are co-added in one stripe and each stripe represents 3 degrees in horizontal width. The rescells nominally would translate to a 4 × 4 binned CCD pixel on a 256 × 256 matrix of the detector however the imager optics has substantial non-linearity that has to be accounted for. A single strip is illustrated on the right and the limb view region is shown in red. Below 130 km tangent height the instrument is viewing a region where all FUV emissions in the background are absorbed by O2 and this "sublimb" or "disc" region is illustrated in blue. The six profiles are generated by summing pixels horizontally in the direction of satellite motion without smearing in the vertical direction. The co-adding process is relatively straight forward when the turret is in its baseline (0°) position and the horizontal direction in the image of the limb is parallel with the pixel *x*-coordinate in the image.

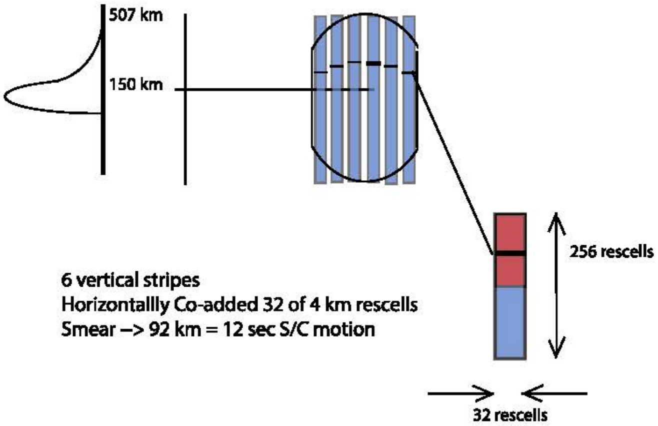

Fig 3.6: Illustration of limb altitude profiles. There are 6 vertical strips. In each strip the pixels are co-added horizontally. During daytime data is taken for both channels while during nighttime only for the 135.6 nm channel. Below 150 km altitude there is substantial O2 absorption in the FUV and it is not possible to get limb views of the atmosphere. The linear dimension of a "resolution element" or "rescell" is 0.093° or 1/256 of the 24° vertical FOV

When the turret is at another angle, the co-adding of pixels has to take place along a slant path in the imager frame of reference. This is accomplished by transposing the images and modifying the pixel addresses during the transposition, thereby removing the geometric distortion and applying an *x* and *y* pixel shift to facilitate co-adding along contours that represent horizontal paths. The pixel addresses for the transposition use an address matrix stored in a Look-Up-Table (LUT).

The second type of motion compensation scheme produces a data stream containing Time Delay Integrated (TDI) images reproducing a mapped view of a two dimensional horizontal intensity distribution (Wilkins et al. 2017). In this mode, the individual frames are digitally co-added in the ICP memory after they have been projected on an imaginary horizontal surface, which is moving uniformly in the satellite frame of reference. During the co-adding process, a constant offset is applied to the address of each pixel in each frame to shift the image. This offset is computed from the orbital speed of the satellite so that it compensates for the satellite motion.

During nighttime the 135.6-nm emission maps are treated as two dimensional images viewed from above. The 135.6-nm emission is produced by recombination of O^+ and its intensity is expected to peak at the bottom of the F region at an altitude of approximately 300 km. We divided the view of the atmosphere into two regions. Imaging at elevation angles corresponding to ray tangent height of 300 km or higher we map the emissions to the appropriate limb tangent because we expect the greatest intensity to be seen there and these images are called "limb view" images. At elevation angles lower than the limb tangent of 300 km, we map the layer to a constant altitude of 300 km below the satellite as "sub-limb" views. We recognize that there is a confusion in the region from tangent heights of 150 to 300 km between structures originating nearer than the tangent point and structures further away from the tangent point. Both of the limb view and sub-limb models define an altitude and a range distance from the satellite and therefore can be mapped as a function of their horizontal position.

Consecutive exposures using the TDI technique can be summed up to a single continuous map of the limb-view and sub-limb images along the orbit. We take 12-second exposures, which is shorter than the travel time of image elements across the FOV. Imaged elements in the middle of the FOV get a full 12 second exposure, however elements at the forward and backward edges of the FOV get only limited exposures.

This TDI technique provides high-resolution images in spite of the substantial motion of the satellite platform during the 12-second exposure. It should be noted that these techniques require sophisticated real-time image manipulations onboard the satellite. This is accomplished in ICP resident Field Programmable Gate Arrays (FPGAs) using firmware because of the high processing speeds needed. This technique is an evolution of the TDI motion compensation that was used in the FUV instrument on the NASA IMAGE satellite (Mende et al., 2000a), with a much more detailed set of performance requirements (Wilkins et al., 2017).

3.2.2.4 ICON FUV Door

ICON FUV is equipped with a one-time open door which protects the system from contamination during storage and early orbit outgassing. The door has a central MgF2 window which would allow for some data collection in the highly unlikely case of a door opening failure. The opening frangibolt also has a secondary actuator in case the first one would fail. During testing the system never failed and also after launch and outgassing of the spacecraft the door opened flawlessly at the first attempt.

3.2.2.5 ICON FUV Sun Sensors

FUV is equipped with two UVB-only photodiodes SG01L-B5 that protect the instrument from accidental pointing to the sun. The sun sensor sends signals to the ICP to set the high voltage to a safe level when the sun comes close to the FOV. The high voltage control is all direct hardware with quick response.

3.2.2.6 ICON FUV High Voltage Power Supplies

The MCP high voltage is provided by flight proven high voltage power supplies. Their output voltage is commanded through the ICP and three pre-set setting provide daytime, nighttime, and safe high voltage levels.

3.2.2.7 ICON FUV Turret

As the multi-instrument nature of the ICON observatory does not permit re-pointing the entire S/C, ICON FUV has a rotating turret with a steering mirror mounted in it to satisfy this requirement over a ±30° range with 5° steps. This allows the local magnetic meridian direction to be contained within the FOV of the FUV instrument for most equatorial crossings. The stepper motor driver controls the turret position.

3.2.2.8 ICON FUV System and Electronics

The ICON FUV system is illustrated below. In addition to the opto-mechanical instrument structure, the ICON FUV flight system also has some dedicated electronics components resident in the Instrument Control Processor (ICP). The instrument operation is controlled and the CCD image data is processed on board by the ICP electronics. There is a wiring harness connecting the ICP to the rest of the instrument. The harness contains power and data connections and provides control commands to each of the ICON FUV sub systems. The camera intensifier high voltage power supply voltages are commanded by the ICP.

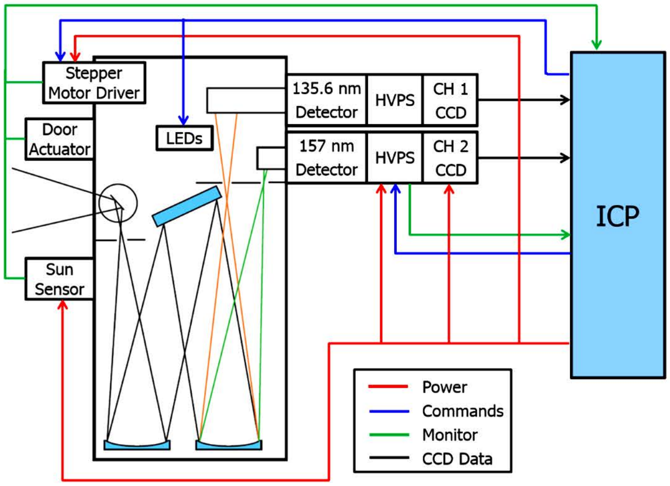

Fig 3.7: The ICON FUV system diagram

3.2.3 FUV Heritage

3.2.3.1 Instrument Heritage

The FUV instrument draws strong heritage from the IMAGE and ISUAL missions. Some updates of electronics components needed to be made that also resulted in some instrument software changes.

FUV SI and Back Imager Optics

The ICON SI draws its heritage from the NASA IMAGE satellite FUV Spectrographic Imager [Mende et al., 2000b], an instrument that operated without any significant problem on the IMAGE spacecraft. The ICON SI design is less critical than IMAGE-FUV SI because the science does not require the narrowband Lyman alpha channel. Also the non-spinning platform makes the operation of the instrument considerably simpler. In the ICON application the wavelength of one of the imager channels was changed to image the LBH 155 nm region instead of the Doppler shifted Lyman alpha at 121.8 nm. This is accomplished by moving the exit slit laterally to the appropriate location for 155 nm collection. Since the ICON instrument does not have the high spectral resolution as its driving requirement for Doppler shift discrimination of Lyman alpha, the instrument was optimized for improved spatial resolution. As the reflection efficiency is much better at 135.6 and at 155 than at Lyman alpha, another mirror was introduced to further minimize the criticality of the design and produce an instrument that has larger tolerances than the IMAGE-SI.

FUV MCP Intensifier

FUV imaging systems generally require incoming photons to be amplified and/or converted to pulses that either 1) impact a phosphor screen that is coupled to a CCD or CMOS detector or 2) impact an event counting detector such as a wedge-and-strip detector or a crossed delay line detector (XDL). The IMAGE-SI successfully used XDL detectors. However, given the larger etendue of the ICON imager, and Earth's ultraviolet horizon completely filling the limb-viewing scene, the count-rate limitation of the XDL detectors was determined likely to adversely affect instrument performance. It was decided to use a phosphor screen/CCD detector that could handle the MCP event rates expected for ICON FUV. The IMAGE-WIC camera and the Imager on ISUAL both used a CCD-based system. This detector consists of a photoelectric converter tube with a microchannel plate and phosphor that is fiber-optically coupled to a CCD. This detector has more dynamic range than the XDL and has no trouble covering all possible scenes. The simplest instrument of this type was the ISUAL CCD camera system and we adopted it to use an FUV photocathode. Similar to ISUAL we implemented a UCB-built sealed image intensifier tube.

High Voltage Power Supplies, CCDs and Front End Electronics

The overall heritage for this part of the instrument is from the IMAGE-WIC detector. The IMAGE SI used Cross Delay Line (XDL) detectors. The XDL detectors are count rate limited. We expected that on ICON during limb view observations the field of view of the FUV imager could be completely filled with sunlit atmospheric dayglow and the total count rate could be much higher than with IMAGE-FUV. We decided that it was more prudent to use a detector system that suffers less from saturation at high count rates. We had such detectors on the IMAGE-WIC camera and the Imager on ISUAL. This detector consists of a photoelectric converter tube with a microchannel plate and phosphor that is fiber-optically coupled to a CCD. This detector has more dynamic range than the XDL and has no trouble covering all possible scenes. The simplest instrument of this type was the ISUAL CCD camera system. ICON FUV has an FUV cathode in the converter tube just like FUV WIC.

FUV Steering Mirror

The steering mirror, its stepper motor and drive electronics are copies of the ISUAL filter wheel drive. Since the mass of the mirror and the torque requirements were much less in the ICON application we used a smaller stepper motor. The gearing used for ISUAL was replaced by a harmonic drive, which ensured the proper gearing for the required steps in the ICON application.

FUV Front Aperture Cover

The FUV front aperture is protected by a one-time on-orbit openable door. The mechanism draws its strong heritage from the similar door on the IMAGE SI. The door has an MgF_2 window that in the unlikely event of a failure to open would still allow limited measurements to be taken. The door release mechanism underwent extensive testing on IMAGE and the redundant actuator did not have to be used on orbit.

3.2.3.2 Algorithm and Calibration Heritage

The calibration of FUV followed established practices which were used in the same way with IMAGE FUV and that are summarized in Table 3.2.

Imaging capability	
	Aperture size
	Field of view
	Pointing accuracy, knowledge, ***repeatability***
Imaging quality	
	Imaging geometric distortions
	Spot size or spatial resolution
	Flatfield or imaging homogeneity
Quantitative sensitivity	

	Pass band
	Radiometric sensitivity
	Detector background
	Stray light background
	Linearity
	Dynamic range

Table 3.2: Main calibration tasks for wide-field UV instruments. Properties that can be temperature dependent are shown in bold italic letters (from Frey et al., 2017).

The Time Delay Integration (TDI) algorithm draws its heritage from the similar algorithm that was used on IMAGE (Mende et al., 2000). The general philosophy is the same, first correcting the distortions of the system, then determining the offset due to the spacecraft motion and viewing geometry, and then add short exposure frames together in order to get longer exposures with more signal. The only updates were the specific look up tables and offset determinations.

4. FUV Calibration Plan

4.1 Overall Calibration Scheme

All ground calibrations were performed in the large vacuum chamber at CSL Liege. In the case of ICON-FUV the instrument was placed on a tip/tilt and rotation stage. This Mechanical Ground Support Equipment (MGSE) provided the ability to rotate the instrument around the entrance pupil. The rotation range covered more than the entire FoV (24° vertical, 18° horizontal). The manipulator is composed of three linear actuators (tripod) on which a rotation table is placed through a kinetic mount support.

Before manipulating the flight instrument in vacuum a dummy mass has been placed on the manipulator to characterize and simulate the motion range, accuracy, and repeatability of the manipulator in easier air conditions. The dummy mass was used to completely characterize the MGSE independent of the instrument and isolate MGSE-induced uncertainties from instrument-induced uncertainties. A metal strip simulated the entrance pupil of the instrument. The light beam was then adjusted in such a way that the optical axis passes through the rotation axis of the main rotation stage. A reference optical cube was placed on the outside of the dummy mass so that all MGSE motions could be characterized with the aid of a laser tracker and theodolites. The absolute accuracy and repeatability of the manipulator was 3 arcsec. The incoming light beam and the optical portion of the test equipment, the Optical Ground Support Equipment (OGSE), has thus been characterized and referenced with the MGSE for all the testing under vacuum. The general setup is shown in the figure below.

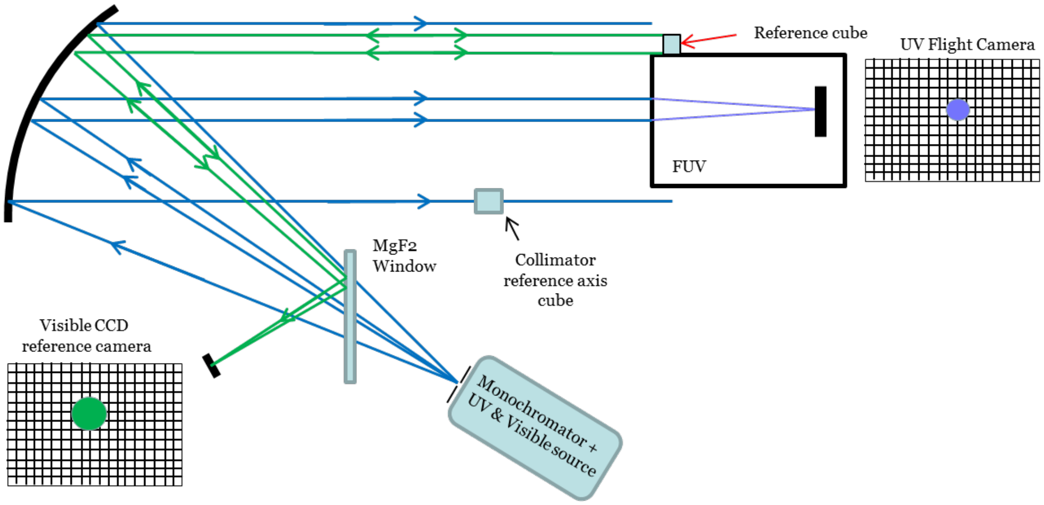

Fig 4.1: Overall setup for the alignment of the ICON-FUV instrument.

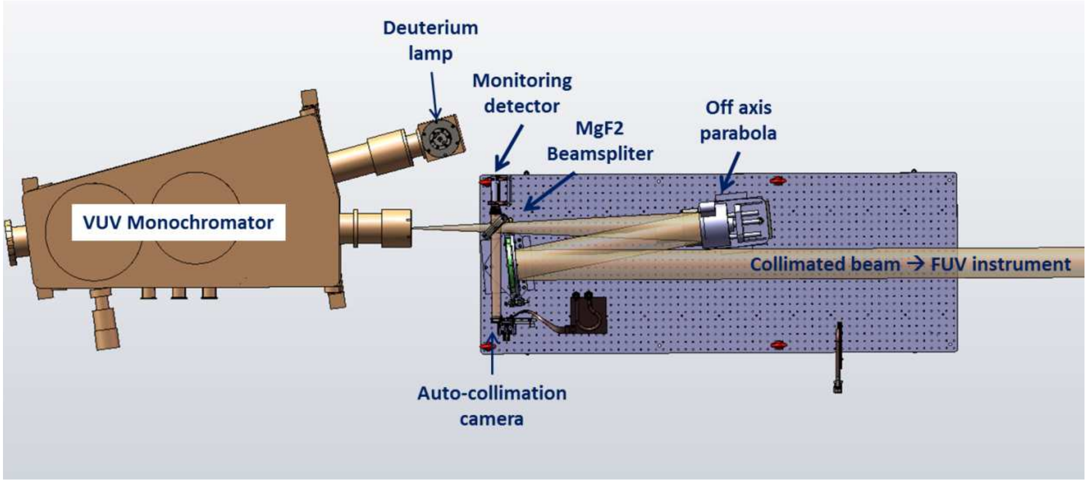

Fig 4.2: Setup for the external portion of the ICON-FUV alignment. All this equipment is under vacuum and connected to the test chamber through vacuum tubes.

The setup is similar to the setup which was used for the IMAGE FUV Spectrographic Imager, only in a different vacuum chamber and with a newer deuterium lamp source.

The setup is not only used during ambient temperature tests but also during thermal vacuum testing (TVAC) in order to characterize the response to external temperature variations. As a first step the thermal behavior of the test environment has to be characterized so that it can later be separated from the thermal response of the device under test. The control of the line of sight during thermal cycles is enabled with a reference mirror cube placed on the instrument body and an auto-collimation process with a reference CCD camera. Light reflected by the reference cube returns back into the collimator and is focused into the reference camera. The comparison of the reflected beam imaged onto the reference camera as a function of the different angles and temperatures gives the ability to realign the instrument and compensate for misalignments due to the thermo-mechanical constraints of the MGSE structure. Any remaining shifts of beam positions in the UV instrument for different temperatures are then a result of thermal effects on the instrument structure. The angular resolution of the reference camera and the accuracy and repeatability of the mechanical stage (3 arcsec) have to be better than the angular resolution of the instrument (for ICON-FUV 3 arcmin) in order for this procedure to provide reliable results. Later the alignment with respect to the spacecraft structure is determined by theodolites looking at the instrument alignment cube and alignment cubes on the spacecraft structure.

4.2 Pre-flight Calibration Plans

4.2.1 Plan for Distortion correction Pre-flight Calibrations

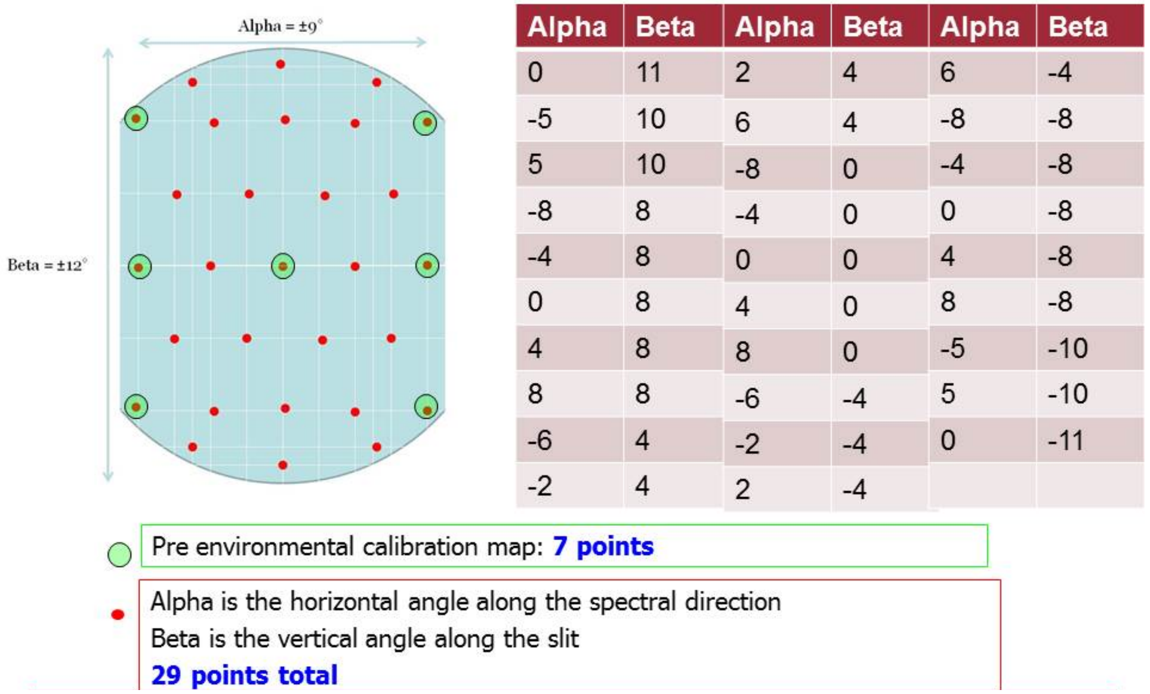

Alpha	Beta	Alpha	Beta	Alpha	Beta
0	11	2	4	6	-4
-5	10	6	4	-8	-8
5	10	-8	0	-4	-8
-8	8	-4	0	0	-8
-4	8	0	0	4	-8
0	8	4	0	8	-8
4	8	8	0	-5	-10
8	8	-6	-4	5	-10
-6	4	-2	-4	0	-11
-2	4	2	-4		

🟢 Pre environmental calibration map: **7 points**

● Alpha is the horizontal angle along the spectral direction
Beta is the vertical angle along the slit
29 points total

Fig 4.3: Field angles for the determination of the FUV instrument distortion maps

The pre-flight calibration plan to determine the instrument distortion is detailed in the document ICN-FUV-077_distortion.docx and 29 calibration points were determined where the relative relationship between the position angles of the mechanical manipulator were compared to the registered location of the ultraviolet light beam on the detector. The specific steps for the calibration procedure were:

1.1.1 FUV instrument installed in CSL vacuum chamber with door opened
1.1.2 Proper movability of cradle confirmed
1.1.3 Electric connection through feedthrough confirmed
1.1.4 Communication between ICP and FUV confirmed
1.1.5 Communication between FUV and SDL PC confirmed
1.1.6 Verify Proper FUV Test Configuration
1.1.7 Verify proper vacuum chamber pressure of <10^-3 Pa
1.1.8 Start UV source
1.1.9 Tune monochromator to 135.6 nm
1.1.10 Characterize incoming beam with CSL photodiode
1.1.11 Verify computer time is correct and note start time
1.1.12 Verify cover is open
1.1.13 Note temperature as this test has to be performed at three different nominal temperature settings

1.1.14 Instrument Payload Power On

1.1.14.1 Execute Section 8.9 in the FUV CPT (ICN-FUV-068) for ICP power on.

1.1.15 FUV Camera Power Control

1.1.15.1 Send script: **start FUV_on** to power on FUV-Short Wave (SW) camera

1.1.15.2 Verify FUV A (SW) enable, current draw and data

1.1.15.3 Verify FUV A (SW) Camera Ancillary Data

1.1.15.4 Send script: **start FUV_on** to power on and initialize FUV-short wave and FUV-long wave cameras

1.1.15.5 Verify FUV B (Long Wave) enable, current draw and data

1.1.15.6 Verify FUV B LW Camera Ancillary Data

1.1.15.7 Verify receipt of FUV APID 0xE1 (realtime) and 0xE2 (nominal) data

1.1.15.8 Set up SDL computer to collect 2x2 binned images (512x512 nominal pixel) and single left tap readout for Shortwave camera

1.1.15.9 Send script FUV_TAKE_PICTURE_SW.PY to capture and store SW image on SDL computer.

1.1.15.10 Verify receipt of SW FUV data

1.1.15.11 Repeat sections 8.4.8 to 8.4.10 for LW channel

1.1.16 FUV High Voltage (HV) On

1.1.16.1 Execute Section 8.13 in the FUV CPT (ICN-FUV-068) for FUV High Voltage setup.

1.1.17 SW channel distortion map determination

1.1.17.1 Verify Monochromator is set to 135.6 nm

1.1.17.2 Characterize incoming beam

1.1.17.3 Set up SDL computer to collect 2x2 binned images (512x512 nominal pixels) and single tap readout

1.1.17.4 Verify that turret is at nominal 0 degrees position

1.1.17.5 Verify that cradle is set to normal incidence 0 degrees

1.1.17.6 Send script: **FUV_TAKE_PICTURE_SW.PY** to take an integrated picture of 100 frames of 120 msec exposure time and save on SDL PC with appropriate header information about time, number of frames, cradle position, wavelength, channel,

1.1.17.7 Verify appearance of a spot in the SW channel located at approximately the center of the image

1.1.17.8 Move cradle to input field positions listed in the table below and repeat step 8.6.6 for each field position. Note the approximate pixel position of the spot center as the detailed analysis will be done later.

1.1.18 FOV edge determination

1.1.19 For each extreme field view angle approach edge of FOV in small steps and determine when the incoming beam reaches the edge of the FOV

1.1.20 Grating edge

Based on prior measurement at room temperature take image while the lower grating border is illuminated to compare edge location at different temperatures

1.1.21 LW channel distortion map determination

1.1.21.1 Change Monochromator setting to 157 nm

1.1.21.2 Characterize incoming beam

1.1.21.3 Set up SDL computer to collect 2x2 binned images (512x512 nominal pixels)

1.1.21.4 Verify that turret is at nominal 0 degrees position

1.1.21.5 Verify that cradle is set to normal incidence 0 degrees

1.1.21.6 Send script: **FUV_TAKE_PICTURE_LW.PY** to take an integrated picture of 100 frames of 120 msec exposure time and save on SDL PC with appropriate header information about time, number of frames, cradle position, wavelength, channel,

1.1.21.7 Verify appearance of a spot in the LW channel located at approximately the center of the image

1.1.22 Move cradle to input field positions listed in the table below and repeat step 8.8.6 for each field position. Note the approximate pixel position of the spot center as the detailed analysis will be done later

1.1.23 Determine edge of FOV for LW channel

1.1.23.1 For each extreme field view angle approach edge of FOV in small steps and determine when the incoming beam reaches the edge of the FOV

1.1.24 Grating edge

1.1.25 Based on prior measurement at room temperature take image while the lower grating border is illuminated to compare edge location at different temperatures

1.1.26 ITOS power down

4.2.2 Results of the pre-flight distortion correction calibration

Results of the pre-flight distortion correction calibration are summarized in the document ICN-FUV-136-REP-Distortion.pdf.

Distortion maps were measured on different dates and in different environments. The test dates and average temperatures were:

2016-01-18; room temperature; 27 spots;
2016-01-25; cold gradient; 84 spots;
2016-01-26; hot balance; 95 spots;
2016-01-31; room temperature; 87 spots;
2016-02-02; cold balance; 83 spots;
2016-02-03; hot calibration; 83 spots;

Fit of positions

Pixel positions and angle settings were fitted to a 36-parameters mixed function of polynomials and trigonometric functions. This is potentially an overkill but as there are at least twice as many measured spot positions than unknowns the mathematical mpfit IDL-package was capable of fitting the final result with very small errors. The general format of the fitted function is:

```
Zmod = p[0] + $
  p[1]*x + $
  p[2]*y + $
  p[3]*(x*y) + $
  p[4]*(x*x) + $
  p[5]*(y*y) + $
  p[6]*(x*x*x) + $
  p[7]*(x*x*y) + $
  p[8]*(x*y*y) + $
  p[9]*(y*y*y) + $
```

```
p[10]*(x*x*x*x) + $
p[11]*(x*x*x*y) + $
p[12]*(x*x*y*y) + $
p[13]*(x*y*y*y) + $
p[14]*(y*y*y*y) + $
p[15]*(x*x*x*x*x) + $
p[16]*(x*x*x*x*y) + $
p[17]*(x*x*x*y*y) + $
p[18]*(x*x*y*y*y) + $
p[19]*(x*y*y*y*y) + $
p[20]*(y*y*y*y*y) + $
p[21]*(x*x*x*x*x*x) + $
p[22]*(x*x*x*x*x*y) + $
p[23]*(x*x*x*x*y*y) + $
p[24]*(x*x*x*y*y*y) + $
p[25]*(x*x*y*y*y*y) + $
p[26]*(x*y*y*y*y*y) + $
p[27]*(y*y*y*y*y*y) + $
p[28]*sin(x) + $
p[29]*sin(y) + $
p[30]*sin(x*y) + $
p[31]*sin(x+y) + $
p[32]*cos(x) + $
p[33]*cos(y) + $
p[34]*cos(x*y) + $
p[35]*cos(x+y)
```

The results of the SW-channel measurements are given at the end of the report in the format of tables with the input angles, measured spot positions, calculated angles from fits, calculated spot positions from fits, and errors between input and fitted values. Only those spots were used for the fits where the total counts in the spot exceeded 10,000 counts so that measurements outside of the valid detector area (outside of FoV) did not disturb the fitting. Note, that the image sizes are [536x515] pixels. Distortion tables for the instrument were then calculated using a [256x256] matrix, but everything shown in this report refers to the 2-times bigger size. The fit-parameters for the individual measurement series are given in the tables at the end of the document.

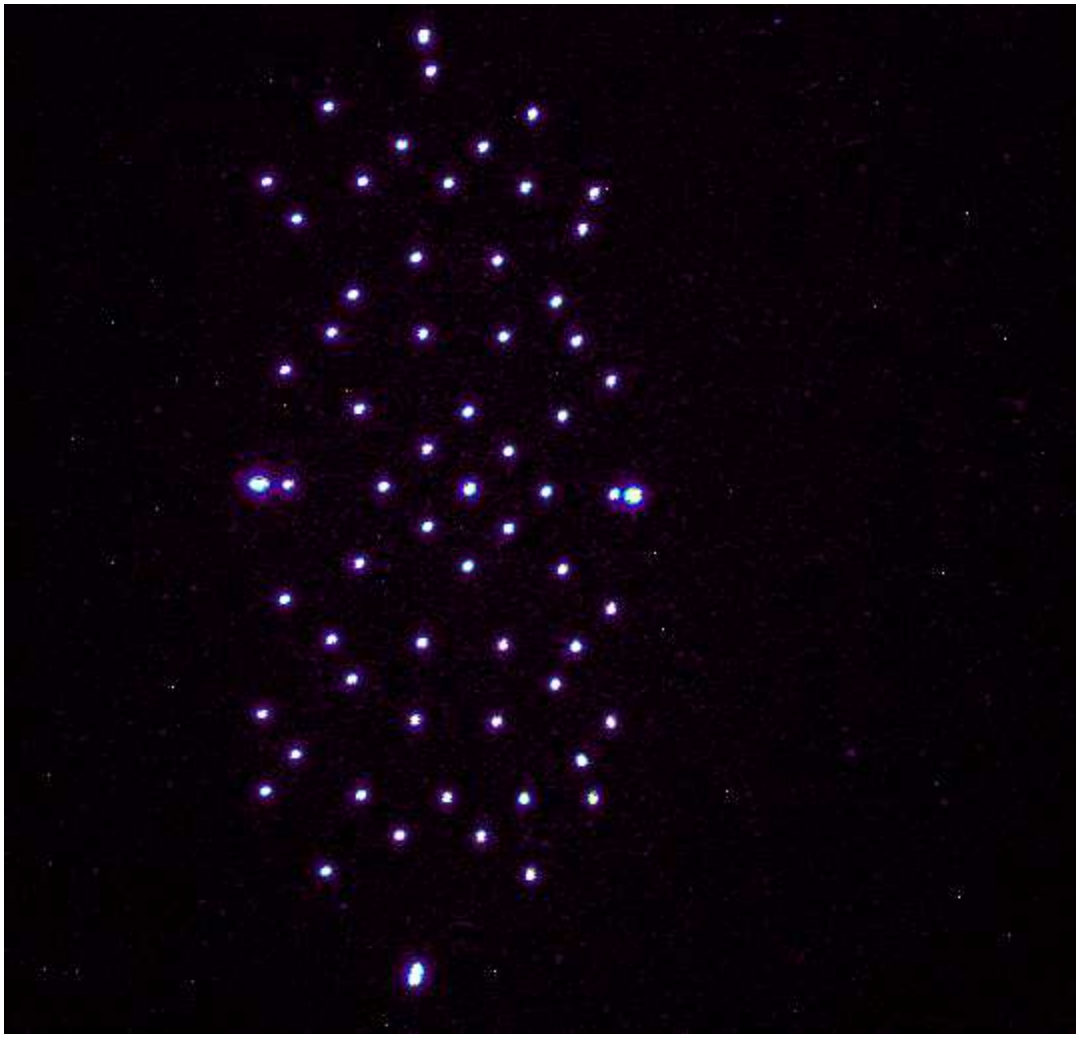

Fig 4.4: SW-channel spots that were measured on 2016-01-31 at room temperature. The spots at the top, bottom, right, and right sides appear larger as they contain positions in 0.1 degrees steps in order to determine the edges of the field of view.

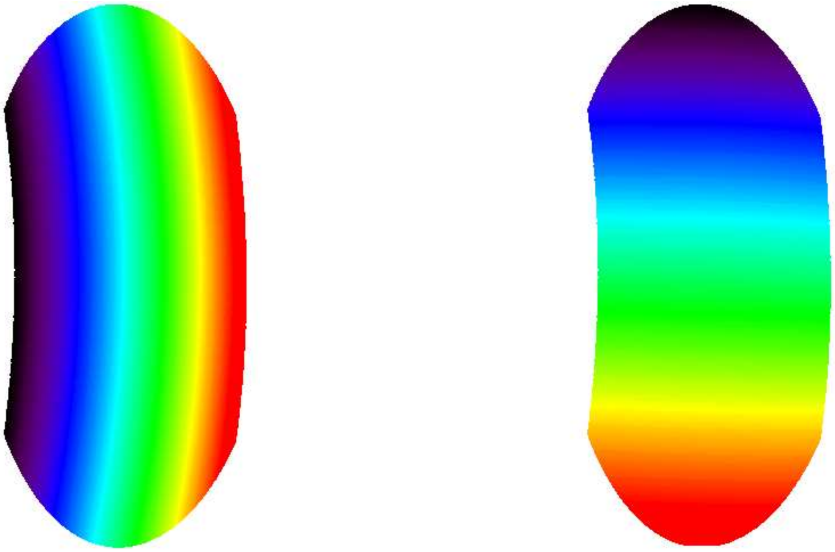

Fig 4.5: SW-Distortion maps in horizontal and vertical angles for the SW-channel as determined for 2016-01-31.

The results of the LW-channel measurements are given at the end of the report in the format of tables with the input angles, measured spot positions, calculated angles from fits, calculated spot positions from fits, and errors between input and fitted values. Only those spots were used for the fits where the total counts in the spot exceeded 10,000 counts so that measurements outside of the valid detector area (outside of FoV) did not disturb the fitting. Note, that the image sizes are [536x515] pixels. Distortion tables for the instrument were then calculated using a [256x256] matrix, but everything shown in this report refers to the 2-times bigger size. The fit-parameters for the individual measurement series are given in the tables at the end of the document.

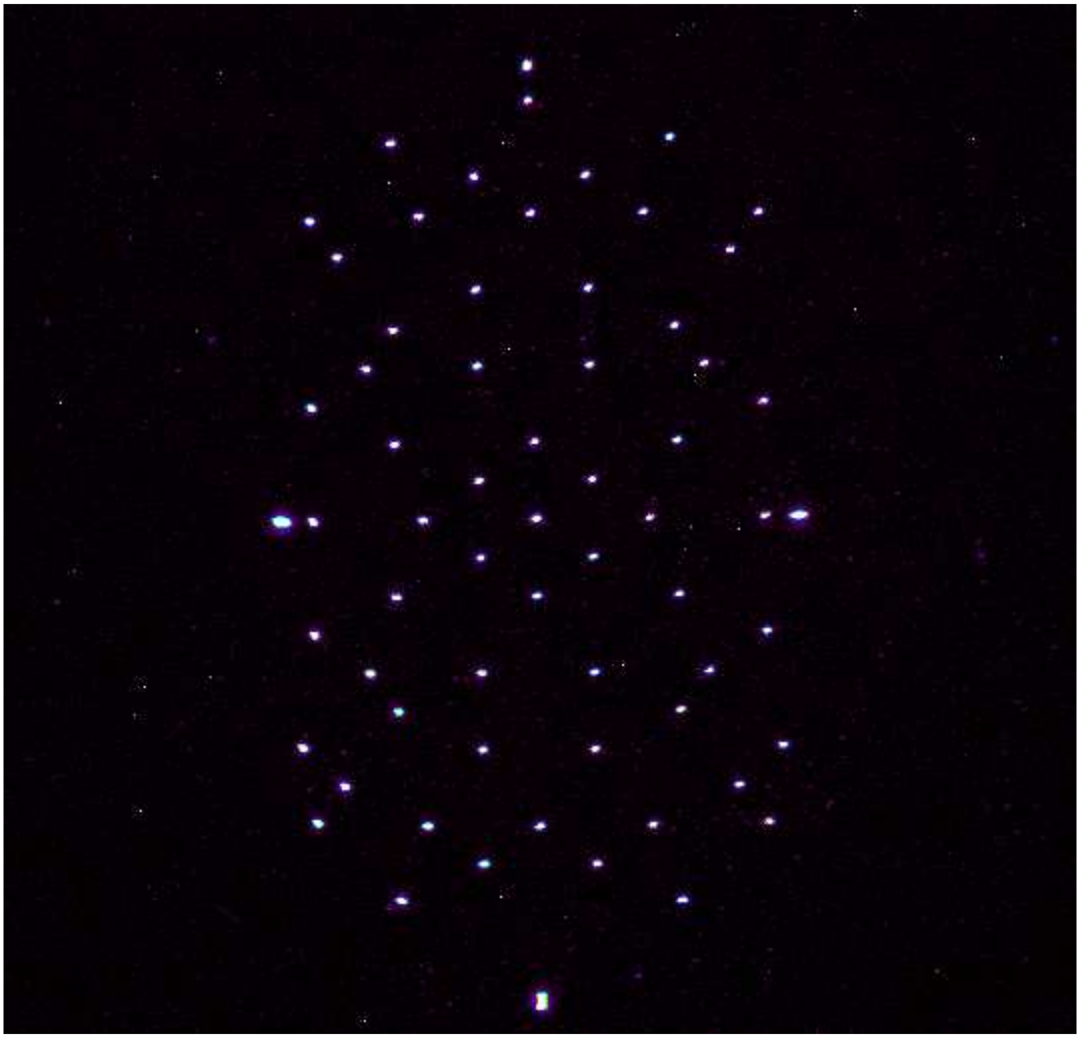

Fig 4.6: LW-spots that were measured on 2016-01-31 at room temperature. The spots at the top, bottom, right, and right sides appear larger as they contain positions in 0.1 degrees steps in order to determine the edges of the field of view.

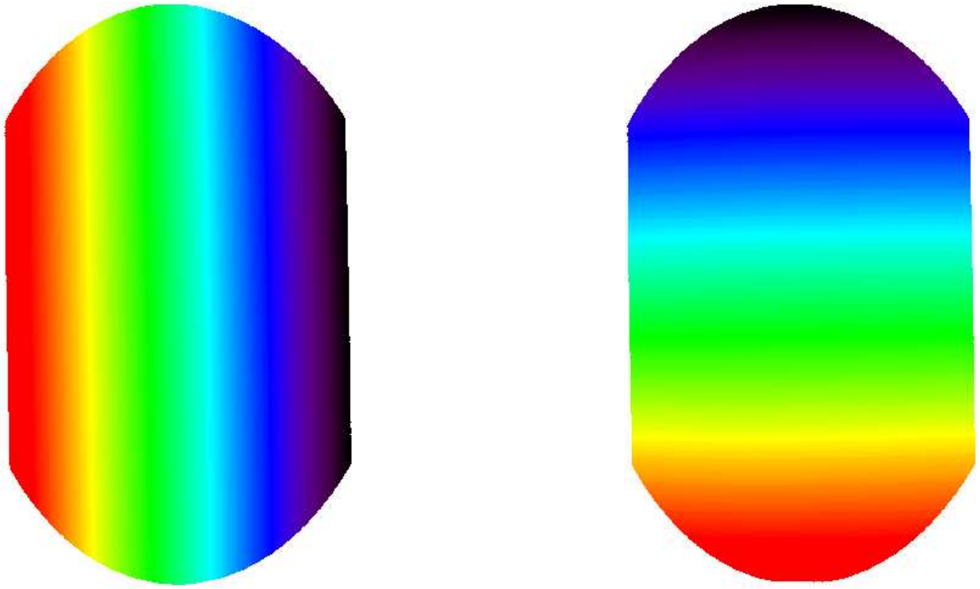

Fig 4.7: LW-Distortion maps in horizontal and vertical angles for the SW-channel as determined for 2016-01-31. Note the reversed orientation of the horizontal angles compared to the SW-channel due to the additional fold-mirror in LW.

The maximum error for any single spot in the SW-channel measurements is 0.65 pixels or 0.04 degrees which correspond to the size of half a science pixel. The mean values for all the measured spots in the SW-channel are almost a factor of 10 smaller (0.082 pixels and 0.009 degrees) and show that the measurements and fitting provide a reliable way to describe the geometric distortions in the SW-channel.

In the LW-case there are slightly larger maximum errors of 1.697 pixels and 0.064 degrees which are caused by a few measurements around the extreme beta angles of 12.3-12.8 degrees. It is not really obvious why these spots are reconstructed less reliably than others as the count rates still indicate perfect coverage within the sensitive region of the detector. Nevertheless, the overall fit of the distortion is still much smaller than one science pixel.

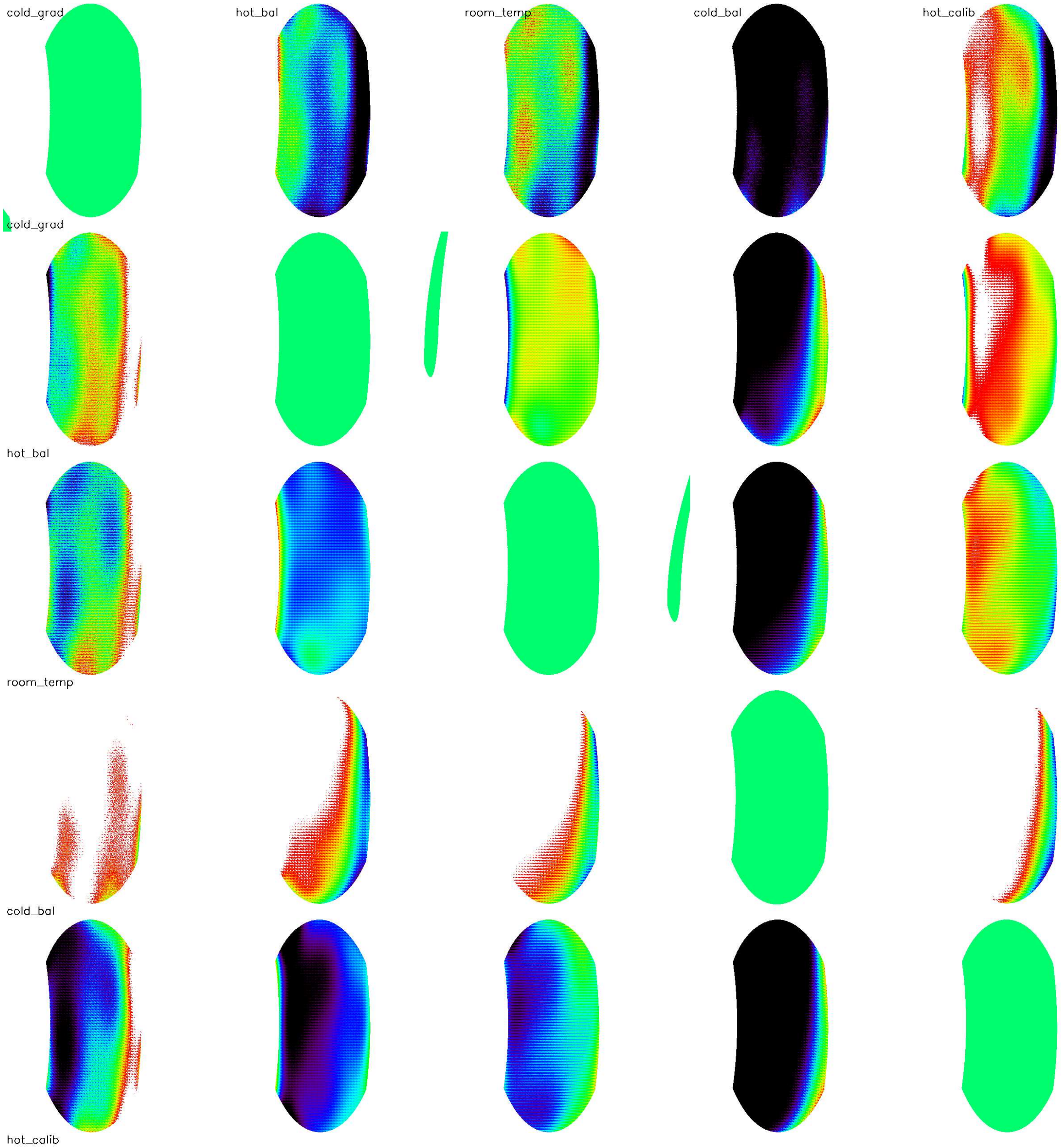

Fig 4.8a: Comparison of the five alpha-angle fits for the SW channel. The differences between the fit results are shown in a matrix pattern. Anything in black or in white marks a pixel where the difference between two fits is bigger than one science pixel. The cold-balance case (column #4 with a lot of black; row #4 from top with a lot of white) is quite different from the other cases.

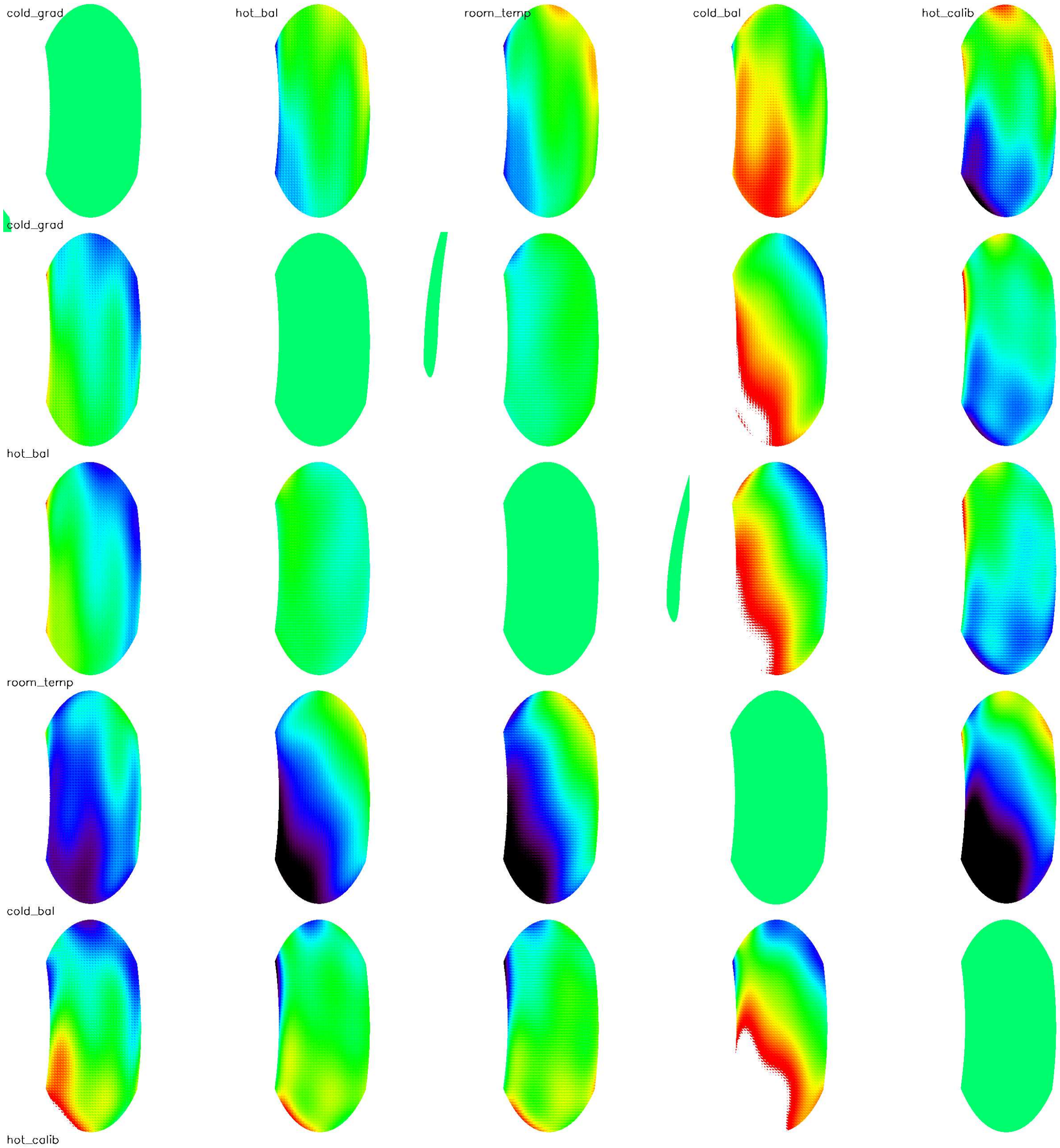

Fig 4.8b: The same as the prior figure just for the SW-channel beta-angle.

4.2.3 Plan for turret Pre-flight Calibrations

The pre-flight calibration plan for the turret is detailed in the document ICN-FUV-078_turret.docx. This procedure provides the steps to obtain the angle between the turret rotation and the FUV instrument optical axes. The general setup is similar to the measurement of the distortion map except that the turret is rotated and the MGSE compensates nominally for this rotation. If the turret rotation axis and the turret mirror are aligned per the design the resulting spot should always fall into the center of the image. This procedure was used at CSL in Belgium with FUV in the 6.5 m vacuum chamber. The specific steps for the calibration procedure were:

1.2 FUV instrument installed in CSL vacuum chamber with door opened
1.3 Proper movability of cradle confirmed
1.4 Electric connection through feedthrough confirmed

1.5 Communication between ICP and FUV confirmed
1.6 Communication between FUV and SDL PC confirmed
1.7 Verify Proper FUV Test Configuration
1.8 Verify proper vacuum chamber pressure of <10^-3 Pa
1.9 Start UV source
1.10 Tune monochromator to 135.6 nm
1.11 Characterize incoming beam with CSL photodiode
1.12 Verify computer time is correct and note start time
1.13 Verify cover is open
1.14 Note instrument temperatures for the record
1.15 Instrument Payload Power On
1.16 Execute Section 8.9 in the FUV CPT (ICN-FUV-068) for ICP power on.
2.0 FUV Camera Power Control
2.1.1 Send script: **start FUV_on** to power on FUV-Short Wave (SW) camera

Enter **SW** when prompted

2.1.2 Verify FUV A (SW) enable, current draw and data
2.1.3 Verify FUV A (SW) Camera Ancillary Data
2.1.4 Send script: **start FUV_on** to power on and initialize FUV-short wave and FUV-long wave cameras *(note: FUV B cannot be separately enabled)*

Enter **BOTH** when prompted

2.1.5 Verify FUV B (Long Wave) enable, current draw and data
2.1.6 Verify FUV B LW Camera Ancillary Data
2.1.7 Verify receipt of FUV APID 0xE1 (realtime) and 0xE2 (nominal) data
2.1.8 Set up SDL computer to collect 2x2 binned images (512x512 nominal pixel)
2.1.9 Send script FUV_TAKE_PICTURE_SW.PY to capture and store SW image on SDL computer.
2.1.10 Verify receipt of FUV SW data
3.0 FUV High Voltage (HV) On
3.1 Execute Section 8.13 in the FUV CPT (ICN-FUV-068) for FUV High Voltage setup. Attach As-run paper procedure to the appendix. Note FUV CPT Revision used
4.0 SW channel spot position determination
4.1 Verify Monochromator is set to 135.6 nm
4.2 Characterize incoming beam
4.3 Set up SDL computer to collect 2x2 binned images (512x512 nominal pixels) and single tap readout
4.4 Verify that turret is at nominal 0 degrees position
4.5 Verify that cradle is set to normal incidence 0 degrees
4.6 Send script: **FUV_TAKE_PICTURE_SW.PY** to take an integrated picture of 100 frames of 120 msec exposure time and save on SDL PC with appropriate header information about time, number of frames, cradle position, wavelength, channel,
4.7 Verify appearance of a spot in the SW channel located at approximately the center of the image
4.8 Rotate turret in 5 degrees steps and move cradle to compensate for turret rotation. Repeat step 8.6.5 for each turret angle. Note the approximate pixel position of the spot center as the detailed analysis will be done later.
4.9 ITOS power down (this step may be skipped if the following calibration procedure will be run without interruption)
4.10 Record time of Instrument Power Off

End of Test

4.2.4 Results of the pre-flight turret calibration

Results of the pre-flight turret calibrations are summarized in the document ICN-FUV-139-REP-turret.pdf.

The turret tests were performed on two days, January 18, 2016 and January 31, 2016.

The procedure ICN-FUV-078 was used for those tests.

Several extreme angles (-11 to +11, -8 to +8) were used for the field direction with different turret angles. The table summarizes the results. It is obvious that within the measurement uncertainty the rotation center is constant for all turret angles except for +30 degrees. The reason for that deviation is the misplacement of the hard turret stop which does not allow for a full rotation to 30.0° but rather stops at 29.1°. As the CSL MGSE counteracted a supposed +30° degree of the turret, which indeed only rotated by 29.1°, the rotation center appears to disagree. In the analysis of data from space the different angle has to be taken into account. Please note that the values below are for the engineering mode larger images of 536x515 pixels.

Turret angle	X-center	Y-center
-15	232	273
-10	232	273
-5	231	272
0	231	272
+5	232	272
+10	232	272
+15	232	272
+20	232	272
+25	232	272
+30 (actually +29.1)	241	261

Table 4.1: Turret angle calibration results

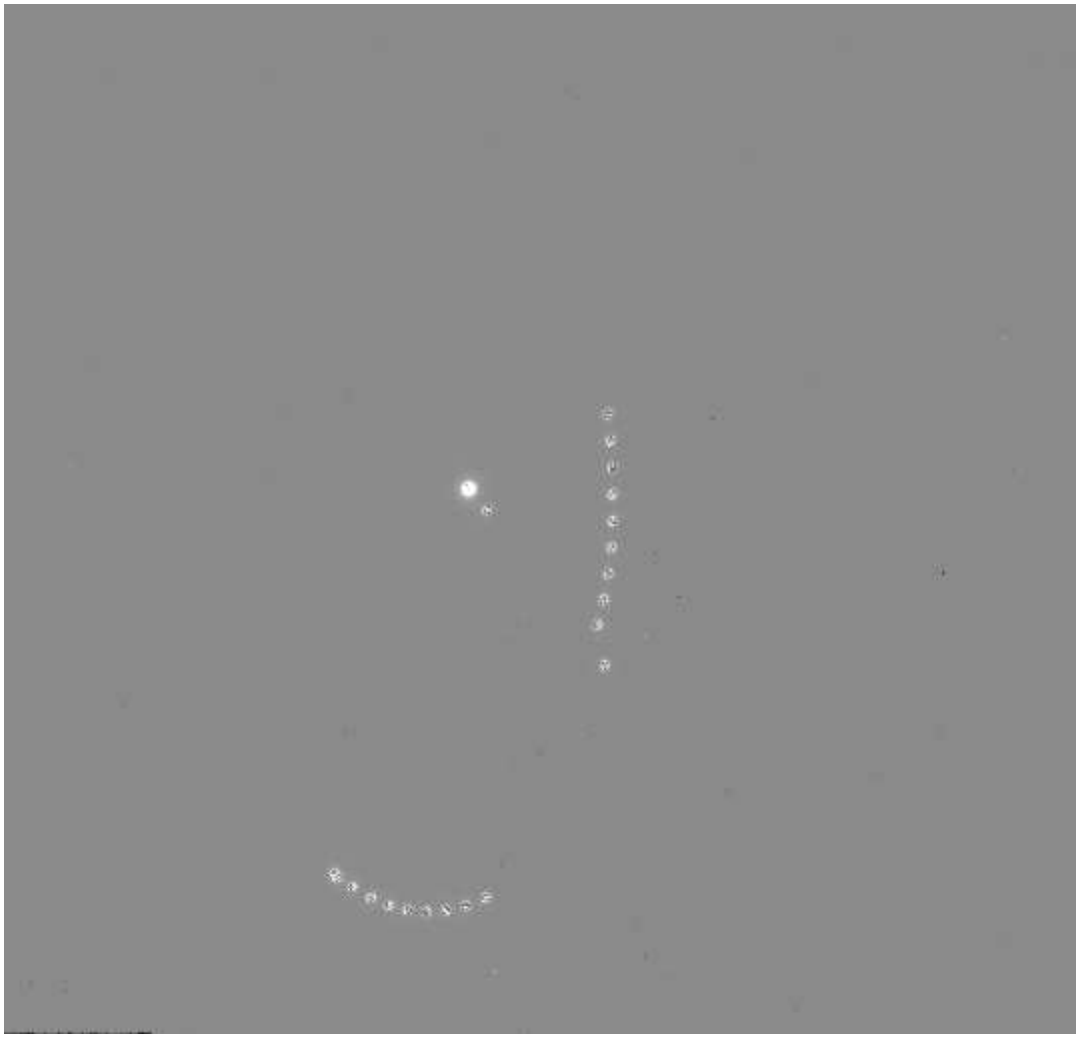

Fig 4.9: SW-channel spots for different turret angles between -15 to +30 degrees as measured on 2016-01-31 at room temperature. The three main spot groups are for view directions [0, 0], [8, 0] and [0, 11] degrees. The three outliers are from the +30° turret angle measurement series.

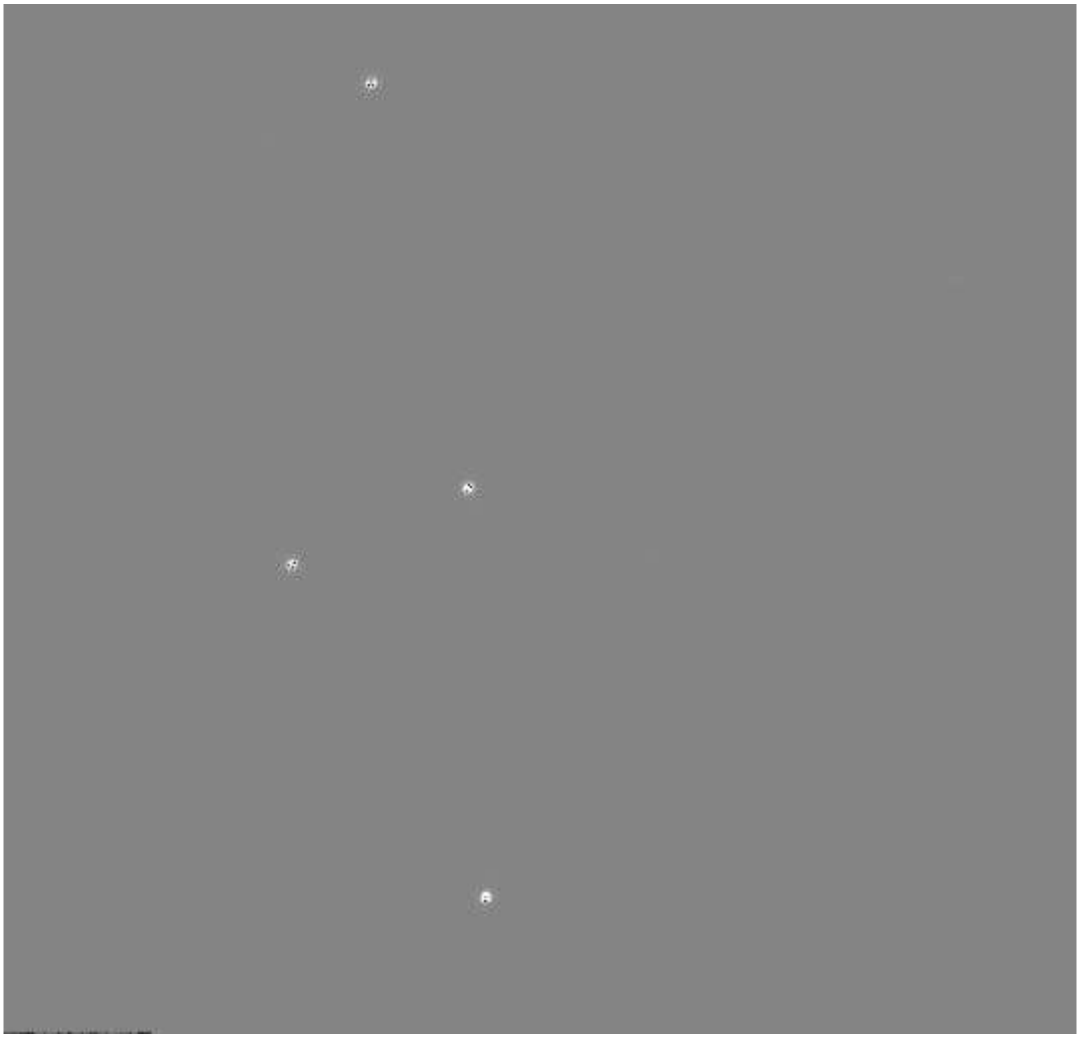

Fig 4.10: The same as figure 4.9 but for measurements on 2016-01-18 for -15° turret angle. The position [8, 0] was not measured.

The rotation center of the LW channel is at [266,257]. Overall the turret rotation center is constant within less than 0.5 science pixels. Extensive measurements were only made at room temperature. Spot checks were done at other temperatures and the results are given below. There is no clear trend that the rotation center would be different for the temperature extremes.

Date	Temperature	SW-X	SW-Y	LW-X	LW-Y
01-25-2016	Cold	232	272	265	257
02-02-2016	Cold	231	272	265	255
01-18-2016	Room	231	272	267	257
01-31-2016	Room	232	272	265	257
01-26-2016	Hot	232	272	266	257
02-03-2016	Hot	233	273	266	258

Table 4.2: Rotation centers during temperature variations

4.2.5 Results of the pre-flight field of view calibration

The results of the distortion measurements were also used to determine the field of view of FUV. Results are summarized in the document ICN-FUV-138-FOV.pdf. It summarizes the results of ICON-FUV instrument field of view (FOV) measurements obtained at different temperatures. The prime objective was to confirm modelling results if and how the FOV varied as a function of temperature. This report aims to collect all of the relevant information about test environment, setup, and results in one place.

Test date and procedures

Distortion maps were measured on different dates and in different environments. Scans across the edge of the visible region were obtained and provide the basis for the FOV determination. The procedure ICN-FUV-077 was used for those tests even though additional points were measured when considered necessary, especially for the scans across the grating edge. The measurements were performed at room temperature and both hot and cold gradients.

This test scanned across the grating edges at the top, bottom, left, and right in both the LW and SW channels at both hot and cold gradients with the turret at 0 degrees. The temperature readings are attached to the end of this report in its pdf-version.

Edge determination SW channel

The input field angles were varied by 0.1 degree steps and the total counts in the spot were taken as a measure if the input beam was still captured inside the field of view of the instrument or if it was cut off by the grating edge. The results of the SW-channel measurements are given below.

	Top	Bottom	Left	Right
Cold gradient	-12.0	12.8	-9.3	9.4
Hot balance	-12.0	12.8	-9.2	9.5
Room temperature	-12.0	12.8	-9.3	9.4
Cold balance	-12.0	12.8	-9.3	9.4
Hot calibration	-12.0	12.8	-9.2	9.4

Table 4.3: Results of the SW channel calibration.

	Top	Bottom	Left	Right
Cold gradient	-12.0	*	-9.3	9.4
Hot balance	-12.0	12.8	-9.2	9.3
Room temperature	-12.0	12.8	-9.3	9.3
Cold balance	-12.0	12.8	-9.3	9.3
Hot calibration	-12.0	12.8	-9.3	9.3

Table 4.4: Results of the SW channel calibration. Note: During cold gradient the scan was not performed completely across the edge.

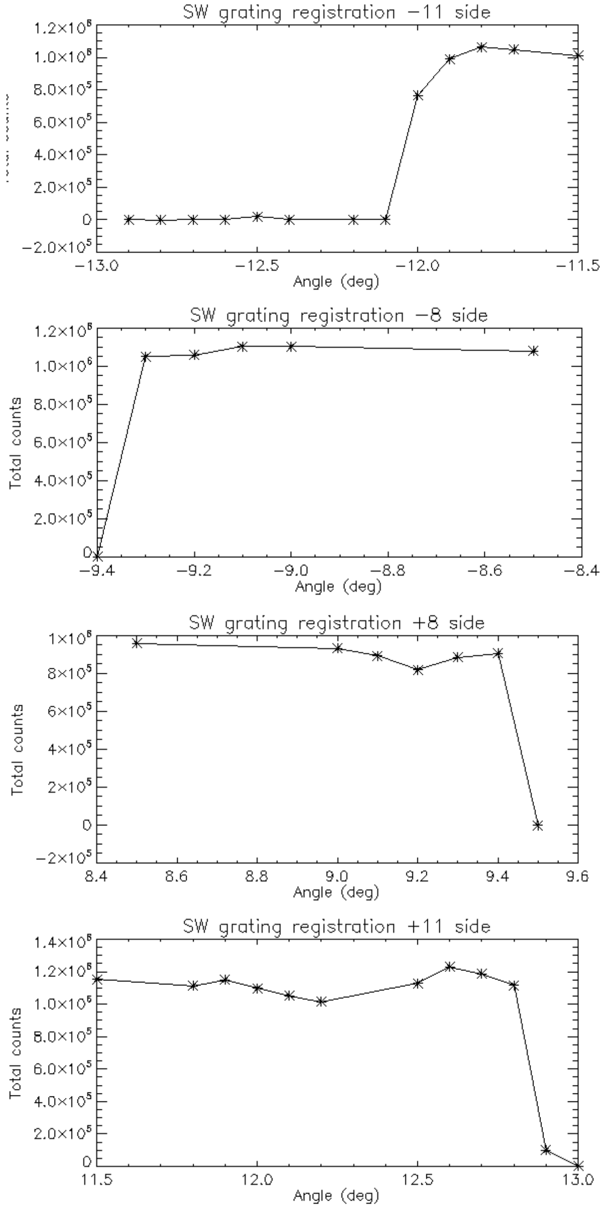

Fig 4.11: Results of field of view determination

The maximum error for any single spot in the SW-channel measurements is 0.65 pixels or 0.04 degrees which correspond to the size of half a science pixel. The mean values for all the measured spots in the SW-channel are almost a factor of 10 smaller (0.082 pixels and 0.009 degrees) and show that the measurements and fitting provide a reliable way to describe the geometric distortions in the SW-channel.

In the LW-case there are slightly larger maximum errors of 1.697 pixels and 0.064 degrees which are caused by a few measurements around the extreme beta angles of 12.3-12.8 degrees. It is not really obvious why these spots are reconstructed less reliably than others as the count rates still indicate perfect coverage within the sensitive region of the detector. Nevertheless, the overall fit of the distortion is still much smaller than one science pixel.

4.2.6 Results of the pre-flight spot size calibration

The report ICN-FUV-143-REP-spots.pdf summarizes the results of ICON-FUV instrument spot size measurements at different instrument temperatures. The spot sizes were determined by illuminating the FUV instrument with a parallel beam of UV photons and running the cameras in 12-second total integration mode with 120 ms frame integration times. The test dates were:

- 2016-01-18; hot balance;
- 2016-01-25; cold gradient;
- 2016-01-26; hot balance;
- 2016-01-31; room temperature;
- 2016-02-01; room temperature;
- 2016-02-02; cold balance;
- 2016-02-03; hot calibration;

No particular test procedure was used for this investigation as all measurements done during spectral scan, distortion measurements, and HV tests were used for the evaluation.

The following plots shows the CCD temperatures during all the tests done between 2016-01-18 and 2016-02-03.

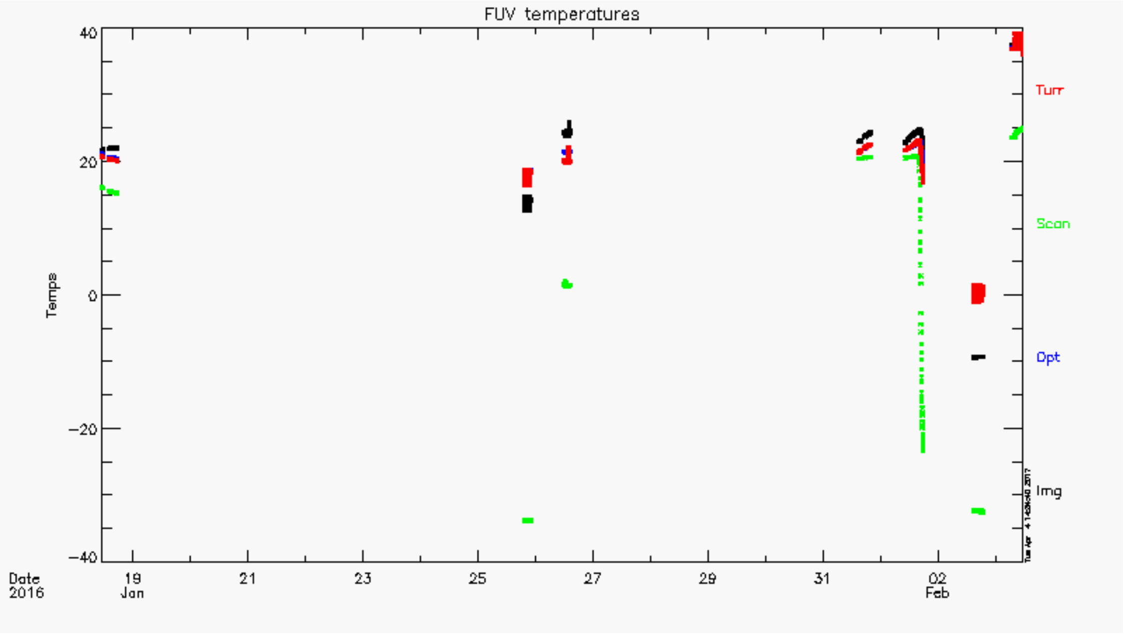

Fig 4.12: FUV instrument temperatures during the days of testing between January-18 and February-3, 2016

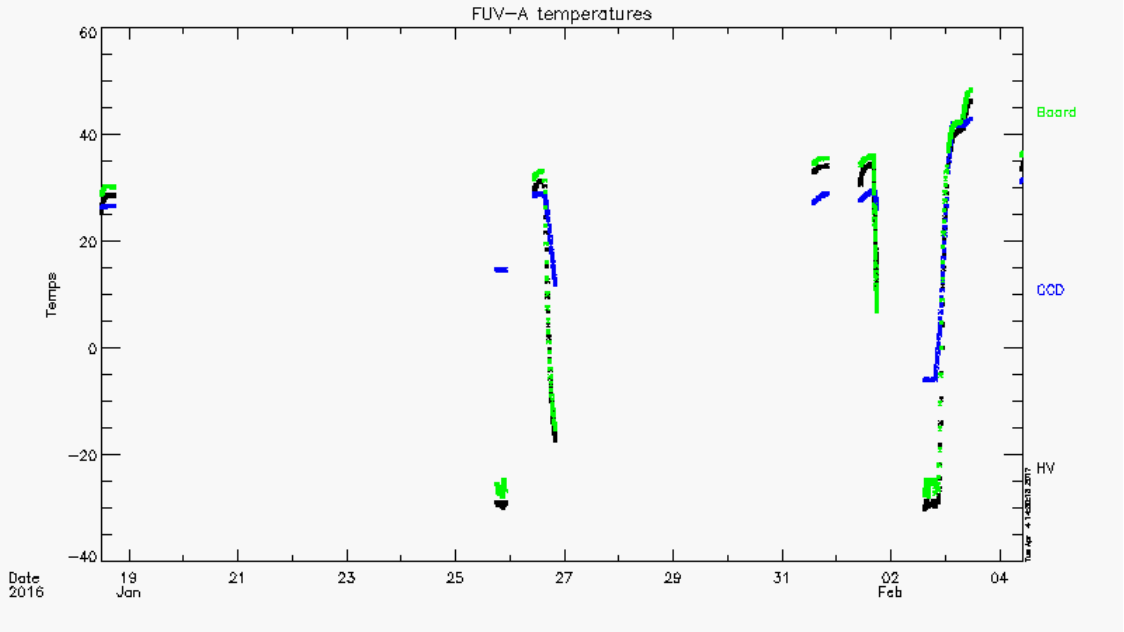

Fig 4.13: FUV-A temperatures during the days of testing between January-18 and February-3, 2016.

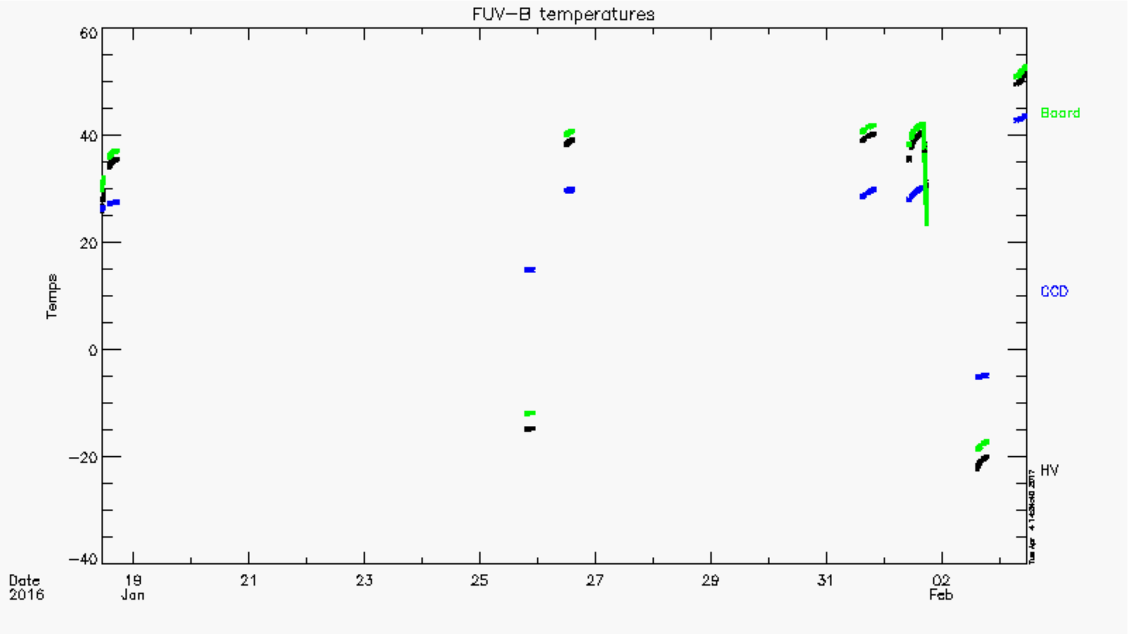

Fig 4.14: FUV-B temperatures during the days of testing between January-18 and February-3, 2016.

The spot sizes were determined by fitting 2D Gaussian surfaces to the pixel counts around the spot center. The fitting was done with two different IDL procedures, the built-in GAUSS2DFIT procedure, and with the MPFIT package by defining a 2D Gaussian as :

Z = A[0] + A[1] * exp (-U/2.)

U = ((X’/A[2])^2 + (Y’/A[3])^2)

X’ = (x-A[4])*cos(A[6]) – (y-A[5])*sin(A[6])

Y’ = (x-A[4])*sin(A[6]) + (y-A[5])*cos(A[6]).

Unfortunately, the 2D fitting in IDL is not very mathematically exact and especially with our spots that are only 3-5 pixels wide and the uncertainty due to the counting statistics large uncertainties of the results were obtained for many of the spots. The spot sizes in [x, y] had a large range and we had to eliminate several calculation results due to unrealistic results. Still the scatter of the spot sizes is substantial as we did not separate spots in the center of the field of view and at the extreme edges. The results for FUV-A is given in the following figures. The FWHM of such a surface is given in the usual way for a Gaussian as

FWHM = 2. * sqrt(2. * ln(2.)) * A[2]

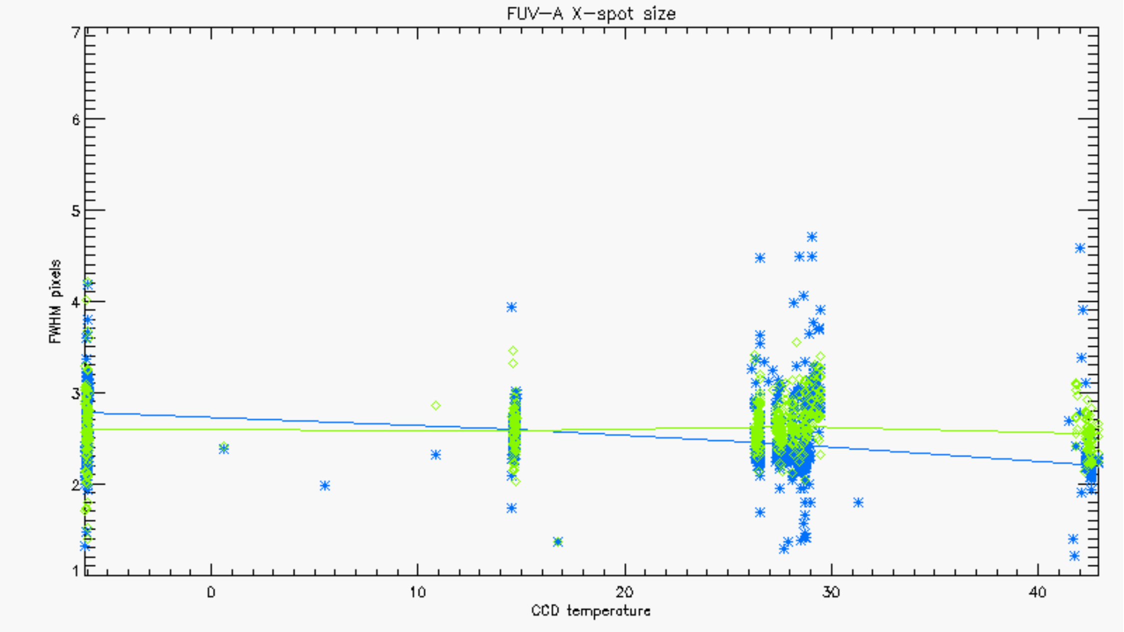

Fig 4.15: SW spot size in the X-direction as a function of the SW camera CCD temperature. The blue points were obtained with the GAUSS2DFIT IDL-function while the green points were obtained with the MPFIT package. The lines connect the centers of the 4 groups at temperatures around -6, +15, +28, and +43 C.

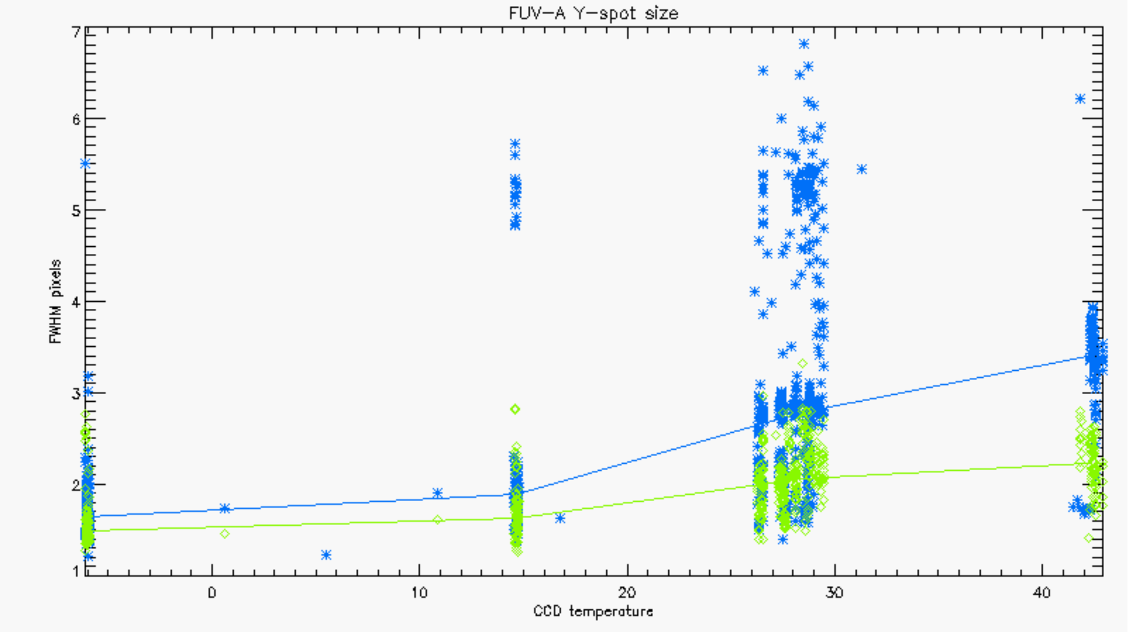

Fig 4.16: SW spot size in the Y-direction

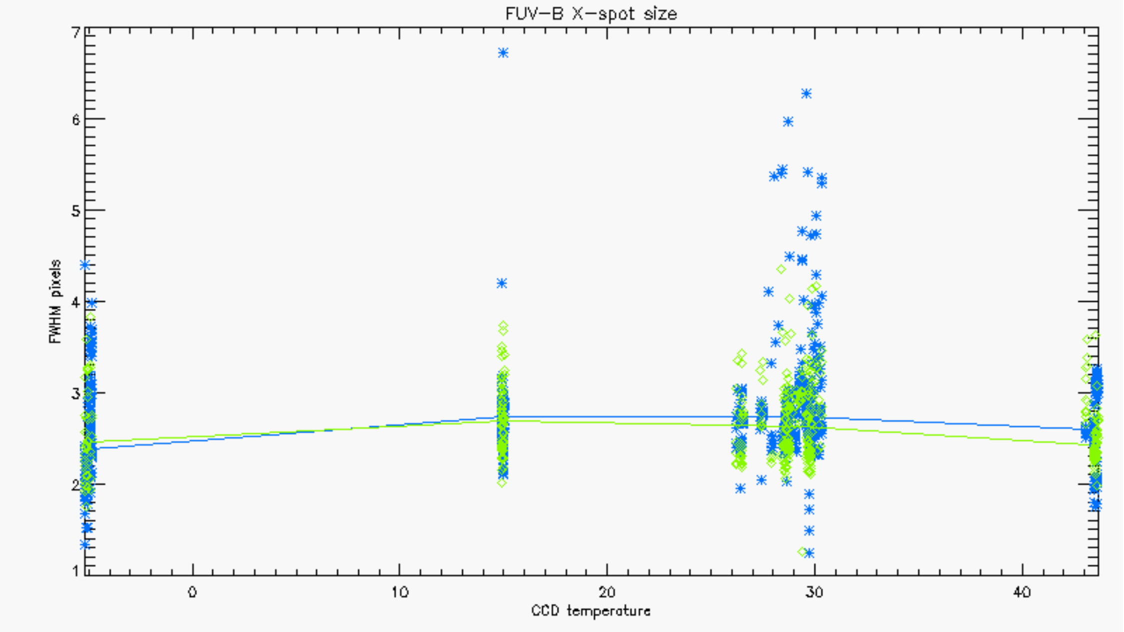

Fig 4.17: LW spot size in the X-direction

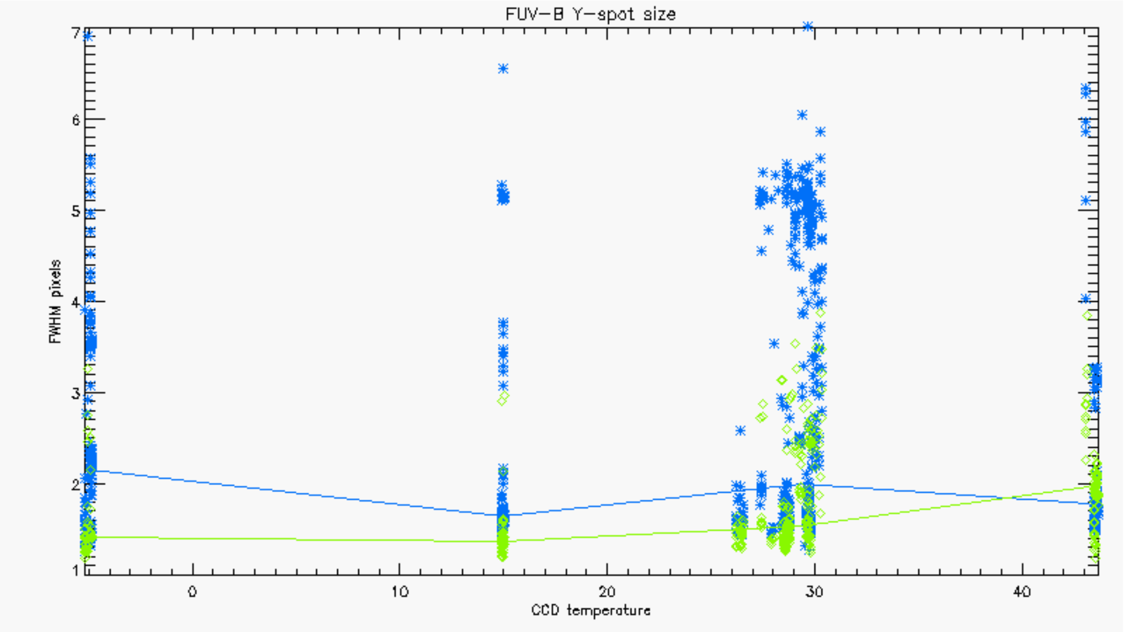

Fig 4.18: LW spot size in the Y-direction

Looking at the figures one should keep in mind that the spot sizes were determined for the unbinned 536x515 pixel images. During science operations in orbit the images will be digitally binned 2x2 before they will be processed by the TDI engines. Thus the size of science pixels is half of what is shown in the figures.

Overall there is no clear trend of spot size changes with temperature. One might see a slight decrease in x-size and increase in y-size for the SW channel with increasing temperature but I don’t think it is really statistically significant. Another view at the situation is the distribution of spot sizes with respect to the view angle as shown in the following figures.

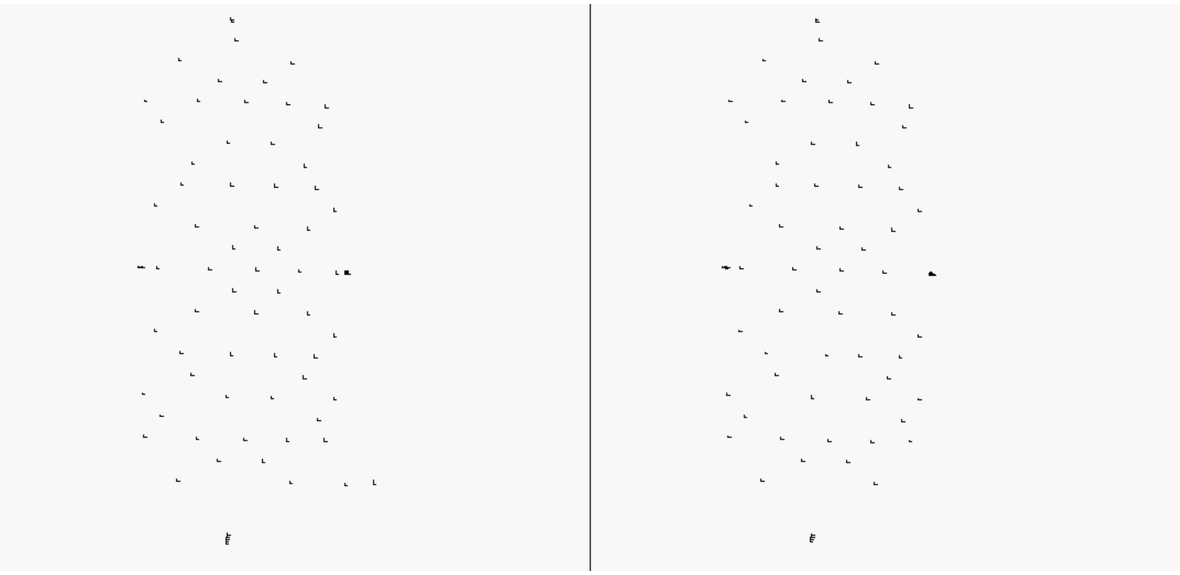

Fig 4.19: Spot sizes at room temperature for different view directions in the SW channel. The horizontal and vertical bars represent the FWHM in X- and Y-directions, respectively. The left plot was done with the results from the IDL function GAUSS2DFIT while the right plot was done with the MPFIT package.

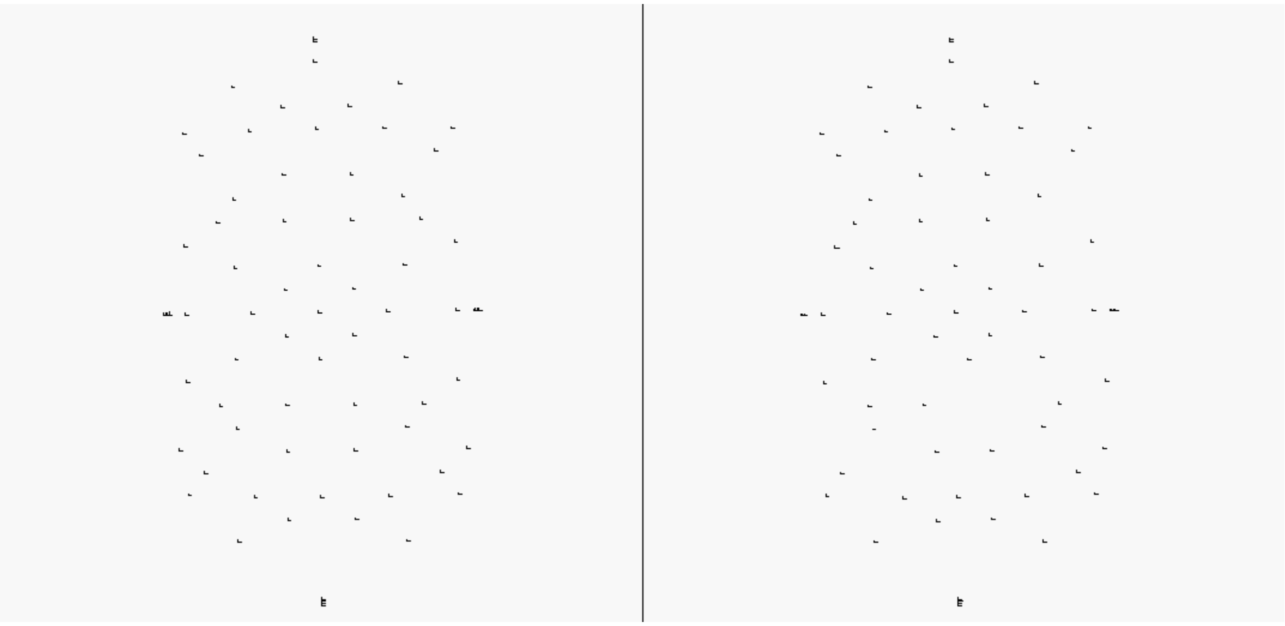

Fig 4.20: The same as the previous figure but for the LW channel.

There is no clear trend of spot size changes with temperature. There is also no clear trend of spot size differences across the field of view.

The average FWHM spot sizes for the two channels if converted to the 2x2 binned science pixels are
SW: x-size 1.22 pixels; y-size 1.18 pixels
LW: x-size 1.35 pixels; y-size 0.95 pixels

Of the whole integral under a 1D-Gaussian curve 76% is contained under the portion within the FWHM. Under a 2D-Gaussian only 58% of the whole volume is contained under the two-dimensional

FWHM with equal size in the x- and y-directions. Our science requirement is that 90% of the energy should be within 2x2 science pixels, or in the case of our unbinned images within 4x4 pixels. The result is that in all cases we do not achieve this goal with both the SW and LW channels.

4.2.7 Plan for spectral and sensitivity Pre-flight Calibrations

The pre-flight calibration plan for the spectral properties and sensitivity is detailed in the document ICN-FUV-079_sensitivity.docx. This procedure provides the steps to obtain the spectral sensitivity and the pass band of both FUV channels. This procedure was be used at CSL in Belgium with FUV in the 6.5 m vacuum chamber.

1.1.1 FUV instrument installed in CSL vacuum chamber with door opened
1.2 Proper movability of cradle confirmed
1.3 Electric connection through feedthrough confirmed
1.4 Communication between ICP and FUV confirmed
1.5 Data connection between FUV and ICP confirmed. As prior tests were performed with the SDL PC we need to confirm that this data connection has been done properly after full turn-off of instrument.
1.6 Verify Proper FUV Test Configuration
1.7 Verify proper vacuum chamber pressure of <10^-3 Pa
1.8 Start UV source
1.9 Tune monochromator to 135.6 nm
1.10 Characterize incoming beam with CSL photodiode
1.11 Verify computer time is correct and note start time
1.12 Verify cover is open
1.13 Note instrument temperature as this test has to be performed at three different nominal temperature settings
1.14 Instrument Payload Power On
1.15 Execute Section 8.9 in the FUV CPT (ICN-FUV-068) for ICP power on.
2.0 FUV Camera Power Control
2.1 Execute Section 8.10 of the FUV CPT (ICN-FUV-068) for the Camera Power Control. Add notes to attached As-run paper copy of procedure.
3.0 FUV High Voltage (HV) On
3.1 Execute Section 8.13 in the FUV CPT (ICN-FUV-068) for FUV High Voltage setup. Attach As-run paper procedure to the appendix. Note FUV CPT Revision used.
4.0 SW and LW channel sensitivity determination
4.1 Verify Monochromator is set to 120.0 nm
4.2 Characterize incoming beam at each wavelength step
4.3 Set up ICP to collect nominal 256x256 pixel images
4.4 Verify that turret is at nominal 0 degrees position
4.5 Verify that cradle is set to normal incidence 0 degrees
4.6 Send command: **IOP_FUV_DUMP_ENG_IMG** (enter **TDI ID = 0** for A) to capture and readout image to take an integrated picture of 100 frames of 120 msec exposure time and save through ICP with appropriate header information about time, number of frames, cradle position, wavelength, channel,
4.7 Verify appearance of a spot in the SW channel located at approximately the center of the image and record SW counts. Make sure we record reasonable counts before processing with full wavelength scan. Note counts in table below.
4.8 Send script: FUV_Disable_TDI

4.9 Send command: **IOP_FUV_DUMP_ENG_IMG** (enter **TDI ID = 1** for B) to capture and readout image to take an integrated picture of 100 frames of 120 msec exposure time and save on SDL PC with appropriate header information about time, number of frames, cradle position, wavelength, channel,

4.10 Verify appearance of a spot in the LW channel located at approximately the center of the image

4.11 Send script: FUV_Disable_TDI

4.12 Change wavelength of monochromator to wavelength listed in the table below and repeat steps 8.6.1 to 8.6.11. Note the approximate total counts as the detailed analysis will be done later.

4.13 ITOS power down

4.2.8 Results of the pre-flight spectral calibration

Results of the pre-flight spectral and pass band calibration are summarized in the document ICN-FUV-140-REP-spectral.pdf. The tests were performed at different temperatures. The prime objective was to confirm modelling results and to establish the pass band characteristics for quantitative analysis. This report aims to collect all of the relevant information about test environment, setup, and results in one place. It summarizes the relative shape of the pass bands of the channels. Absolute numbers at the transmission maximum will be summarized in a different report that also considers measurements with different MCP high voltages.

The tests were performed on several days in January/ February 2016. The procedure ICN-FUV-079 was used for those tests. Most tests used the central (0, 0) degrees view position but on February 1, 2016 also all extremes of the field of view were tested.

Test dates and conditions:

- 2016-01-25, cold gradient:
- 2016-01-26, hot balance:
- 2016-01-31, room temperature:
- 2016-02-02, cold balance:
- 2016-02-03, hot calibration:
- 2016-02-01, Scan at FOV edges:

Spectral band pass for the SW channel

Each measurement series included three background images taken with a closed valve between the monochromator and the vacuum chamber to determine the average background counts coming just from the CCD dark current and read-out noise. The input photon flux was recorded for every single measurement. After background subtraction the calculated counts were then divided by the flux to get numbers of counts per unit photon flux. The relative pass band shape is then determined by normalization with the maximum measured counts per unit photon flux.

It has to be noted that the source has a strong wavelength dependence of the photon flux output varying by the equivalent current measured by the source meter from 1.0E-11 A at 119 nm, to 1.3E-10 A at 135.6 nm and to 9.3E-9 A which affects some of the normalization results. Several relative transmission values at low wavelengths show something like -5% which should be regarded as 0% and only appears relatively large (in negative sense) because of the remaining counts from statistical fluctuations being divided by a relatively small number.

A representative example of the pass band determination for the SW channel is shown in Figure 4.21. The maximum of the measured transmission is at 135.0 nm. The profile matches reasonably well a triangular shape. The fitted Gaussian has its peak at 135.93 nm and a FWHM of 4.72 nm. Due to the triangular shape of the measured profile the fall of towards shorter and longer wave lengths is much steeper than for the fitted Gaussian curve.

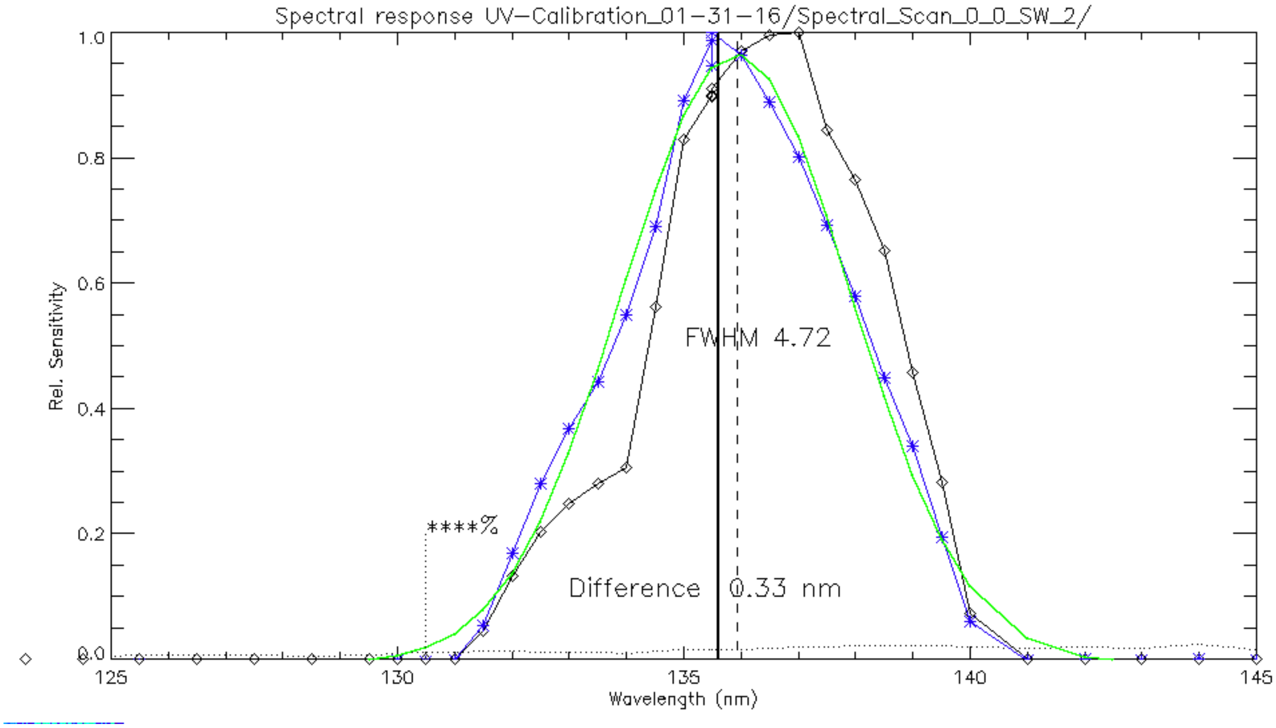

Fig 4.21: Spectral scan measurements on 2016-01-31 at room temperature. The black line with diamonds shows the raw measurements normalized to the maximum counts. The black dotted line is the source meter reading normalized to its maximum around 161 nm. The blue line with asterisks is the counts divided by the source meter current reading normalized to the maximum of that ratio. The green line is a Gaussian fit to the normalized measurements. The maximum of the fitted Gaussian is at 0.33 nm higher than the target wavelength of 135.6 nm. The FWHM of the Gaussian is 4.72 nm. The 130.4 response is basically zero.

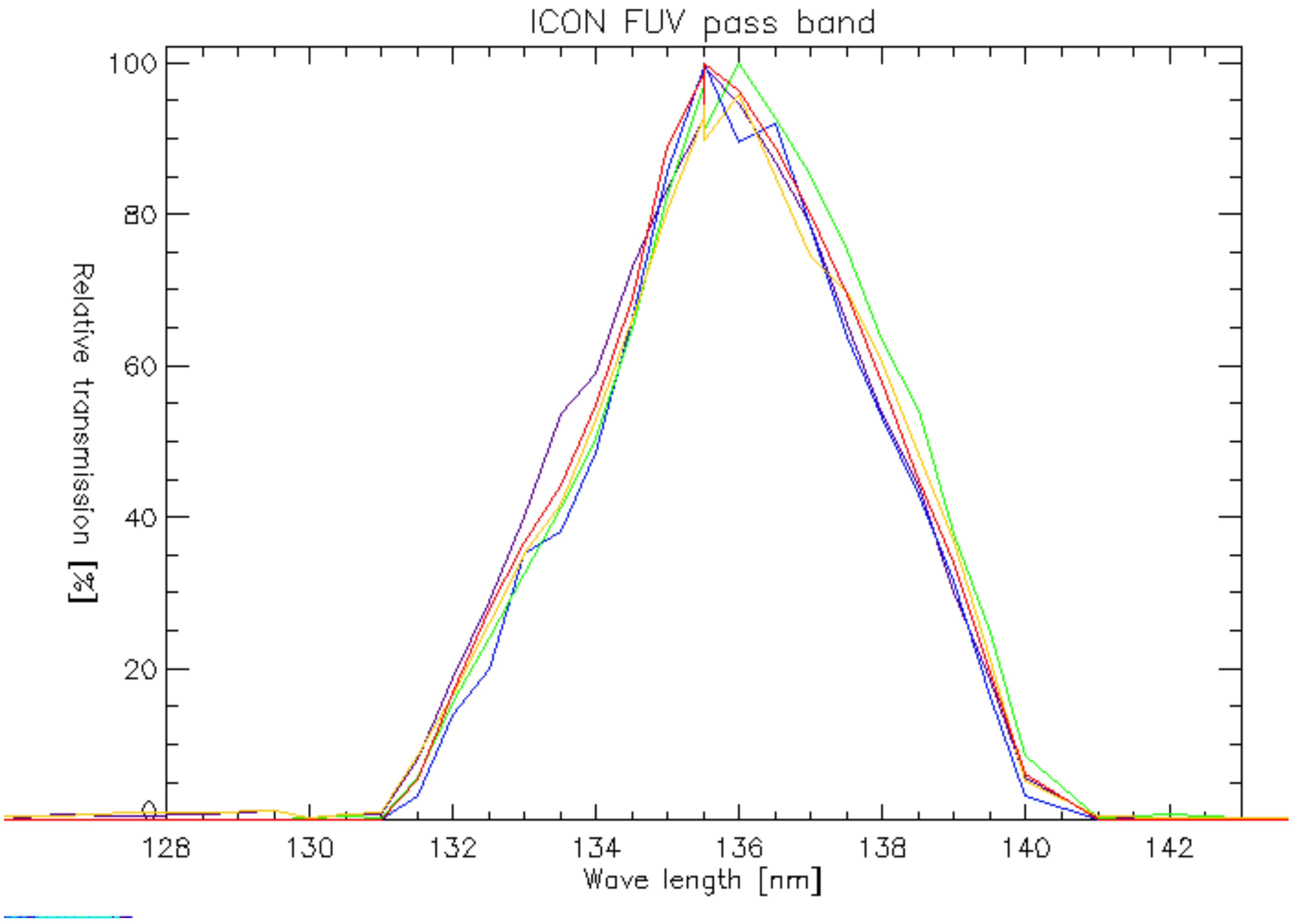

Fig 4.22: Normalized spectral profiles for all measurements at different temperatures. The colors are purple (2016-02-02, 0 C), blue (2016-02-03, 38 C), green (2016-01-25, 15 C), yellow (2016-01-26 25 C), and red (2016-01-31, 22 C).

The previous Figure summarizes all profiles measured at different temperatures. There is a small trend of variation with temperature recognizable at the low wavelength part with the coldest measurement rising first and the hottest measurement rising last with the other measurements aligned in between.

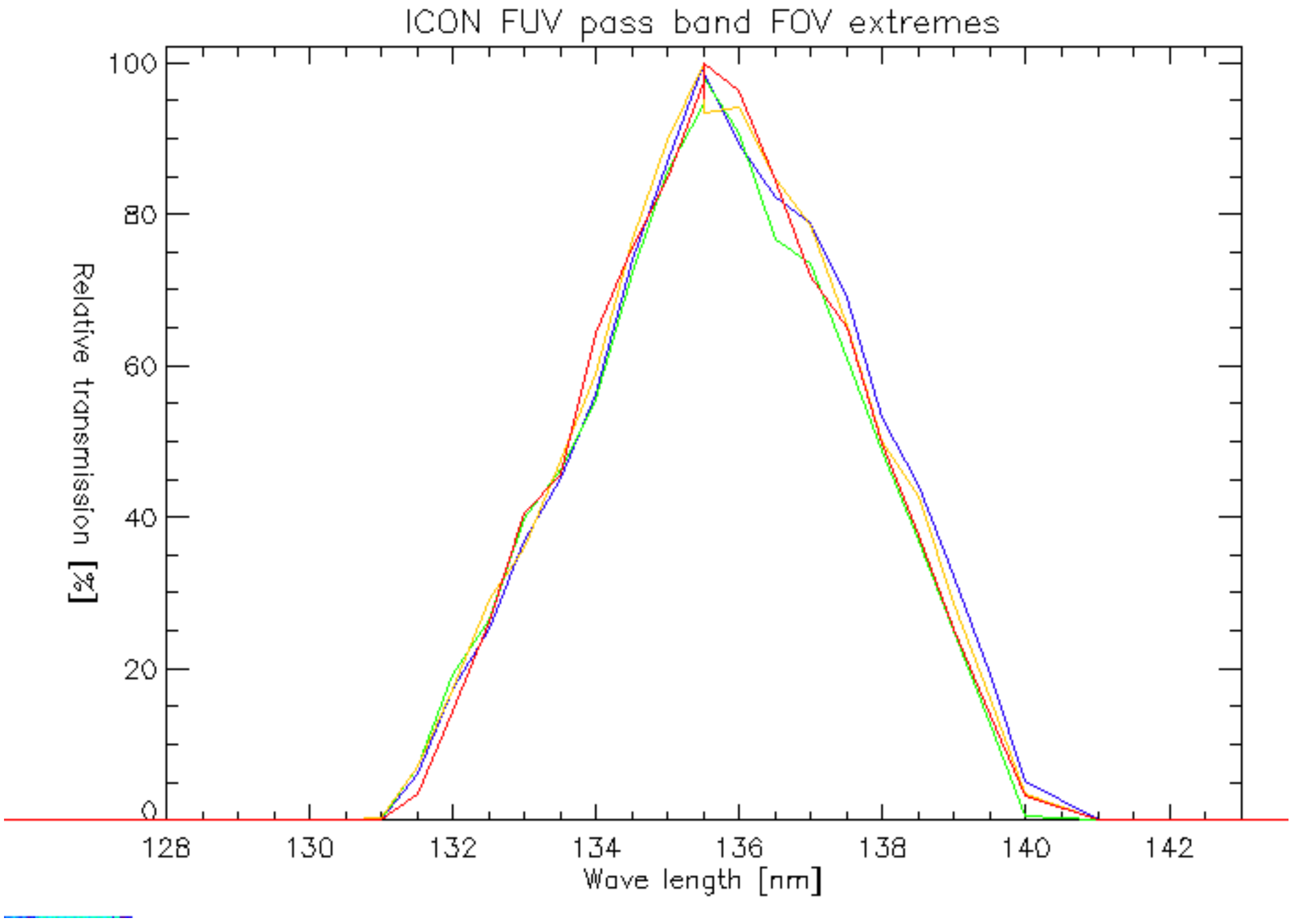

Fig 4.23: Spectral profiles for the extremes of the field of view. The colors are blue (+8, 0), green (0, -11), yellow (0, +11), and red (-8, 0).

Figure 4.23 summarizes the results of measurements at field of view extremes. There is no clear trend to any particular region.

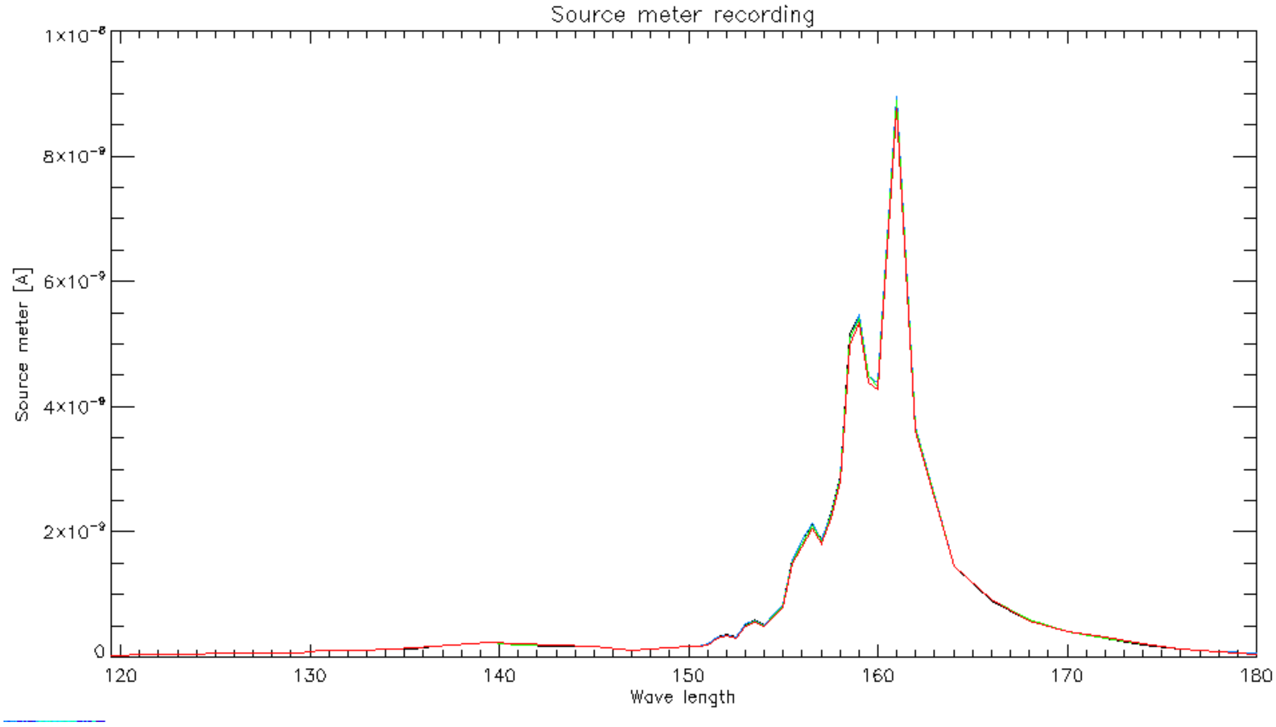

Fig 4.24: Source meter readings during four different spectral scans on 2016-02-01. The large output variability around 160 nm is very distinct.

Spectral band pass for the LW channel

The measurements for the LW channel were made immediately before or after the SW channel measurements under the same experimental temperature conditions and the same field angles.

Figure 4.25 shows a representative spectral profile measured at room temperature. It is clear that the maximum response is shifted towards longer wavelengths compared to the target of 157 nm. The passband is also wider with a FWHM of 5.99 nm compared to 4.72 nm for the SW channel.

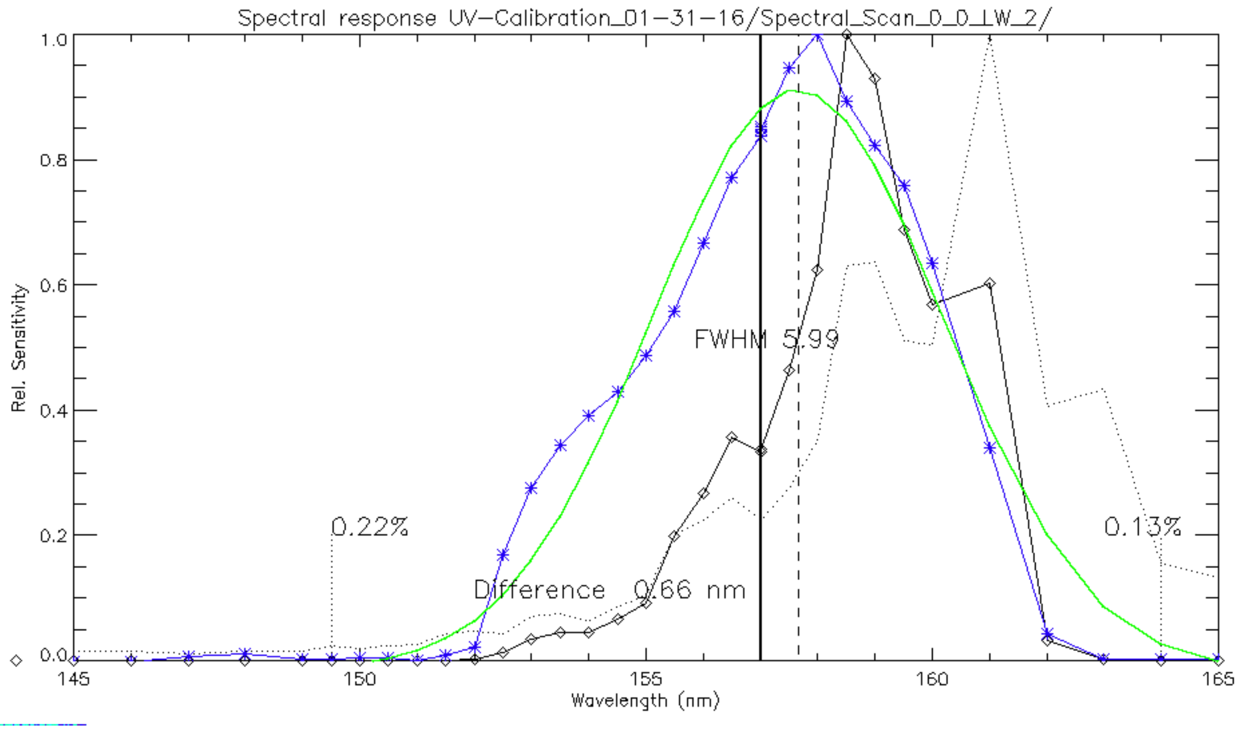

Fig 4.25: The same as Figure 4.21 but for the LW channel.

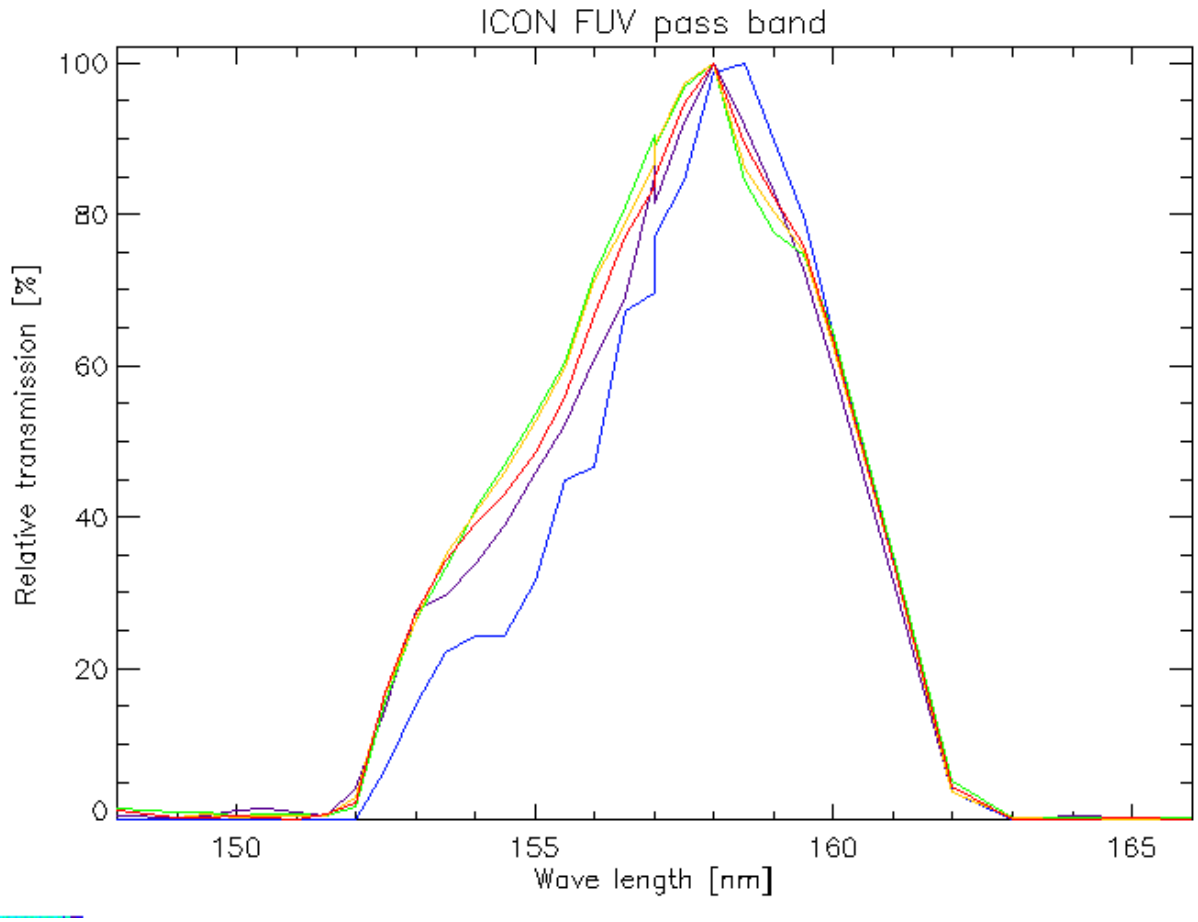

Fig 4.26: The same as Figure 4.22 but for the LW channel.

The curves in Figure 4.26 show the pass band variation with temperature and for most environmental conditions the curves align with each other except for the blue line measured at hot temperatures. The shape of the curve is quite different and much narrower than in the other cases. This hot-case performance has not been investigated or explained. Please note that the test was done at 38 ºC, a temperature extreme that was never realized during science operations on orbit.

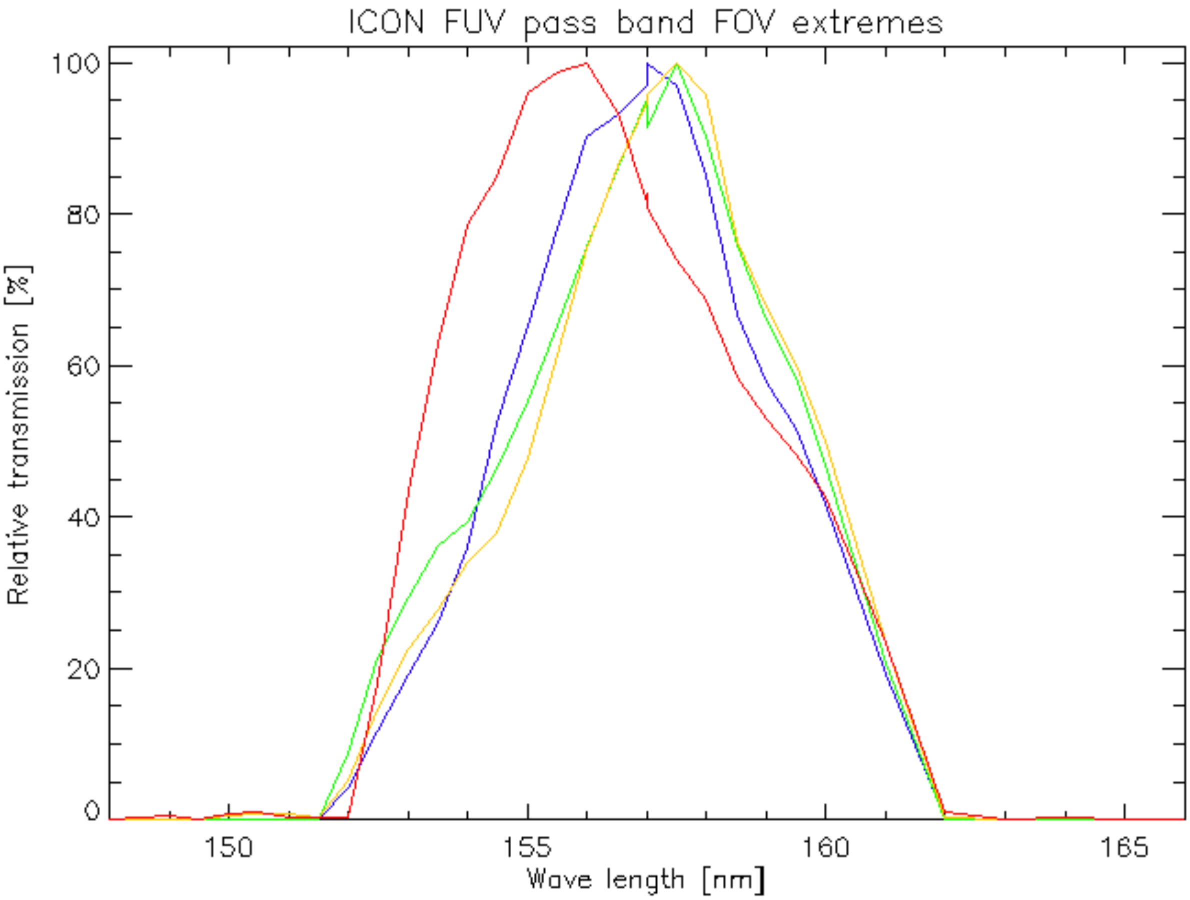

Figure 4.27: The same as figure 4.23 but for the LW channel.

Figure 4.26 shows the spectral profiles for different field angles. There is a clear outlier (red curve) for the (-8, 0) field angle. While all other profiles have maxima close to or above the target wavelength of 157 nm, this position has a maximum at 156 nm. Again, at this moment I don't have a good explanation for this difference.

Overall the spectral profiles show little or no variation with temperature and are also very similar for the different field angles, except for one measurement with the LW channel.

Wave	01-31	02-02	02-03	01-25	01-26		Wave	02-01	02-01	02-01	02-01
	(0,0)	(0,0)	(0,0)	(0,0)	(0,0)			(+8, 0)	(0, -11)	(0, +11)	(-8, 0)
	22 C	0 C	38 C	15 C	25 C			21 C	21 C	21 C	21 C
119.5	-4.78	0.11	-4.87	-2.64	1.49		119.5	-1.05	-5.52	-2.12	-1.87
120.5	-4.32	0.01	-2.81	-1.82	2.45				-4.15	-3.60	-2.42
121.5	-1.69	0.06	-5.22	-0.62	0.54		121.5	-3.80	-4.63	-0.11	-0.88
122.5	-2.86	0.22	-3.58	-1.61	1.61		122.5	-8.53	-9.55	-1.31	-1.80
123.5	-0.97	0.20	-6.81	-1.00	1.62		123.5	-5.48	-6.02	-1.56	-0.90
124.5	-1.42	0.17	-6.06	-1.15	0.45		124.5	-4.54	-4.31	-1.07	-0.37
125.5	-0.94	0.15	-5.31	-0.23	0.84		125.5	-3.98	-3.71	-0.71	-0.57
126.5	-1.58	0.68	-6.14	-0.54	0.47		126.5	-4.03	-4.08	-0.84	-0.36
127.5	-1.20	0.52	-7.34	-0.16	0.96		127.5	-3.38	-3.48	-0.62	-0.57
128.5	-1.19	0.81	-5.10	0.12	1.07		128.5	-5.52	-5.53	-0.89	-0.86
129.5	-1.04	1.29	-7.69	0.03	1.21		129.5	-4.17	-4.44	-0.06	-0.43
130.0	-0.24	0.40	-5.37	0.33	0.20		130.0	-2.98	-2.73	-0.57	-0.60
130.5	-0.53	0.44	-3.59	0.44	0.72		130.5	-1.77	-2.52	-0.21	-0.28
131.0	-0.32	0.79	-4.05	0.35	1.07		131.0	-1.40	-0.96	0.39	-0.08
131.5	5.41	7.98	3.08	5.52	8.64		131.5	6.18	7.06	7.04	3.35
132.0	16.84	18.70	13.96	15.59	16.47		132.0	17.31	19.21	17.22	14.39
132.5	28.02	28.84	20.04	24.05	26.05		132.5	25.31	26.38	29.05	26.24
133.0	36.68	40.00	35.11	32.59	35.21		133.0	36.91	39.90	35.89	40.56
133.5	44.13	53.71	38.12	41.28	41.85		133.5	45.12	46.23	47.47	45.52
134.0	54.86	59.02	48.41	50.40	52.97		134.0	56.33	55.66	59.04	64.19
134.5	68.83	72.93	66.11	64.91	66.23		134.5	73.97	72.33	76.54	75.69
135.0	89.07	83.36	85.52	82.48	80.57		135.0	86.73	85.57	89.65	84.67
135.5	98.45	92.72	99.55	97.02	92.78		135.5	100.00	94.59	100.00	97.44
135.5	94.62	100.00	98.55	98.24	100.00		135.5	97.63	100.00	95.30	95.27
135.5	100.00	99.43	100.00	91.24	89.77		135.5	98.45	98.03	93.35	100.00
136.0	96.32	94.47	89.41	100.00	95.76		136.0	89.25	90.76	94.07	96.22
136.5	88.81	86.83	91.94	92.72	84.89		136.5	82.11	76.72	84.74	84.38
137.0	80.04	78.68	78.44	85.09	74.58		137.0	78.78	73.60	78.64	71.68
137.5	69.26	65.53	63.71	75.15	69.72		137.5	68.98	60.99	65.23	64.93
138.0	57.84	53.67	53.19	63.21	60.44		138.0	53.15	48.85	49.94	49.80

138.5	44.92	44.07	42.94	54.01	48.27		138.5	44.20	36.94	42.68	37.60
139.0	33.89	30.06	31.52	37.98	36.92		139.0	32.22	24.95	28.53	25.18
139.5	19.46	18.35	16.40	24.76	21.15		139.5	19.25	12.61	15.94	13.86
140.0	6.04	5.69	3.25	8.42	5.17		140.0	5.21	0.63	3.50	3.17
141.0	-0.13	0.36	-1.80	0.40	0.42						
142.0	-0.13	0.16	-1.23	0.75	0.22		142.0	-0.83	-1.07	-0.08	0.01
143.0	-0.25	0.09	-1.28	0.40	0.21						
144.0	0.05	0.15	-1.02	0.46	0.50		144.0	-0.79	-0.80	0.02	-0.11
145.0	-0.18	0.04	-1.09	0.78	0.27						
146.0	-0.37	-0.09	-0.95	0.38	0.02		146.0	-1.23	-1.23	0.14	-0.27
147.0	-0.33	-0.01	-1.31	0.20	-0.04						
148.0	-0.20	-0.11	-0.93	0.18	0.07		148.0	-1.11	-1.38	0.19	-0.23
149.0	-0.47	-0.31	-1.15	0.16	0.02						
149.5	-0.24	-0.24	-0.71	0.17	0.13						
150.0	-0.35	-0.56	-0.97	0.11	0.12		150.0	-1.49	-1.53	0.09	-0.23
150.5	-0.31	-0.52	-1.18	0.11	0.03						
151.0	-0.10	-0.25	-0.92	0.19	0.02						
151.5	0.07	-0.36	-0.81	0.08	0.09						
152.0	-0.05	-0.34	-0.90	0.08	-0.03		152.0	-0.46	-0.70	-0.01	-0.10
152.5	0.06	-0.43	-1.36	0.09	0.01						
153.0	0.00	-0.35	-1.15	0.07	0.00						
153.5	0.02	-0.38	-0.92	0.05	-0.02						
154.0	-0.03	-0.40	-1.87	0.09	-0.01		154.0	-0.37	-0.43	0.00	0.02
154.5	-0.02	-0.19	-1.66	0.08	0.01						
155.0	-0.04	-0.28	-1.69	0.05	-0.01						
155.5	0.01	-0.03	-0.93	0.03	0.01						
156.0	0.03	-0.06	-0.98	0.03	0.02		156.0	-0.05	-0.11	0.05	0.02
156.5	0.03	0.07	-1.27	0.04	0.02						
157.0	0.00	-0.04	-1.38	0.03	0.01						
157.5	0.02	-0.05	-0.91	0.03	0.01						
158.0	0.03	-0.01	-0.73	0.01	0.01		158.0	-0.06	-0.08	0.00	0.01
158.5	0.02	0.02	-0.31	0.01	0.01						
159.0	0.02	0.01	-0.50	0.01	0.00						
159.5	0.02	-0.01	-0.43	0.01	0.01						

160.0	0.01	0.00	-0.45	0.01	0.01	160.0	-0.04	-0.06	0.01	0.02
161.0	0.01	-0.01	-0.09	0.01	0.01					
162.0	-0.02	-0.01	-0.07	0.01	0.01	162.0	-0.05	-0.04	0.02	0.02
163.0	0.00	-0.02	-0.28	0.01	-0.01					
164.0	-0.02	-0.12	-0.48	-0.01	-0.03	164.0	-0.12	-0.17	0.01	0.04
165.0	-0.04	-0.10	-0.81	-0.04	-0.05					
166.0	-0.01		-0.63	-0.05	-0.03	166.0	-0.25	-0.26	0.00	0.01
167.0	-0.02	-0.06	-1.13	-0.04	-0.05					
168.0	-0.05	-0.13	-0.71	-0.14	-0.02	168.0	-0.37	-0.41	0.01	0.03
169.0	-0.06	-0.19	-0.52	-0.19	-0.01					
170.0	0.06	-0.13	-0.45	-0.27	-0.05	170.0	-0.44	-0.59	-0.01	0.08
171.0	-0.07		-0.68	-0.37	-0.09					
172.0			-0.82	-0.42	-0.16					
173.0			-0.80	-0.42	-0.04					
174.0			-0.37	-0.81	-0.45					
175.0			0.26	-0.99	0.04					
176.0			0.20	-1.61	-0.09					
177.0				-1.55	0.27					
178.0				-1.74	0.65					
179.0				-2.83	0.38					
180.0				-2.50	0.85					

Table 4.5: Normalized spectral transmission profiles for the SW channel. The wave columns show wavelength in nanometers. The header shows date of test, field angle, and instrument temperature. All measurements were normalized to the maximum during that particular measurement day and field angle.

Please note that at the wavelength of interest (135.5 nm) three separate measurements were performed. The values in the table show that there is no clear trend of a shift of the passband with temperature or with field angle across the field of view.

Wave	01-31	02-02	02-03	01-25	01-26		Wave	02-01	02-01	02-01	02-01
	0,0	0,0	0,0	0,0	0,0			+8, 0	0, -11	0, +11	-8, 0
	22 C	0 C	38 C	15 C	25 C			21 C	21 C	21 C	21 C
119.5	-5.08	0.88	-3.42	9.10	-1.40		119.5	-3.04	-8.75	-0.03	-0.23
120.5	-5.11	1.44	-7.49	0.11	-5.93						
121.5	-3.65	0.73	-6.49	1.50	1.18		121.5	-7.31	-2.01	-0.82	1.05
122.5	-7.34	0.71	-8.26	1.19	5.95						
123.5	-5.10	0.15	-6.54	1.79	-0.90		123.5	-5.43	-4.05	-2.73	-0.74
124.5	-3.93			0.43	-1.47						
125.5	-2.46	0.62	-6.44	3.70	2.82		125.5	-5.44	-8.08	-0.72	0.16
126.5	-2.02	0.41	-8.68	1.66	1.71						
127.5	-2.28	0.34	-8.84	2.07	1.22		127.5	-6.87	-9.31	-0.10	1.00
128.5	-3.26	0.60	-5.59	3.05	1.38						
129.5	-3.60	0.79	-8.52	4.14	4.60		129.5	-5.43	-9.46	1.13	-0.47
130.0	-0.85	0.76	-5.95	1.93	2.67						
130.5	-1.78	0.38	-5.12	2.66	3.08		130.5	-3.08	-4.69	-0.18	0.18
131.0	-1.90	0.94	-4.91	0.34	0.88						
131.5	-0.45	0.58	-4.35	1.96	2.76						
132.0	-0.77	0.24	-5.19	1.08	2.39						
132.5	-1.12			1.92	2.13		132.5	-3.47	-4.60	-0.18	0.03
133.0	-1.40	0.39	-6.45	1.04	4.12						
133.5	-1.02	1.13	-6.30	1.89	3.15						
134.0	-2.18	0.57	-6.46	5.48	2.98						
134.5	-0.80	0.62	-4.44	1.32	0.79		134.5	-2.79	-3.70	0.46	-0.04
135.0	-0.12	0.43	-3.39	0.75	1.58						
135.5	-0.39	0.76	-2.50	2.47	1.33		135.5	-2.55	-3.25	-0.28	0.06
136.0	-1.11	0.42	-3.62	2.18	2.20						
136.5	0.33		-4.17	1.95	-0.31		136.5	-1.90	-2.67	0.24	0.36
137.0	0.31	0.67	-3.20	1.59	0.09						
137.5	-0.40	0.41	-3.45	1.27	1.26		137.5	-1.57	-2.31	-0.30	-0.10
138.0	0.55	0.46	-2.64	1.41	0.68						
138.5	0.15	0.72	-1.42	1.16	1.11						
139.0	-0.20	0.54	-2.14	0.98	-0.08						
139.5	-0.38		-2.31	0.79	0.22		139.5	-1.06	-2.06	-0.50	0.37

140.0	-0.43	0.65	-2.38	1.93	2.47					
141.0	0.34	0.69	-2.48	1.08	2.80		141.0	-1.70	-2.43	-0.27	0.25
142.0	0.44	0.47		2.85	1.85					
143.0	0.89	0.56	-2.20	2.73	3.49		143.0	-1.55	-2.58	-0.16	0.24
144.0	0.09	0.39	-1.33	2.03	0.98					
145.0	-0.13	0.89	-1.71	1.97	3.50		145.0	-1.67	-2.97	-0.33	0.02
146.0	-0.20	0.74	-1.13	1.91	2.74					
147.0	0.74	0.66	-2.05	1.84	2.71		147.0	-2.47	-4.31	-0.66	0.02
148.0	1.17	0.62	-0.89	1.40	1.26					
149.0	0.23	0.29	-0.04	0.99	0.31		149.0	-1.21	-2.78	0.11	0.52
149.5	0.22	0.63	-0.67	0.94	0.70					
150.0	0.50	1.33	-0.82	0.58	0.32		150.0	-1.01	-1.31	0.56	0.72
150.5	0.41	1.45	-1.23	0.70	0.49		150.5	-1.52	-2.55	0.79	1.09
151.0	0.04	1.03	-1.16	0.80	0.60		151.0	-1.40	-2.19	0.67	0.24
151.5	0.76	0.56	-0.68	0.59	0.55		151.5	-0.06	-0.99	0.30	0.36
152.0	2.22	4.18	0.09	1.82	3.00		152.0	4.28	8.71	5.03	0.25
152.5	16.84	14.51	6.70	15.44	16.42		152.5	11.71	21.45	14.55	17.93
153.0	27.53	27.74	15.36	26.50	26.48		153.0	19.15	29.33	22.67	43.40
153.5	34.30	29.66	22.02	33.28	34.90		153.5	26.03	36.08	27.72	62.78
154.0	39.13	33.63	24.35	41.04	40.57		154.0	35.91	39.30	34.07	78.57
154.5	43.00	38.80	24.26	46.93	45.98		154.5	52.43	46.26	37.81	85.00
155.0	48.64	45.89	31.50	53.52	52.55		155.0	65.14	55.22	47.73	96.03
155.5	55.76	52.06	45.01	60.32	59.71		155.5	78.07	65.16	61.33	98.79
156.0	66.66	60.97	46.57	72.09	71.29		156.0	90.17	75.71	75.49	100.00
156.5	77.16	69.11	67.17	80.96	78.89		156.5	93.06	86.16	86.33	93.29
157.0	83.77	85.12	69.71	90.38	86.79		157.0	97.00	95.41	94.84	81.49
157.0	85.19	86.92	72.87	90.17	89.31		157.0	98.61	92.22	95.81	82.73
157.0	84.89	81.59	77.13	88.96	88.95		157.0	100.00	91.36	95.81	80.79
157.5	94.67	92.09	84.46	96.84	97.33		157.5	96.91	100.00	100.00	74.09
158.0	100.00	100.00	98.63	100.00	100.00		158.0	85.06	90.14	95.69	68.64
158.5	89.28	91.57	100.00	84.38	86.09		158.5	66.78	75.99	76.35	58.56
159.0	82.31	82.89	89.83	77.57	80.16		159.0	57.67	66.03	67.78	52.86
159.5	75.85	72.76	79.89	74.62	75.21		159.5	51.65	58.36	60.22	48.18
160.0	63.48	59.97	64.40	64.45	62.77		160.0	41.69	46.76	49.89	42.83

161.0	33.97	31.49	34.77	35.07	33.99		161.0	19.10	20.75	23.36	23.42
162.0	4.32	3.68	3.59	5.20	3.70		162.0	0.28	0.06	0.38	1.03
163.0	0.15	0.09	0.02	0.20	0.22						
164.0	0.13	0.43	-0.35	0.35	0.15		164.0	-0.08	-0.12	0.17	0.18
165.0	0.23	0.23	0.07	0.28	0.04						
166.0	0.15	0.40	-0.49	0.39	0.20		166.0	-0.19	-0.39	0.08	0.12
167.0	0.15	0.27	-0.70	0.41	0.08						
168.0	0.05	0.37	0.14	0.49	-0.11		168.0	-0.38	-0.74	0.07	-0.01
169.0	0.36	0.25	-0.81	0.23	0.16						
170.0	0.68	0.23	-0.12	0.51	0.40		170.0	-0.51	-0.88	0.19	-0.17
171.0	0.27		-0.33	0.79	0.42						
172.0			-0.06	0.68	0.24		172.0	-1.02	-1.40	-0.03	0.00
173.0			-1.22	0.71	0.12						
174.0			-0.93	0.56	0.60		174.0	-1.35	-1.46	0.20	0.01
175.0			-0.63	2.06	0.04						
176.0			-0.50	1.10	1.44		176.0	-2.66	-3.17	-0.30	0.36
177.0				3.43	1.75						
178.0				3.63	-2.10		178.0	-3.61	-4.61	-0.34	0.65
179.0				5.56	-2.49						
180.0				5.44	-3.22		180.0	-5.72	-7.34	-0.11	1.39

Table 4.6: Normalized spectral transmission profiles for the LW channel. The wave columns show wavelength in nanometers. The header shows date of test, field angle, and instrument temperature. All measurements were normalized to the maximum during that particular measurement day and field angle.

Please note that at the wavelength of interest (157 nm) three separate measurements were performed.

4.2.9 Plan for flatfield Pre-flight Calibrations

The pre-flight calibration plan for the flatfield is detailed in the document ICN-FUV-080_flatfield.docx, available on the ICON public FTP server (ftp://icon-science.ssl.berkeley.edu/pub/Documentation/CMAD/ICN-FUV-080_flatfield.docx). This procedure was be used at CSL in Belgium with FUV in the 6.5 m vacuum chamber. The test is similar to the determination of the distortion map but without the diffuser in the beam and data readout through the ICP.

1.1.1 FUV instrument installed in CSL vacuum chamber with door opened
1.1.2 Proper movability of cradle confirmed
1.1.3 Electric connection through feedthrough confirmed
1.1.4 Communication between ICP and FUV confirmed
1.1.5 Verify Proper FUV Test Configuration
1.1.6 Verify proper vacuum chamber pressure of <10^3 Pa

1.1.7 Start UV source
1.1.8 Tune monochromator to 135.6 nm
1.1.9 Characterize incoming beam with CSL photodiode
1.1.10 Verify computer time is correct and note start time
1.1.11 Verify cover is open
1.2 Note instrument temperature for the record
2.0 Instrument Payload Power On (Steps 8.3 to 8.5 could potentially get skipped if prior test did not power off FUV, ICP, and SDL PC)
2.1 Execute Section 8.9 in the FUV CPT (ICN-FUV-068) for ICP power on.
3.0 FUV Camera Power Control
3.1 Execute Section 8.10 of the FUV CPT (ICN-FUV-068) for the Camera Power Control.
4.0 FUV High Voltage (HV) On
4.1 Execute Section 8.13 in the FUV CPT (ICN-FUV-068) for FUV High Voltage setup.
5.0 SW channel flatfield determination
5.1 Verify Monochromator is set to 135.6 nm
5.2 Characterize incoming beam
5.3 Set up ICP to collect 256x256 pixel images
5.4 Verify that turret is at nominal 0 degrees position
5.5 Verify that cradle is set to normal incidence 0 degrees
5.6 Send command: **IOP_FUV_DUMP_ENG_IMG** (enter **TDI ID = 0** for A) to capture and readout image to take an integrated picture of 100 frames of 120 msec exposure time and save through ICP with appropriate header information about time, number of frames, cradle position, wavelength, channel,
5.7 Verify appearance of a spot in the SW channel located at approximately the center of the image
5.8 Move cradle to input field positions listed in the table below and repeat step 8.6.6 for each field position. Note the approximate pixel position of the spot center as the detailed analysis will be done later.
5.9 LW channel distortion map determination
5.9.1 Change Monochromator setting to 157 nm
5.9.2 Characterize incoming beam
5.10 Set up ICP to collect 256x256 pixel images
5.11 Verify that turret is at nominal 0 degrees position
5.12 Verify that cradle is set to normal incidence 0 degrees
5.13 Send command: **IOP_FUV_DUMP_ENG_IMG** (enter **TDI ID = 1** for B) to capture and readout image to take an integrated picture of 100 frames of 120 msec exposure time and save on SDL PC with appropriate header information about time, number of frames, cradle position, wavelength, channel,
5.14 Verify appearance of a spot in the LW channel located at approximately the center of the image
5.15 Move cradle to input field positions listed in the table below and repeat step 8.7.6 for each field position. Note the approximate pixel position of the spot center as the detailed analysis will be done later
5.16 ITOS power down

4.2.10 Results of the pre-flight flatfield calibration

The report ICN-FUV-137-REP-Flatfield.pdf summarizes the results of ICON-FUV instrument flatfields obtained at different temperatures with diffuse illumination at SDL and with spot measurements at CSL. The prime objective is to confirm that we understand the relative response variation over different field angles in the field of view.

Flatfield measurements using a diffuse illumination of the camera systems were performed at SDL in October 2015 on FM1 (LW-channel) and in November 2016 on FM2 (SW-channel).

Distortion maps were measured on different dates and in different environments. The test dates and average temperatures were:

- 2016-01-25; cold gradient; 84 spots;
- 2016-01-26; hot balance; 95 spots;
- 2016-01-31; room temperature; 87 spots;
- 2016-02-02; cold balance; 83 spots;
- 2016-02-03; hot calibration; 83 spots;

The procedure ICN-FUV-077 was used for those tests even though additional points were measured when considered necessary.

The measurements at SDL were performed in TVAC environment with cold/hot operational and cold/hot performance conditions.

The tests at CSL were performed at room temperature and both hot and cold gradients. The turret was set to 0 degrees. The temperature readings at CSL are attached to the end of this report in its pdf-version.

Instrument parameters

The phosphor and MCP current and voltage monitor readings are attached to the end of this report in its pdf-version.

At SDL high voltages between 2000 and 2500 V were used for the MCP.

The SW-MCP voltage was fixed at 2450 V for all tests at CSL.

The LW-MCP voltage was set to 2250 V for the tests up to February 1, 2016. After 2016-02-01/10:00:00 UT the MCP high voltage was set to 2300 V. All test results in this report will be scaled to the 2300 V setting.

Fit of positions

Pixel positions and angle settings were fitted to a 28-parameters function of polynomials. This is potentially an overkill but as there are at least twice as many measured spot positions than unknowns the mathematical mpfit IDL-package was capable of fitting the final result with very small errors. The fitting was based on the spot positions and parameters that were already obtained for the distortion fitting. Because the total counts in each spot depend on the incoming photon flux the counts were first corrected before the fitting using

Corrected_counts = counts / (source_meter_reading/1.E15)

. The general format of the fitted function is:

```
Zmod = p[0] + $
   p[1]*x + $
   p[2]*y + $
   p[3]*(x*y) + $
   p[4]*(x*x) + $
   p[5]*(y*y) + $
   p[6]*(x*x*x) + $
   p[7]*(x*x*y) + $
   p[8]*(x*y*y) + $
   p[9]*(y*y*y) + $
   p[10]*(x*x*x*x) + $
   p[11]*(x*x*x*y) + $
   p[12]*(x*x*y*y) + $
   p[13]*(x*y*y*y) + $
   p[14]*(y*y*y*y) + $
   p[15]*(x*x*x*x*x) + $
   p[16]*(x*x*x*x*y) + $
   p[17]*(x*x*x*y*y) + $
   p[18]*(x*x*y*y*y) + $
   p[19]*(x*y*y*y*y) + $
   p[20]*(y*y*y*y*y) + $
   p[21]*(x*x*x*x*x*x) + $
   p[22]*(x*x*x*x*x*y) + $
   p[23]*(x*x*x*x*y*y) + $
   p[24]*(x*x*x*y*y*y) + $
   p[25]*(x*x*y*y*y*y) + $
   p[26]*(x*y*y*y*y*y) + $
   p[27]*(y*y*y*y*y*y)
```

SW channel flatfield as measured at SDL

Examples of the flatfields as measured at SDL are given in the following figures. There the whole camera detector could be stimulated by the diffuse UV illumination. Because different flux levels were used for different MCP high voltages the absolute levels cannot be compared to each other. But the relative variations in horizontal and vertical directions are very similar except for the very lowest voltage of 2100V. The figures show the relative sensitivity variation from 0.5 to 1.5 with 1.0 for the average over the sensitive area of the detector. The variations for the different tested temperatures are small enough that they do not show up in any recognizable way.

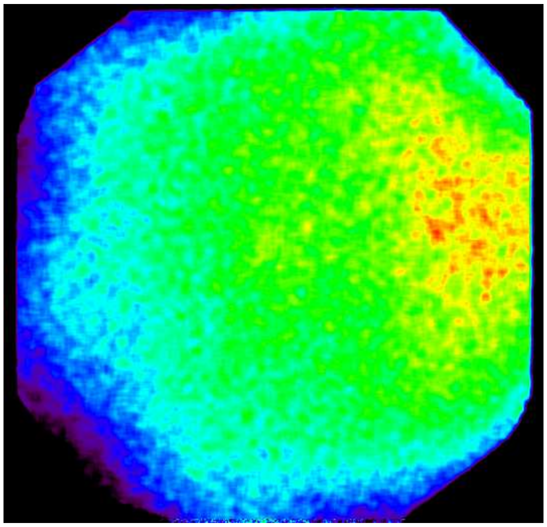

Fig 4.28: FM2 Cold operational at 2500 V MCP voltage

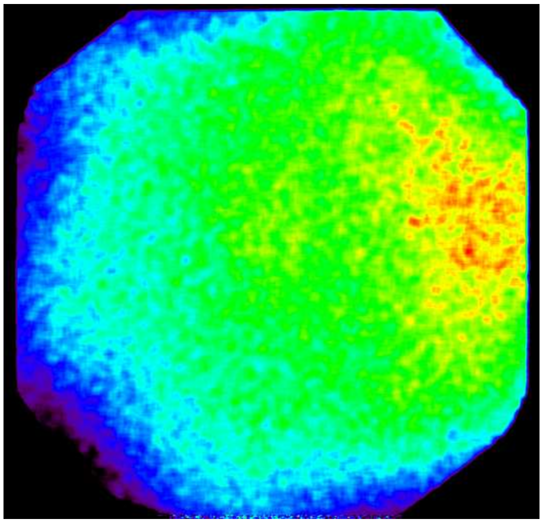

Fig 4.29: FM2 Cold performance at 2500 V MCP voltage

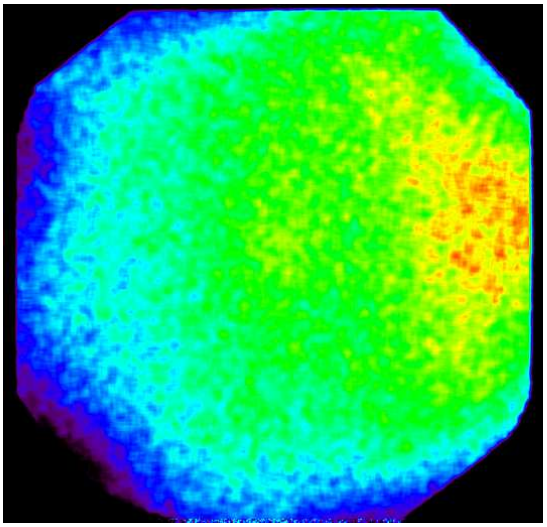

Fig 4.30: FM2 Hot operational at 2500 V MCP voltage

SW channel flatfield as determined from spot measurements at CSL

The results of the SW-channel measurements are given at the end of the distortion report ICN-FUV-136-REP-Distortion report in the format of tables with the input angles, measured spot positions, calculated angles from fits, calculated spot positions from fits, and errors between input and fitted values and will not be repeated here. Only those spots were used for the fits where the total counts in the spot exceeded 100,000 counts in SW and 50,000 counts in LW so that measurements outside of the valid detector area (outside of FoV) did not disturb the fitting. Note, that the image sizes are [536x515] pixels. The fit-parameters for the individual measurement series are given in the tables at the end of the document.

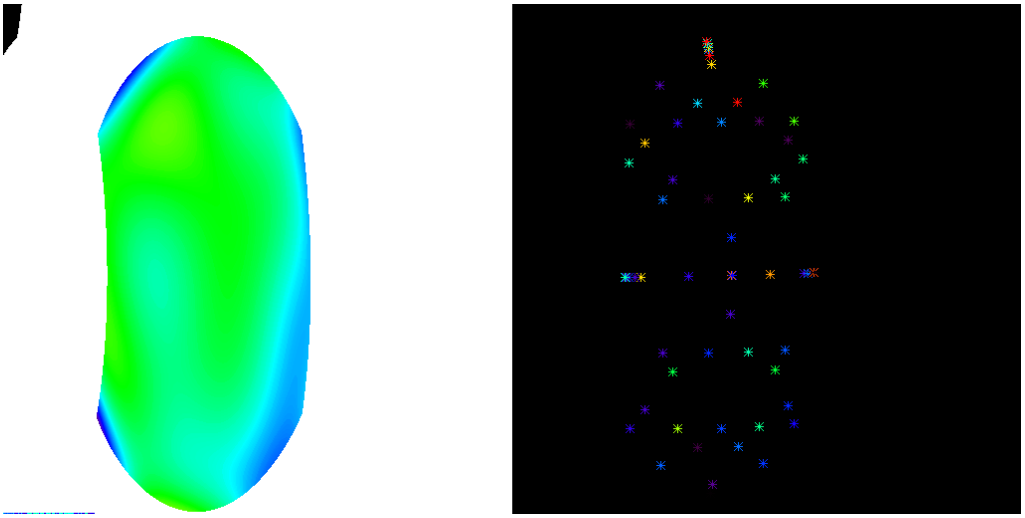

Fig 4.31: left: SW relative flatfield between 0.5 and 1.5 (Green is 1.0) for the cold gradient measurements on 2016-01-25; right: relative error between measured and fitted values at the locations of spot measurements. Blue is less than 2% difference, green is around 5%, and red is around 8% difference

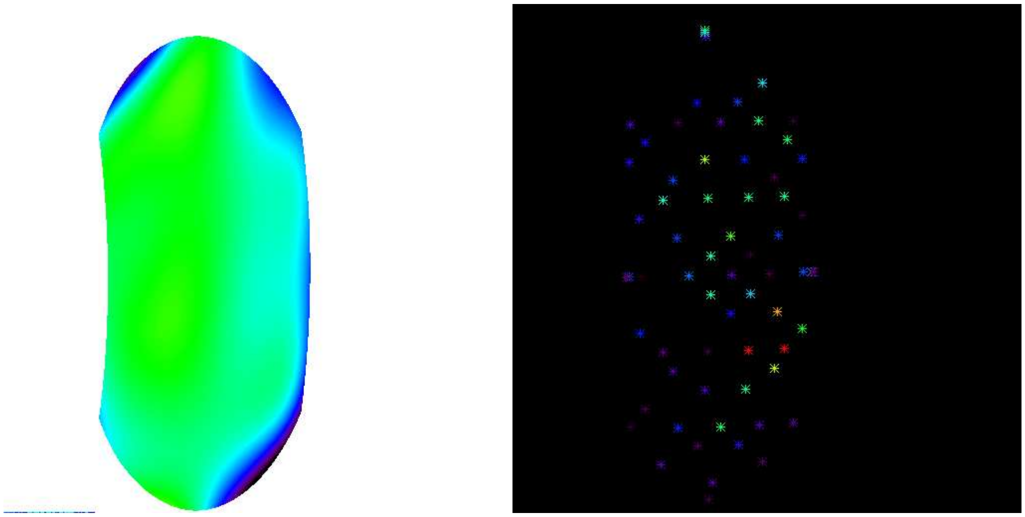

Fig 4:32: SW relative flatfield as determined for hot balance on 2016-01-26

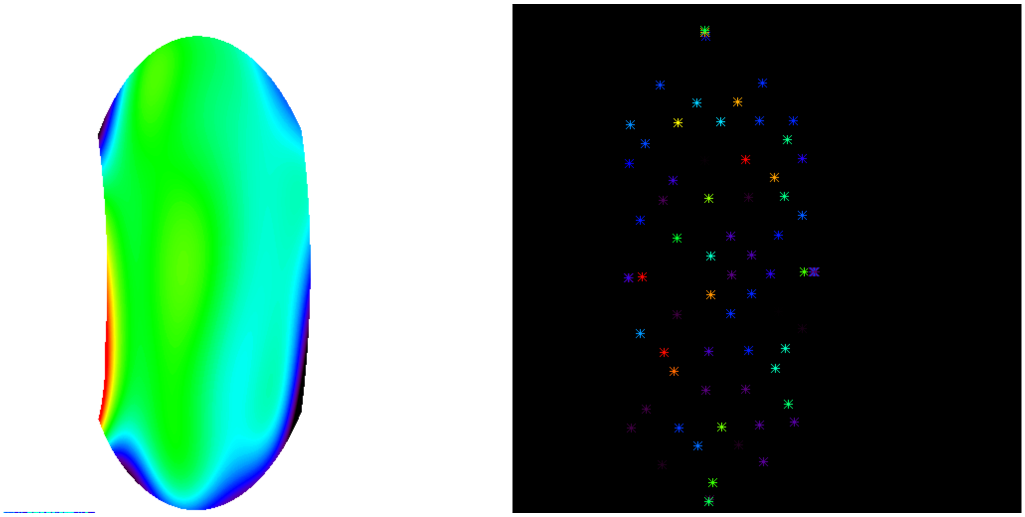

Fig 4.33: SW relative flatfield as determined for room temperature on 2016-01-31

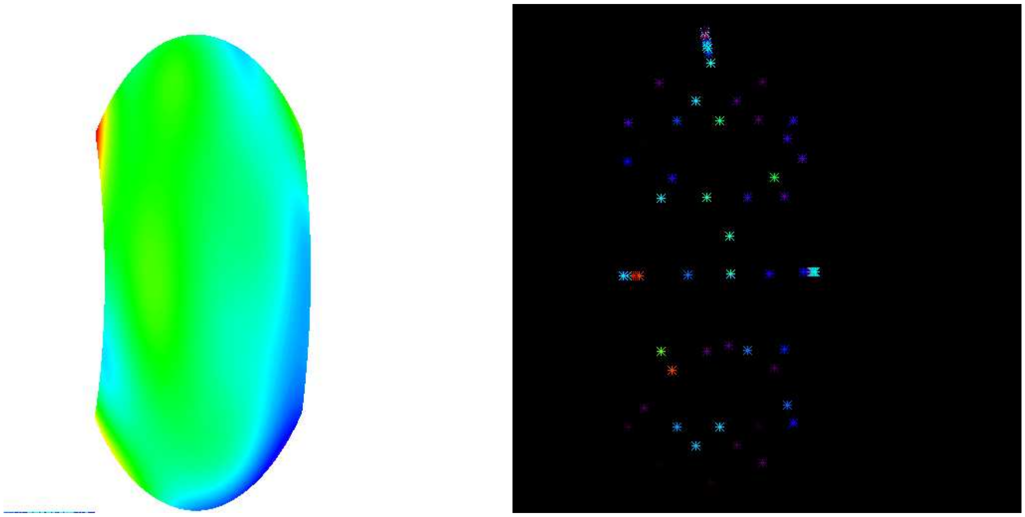

Fig 4.34: SW relative flatfield as determined for cold balance on 2016-02-02

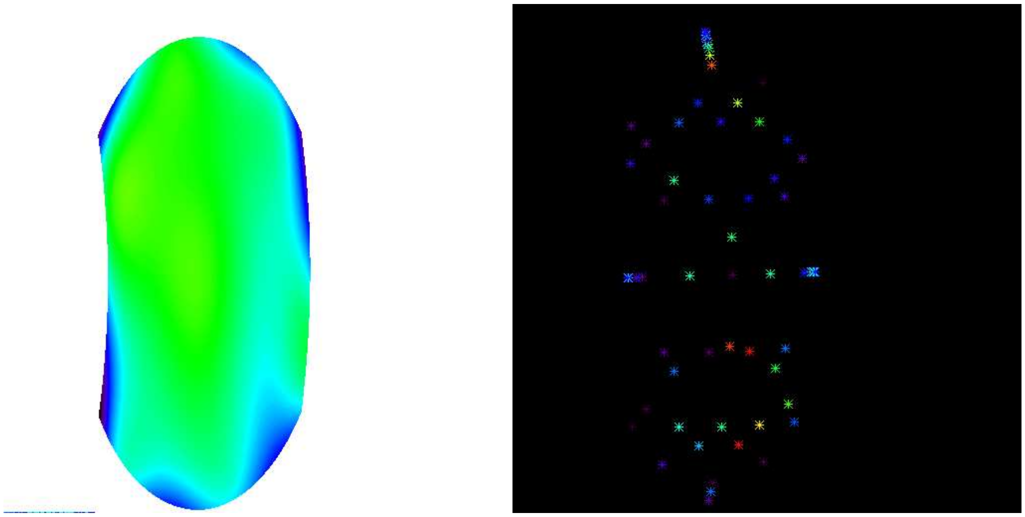

Fig 4.35: SW relative flatfield as determined for hot calibration on 2016-02-03

LW channel flatfields as determined from spot measurements at CSL

The results of the SW-channel measurements are given at the end of the distortion report ICN-FUV-136-REP-Distortion report in the format of tables with the input angles, measured spot positions, calculated angles from fits, calculated spot positions from fits, and errors between input and fitted values and will not be repeated here. Only those spots were used for the fits where the total counts in the spot exceeded 100,000 counts in SW and 50,000 counts in LW so that measurements outside of the valid detector area (outside of FoV) did not disturb the fitting. Note, that the image sizes are [536x515] pixels. The fit-parameters for the individual measurement series are given in the tables at the end of the document.

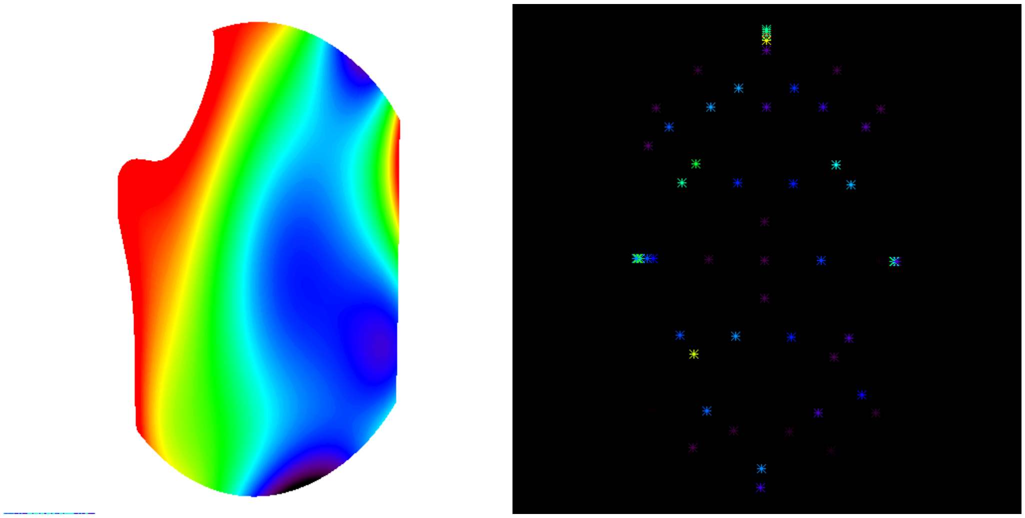

Fig 4.36: left: LW relative flatfield between 0.5 and 1.5 (Green is 1.0) for the cold gradient measurements on 2016-01-25; right: relative error between measured and fitted values at the locations of spot measurements. Blue is less than 2% difference, green is around 5%, and red is around 8% difference

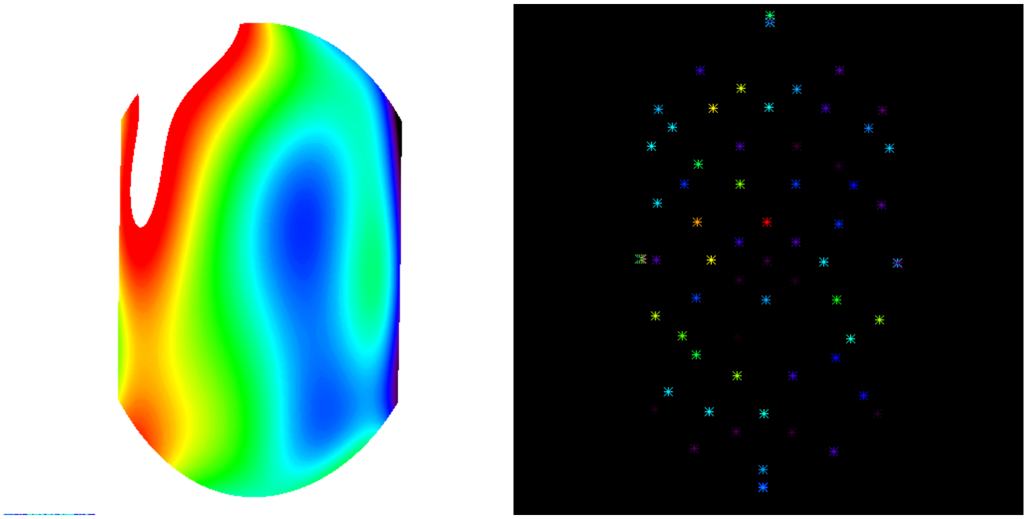

Fig 4.37: LW relative flatfield as determined for hot balance on 2016-01-26

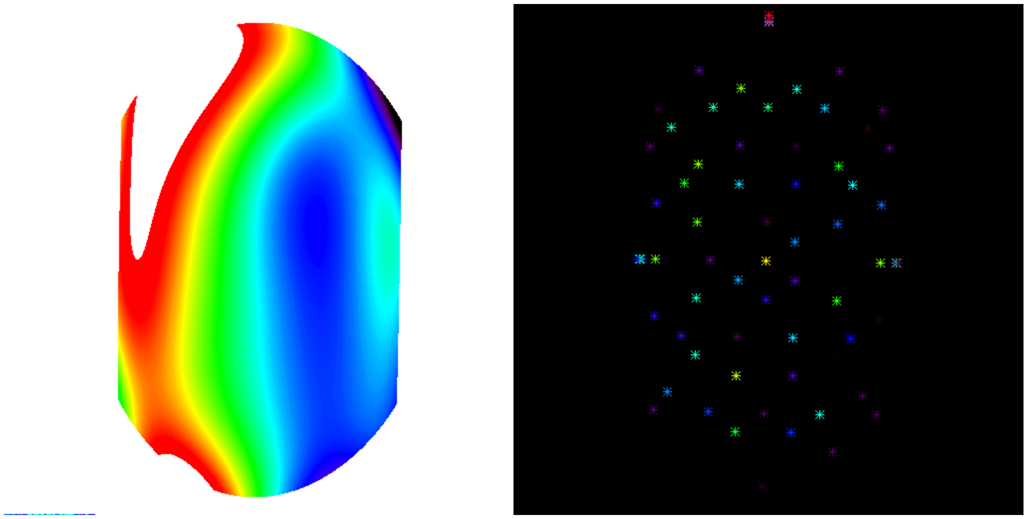

Fig 4.38: LW relative flatfield as determined for room temperature on 2016-01-31

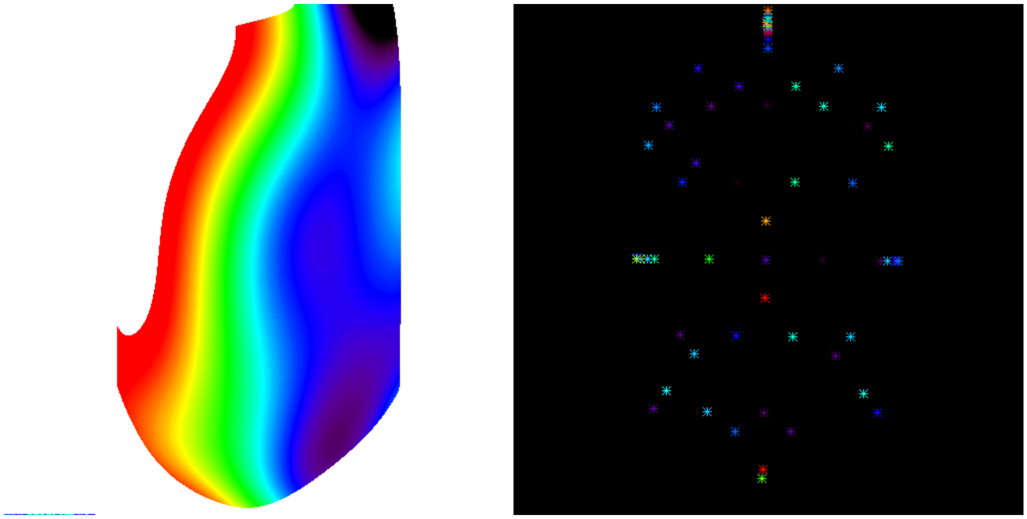

Fig 4.39: LW relative flatfield as determined for cold balance on 2016-02-02

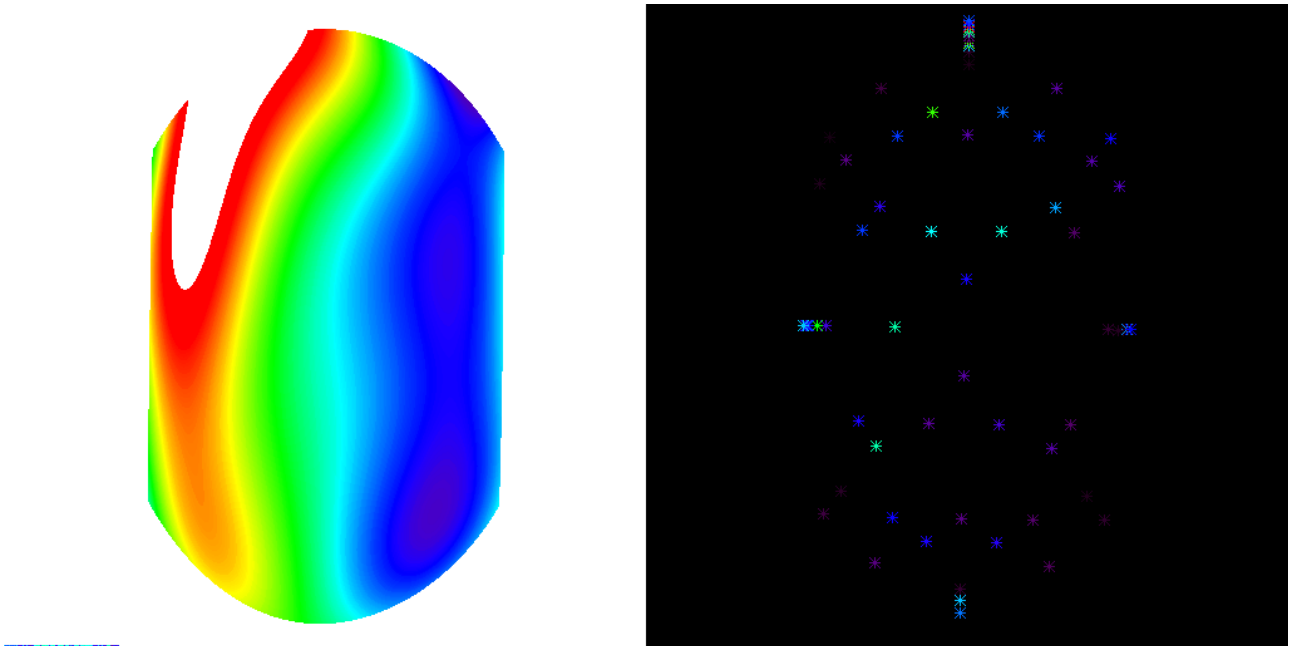

Fig 4.40: LW relative flatfield as determined for hot calibration on 2016-02-03

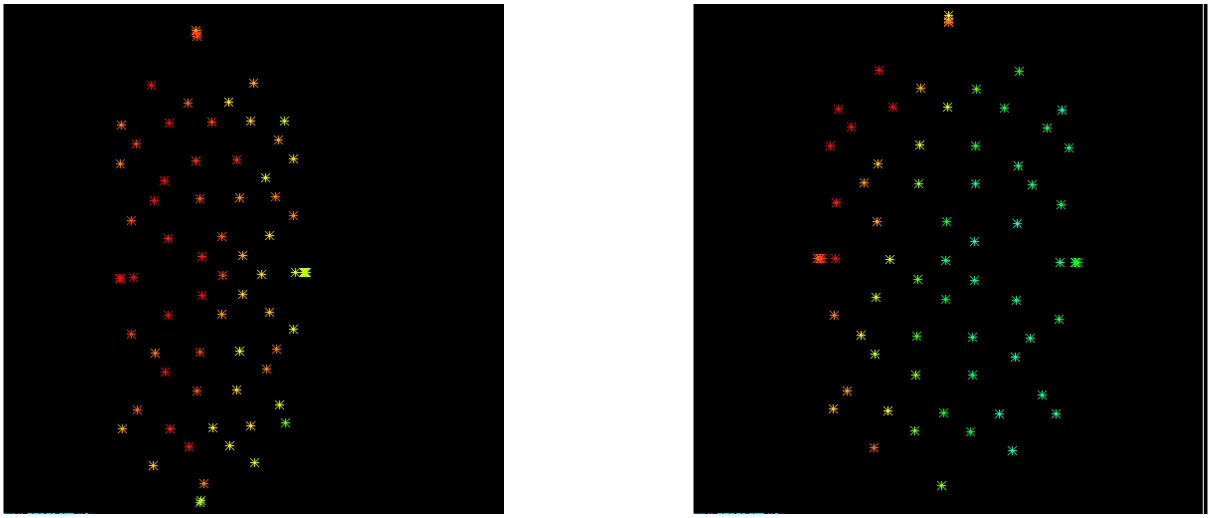

SW channel

LW channel

Fig 4.41: Relative variability of the flatfield in the SW (left) and LW (right) fields during the room temperature measurements. The spot colors are scaled to the maximum counts in any of the points in red, smaller values are given in yellow/green

The flatfields of the SW and LW channels behave slightly differently as the SW channel has a relatively large region in the left portion of the images with measured high total counts in the spots, while the LW channel has a relatively large region in the right portion of the images with medium total counts in the spots. That is also obvious in the figures in sections 8/9 and 10/11 where the SW channel appears more homogeneous and less variable compared to the LW channel. This is a slightly unexpected result (at least for me) and I need to find out why we see that behavior which was not so obvious from the simulations. This behavior is also visible in the vertical and horizontal relative flatfield profiles that are given below.

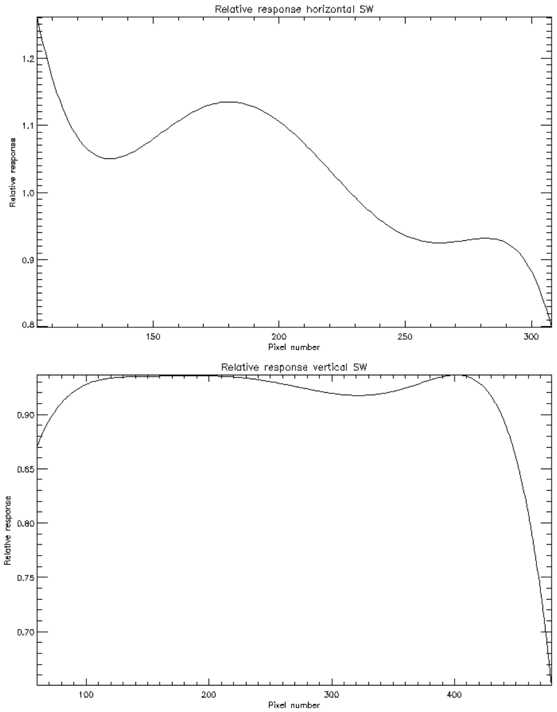

Fig 4.42: Profiles SW

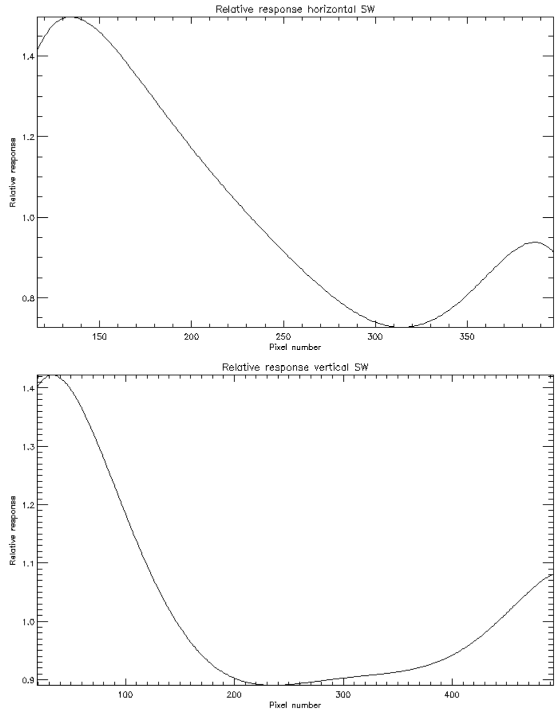

Fig 4.43: Profiles LW

4.2.11 Results of the pre-flight dark signal calibration

The results of these calibrations are summarized in the document ICN-FUV-141-REP-dark.pdf. The measurements at different temperatures (spectral band, distortion) were used to determine the dark signal in the areas surrounding the single bright spots in the images. The prime objective was to establish the dark signal for the subtraction before quantitative analysis of the real photon signal.

The tests were performed on several days in November/December 2015 and January/ February 2016. The test results from spot size, FOV, spectral band, and distortion measurements were used and not a specific single procedure was used for those different tests.

The tests were performed in the 6.5 m chamber at CSL. The high voltage of the MCP and phosphor should not have an effect on the dark signal which is generated by the dark current in the CCD. The dark current is due to thermal energy and created by the random generation of electrons and holes within the depletion region of photosensitive devices. The electron/hole pairs generate a relatively small electric current even when no photons hit the device. The dark current is temperature dependent. For a fixed temperature the dark current creates a constant offset, but because the charge generation has a Poisson distribution it also creates a randomly varying noise contribution in addition to a potential pixel-to-pixel variation of the noise background. For the quantitative analysis of measurements we want to determine the average dark signal at different temperatures.

The CCDs of the ICON FUV cameras are frame transfer devices FTT1010M from Dalsa. The way how frame transfer devices first transfer the integrated image quickly into the storage area and then read out the individual lines leads to a slight variation of the dark signal from the first readout line to the last one. Also the particular device has 1072x1030 total pixels (horizontal x vertical) with 1024x1024 active pixels. That leads to inactive pixels at the right and left side of the full image which is however not a problem for ICON FUV as we use only the central part of the image for our 18 degrees wide field of view. Figure 4.44 shows a representative dark image and the average dark counts in the horizontal and vertical directions in the final image. It is noticeable that the very last (top) vertical line contains on average many more counts (23,900 counts) compared to the prior lines that contain on average 21,500 counts.

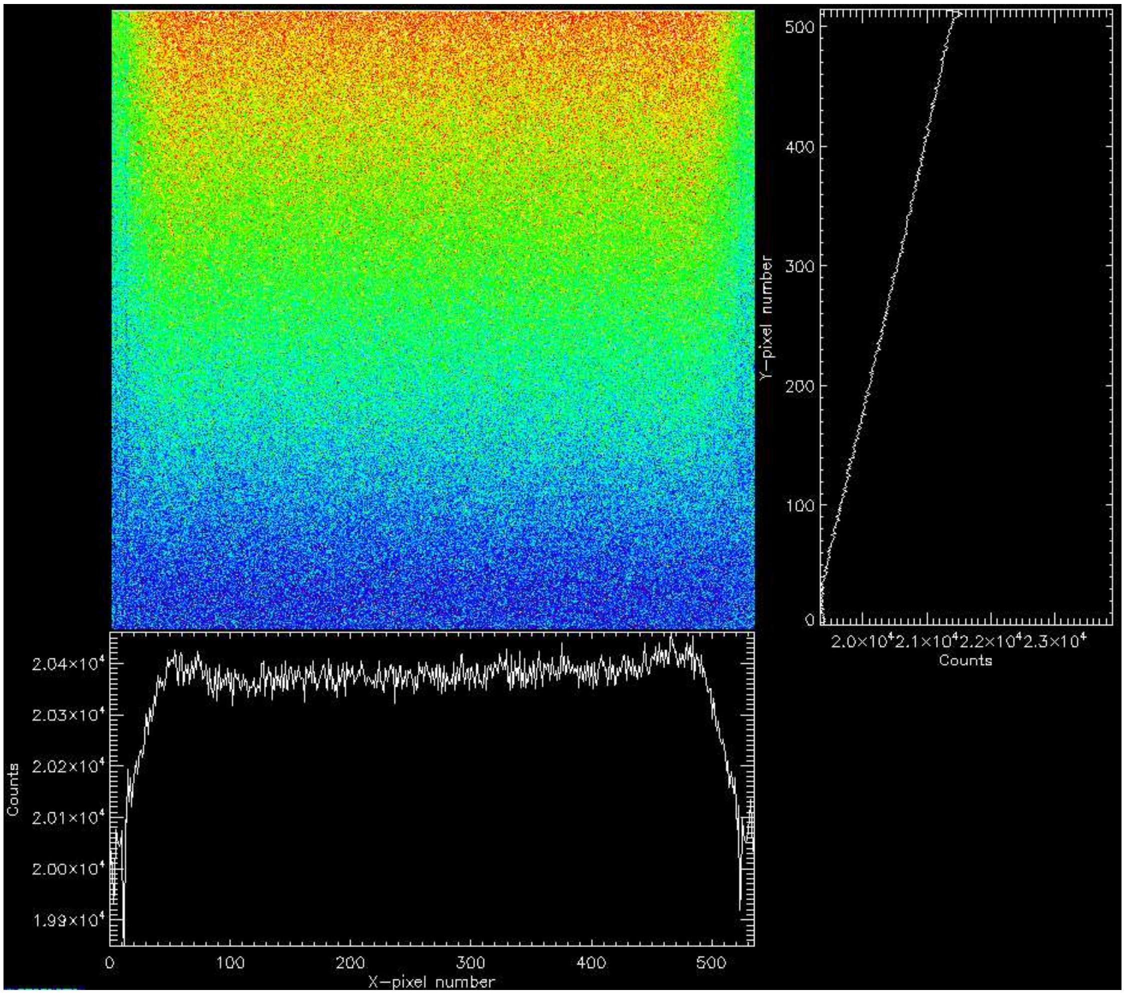

Fig 4.44: Representative dark image of the ICON FUV SW channel.

Figure 4.45 is an overview of all measurements and CCD temperatures that were used for this report. Two different levels of DAC offsets were used during these tests:

210/255 (high-DAC) resulting in medians around 20,000 counts (black symbols) for the SW channel and 22,000 counts (green symbols) for the LW channel and

201/255 (low-DAC) resulting in medians around 13,000 counts (red symbols) for the SW channel and 14,500 counts (blue symbols) for the LW channel

For details about the DAC settings we refer to the document ICN_ICD_003_FUV-ICD (whichever version is the latest).

We will separate the two DAC setting in the remainder of this document. During science operations we will use the 210/255 setting which has to be specifically commanded during instrument setup and can be checked with the iop_fuv_dump_cam_regs command.

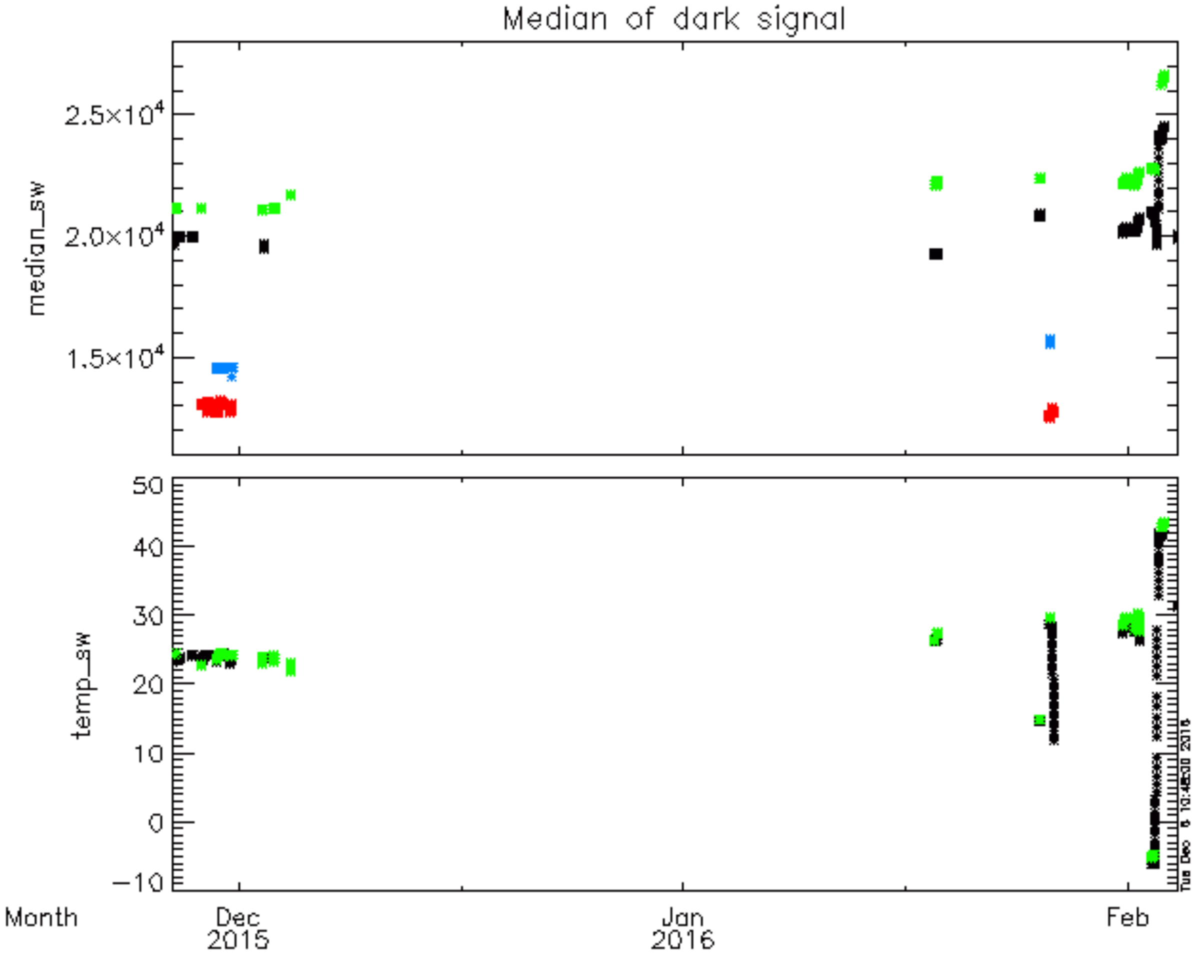

Fig 4.45: Summary of all measurements used for the dark signal determination. The horizontal axis is the date of the tests. The top plot shows the median values of the dark signal across the whole image (536x515 engineering images) for the two channels. Details about the colors are given in the text. The bottom plot shows the CCD temperatures at the time of the measurements, the black symbols for SW and the green symbols for LW.

During science operations on orbit the CCD temperature will be primarily determined by the heat that is created during normal operations and secondarily by the external temperature surrounding the cameras. The tests at CSL therefore never achieved measurements with CCD temperatures below -10 C but reached as high as +43C during the hot tests. A comparison of SW-CCD temperature and the measured median dark signal is shown in Figure 4.45. There is a clear trend to larger dark signal going from 20C to 43 C which is expected. There is also a small trend to higher dark signal for colder temperatures even though it appears to level out below 0C.

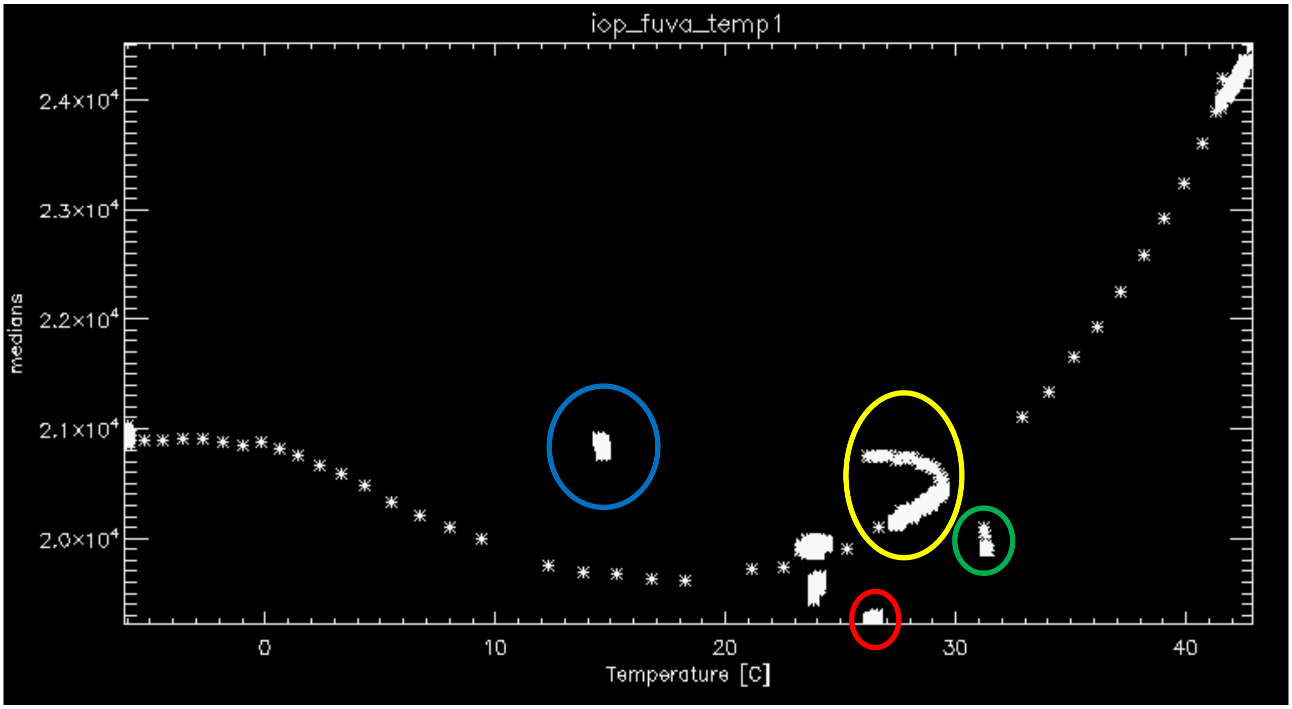

Fig 4.46: Comparison of the average dark signal for the high-DAC case and the SW-CCD temperature.

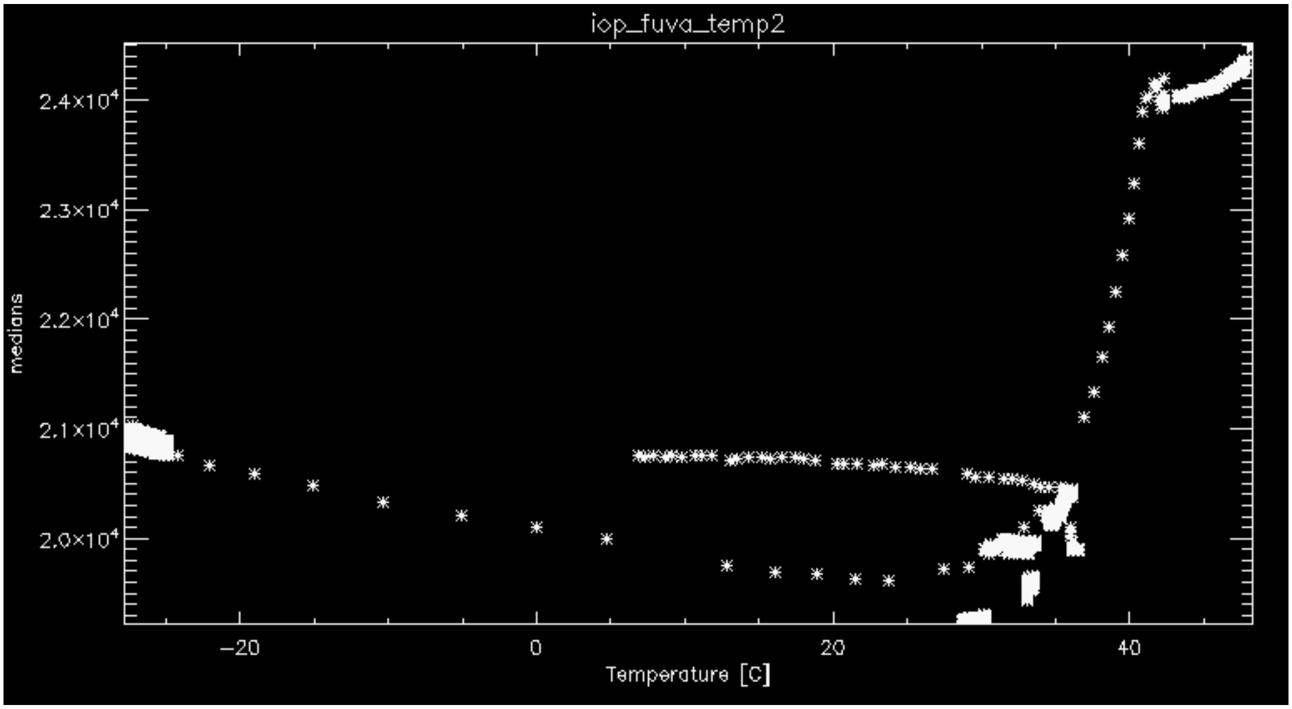

Fig 4.47: Comparison of the digital board temperature and the average dark signal for the high-DAC case of SW measurements

There are a few groups of measurements that deviate from the general trend and some of them are marked in Figure 4.46. All measurements marked by the blue circle were done during cold gradient testing on January 25, 2016. All measurements marked by the red circle were done on January 18 and hot balance on January 26. All measurements marked in green were done on February 2, 2016. All measurements marked in yellow were done on January 31 and February 1, 2016.

Similar trends of increasing dark signal with temperature and grouping of results for specific dates and test environments can be seen for the comparison between the dark signal and the digital board temperature (Figure 4.47). As the digital board is less isolated from the environment compared to the CCD chip temperature extremes below -25C and above +45C were encountered during the tests.

For comparison we show the relation between the instrument optics and the SW dark signal in Figure 4.48. But it is not expected that there is a real one-to-one relation between these two measurements, they only demonstrate the general trends and follow the driving by the external temperatures.

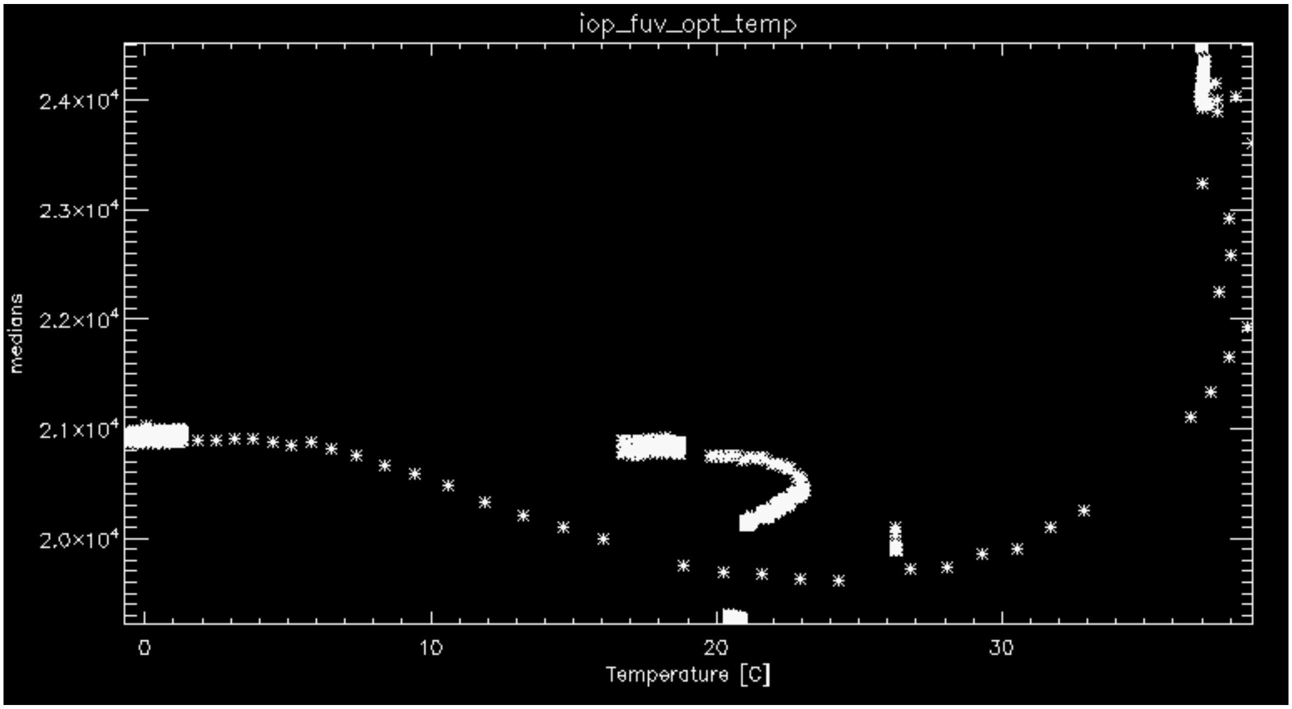

Fig 4.48: Comparison between the instrument optics temperature and the average dark signal for the high-DAC SW measurements.

There have been fewer measurements for the low-DAC case and they were performed over a much narrower temperature range (Figure 4.49). These limited measurements do not allow seeing the strong trends as in the high-DAC case, especially as the highest CCD temperature was only 29C when we still see a reasonably constant dark signal in the high-DAC case.

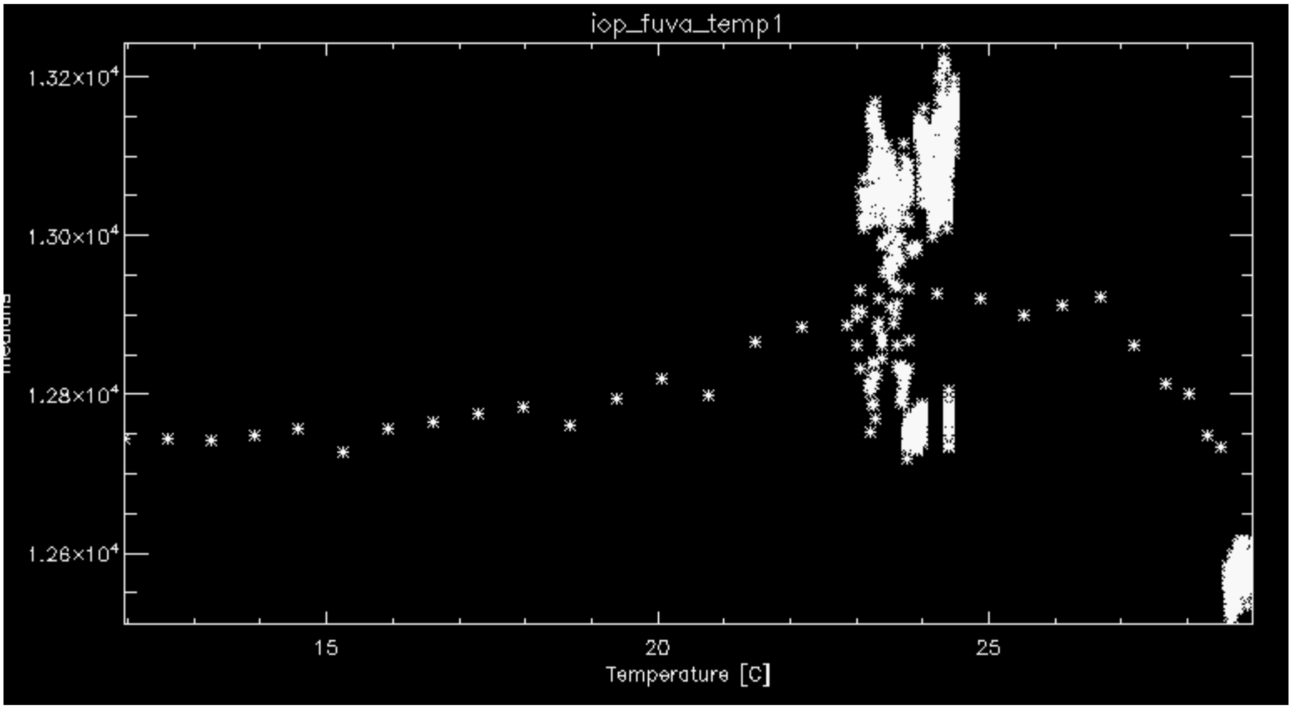

Fig 4.49: Comparison of CCD temperature and average dark signal for the low-DAC SW measurements.

Dark signal for the LW channel

The measurements for the LW channel were made mostly simultaneously with the SW measurements. We see a higher dark signal in LW compared to SW for the same test conditions (Figure 4.45). Besides the slightly higher count rates we can also recognize the same general trend of count rate changes comparing Figure 4.49 with the corresponding Figure 4.46 for the SW case.

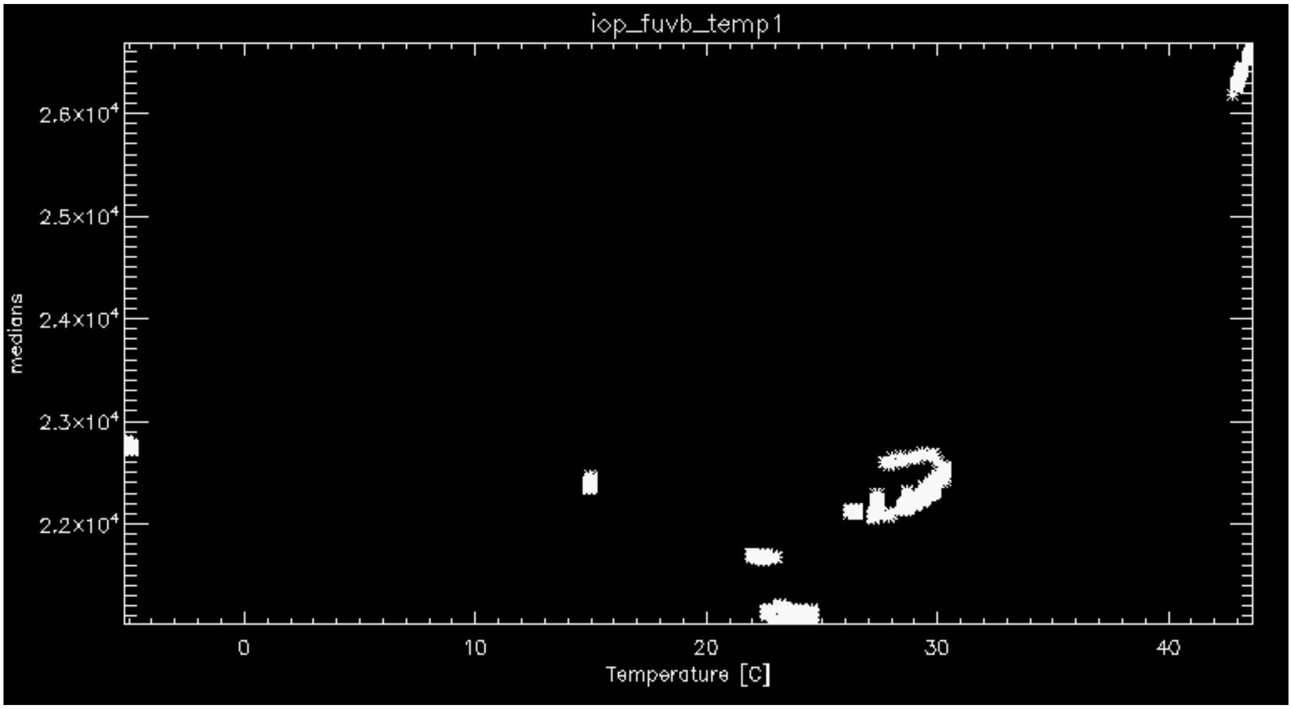

Fig 4.50: Comparison of CCD temperature and dark signal for the high-DAC LW case.

During the measurements we found a slight dependence of the average dark counts on the CCD temperature. One way of looking at this is to collapse the individual images horizontally and then plot the averaged profiles with an indication of the CCD temperature at the time of test. For the SW channel this is shown in Figure 4.50.

It is clear that the average dark signal does not proportionally shift up with increasing temperature, but the relative shape of the dark signal also changes. The profiles that were measured around room temperature are much shallower than the profiles measured at high temperatures which show a steeper increase from the bottom of the CCD to the top.

During science operation on orbit we need to monitor the CCD temperature and adjust the background subtraction for the different levels and profile shapes.

4.2.12 Results of the pre-flight pulse height calibration

The results of the pulse height measurements are summarized in the document ICN-FUV-142-Pulse-height.pdf. The prime objective was to confirm tests performed at SDL.

The pulse height distribution functions were determined by illuminating the FUV instrument with a low flux diffuse beam of UV photons and running the cameras in video mode with 120 ms integration times so that individual pulses could be recorded with very low dead times and very low probability of pile-up. The test dates and average temperatures were:

- 2016-02-02; cold balance;
- 2016-02-03; hot calibration;
- 2016-02-04; room temperature;

The procedure ICN-FUV-079 was used for those tests with HV settings changed by 50 V.

The measurements were performed at hot and room temperatures and cold balance always in the center of the image with 536x515 pixel setting for the camera readout.

The MCP voltage was varied in 50 V steps. 1000 individual images were recorded and they were evaluated in their original 536x515 pixel format and then also binned 2x2 and evaluated with the IDL diaphot function find.pro.

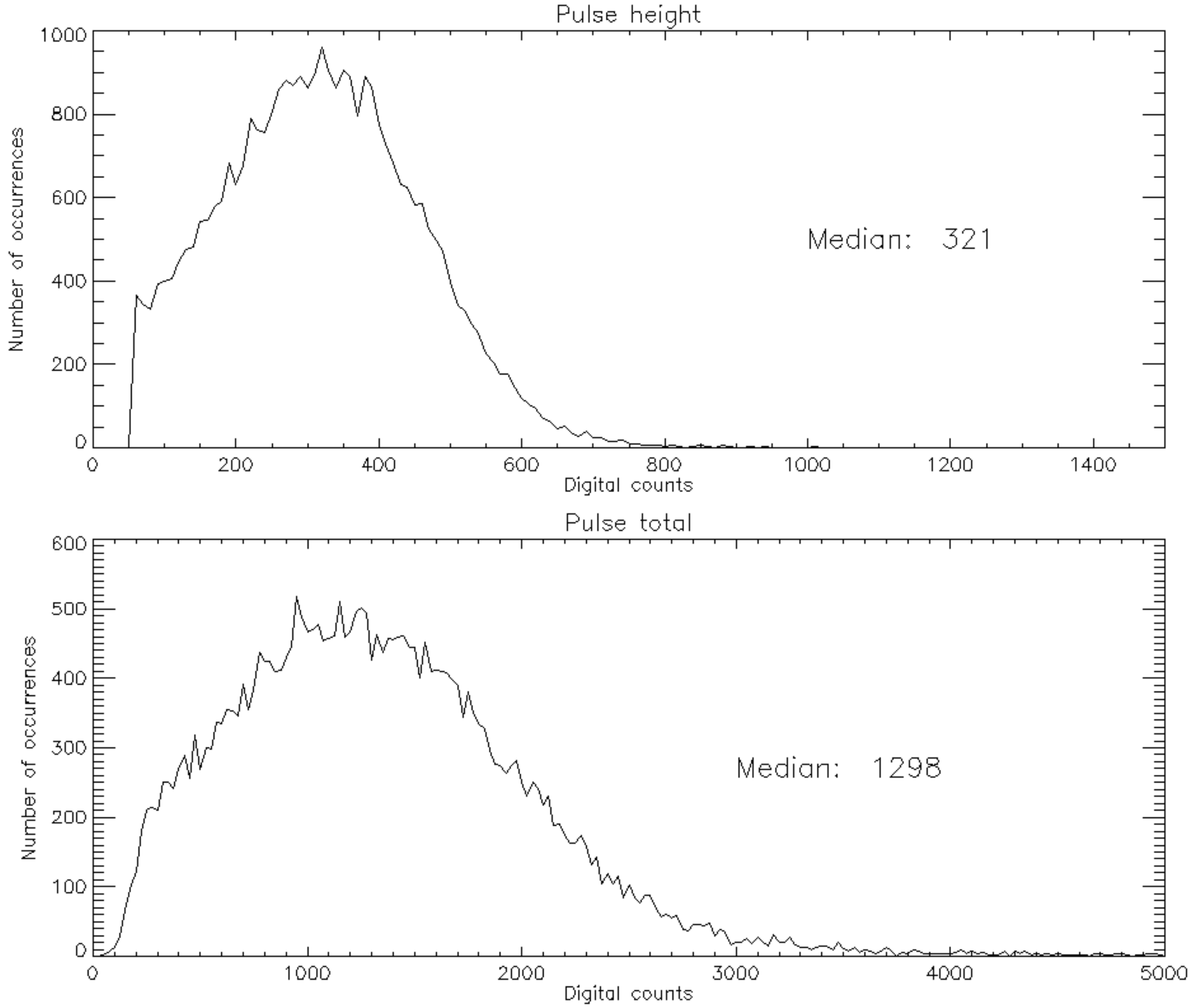

Fig 4.51: SW Pulse height distributions for file 01673 with MCP HV=2400 V

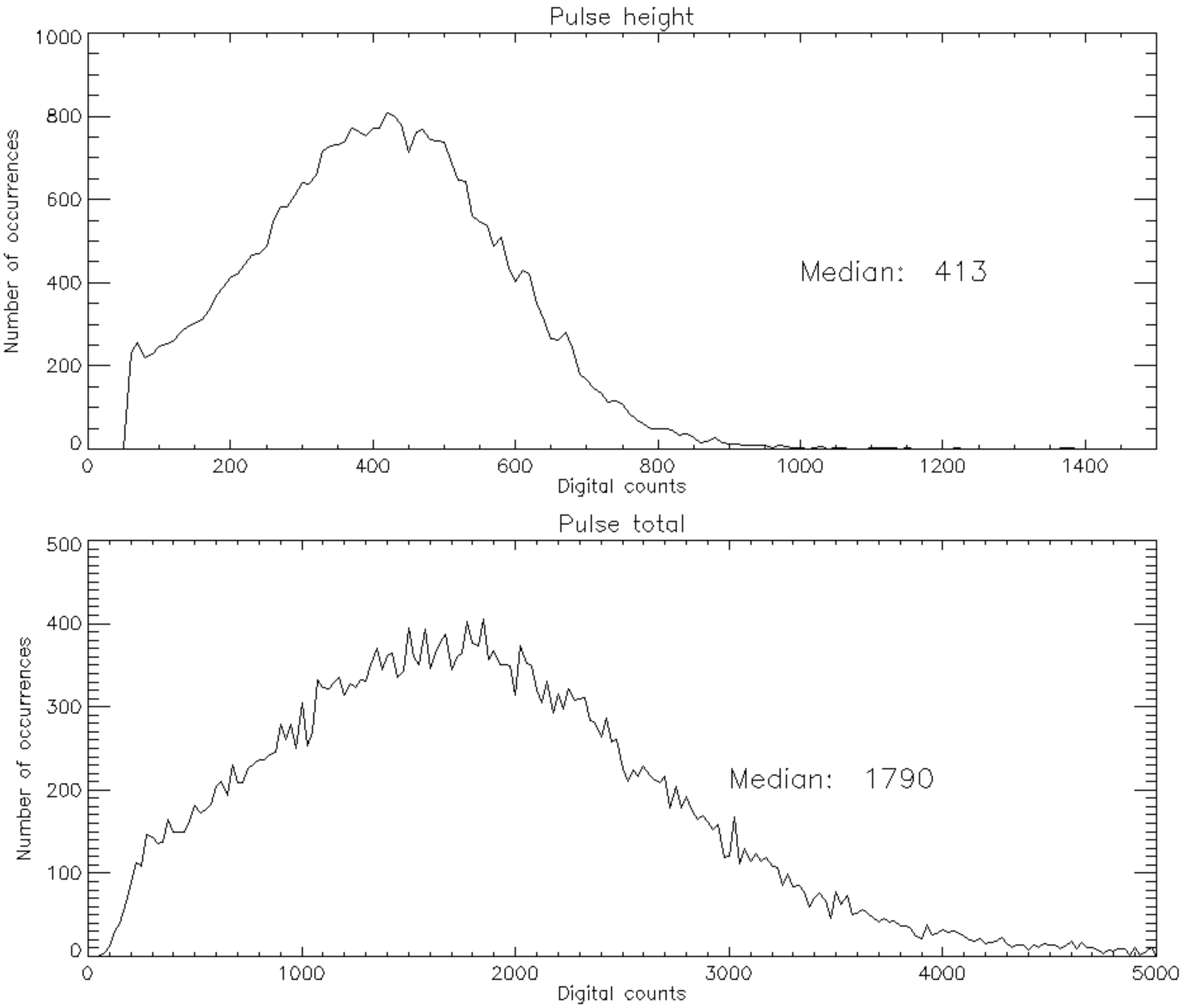

Fig 4.52: SW Pulse height distribution for file 01674 with MCP HV=2450 V

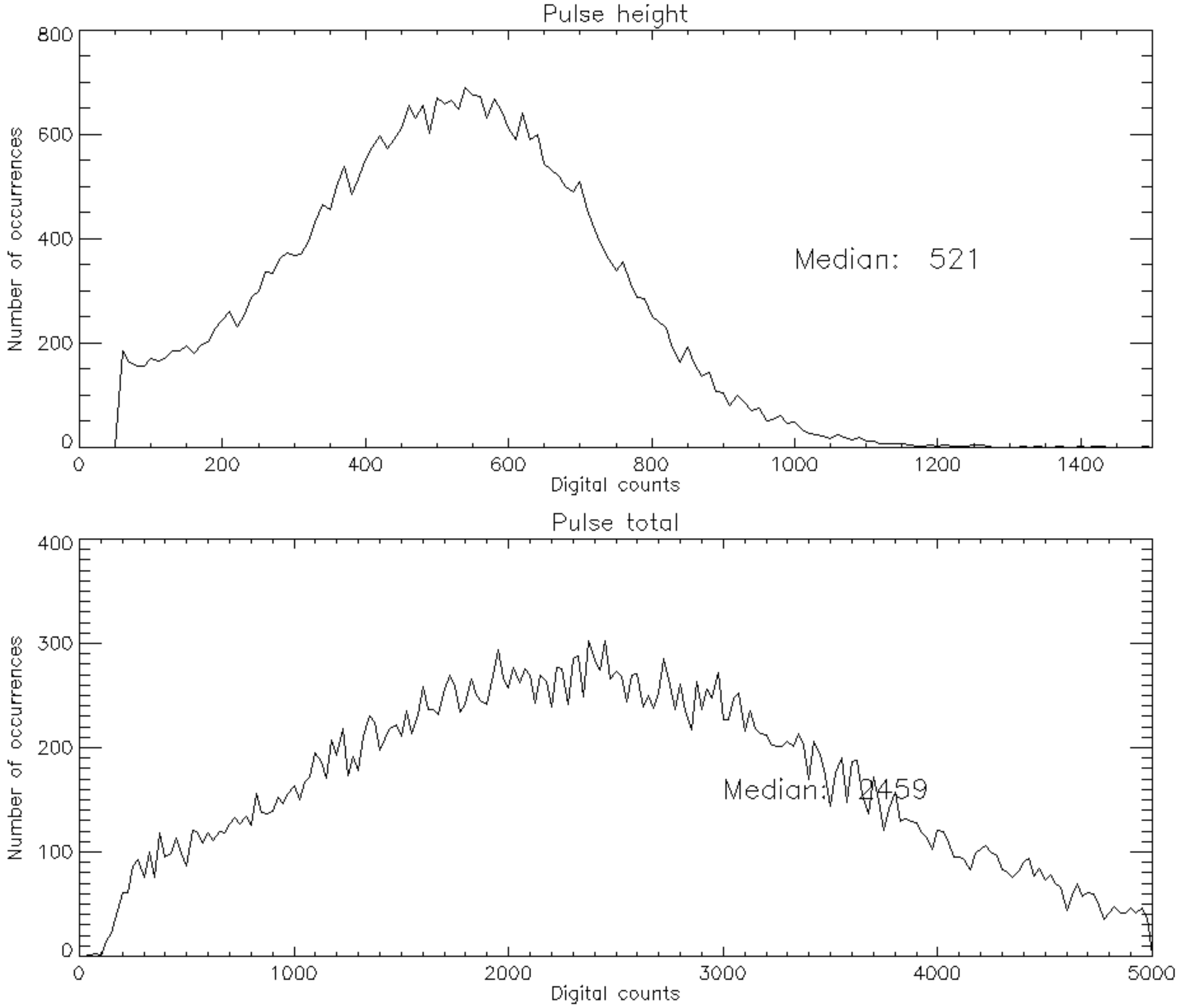

Fig 4.53: SW Pulse height distribution for file 01675 with MCP HV=2500 V

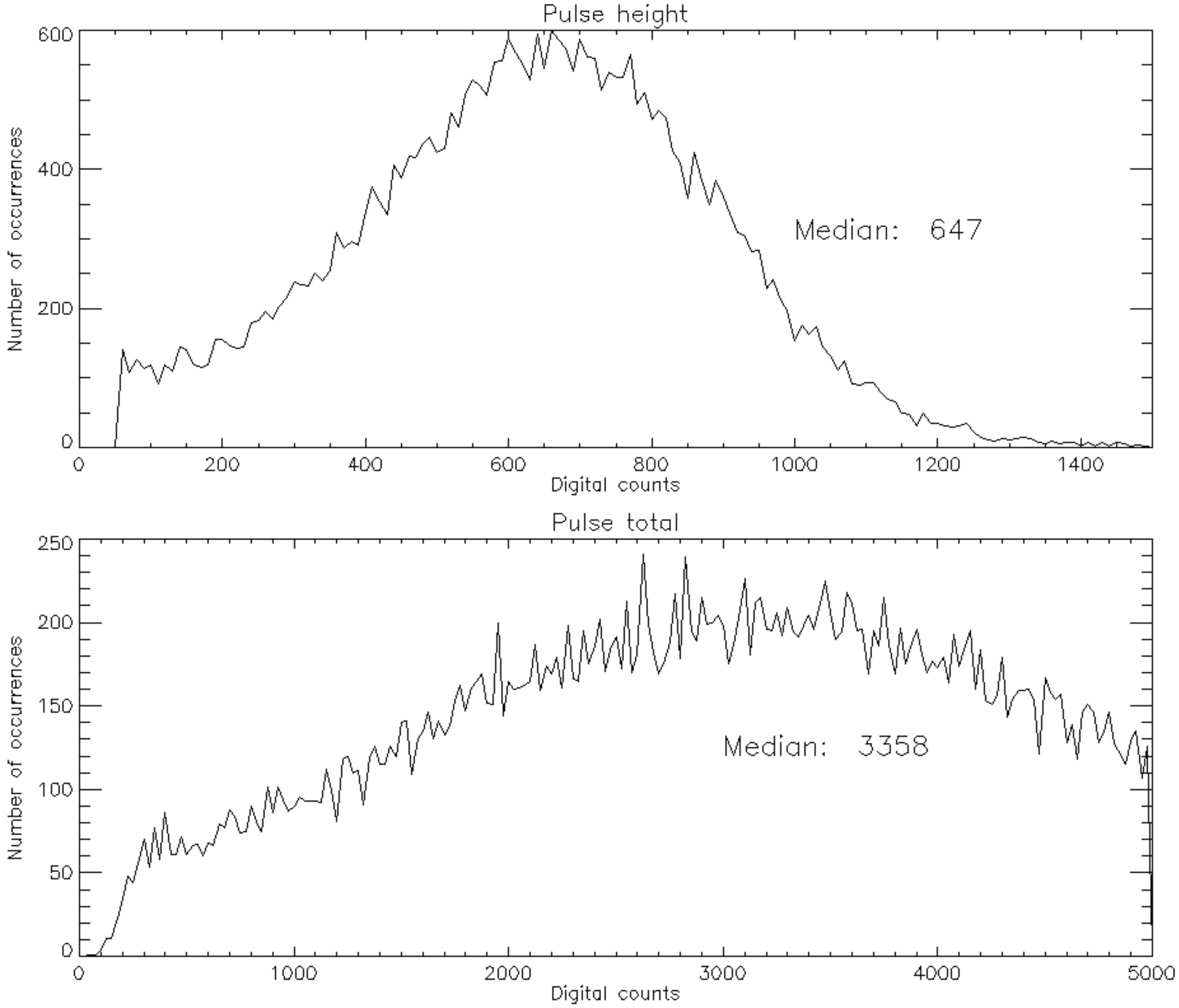

Fig 4.54: SW Pulse height distribution for file 01676 with MCP HV=2550 V

MCP HV SW	Date	File	PH mean 536x515	PH mean 268x257	Pulse total mean	Pulses
2400	2016-02-02	01673	325	547	1575	32832
2450	2016-02-02	01674	413	733	2155	34232
	2016-02-03	01909	370	684	1886	47251
	2016-02-04	01912	381	715	1973	37244
	2016-02-04	01913	379	714	1886	37188
	2016-02-04	01914	380	715	1917	37403
	2016-02-04	01915	379	713	1812	36903
	2016-02-04	01916	380	713	1839	36902
2500	2016-02-02	01675	518	970	2911	34993
	2016-02-03	01910	443	876	2384	51905
	2016-02-04	01917	469	924	2705	39680
2550	2016-02-02	01676	640	1268	3889	35360
	2016-02-03	01911	541	1127	3299	54168
	2016-02-04	01918	573	1200	3486	41574

Table 4.7: Pulse height results for the SW channel

Pulse height distribution LW channel

The same methods and procedures were used for the LW channel as for the SW channel.

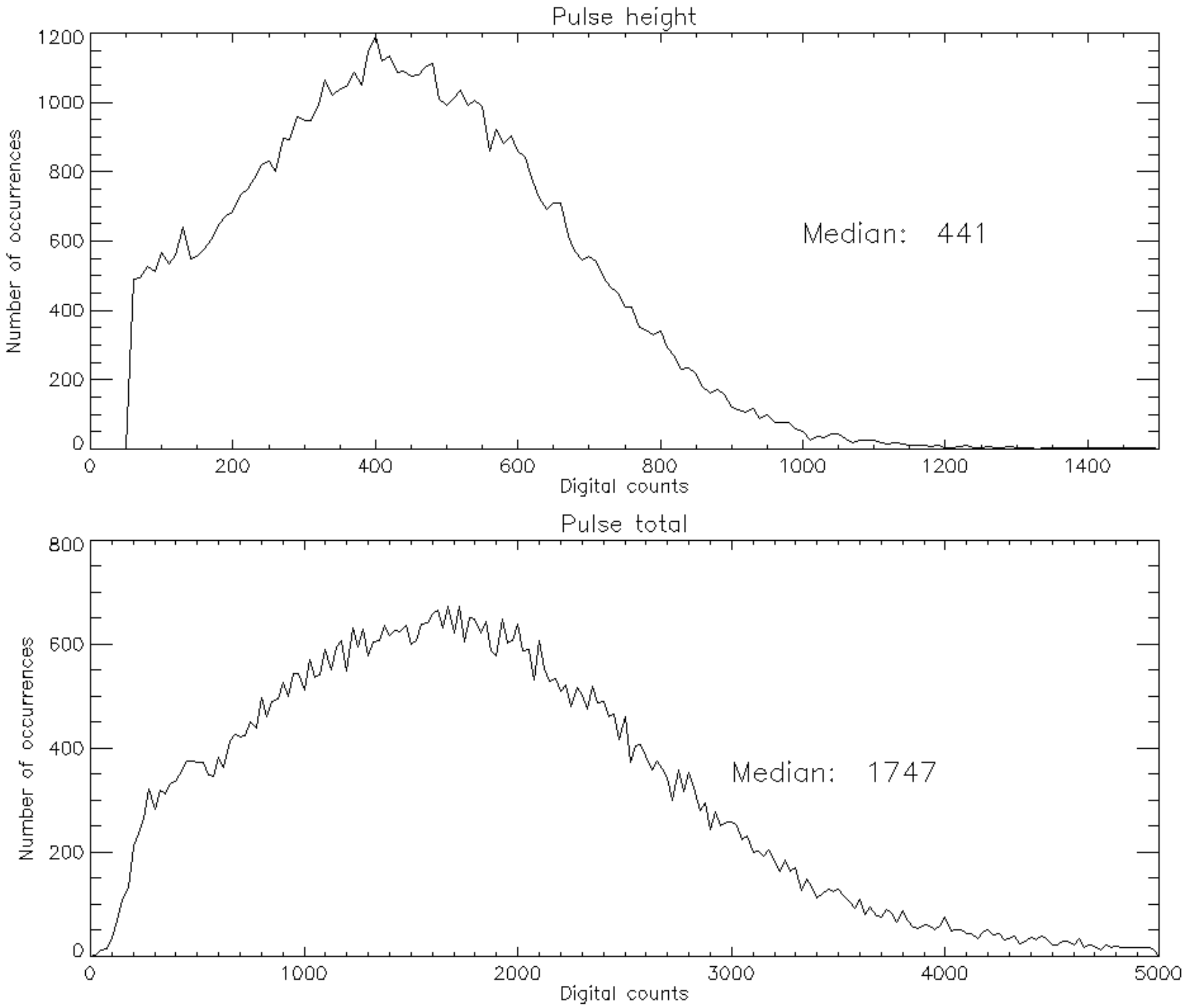

Fig 4.55: LW Pulse height distribution for file 01663 with MCP HV=2300 V

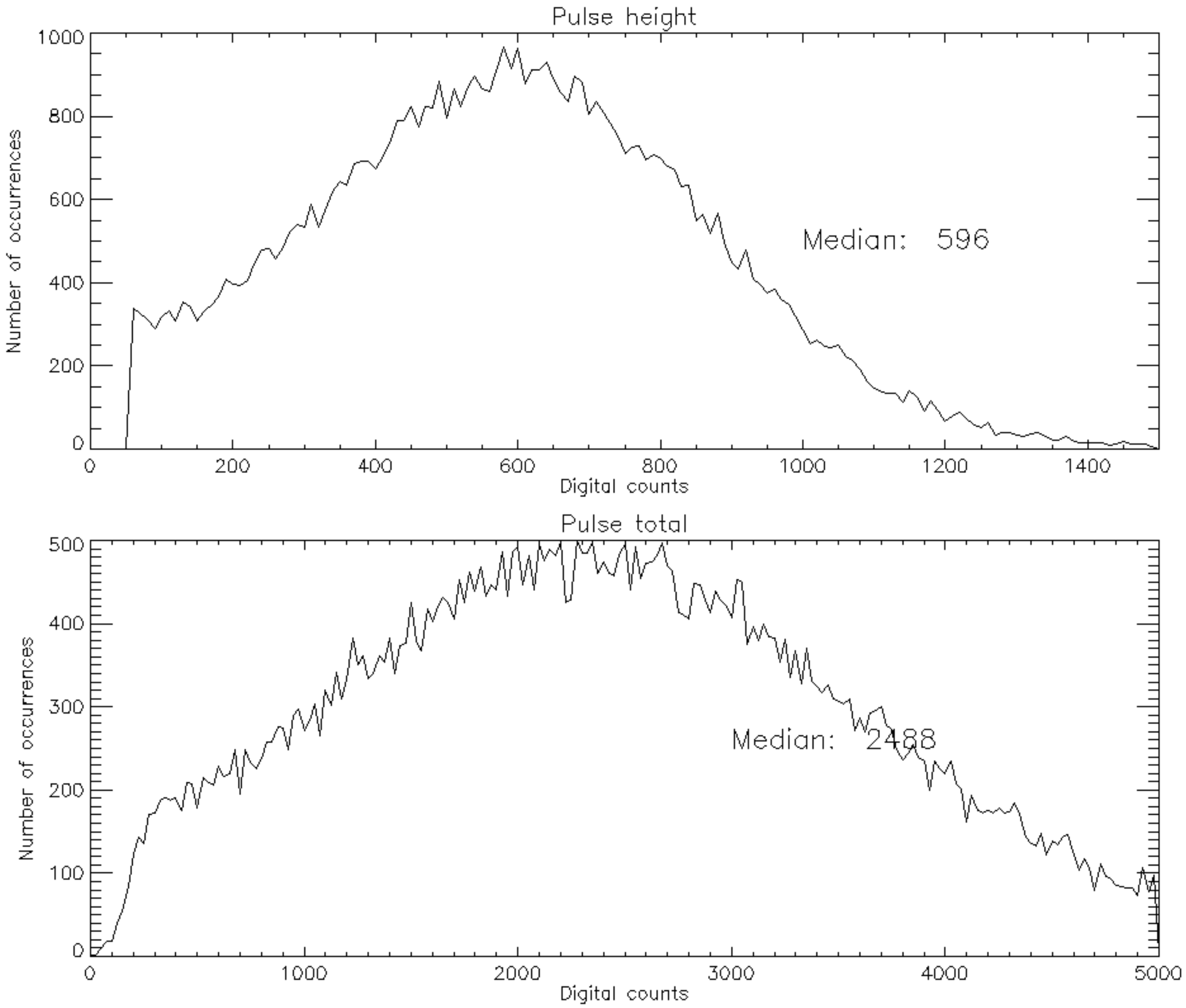

Fig 4.56: LW Pulse height distribution for file 01664 with MCP HV=2350 V

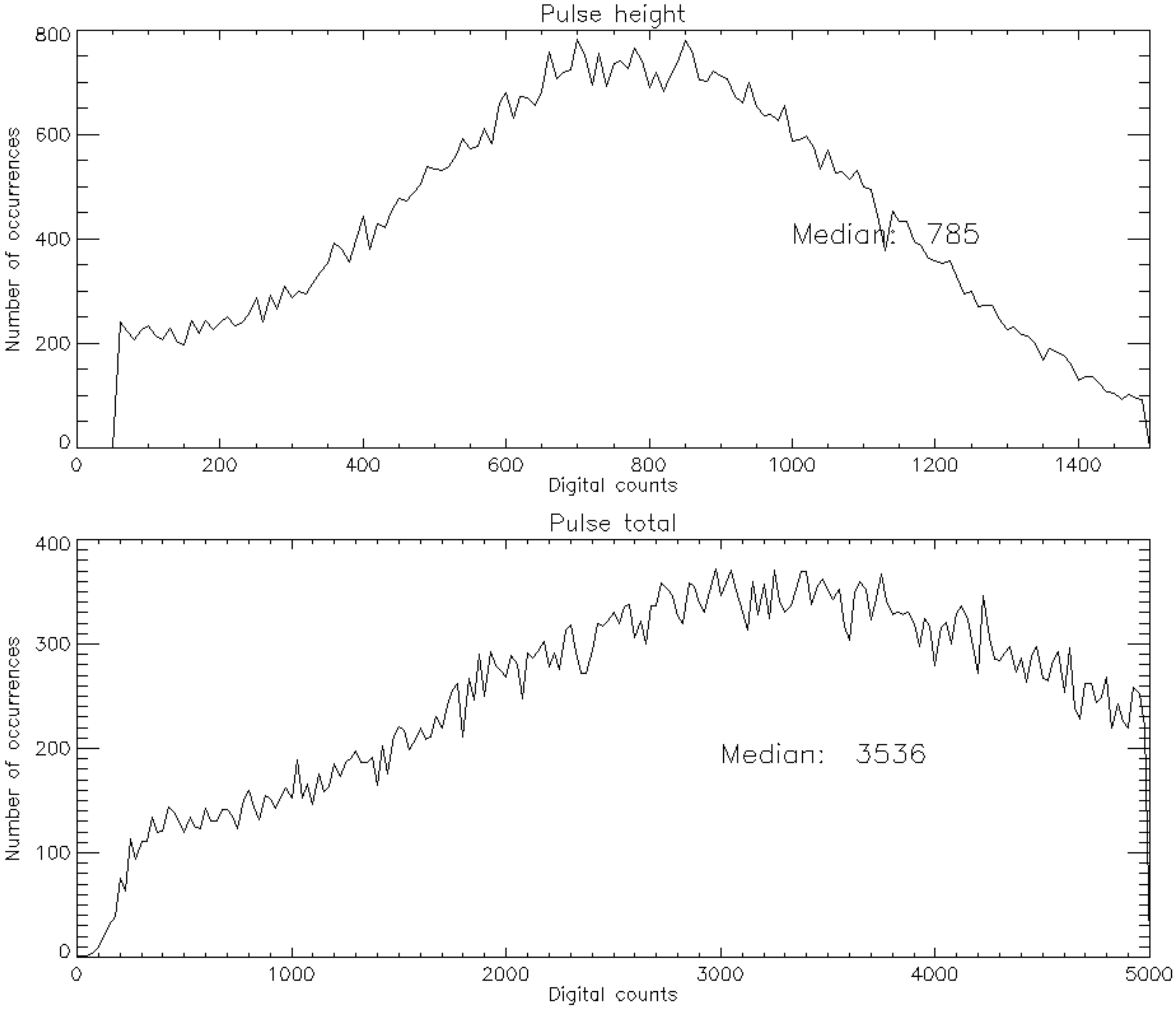

Fig 4.57: LW Pulse height distribution for file 01665 with MCP HV=2400 V

MCP HV LW	Date	File	PH mean 536x515	PH mean 268x257	Pulse total mean	Pulses
2250	2016-02-02	01661	332	574	1444	59487
2300	2016-02-02	01663	454	813	2126	62228
	2016-02-03	01834	424	738	1998	62490
	2016-02-04	01837	365	656	1576	31837
	2016-02-04	01841	362	648	1541	32223
	2016-02-04	01842	361	647	1527	32104
	2016-02-04	01843	361	644	1539	31831
	2016-02-04	01845	365	663	1546	31555
2350	2016-02-02	01664	603	1118	3036	63294
	2016-02-03	01835	531	979	2679	69568
	2016-02-04	01846	470	890	2096	33029
2400	2016-02-02	01665	793	1532	4284	65340
	2016-02-03	01836	675	1308	3479	72781
	2016-02-04	01847	626	1201	3026	33178

Table 4.8: Pulse height results for LW channel

Measurements on the same day under the same conditions (2016-02-04) show very small variability between different data sets. However the variation from day to day is quite large and should be attributed to the different instrument temperatures during the three test days. This will be verified with the SDL data that were taken with the bare cameras during thermal vacuum cycling.

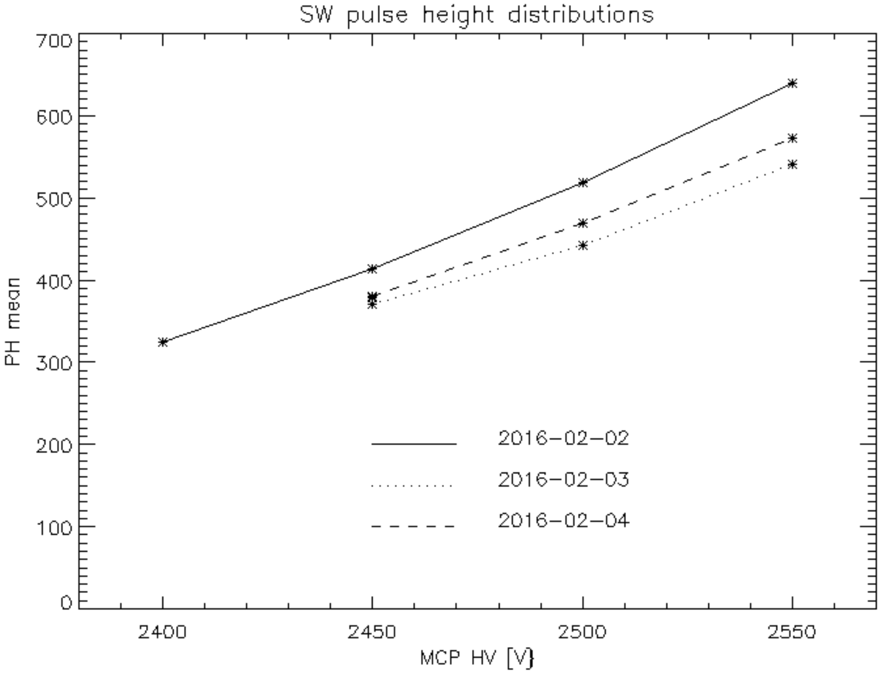

Fig 4.58: Pulse height distribution mean values with different SW MCP HVs

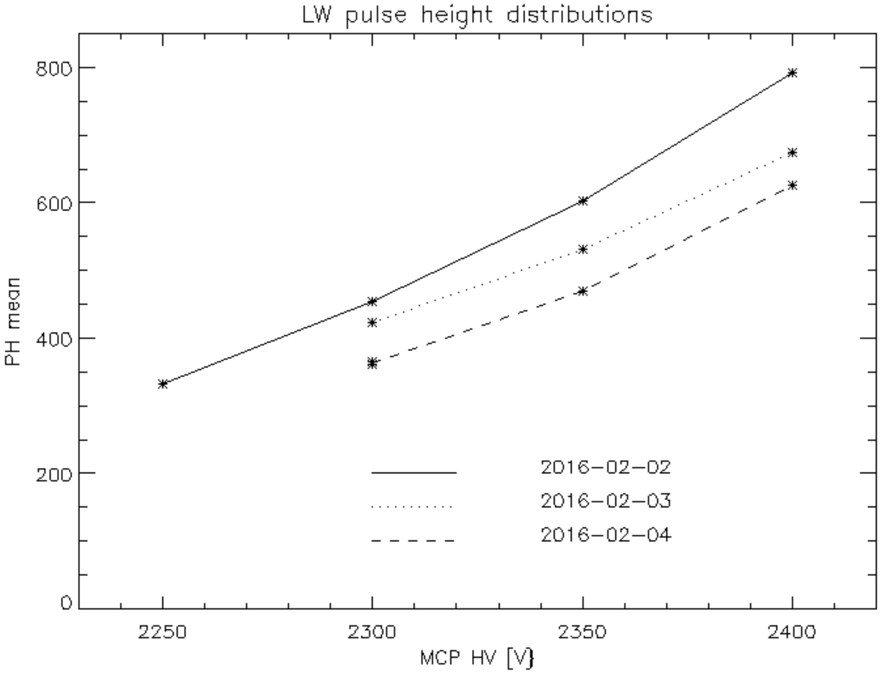

Fig 4.59: Pulse height distribution mean values with different SW MCP HVs

4.2.13 Plan for stray light Pre-flight Calibrations

The procedure for the pre-flight determination of stay light and response to unwanted photon wavelengths is written in the document ICN-FUV-081_stray-light.docx. This procedure was used at CSL in Belgium with FUV in the 6.5 m vacuum chamber. This procedure was run three times with light input at 120 nm, 180 nm, and in the visible between 400-700 nm wherever the light source provided the brightest signal.

4.10.1 FUV instrument installed in CSL vacuum chamber with door opened
4.10.2 Proper movability of cradle confirmed
4.10.3 Electric connection through feedthrough confirmed
4.10.4 Communication between ICP and FUV confirmed
4.10.5 Verify Proper FUV Test Configuration
4.10.6 Verify proper vacuum chamber pressure of <10^-3 Pa
4.10.7 Start UV source
4.10.8 Tune monochromator to 135.6 nm
4.10.9 Characterize incoming beam with CSL photodiode
4.10.10 Verify computer time is correct and note start time
4.10.11 Verify cover is open
4.11 Record instrument temperatures for the record
4.12 Instrument Payload Power On
4.13 Execute Section 8.9 in the FUV CPT (ICN-FUV-068) for ICP power on.
5.0 FUV Camera Power Control
5.1 Execute Section 8.10 of the FUV CPT (ICN-FUV-068) for the Camera Power Control.
6.0 FUV High Voltage (HV) On
6.1 Execute Section 8.13 in the FUV CPT (ICN-FUV-068) for FUV High Voltage setup.
7.0 SW and LW in-field stray light sensitivity at turret angle 0 degrees
7.1 Change Monochromator to 120 nm
7.2 Characterize incoming beam
7.3 Set up ICP to collect 256x256 pixel images
7.4 Verify that turret is at nominal 0 degrees position
7.5 Verify that cradle is set to normal incidence 0 degrees
7.6 Send command: **IOP_FUV_DUMP_ENG_IMG** (enter **TDI ID = 0** for A) to capture and readout image to take an integrated picture of 100 frames of 120 msec exposure time and save through ICP with appropriate header information about time, number of frames, cradle position, wavelength, channel,
7.7 Check if spot is recognizable in the SW channel at approximately the center of the image
7.8 Send command: **IOP_FUV_DUMP_ENG_IMG** (enter **TDI ID = 1** for B) to capture and readout image to take an integrated picture of 100 frames of 120 msec exposure time and save through ICP with appropriate header information about time, number of frames, cradle position, wavelength, channel,
7.9 Check if spot is recognizable in the LW channel at approximately the center of the image
7.10 Move cradle to input field positions listed in the table below and repeat steps 8.6.6-8.6.9 for each field position. Note total image counts and if a spot is recognizable at all.
7.11 SW and LW in-field stray light sensitivity at turret angle 0 degrees
7.11.1 Change Monochromator to 180 nm
7.11.2 Characterize incoming beam

7.11.3 Set up ICP to collect 256x256 pixel images
7.11.4 Verify that turret is at nominal 0 degrees position
7.11.5 Verify that cradle is set to normal incidence 0 degrees
7.11.6 Send command: **IOP_FUV_DUMP_ENG_IMG** (enter **TDI ID = 0** for A) to capture and readout image to take an integrated picture of 100 frames of 120 msec exposure time and save through ICP with appropriate header information about time, number of frames, cradle position, wavelength, channel,
7.11.7 Check if spot is recognizable in the SW channel at approximately the center of the image
7.11.8 Send command: **IOP_FUV_DUMP_ENG_IMG** (enter **TDI ID = 1** for B) to capture and readout image to take an integrated picture of 100 frames of 120 msec exposure time and save through ICP with appropriate header information about time, number of frames, cradle position, wavelength, channel,
7.11.9 Check if spot is recognizable in the LW channel at approximately the center of the image
7.12 Move cradle to input field positions listed in the table below and repeat steps 8.7.6-8.7.9 for each field position. Note total image counts and if a spot is recognizable at all.
7.13 SW and LW in-field stray light sensitivity at turret angle 0 degrees
7.13.1 Change Monochromator to ~400 nm
7.13.2 Characterize incoming beam
7.13.3 Set up ICP to collect 256x256 pixel images
7.13.4 Verify that turret is at nominal 0 degrees position
7.13.5 Verify that cradle is set to normal incidence 0 degrees
7.13.6 Send command: **IOP_FUV_DUMP_ENG_IMG** (enter **TDI ID = 0** for A) to capture and readout image to take an integrated picture of 100 frames of 120 msec exposure time and save through ICP with appropriate header information about time, number of frames, cradle position, wavelength, channel,
7.13.7 Check if spot is recognizable in the SW channel at approximately the center of the image
7.13.8 Send command: **IOP_FUV_DUMP_ENG_IMG** (enter **TDI ID = 1** for B) to capture and readout image to take an integrated picture of 100 frames of 120 msec exposure time and save through ICP with appropriate header information about time, number of frames, cradle position, wavelength, channel,
7.13.9 Check if spot is recognizable in the LW channel at approximately the center of the image
7.13.10 Move cradle to input field positions listed in the table below and repeat steps 8.8.6-8.8.9 for each field position. Note total image counts and if a spot is recognizable at all.
7.14 SW in-field stray light sensitivity at turret angle -30 degrees (LW will not be used)
7.14.1 Change Monochromator to 120 nm
7.14.2 Characterize incoming beam
7.14.3 Set up ICP to collect 256x256 pixel images
7.14.4 Move turret to -30 degrees position
7.14.5 Move cradle to compensate for turret angle
7.14.6 Send command: **IOP_FUV_DUMP_ENG_IMG** (enter **TDI ID = 0** for A) to capture and readout image to take an integrated picture of 100 frames of 120 msec exposure time and save through ICP with appropriate header information about time, number of frames, cradle position, wavelength, channel,
7.14.7 Check if spot is recognizable in the SW channel at approximately the center of the image
7.14.8 Move cradle to input field positions listed in the table below and repeat steps 8.9.6-8.9.7 for each field position. Note total image counts and if a spot is recognizable at all.

7.15 SW in-field stray light turret angle -30 degrees (LW will not be used)
7.15.1 Verify Monochromator is set to 180 nm
7.15.2 Characterize incoming beam
7.15.3 Set up ICP to collect 256x256 pixel images
7.15.4 Move turret to -30 degrees position
7.15.5 Move cradle to compensate for turret angle
7.15.6 Send command: **IOP_FUV_DUMP_ENG_IMG** (enter **TDI ID = 0** for A) to capture and readout image to take an integrated picture of 100 frames of 120 msec exposure time and save through ICP with appropriate header information about time, number of frames, cradle position, wavelength, channel,
7.15.7 Check if spot is recognizable in the SW channel at approximately the center of the image
7.15.8 Move cradle to input field positions listed in the table below and repeat steps 8.10.6-8.10.7 for each field position. Note total image counts and if a spot is recognizable at all.
7.16 SW in-field stray light turret angle -30 degrees (LW will not be used)
7.16.1 Verify Monochromator is set to ~400 nm
7.16.2 Characterize incoming beam
7.16.3 Set up ICP to collect 256x256 pixel images
7.16.4 Move turret to -30 degrees position
7.16.5 Move cradle to compensate for turret angle
7.16.6 Send command: **IOP_FUV_DUMP_ENG_IMG** (enter **TDI ID = 0** for A) to capture and readout image to take an integrated picture of 100 frames of 120 msec exposure time and save through ICP with appropriate header information about time, number of frames, cradle position, wavelength, channel,
7.16.7 Check if spot is recognizable in the SW channel at approximately the center of the image
7.16.8 Move cradle to input field positions listed in the table below and repeat steps 8.11.6-8.11.7 for each field position. Note total image counts and if a spot is recognizable at all.
7.17 SW in-field stray light sensitivity at turret angle +30 degrees (LW will not be used)
7.18 Change Monochromator to 120 nm
7.19 Characterize incoming beam
7.20 Set up ICP to collect 256x256 pixel images
7.21 Move turret to +30 degrees position
7.22 Move cradle to compensate for turret angle
7.23 Send command: **IOP_FUV_DUMP_ENG_IMG** (enter **TDI ID = 0** for A) to capture and readout image to take an integrated picture of 100 frames of 120 msec exposure time and save through ICP with appropriate header information about time, number of frames, cradle position, wavelength, channel,
7.24 Check if spot is recognizable in the SW channel at approximately the center of the image
7.25 Move cradle to input field positions listed in the table below and repeat steps 8.8.5-8.8.6 for each field position. Note total image counts and if a spot is recognizable at all.
7.26 SW in-field stray light sensitivity at turret angle +30 degrees (LW will not be used)
7.27 Change Monochromator to 180 nm
7.28 Characterize incoming beam
7.29 Set up ICP to collect 256x256 pixel images
7.30 Move turret to +30 degrees position
7.31 Move cradle to compensate for turret angle

7.32 Send command: **IOP_FUV_DUMP_ENG_IMG** (enter **TDI ID = 0** for A) to capture and readout image to take an integrated picture of 100 frames of 120 msec exposure time and save through ICP with appropriate header information about time, number of frames, cradle position, wavelength, channel,

7.33 Check if spot is recognizable in the SW channel at approximately the center of the image

7.34 Move cradle to input field positions listed in the table below and repeat steps 8.8.5-8.8.6 for each field position. Note total image counts and if a spot is recognizable at all.

7.35 SW in-field stray light sensitivity at turret angle +30 degrees (LW will not be used)

7.36 Change Monochromator to ~400 nm

7.37 Characterize incoming beam

7.38 Set up ICP to collect 256x256 pixel images

7.39 Move turret to +30 degrees position

7.40 Move cradle to compensate for turret angle

7.41 Send command: **IOP_FUV_DUMP_ENG_IMG** (enter **TDI ID = 0** for A) to capture and readout image to take an integrated picture of 100 frames of 120 msec exposure time and save through ICP with appropriate header information about time, number of frames, cradle position, wavelength, channel,

7.42 Check if spot is recognizable in the SW channel at approximately the center of the image

7.43 Move cradle to input field positions listed in the table below and repeat steps 8.8.5-8.8.6 for each field position. Note total image counts and if a spot is recognizable at all.

7.44 ITOS power down

4.2.14 Results of the pre-flight light leak and out of band calibration

The results of this calibration are summarized in the document ICN-FUV-144-REP-Lymanalpha.pdf. The procedures to check for any out-of-band light leaks, especially Lyman-alpha were ICN-FUV-081_stray-light.docx and ICN-FUV-127-Lyman-Alpha-hfrey.docx.

On December 2nd a SW spectral scan from 129 nm to 141 nm revealed stray light. This test was repeated on December 4th in the LW channel from 148 nm to 165 nm and the same result was observed. Figures 4.60 and 4.61 show the out of band signal in each channel and the results are summarized in Table 4.9.

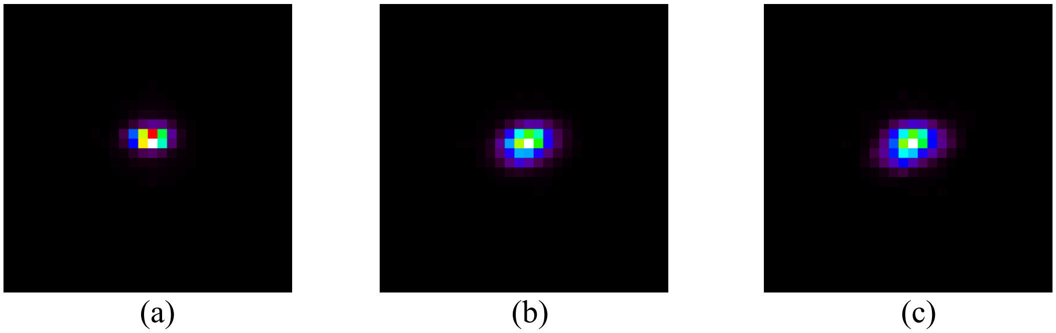
(a) (b) (c)

Fig 4.60: LW out of band signal at 2250 V (a) 157nm (b) Lyman alpha (c) 170nm

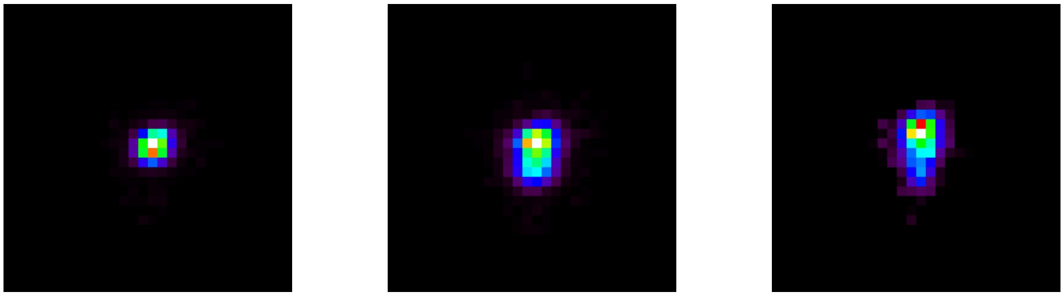

(a) (b) (c)

Fig 4.61: SW out of band signal at (a) 135.5 nm (b) Lyman alpha (c) 170 nm

Channel	HV	Wavelength (nm)	Photometer Current (A)	Total Counts in spot
LW	2250	157	3.696 E-10	1.603 E6
		Lyman alpha	1.438 E-8	3.036 E6
		170	1.072 E-8	9.968 E5
SW	2450	157	6.599 E-11	1.598 E6
		Lyman alpha	1.443 E-8	7.482 E5
		170	1.084 E-8	1.227 E5

Table 4.9: Summary of stray light observations

In order to identify the source of the leak as coming from either the source or the instrument, on Jan 18th a BaF2 window was placed directly in front of the monochromator slit to remove any Lyman-alpha photons from the spectral band of light exiting the monochromator.

pinhole	CaF2 window	BaF2 window	Source	Counts
8 mm			2.50E-10	60,000
8 mm		installed	2.70E-11	50,000
no		installed	3.60E-11	400,000
no	installed		5.30E-11	600,000
no			1.80E-09	700,000

Table 4.10: LW channel results with source tuned to Lyman-alpha

pinhole	CaF2 window	BaF2 window	Source	Counts
8 mm			2.50E-10	2,500
8 mm		installed	2.70E-11	1,500

no		installed	3.60E-11	2,500
no	installed		5.30E-11	75,000
no			1.80E-09	190,000

Table 4.11: SW channel with source tuned to Lyman-alpha. Source currents and total counts for several test runs with and without CaF2 and BaF2 windows.

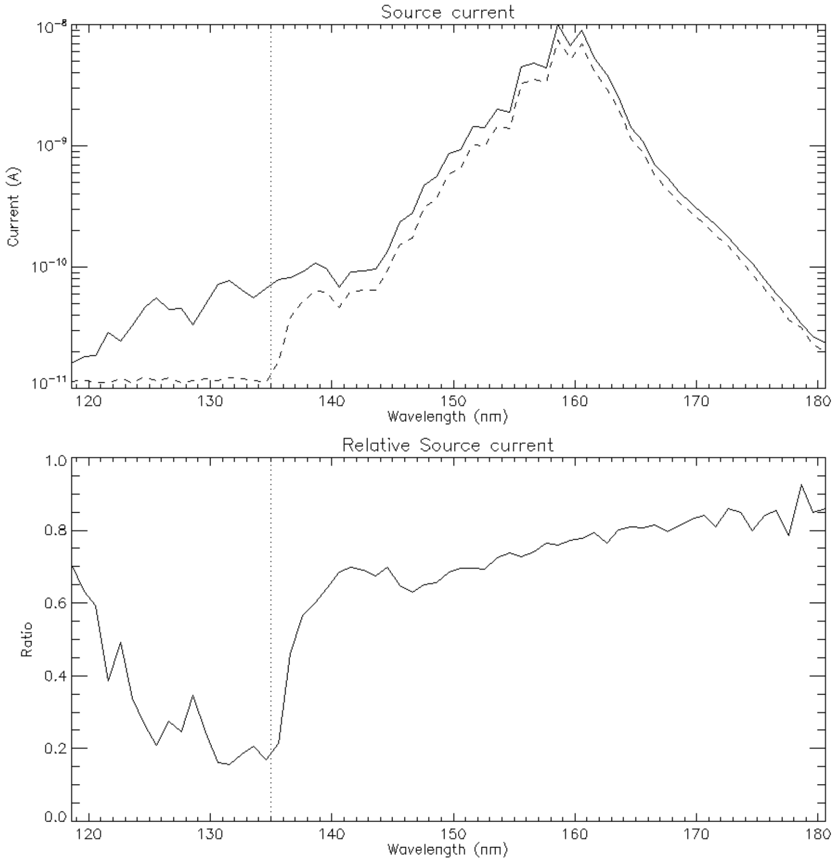

Fig 4.62: Source intensity as measured by the source meter for the full spectral scan in the solid line and the scan with the BaF2 window installed as the dashed line

Figure 4.62 shows the source intensity as measured by the source meter for the full spectral scan in the solid line and the scan with the BaF2 window installed as the dashed line. In both cases the 8mm pinhole was in the beam. The top plot is in logarithmic scale and shows that the BaF2 window cuts the light off below 140 nm. Below 135 nm the BaF2 window has cut off all the light and the ratio of the without/with BaF2 window reaches 20% but only because it seems a source current of 1.15E-11 is the stable background level of the photometer. The dashed line is flat around that value and we can assume that really no UV light should reach our instrument below 135 nm when the BaF2 window is installed.

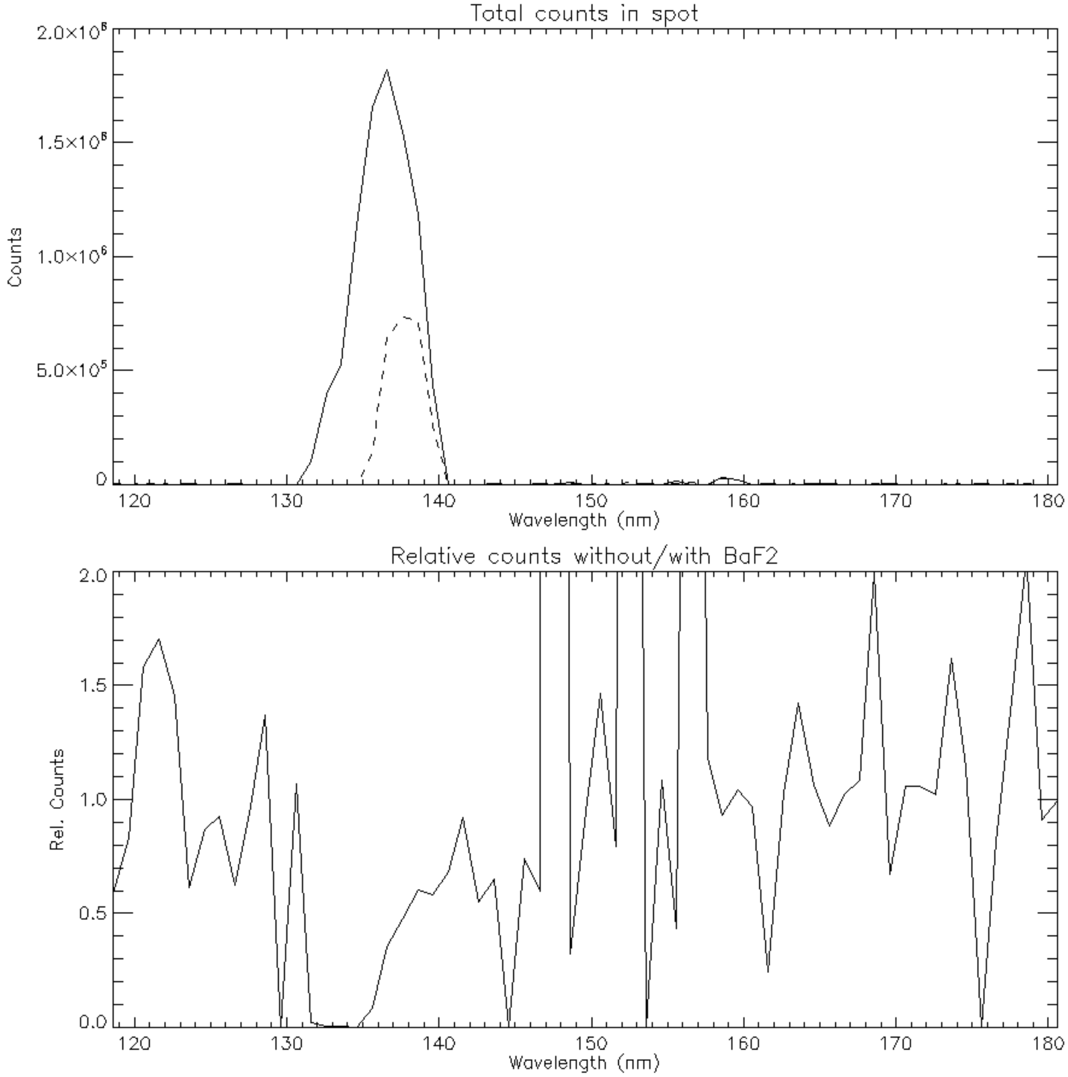

Fig 4.63: Total counts in the SW channel around the center wavelength without (solid line) and with the BaF2 window installed. The bottom plot shows the ratio with/without and all the values below 132 nm and above 145 nm are meaningless because the low counting statistics numbers make the ration meaningless.

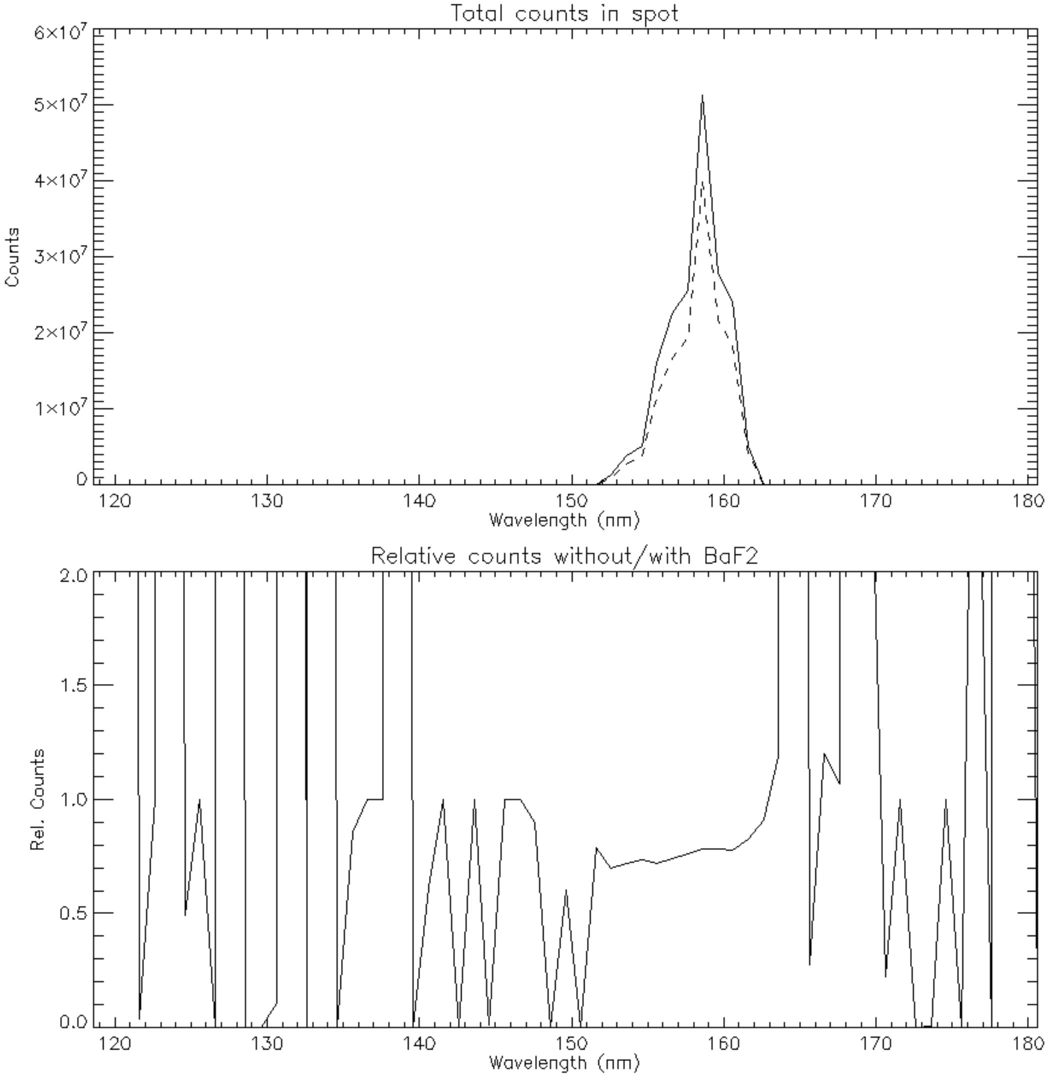

Fig 4.64: The same a Figure 4.63 but for the LW channel. The ratio of with/without of 0.8 is the expected BaF2 reduction around 160 nm.

Spectral scans showed that the BaF_2 window removed the Lyman alpha spot that was previously observed and it was therefore determined that the leak was coming from within the MacPhearson Monochromator and not within the FUV instrument.

Further investigation showed that close to the 121 nm grating position of the monochromator a part of the zeroth order is reflecting on a chamfer of the exit channel (Email by Jerome Loicq on January 20, 2016). This reflection created an “image” on the rear of a baffle and very close to the line of sight of the monochromator which was able to go back in the exit channel.

The reflection was removed by placing, Acktar tape (highly diffusing and absorber tape – vacuum compatible), on baffles where the strange zeroth order reflections were observed.

All investigations point to a problem with ghost reflections inside the monochromator as the root cause of the out-of-band leak. The installed non-reflective tape reduced the effect but was not able to completely remove it. Overall the opinion is that the instrument fulfills the requirement of a 10^5 reduction of unwanted transmission away from the center wavelengths of the two channels.

4.2.15 Instrument Description

See Section 3.2.

4.3 In-flight Tracking of Short-Term Changes

Short term changes of the FUV instrument performance are monitored with regularly scheduled:

- Recording of the instrument performance through the collection of a "postage stamp" for the dynamic background correction
- Daily determinations of both channel's background during passages through the South Atlantic Anomaly when there is no high voltage applied to the MCPs. The turret is always in its nominal zero degree position for dayside measurements.
- Weekly scheduled background determinations for the SW channel on the night side with the turret going through all used 7 positions between -30° and +30° in steps of 10°
- Monthly scheduled nadir observations with the assumption that the dayglow if "flat" at the subsolar point allowing for the pixel-to-pixel variation monitoring
- Monthly scheduled stellar calibration with pointing to a predetermined set of bright UV stars

4.4 Long-term Absolute Calibration Tracking (Re-Calibration)

As was previously done with the IMAGE-FUV instrument monthly scheduled observations of well-characterized bright UV stars are used to verify the absolute ground calibration and monitor long-term absolute variations. The FUV instrument was calibrated in a vacuum chamber illuminating it with monochromatic UV light, measuring the incoming flux, and determining the response of the instrument (Mende et al., 2017). One of the most important properties of the instrument is its pass band and response to photons of different wavelengths (Frey et al., 2017). The careful characterization of the pass band allows for a confirmation or improvement of the accuracy calibration process on orbit using regular observations of bright early type-B UV stars (Frey et al., 2003).

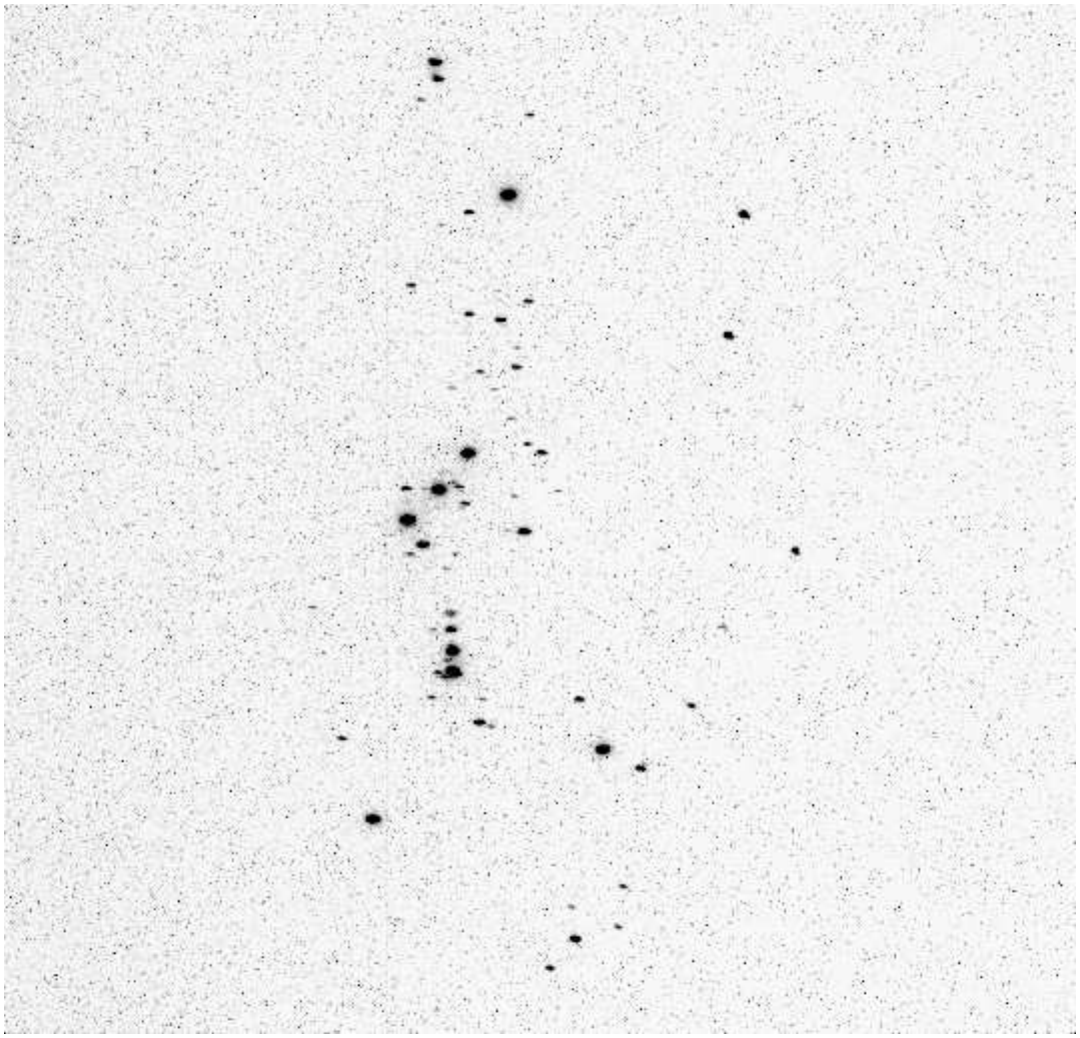

Fig 4.65: Star calibration image of the LW channel while pointed to the constellation Orion on November 17, 2020.

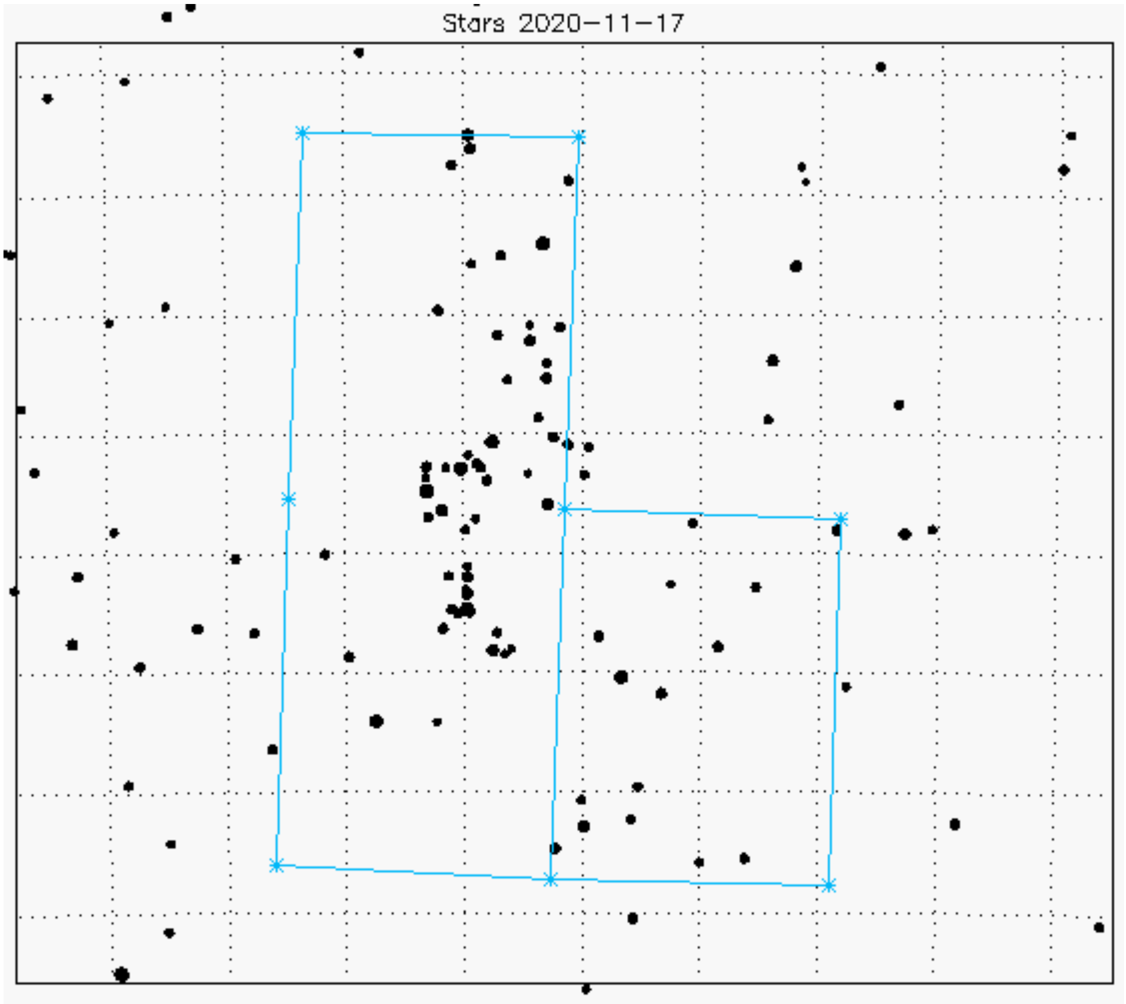

Fig 4.66: Corresponding star atlas region with the approximate outline of the FUV field of view outlined in blue. The open corner represents the upper right corner of the star image in the top display.

Once every month the ICON spacecraft rotates away from the nominal limb-pointing view of the remote sensing instruments and points FUV towards a pre-determined star field with a large number of bright UV stars (Figure 4.63). The quaternions of the spacecraft orbit and attitude are used to calculate the view of the instrument (Figure 4.64) and identify stars. A catalog of the 1000 brightest UV stars from observations by the International Ultraviolet Explorer IUE (Hartline, 1979) is then used to determine the response of the FUV instrument by convolving the instrument pass bands with the calibrated IUE spectra (Figure 4.67).

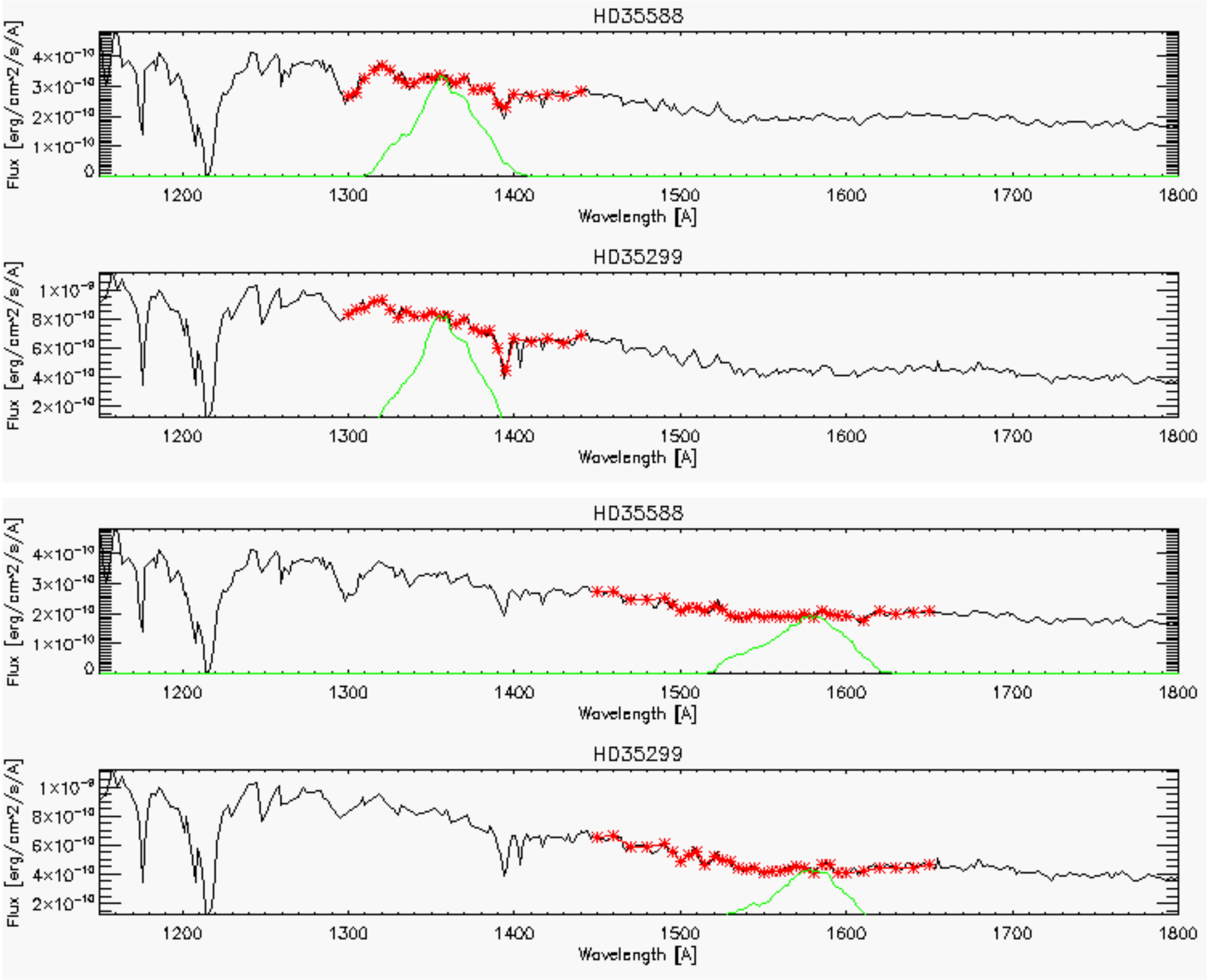

Fig 4.67: Representative IUE spectra of two stars (black lines) together with the wavelength region (red) that was convolved with the ground measured spectral pass bands of the SW and LW channels (green). The integral under the green curves represents the portion of the star photons that reach the detectors.

During each star observation two different star fields are observed with three images taken each time by both channels. The total counts in the individual stars are then compared to the photon flux going through the instrument and the result for one particular day is shown in Figure 4.68.

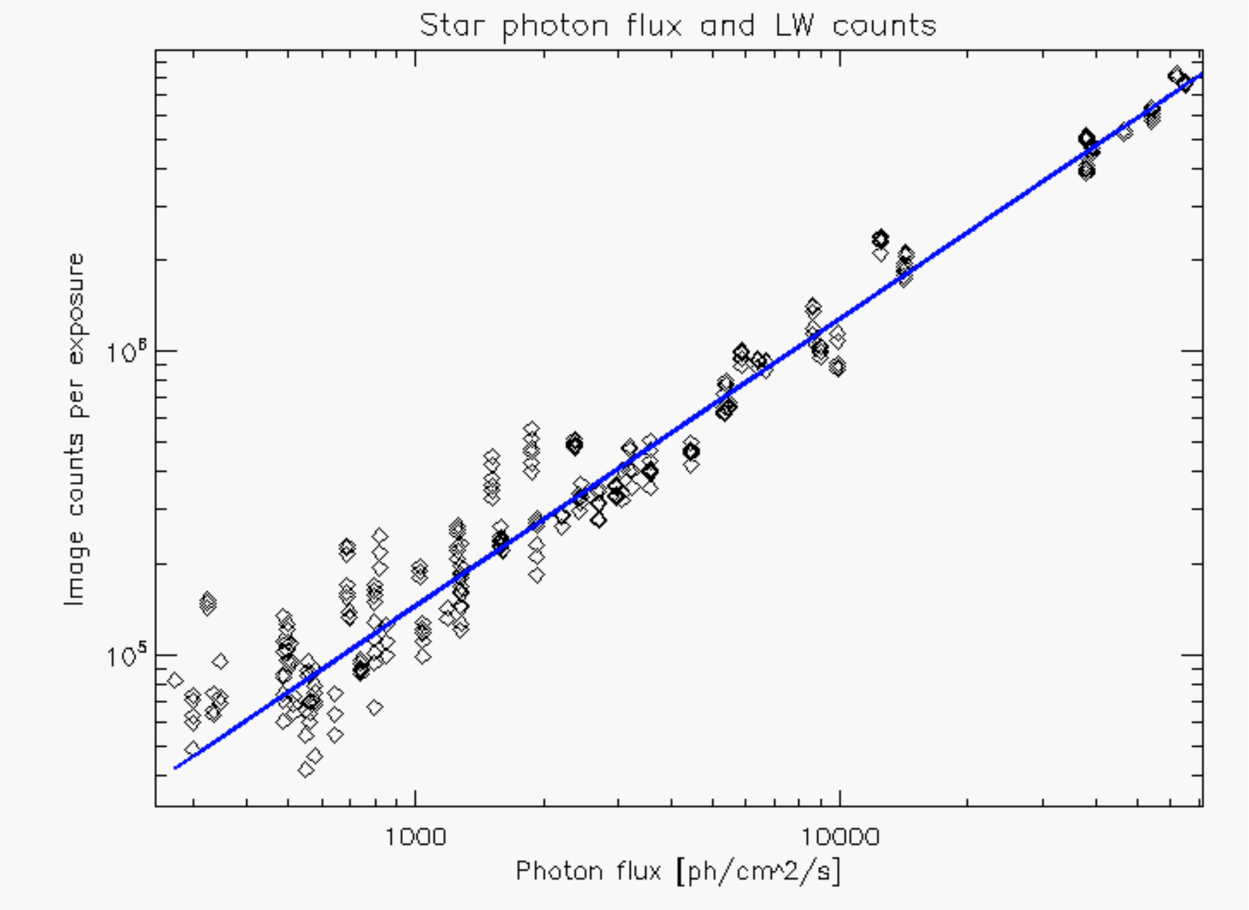

Fig 4.68: Evaluation of the star observation on 2021-12-26 for the LW channel. The total counts in the 297 individual star observations are plotted over the photon flux from those stars. The least squares fit is used to determine the relationship of counts per incoming flux. The correlation coefficient is 0.985.

All the star observations since the beginning of the science mission are used to monitor the long-term temporal change of the instrument response (and also establish the on-orbit calibration, see Section 5.2). Figure 4.69 shows the results of this analysis for both channels. Over the ~2.5 years of the mission the high voltage to the MCPs has been changed two times in order to get a stronger response in terms of Counts/Rayleigh and thus improve the signal to noise ratio of the observations. All results in Figure 4.69 however are shown as if they were done with the latest high voltage settings of 2300 V for the LW channel and 2400 V for night observations of the SW channel. During the day the SW channel operates with 2200 V because the airglow is so much brighter in sunlight than the relatively dim nightglow. The relative change of the instrument output for different MCP high voltage settings has been determined during the ground calibrations.

The data in the top panel (Figure 4.69) show that the relative response of the LW channels has changed so far by -6.5% per year (LW) and the third panel shows -7.8% gain reduction per year for SW. Changes of this order are not unexpected and demonstrate the technical capability of the FUV system to operate in space for many more years.

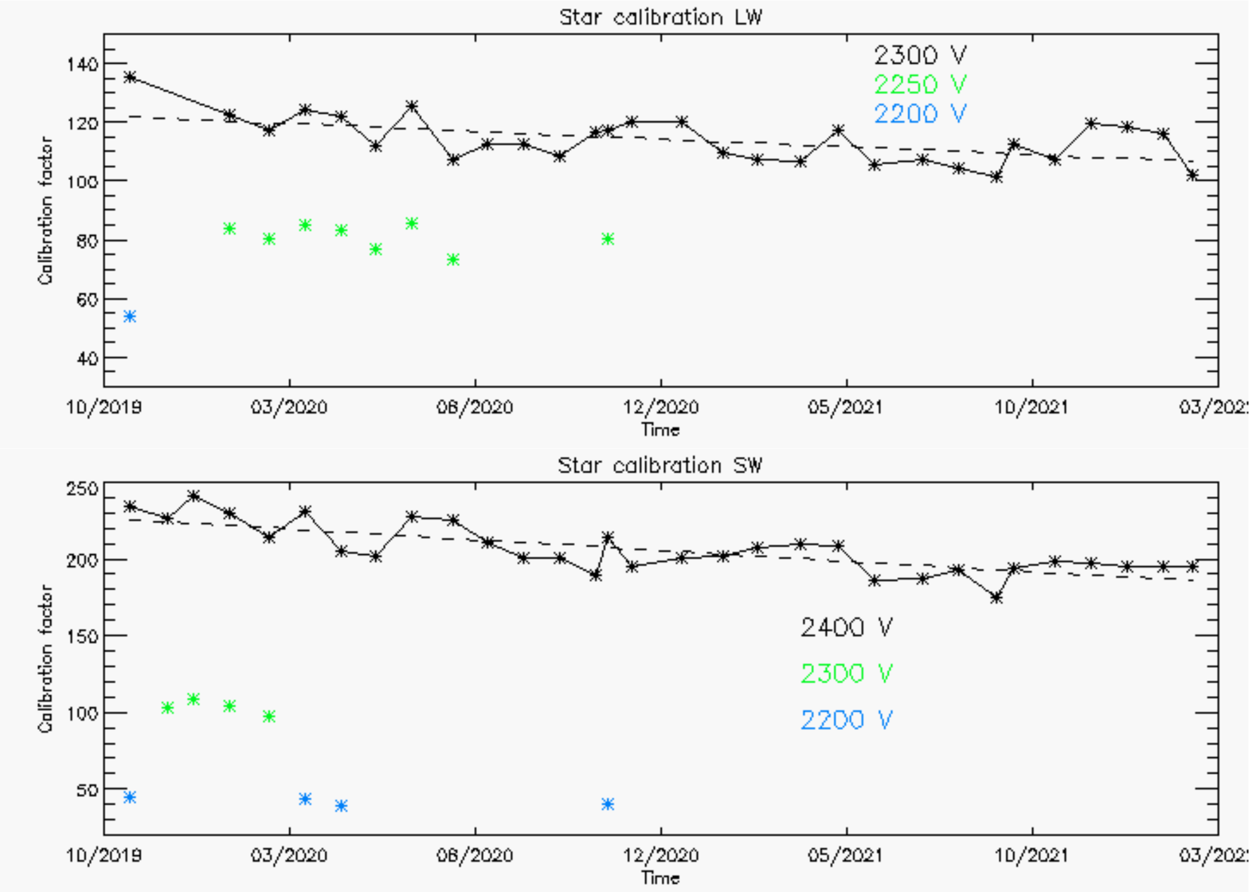

Fig 4.69: Results of the long-term monitoring of the FUV instrument response for the LW channel (top) and the SW channel (bottom). So far the LW channel lost 6.5% response per year, and the SW channel lost 7.8% per year.

4.5 Validation

Measurements by the COSMIC-2 spacecraft and the Millstone Hill ionospheric radar were used to validate the FUV measurements. The nightside observations of FUV enabled the determination of the ionospheric oxygen ion peak height hmF2 and peak density NmF2 and thus the F-region electron density following the method described in (Kamalabadi et al., 2018). A comparison with measurements by the COSMIC-2 constellation (Cook et al., 2013) and ionosondes revealed that the FUV observations are consistent with the COSMIC-2 and ionosonde measurements, with an average positive bias lower than 1 × 10^{11} e/m^3. When restricting the analysis to cases having an NmF2 value larger than 5 × 10^{11} e/m^3, FUV provides the peak electron density with a mean difference with COSMIC-2 of 10% (Wautelet et al., 2021). The peak altitude, also determined from FUV observations, is found to be 15 km above that obtained from COSMIC-2, and 38 km above the ionosonde value on average.

Another confirmation of the FUV data quality was obtained through the comparison to radar measurements by the Millstone Hill Incoherent Scatter Radar. The probed volume of the radar is regularly within the region observed by ICON-FUV and during 38 coordinated radar measurements during 2021 the results were compared. An example is given in Figure 4.69, which shows the measured FUV brightness and the estimated O^+ density by ICON (Kamalabadi et al.,

2018) together with the measured electron density by MHO and the associated airglow brightness (Qin et al. 2015). The NmF2 results of both measurements agree within 10% and the hmF2 difference is within the altitude resolution of the radar.

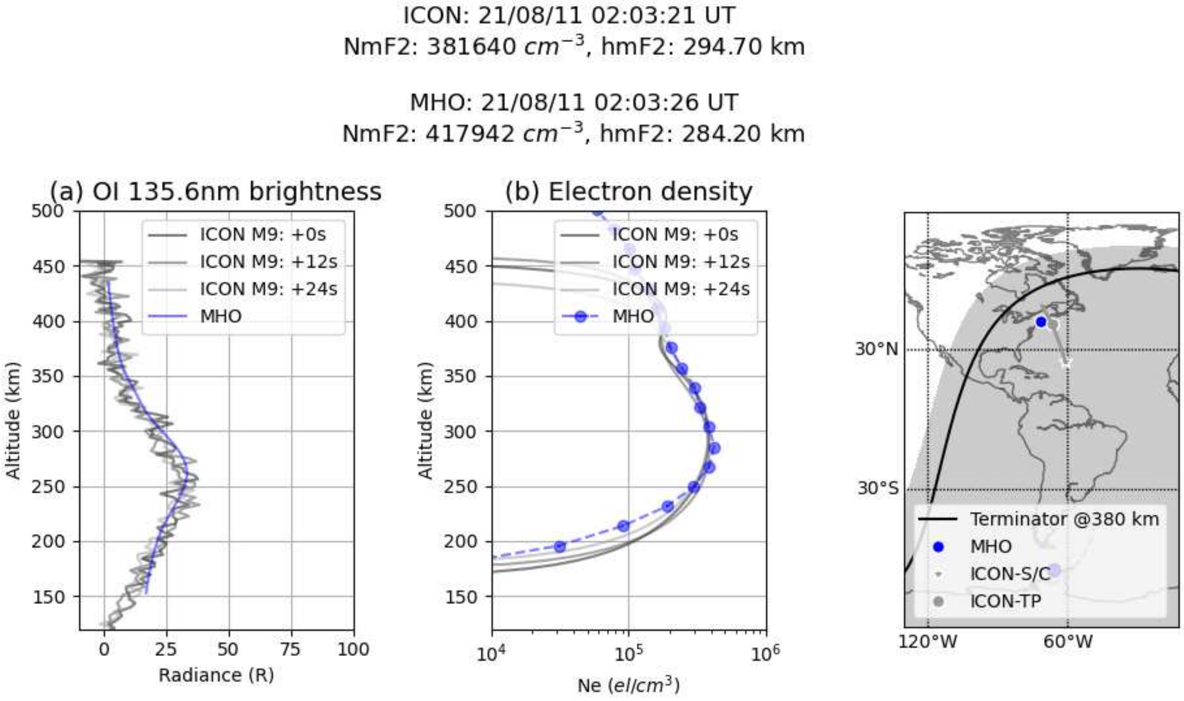

Fig 4.70: Comparison between nightside measurements of ICON-FUV and the Millstone Hill Incoherent Scatter Radar (MHO). The derived ionospheric peak densities agree within 10% and the peak altitude difference is within the radar altitude resolution.

4.6 Conversion of Instrument Signals to Rayleigh

4.6.1 Measurement Equations

The photon collection in a science pixel during a sampling interval *dt* is given as:

$$P_0 = \frac{10^6}{4\pi}\, I\, A\, \frac{da}{R^2}\, dt \qquad (1)$$

where *I* is source intensity in Rayleighs, *A* the input aperture of the imager, *da* the area to be resolved, *R* is the range distance to the target and *dt* is the sampling time. Since the solid angle $d\alpha = da/R^2$ we can write:

$$P_0 = \frac{10^6}{4\pi}\, d\alpha\, I\, A\, dt \qquad (2)$$

The instrument converts the P_0 photons to P_1 information quanta with a conversion efficiency of ε:

$$P_1 = \frac{10^6}{4\pi}\, d\alpha\, dt\, I\, A\, \varepsilon \qquad (3)$$

The constant term in (3) $(10^6/4\pi)$ is often approximated as 80,000. The product of terms I, $d\alpha$ and dt are independent of the imager instrument choice and they are simply a statement of the scientific requirements of the spatial, temporal and intensity resolution. The choice of the imager defines only the product of the last two terms, A and ε. which is the figure of merit when comparing imager types. It is also sufficient to calibrate an instrument in terms of these parameters provided the angular and temporal resolution of the imager satisfies the science requirements.

The throughput efficiency ε can be regarded as the product of the optical transmission T and the quantum efficiency, q_e—namely the rate of photoelectron production per input photon. The input photon beams have Poissonian intensity distribution and this treatment would assume that the output signal also exhibits Poissonian fluctuations. In an efficient system this should be approximately true however strictly speaking we should take into account other noise sources and calculate the true equivalent quantum efficiency q_{eq} which is the ratio of the square of the signal to noise at the output signal, ∇P_1^2 divided by the photon noise squared at the input, $\nabla P_0^2 = P_0$.

The responsivity of an instrument is usually given in counts Rayleighs^{-1} s^{-1} which is from (3):

$$\frac{P1}{I} = \frac{10^6}{4\pi}\, d\alpha\, A\, T\, qe \qquad (4)$$

The expected responsivity of an instrument can be derived from a mechanical measurement of the input aperture area, A, the angular resolution of pixels $d\alpha$ from geometric calibration and the instrument throughput efficiency, $\varepsilon = T\, q_e$ from the instrument response to a collimated light source. Using these quantities of the input aperture, A, and the solid angle of acceptance of a resolution element, dα, provides a per-pixel photon rate. Adjusting for the throughput efficiency of a UV instrument is usually a 3-4% modifier on this values. Hence the responsivity can be calculated from (4).

A star is a point source in any wide-field UV instrument and the response C_s to incoming star photons in counts/sec can be calibrated against the incoming photon flux P_s in photons/cm^2/sec at the entrance aperture as

$$C_s = P_s * \varepsilon * A \qquad [\text{counts/s} = \text{ph/cm}^2\text{/s} * \text{counts/ph} * \text{cm}^2] \qquad (5)$$

Where ε is the overall efficiency of the system in counts per incoming photon and A is the aperture size in square centimeters. During airglow measurements we observe an extended object that emits R_a Rayleigh and the instrument responds with a count rate per pixel of C_a. One Rayleigh is defined as an apparent emission rate of 10^6 photons/cm^2/s/4πsr (Chamberlain, 1961). The signal from the airglow is then

$$C_a = 10^6/4\pi * R_a * \theta * \varepsilon * A \quad [\text{counts/s/R} = \text{ph/cm}^2\text{/s/sr/R} * \text{R} * \text{counts/ph} * \text{sr} * \text{cm}^2] \qquad (6)$$

Where θ is the solid angle per pixel and for small solid angles θ, the product θ*A is the etendu of the system. Replacing ε*A with the one from equation (1) gives finally the calibration

$$C_a = 10^6/4\pi * R_a * \theta * C_s/P_s \quad [\text{counts/s}] \qquad (7)$$

$$R_a = C_a * 4\pi * P_s / (10^6 * \theta * C_s) \quad [\text{R} = \text{counts/s} * \text{cm}^2 * \text{s} * \text{sr} * \text{R} * \text{ph}/ (\text{ph} * \text{sr} * \text{counts} * \text{cm}^2)] \ (8)$$

The number R_a of Rayleigh emitted by the airglow is then determined with C_s/P_s taken from the results on Figure 5.2 and the solid angle $\theta = 8.567E\text{-}5$ sr for the science pixel.

All the star observations since the beginning of the science mission are used to determine the on-orbit calibration (and also to monitor the temporal change of the instrument response, see Section 4.4). Figure 5.2 shows the results of this analysis for both channels. The relative change of the calibration factor C_s/P_s is used in the conversion from instrument counts to Rayleighs of the observed airglow emissions.

Over the ~2.5 years of the mission the high voltage to the MCPs has been changed two times in order to get a stronger response in terms of Counts/Rayleigh and thus improve the signal to noise ratio of the observations. All results in Figure 5.2 however are shown as if they were done with the latest high voltage settings of 2300 V for the LW channel and 2400 V for night observations of the SW channel. During the day the SW channel operates with 2200 V because the airglow is so much brighter in sunlight than the relatively dim nightglow. The relative change of the instrument output for different MCP high voltage settings has been determined during the ground calibrations.

The data in the top panel (Figure 5.2) show that the relative response of the LW channels has changed so far by -6.5% per year (LW) and the third panel shows -7.8% gain reduction per year for SW. Changes of this order are not unexpected and demonstrate the technical capability of the FUV system to operate in space for many more years. The second panels of Figures 5.2 and 5.3 show the temperatures of key components of the detector system during the star observations, namely the CCD, digital board, and high voltage power supplies (Frey et al., 2017). There are no indications that these temperatures have an impact on the relative response of the detector systems for as long as these temperatures stay within the operating range of 5-30°C.

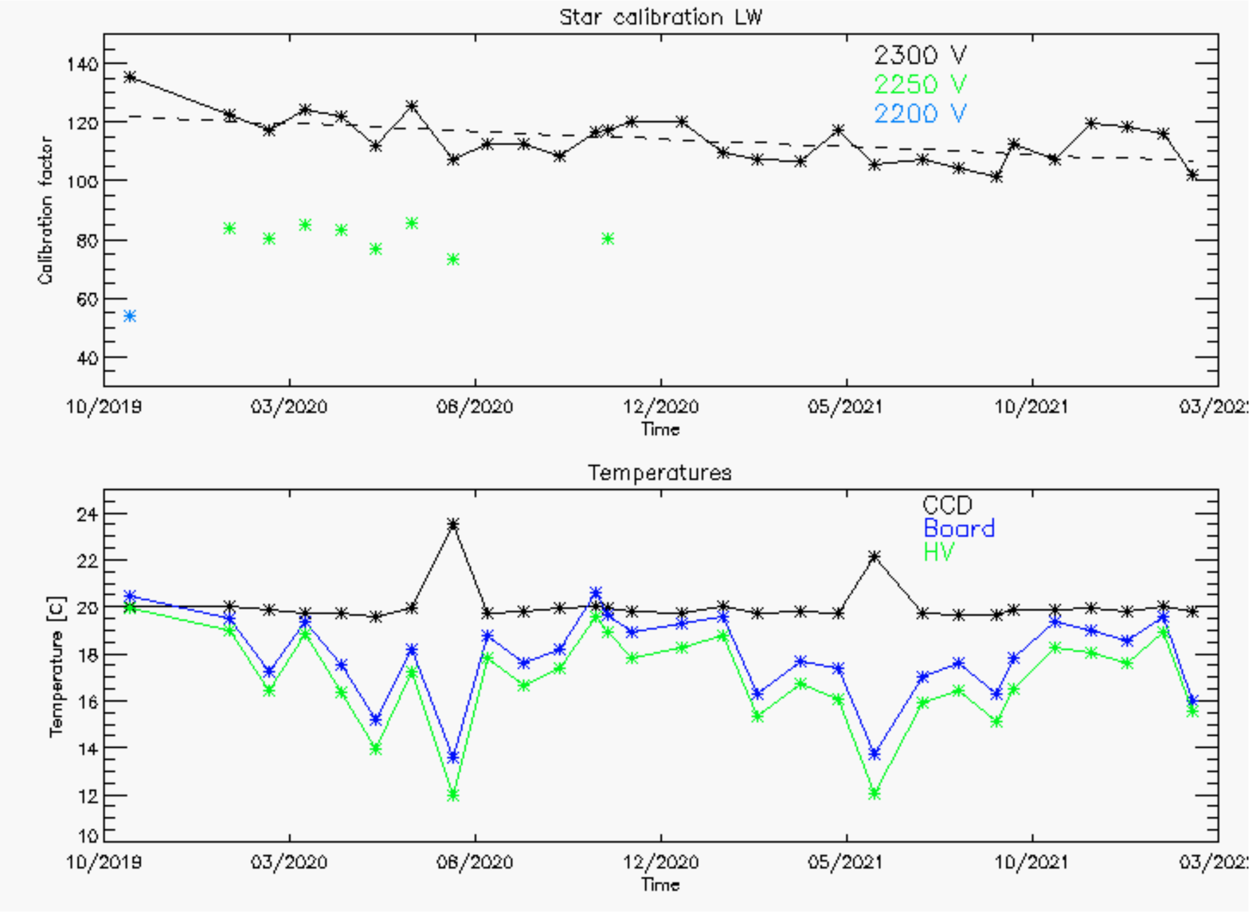

Fig 4.72 Results of the star calibrations during the first 2.5 years of the ICON mission for the LW channel. The calibration factors of Counts/s are shown over time as well as temperatures of key components of the detector system that could have an impact on the relative response.

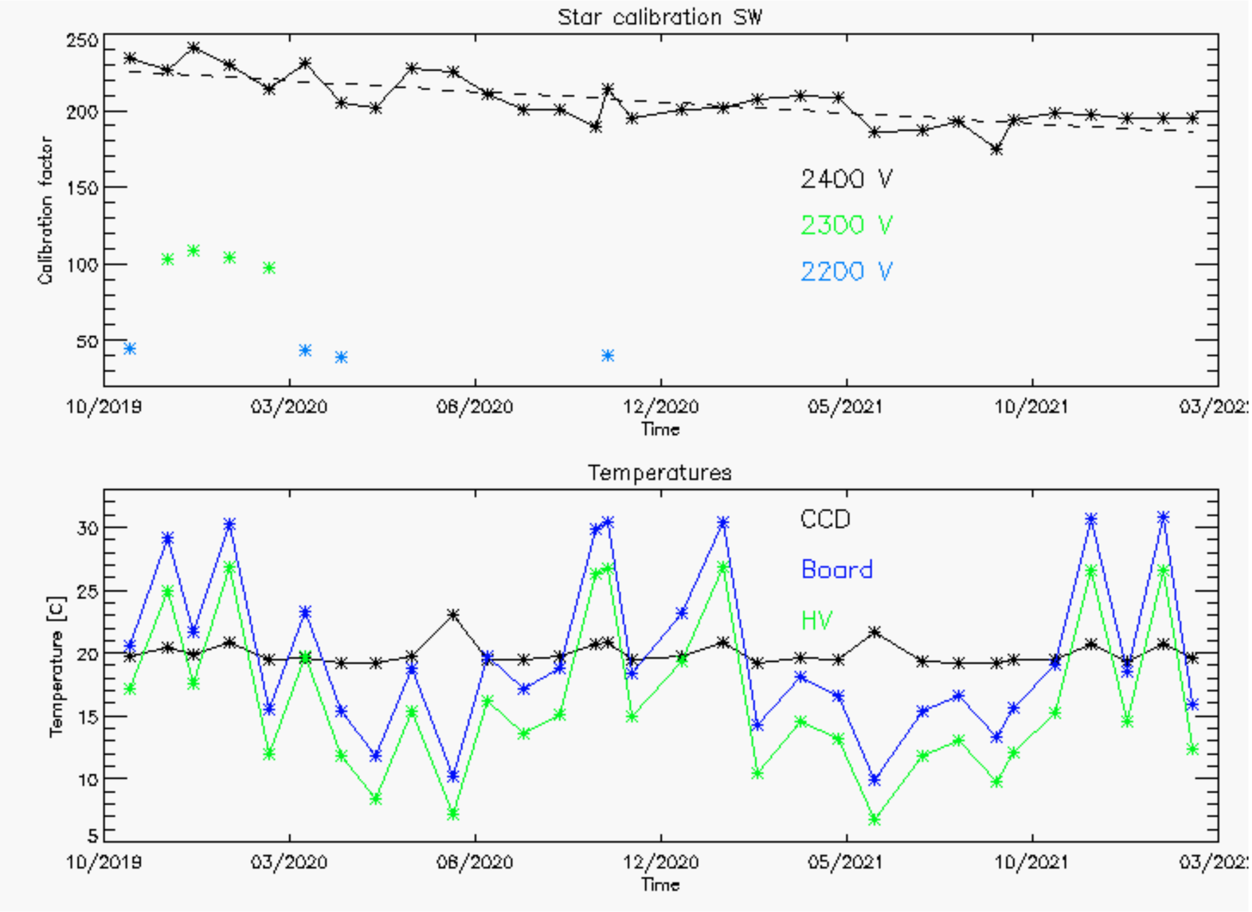

Fig 4.73: Results of the star calibrations during the first 2.5 years of the ICON mission for the SW channel. The calibration factors of Counts/s are shown over time as well as temperatures of key components of the detector system that could have an impact on the relative response.

FUV Algorithm Description

5. Theoretical basis

5.1.1 Theoretical Basis - Observation of Airglow Emissions

The instrument produces signal C_a in A-D units at the CCD when observing R_a Rayleigh of FUV light. The source intensity in Rayleigh is:

$$R_a = \int Q_a(\lambda)\, e(\lambda)\, d\lambda$$

where $Q(\lambda)$ is the source intensity in Rayleigh per nm and $e(\lambda)$ is the transfer efficiency from photons to photoelectrons as a function of wavelength λ.

$$e(\lambda) = T(\lambda)\, q(\lambda)$$

Where T is the optical transmission, q is the quantum efficiency and they are wavelength dependent.

The counting rate of the instrument when it observes R_a Rayleigh is:

$$C_a = (10^6)/(4\pi)\ q\ A\ m\ R_a \qquad (1)$$

where: q is the solid angle for a science pixel, A is the area of the input aperture of the instrument and m is the image intensifier gain from photo-electrons to CCD A-D units.

The purpose of the instrument is to determine airglow brightness R_a in Rayleigh from C_a output signal (in A-D units) when observing airglow. Thus the measured airglow is:

$$R_a = C_a\ 4\pi / [(10^6)\ A\ q\ m] \qquad (2)$$

It should be recognized that the number of Rayleigh seen by the instrument is only the part of the spectral emission which is within the airglow spectrum and in the instrument's spectral passband response.

5.1.2 Theoretical basis - Daytime Thermospheric Composition Retrieval – Limb Retrieval products

The limb observations inform the process of determining altitude profiles of O and N_2 (along with O_2). These are provided in the limb-retrieval data product as well as the required product, the column ratio of these two constituents, e.g. $\Sigma O/N_2$. This is calculated by retrieving height-density profiles from the limb data, and then integrating the retrieved N_2 number density profile vertically downward to find the altitude at which the column density above equals 10^{17} cm^{-2}. The O column density above this N_2 level is then computed and the ratio taken. Thus, although $\Sigma O/N_2$ was originally conceived as an observational quantity to be retrieved from disk images, it can be obtained equally well from limb observations (and models). As a reference, Details of the methodology used to retrieve neutral densities from the GUVI data are given by Meier et al. (2015).

The ICON limb neutral density retrieval algorithm begins with a parameterized forward model that predicts the expected emission rates as a function of look angle for direct comparison to the FUV measurements. The model incorporates a first principles representation of the photoelectron excitation rates and radiative transfer of photons based on a parameterization of the thermospheric densities obtained using the NRLMSISE00 model (Picone et al., 2002). Following Meier and Picone (1994) and Meier et al. (2015), the parameters used in our algorithm are a scalar applied to the $F10.7$ solar radio flux input to NRLMSISE00 that effectively adjusts the altitude profiles of the species, and three altitude-independent scalars of the resulting N_2, O_2 and O density profiles to establish the magnitudes. There are two additional magnitude scalars applied to the computed 135.6 and LBH emission rates to account for any systematic uncertainties in the instrument calibration or magnitude of the photoelectron impact excitation cross section. As of Version 6 of the limb retrieval, these scalars are set to unity. These six parameters of the forward model are then iteratively adjusted using the Levenberg-Marquardt method of nonlinear least squares fitting (Marquardt, 1963) until the output produces the optimal match to the ICON FUV measurements. This method of using a weighted non-linear least squares fit of a model to data is called Discrete Inverse Theory (Menke, 1989), or Optimal Estimation.

As described in Meier et al. (2015), the initial excitation rate j_O, is given by the product of the g-factor of the photoelectron-excited emission and the species number density (N_0 or N_{N2}). The g-factor, $g(\boldsymbol{r})$, at location $\boldsymbol{r}$ along the line of sight through the atmosphere defines the number of excitations per second per atom and is determined from the integral over energy of the product of the photoelectron impact excitation cross section, σ, and the photoelectron flux (electron cm^{-2} s^{-1} eV^{-1}), Φ:

$$g(\boldsymbol{r}) = \int \sigma(E)\Phi(E,\boldsymbol{r})dE \qquad (1)$$

The column emission rates observed by the ICON FUV OI 135.6 nm (short wavelength, SW) and N_2 LBH (long wavelength, LW) channels are then described by the following integrals along the line of sight path segment ds:

$$4\pi\, I_{SW} = \int (j_O + j_{ms}) \sum_{i=135.6}^{135.8} B_i \left[e^{-\tau^i_{O2}}\, T\left(\tau^i_O\right)\right] ds + \int j_{N2} \int B_{SW}(\lambda)\, e^{-\tau_{O2}(\lambda)}\, d\lambda\, ds$$
$$4\pi\, I_{LW} = \int j_{N2} \int B_{LW}(\lambda)\, e^{-\tau_{O2}(\lambda)}\, d\lambda\, ds \qquad (2)$$

where j_O and j_{N2} are the initial volume emission rates for OI 135.6 nm and j_{ms} is the additional contribution to the 135.6 nm emission from multiple scattering. Extinction along the path from the emitting region to ICON by molecular oxygen is accommodated by $e^{-\tau_{O2}}$, and self-absorption (resonant scattering out of the emission path by O) represented by the Holstein transmission function, $T(\tau_O)$ (see Meier 1991), which explicitly includes the wavelength dependence of the resonant scattering cross section and the volume emission rate. The sum over wavelength index, i, accounts for the doublet nature of the O ($^5S_2 \rightarrow {}^3P_{1,2}$) transition at their respective wavelengths, 135.85123 and 135.5977 nm. B_i is the fraction of the emissions emitted in each line of the doublet. The second (double) integral in the SW band takes into account the underlying emission from the N_2 LBH bands that falls within the passband. In this expression, B_{SW} represents the wavelength (λ) dependent branching ratio of the total N_2 LBH excitation that falls within the SW passband, calculated as the product of 0.8871 that corresponds to the fraction of excitations of the N_2 ($a^1\Pi_g$) state that result in LBH emissions (i.e., that do not predissociate) (Ajello and Shemansky 1985), and the fraction of the LBH vibrational transition bands that falls within the SW channel. The extinction factor for each emission by O_2, $e^{-\tau_{O2}}$, includes a detailed representation of the O_2 absorption cross section as a function of wavelength and temperature (Gibson et al. 1983; Gibson and Lewis 1996). The full calculation for ICON includes the rather small contribution from photoelectron impact dissociative excitation of O_2. Because the excited O atoms from this process are kinetically hot, most of the emission resides outside the Doppler core of the thermal line profile and extinction by self-absorption is negligible.

The lower integral in (2) is the LBH band emission within the long wavelength channel, LW. Definitions of the various factors in the LW equation are analogous to those for the SW case. Note that the molecular oxygen number density can also be retrieved from the limb measurements over a limited altitude range because the O_2 optical depth is the product of the absorption cross section and the O_2 column density between ICON and the emitting volume element along the path, s.

To correctly simulate the emission rate observed by the FUV instrument Eq. 2 must include the specifics of the FUV instrument responsivity across each passband. Thus, the simulated column emission rates must include *R(λ)*, the instrument responsivity in the SW and LW channels normalized so that the peak responsivity is unity. Equation (2) thus becomes:

$$4\pi\,\mathrm{I}_{SW} = \int (j_O + j_{ms}) \sum_{i=135.6}^{135.8} R_{sw}(\lambda_i) B_i \left[e^{-\tau^i_{O2}}\, T\left(\tau^i_O\right)\right] ds + \int j_{N2} \int R_{SW}(\lambda) B_{SW}(\lambda)\, e^{-\tau_{O2}(\lambda)}\, d\lambda\, ds$$

$$4\pi\, I_{LW} = \int j_{N2} \int R_{LW}(\lambda) B_{LW}(\lambda)\, e^{-\tau_{O2}(\lambda)}\, d\lambda\, ds \qquad (3)$$

The wavelength-integrated fractions of the total LBH emission that fall within the SW and LW channels, $\int R_{SW,LW}(\lambda) B_{SW,LW}(\lambda) d\lambda$ are 0.122 and 0.0681, respectively.

The fractional emission rates without O_2 extinction are shown in Figure 5.1 for the SW channel (upper) and LW channel (lower) panels. The black spectra are the fractional LBH emission before multiplication by *B*. The red dashed curves are the normalized instrument responsivity (Mende et al. 2017).

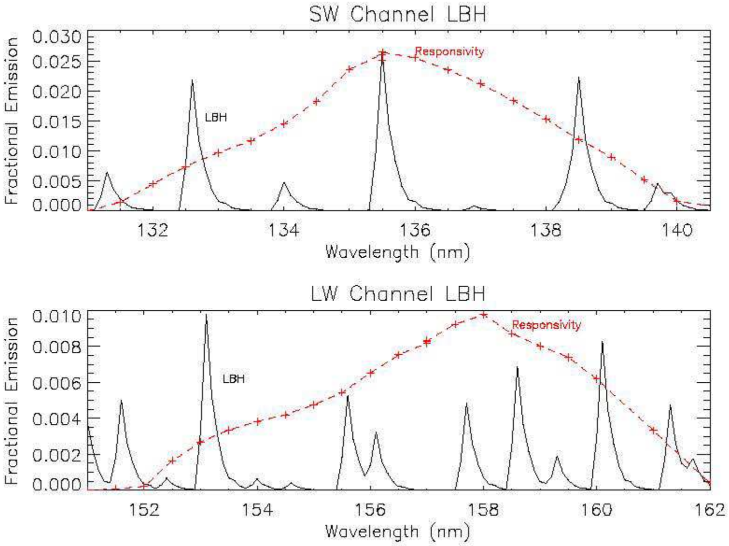

Fig 5.1: Fraction of LBH in SW and LW channels. Black is the spectral distribution of the fractional emission, and red is the FUV instrument channel response, normalized to the peak emission within each channel.

The daytime thermospheric limb analysis implements an algorithm to correct the limb imaging to correct for an internal instrumental light scattering. As noted in an earlier section of this report, a stray light issue was identified and mitigated during test, but the flight data show that stellar sources are broadly spread, with significant scattering out to at least 4-5 pixels from a star. It is unlikely that this broad effect could be entering the back camera slits without appearing as a ghost with significant structure. It is more likely that the optics in the back camera did not achieve the necessary level of smoothness in the process of reflective coating, based upon the stellar source analysis.

The limb data products are each discussed below:

Neutral species densities

Limb profiles of FUV emission rates observed in the SW channel (OI 135.6 nm and some N_2 LBH bands) and the LW channel (N_2 LBH bands) provide information on the altitude profiles of the O, N_2, and O_2 number densities as well as the temperature. The relationship between the FUV emission rates observed in the SW channel (OI 135.6 nm and some N_2 LBH bands) and the LW channel (N_2 LBH bands), and the number densities is highly non-linear. The inversion process to obtain the number densities and temperature is described by Meier and Picone (1994), for GUVI by Meier et al. (2015), and for ICON by Stephan et al. (2018). See Equation 2 and 3 of Stephan et al. to see the relationships and their incorporation of the ICON FUV instrument function, respectively. The process involves estimation of parameters required to obtain the optimal fit of a forward model to the data. The retrieved parameters are altitude-independent scalars of the NRLMSIS00 number densities and ingested solar 10 cm flux. Formally, the relationship between the physical data products and the scalars is:

$$\begin{gathered}
F_{10} = f_{F10}\, F_{10\, MSIS\ input} \\
[O] = f_O\, [O_{MSIS}] \\
[N_2] = f_{N2}\, [N_{2\, MSIS}] \\
[O_2] = f_{O2}\, [O_{2\, MSIS}] \\
[T] = [T_{MSIS}] \\
4\pi I_{sw} = f_{sw}\, 4\pi I_{sw\, FM} \\
4\pi I_{lw} = f_{lw}\, 4\pi I_{lw\, FM}
\end{gathered} \tag{7}$$

where each of the, f_i (i = 0-7), represent altitude-independent scalars of the solar 10 cm flux input to the NRLMSIS 00 model and the number densities, respectively. The brackets indicate the number densities and temperature as a function of altitude. The scalars of the short wave and long wavelength channels are magnitude scalars of the forward model output ($4\pi I_{sw\, FM}$ and $4\pi I_{lw\, FM}$) to adjust for calibration errors or magnitude errors in the photoelectron impact excitation cross sections.

This approach was developed early on by Meier and Picone because measurements of FUV limb emissions do not contain sufficient numbers of independent observations for tomographic inversion. Further opacity effects are present in the emission rates that must be accommodated in the models. Consequently, a priori information in the form of a scalable model atmosphere is needed to constrain the inversion process. This can be thought of as using a Bates-Walker (Walker, 1965) formulation as the model atmosphere, but with more information about departures from diffusive equilibrium.

Temperature

Thermospheric temperature is not measured directly by ICON FUV. Rather, it is inferred from the altitude variation of the emission rates produced by the scalable model atmosphere in the forward model. Thus, while the variation of temperature with altitude is required to follow the functional form in the model atmosphere, its profile is parameterized by the (f_{F10}) scalar of the 10 cm flux that is input to the NRLMSIS 00 model. This method allows for adjustment of the temperature profiles to match the altitude profiles of the dayglow emissions.

Column O/N_2

Once the number densities are retrieved from the limb inversion, the $\Sigma O/N_2$ ratio can readily be obtained by integrating the retrieved vertical number densities as described in Equation 1. Even though the limb and disk algorithms use the same forward model, the extraction of $\Sigma O/N_2$ involves completely different approaches. Note that the limb and disk radiances are captured in the same FUV image although they originate at locations in the atmosphere that can be more than 1000 km apart.

5.1.3 Theoretical basis - Daytime Thermospheric Composition Retrieval – Disc Retrieval products

The daytime thermospheric disk retrieval produces two products, listed here:

Thermospheric Column O/N2 Ratio

The principal disk data product is the column density ratio of O to N_2, commonly designated as $\Sigma O/N_2$ to distinguish the ratio of column densities from the volume density ratio, O/N_2. Strickland et al. (1995) found optimal fidelity in the relationship between $\Sigma O/N_2$ in the terrestrial thermosphere and the ratio of OI 135.6 / N_2 LBH band (earth disk) FUV emission rates when the vertical column densities are calculated above an altitude, z_{17}, corresponding to an N_2 column (from infinity down to z_{17}) of 10^{17} cm^{-2} (= N_{N2} in Equation 1; N_O is the O column density above z_{17}). Thus, $\Sigma O/N_2$ is defined as:

$$\sum \frac{\mathrm{O}}{\mathrm{N_2}} \equiv \frac{\int_{z_{17}}^{\infty} n_O \,\mathrm{dz}}{\int_{z_{17}}^{\infty} n_{N2} \,\mathrm{dz}} = \frac{\int_0^{\mathrm{N_O}} \mathrm{dN'_O}}{\int_0^{\mathrm{N_{N2}}} \mathrm{dN'_{N_2}}} = \frac{\mathrm{N_O}}{10^{17}\mathrm{cm}^{-2}} \propto \frac{OI\ (135.6\ nm)}{N_2\ (LBH)}\,. \qquad (1)$$

In the case of ICON FUV observations, an algorithm was developed by Meier (2021) that incorporates the instrument functions for the short wavelength (SW) channels and long wavelength (LW) channels. Thus,

$$\sum \frac{\mathrm{O}}{\mathrm{N_2}} \propto \frac{SW}{LW} \tag{2}$$

Meier (2021) demonstrated that this relationship holds independent of a reference altitude because the important quantity is the relative mixture of O and N_2 in a column of gas. Altitude is only needed for comparisons of emission rate measurements to atmospheric models.

Solar EUV energy flux

Strickland et al. (1995) were also able to quantify the solar extreme ultraviolet (EUV) energy flux required to produce the observed disk airglow by using the absolute magnitude of either the OI or the N_2 column emission rates (CERs). Strickland et al. designated this solar variable as Q_{euv} the integral over wavelength of the solar spectral irradiance from 1 to 45 nm, in units of W m^{-2}, a quantity directly comparable to independent measurements of solar EUV spectral irradiance (e.g., Woods et al., 2008). This allows for determination of the internal consistency of the FUV airglow observations and extracted geophysical quantities. Q_{euv} can be obtained from either disk or limb observations. Note that the disk Q_{euv} depends directly on the airglow instrument calibration accuracy.

Originally not planned for ICON, it became clear that these disk products could be implemented in the science data center to take advantage of the 2-year period between observatory delivery and launch. It is the first O/N_2 product provided by ICON. As noted above, the limb product required the analysis of stray emissions in the LW (LBH) channel and the development of an inversion kernel to correct for this extra background. The entire description of the ICON Disc Column O/N_2 product, and the lookup tables implemented by ICON specifically for the ICON imaging geometry (a specific, small range of spacecraft zenith angles) are made available by Meier (2021).

Uncertainties

In order to estimate the statistical error in a quantity derived from a measurement of one or more variables, we follow the standard propagation of errors methodology described in Bevington and Robinson (1992) for a normal distribution of counting statistics. For a quantity, x that is a function of two or more variables, u and v, the dependence is described by:

$$x = f(u, v, \dots) \tag{3}$$

If u and v are measured quantities, the above equation allows the computation of x. If the standard deviations of the measured quantities are σ_u, σ_v, … Then the variance in the computed value of x is given by the error propagation equation:

$$\sigma_x^2 \cong \sigma_u^2 \left(\frac{\partial x}{\partial u}\right)^2 + \sigma_v^2 \left(\frac{\partial x}{\partial v}\right)^2 + \cdots + 2\sigma_{uv}^2 \left(\frac{\partial x}{\partial u}\right)\left(\frac{\partial x}{\partial v}\right) + \cdots \tag{4}$$

The column density ratio ($\Sigma\mathrm{O}/\mathrm{N}_2$, equivalent to x above) can be rewritten as a function of the FUV instrument short wavelength (SW) channel column emission rate to long wavelength (LW) channel column emission rate ratio ($\frac{4\pi\mathrm{I}_{\mathrm{SW}}}{4\pi\mathrm{I}_{\mathrm{LW}}}$, equivalent to u above):

$$\Sigma O/N_2 = \mathrm{f}\left(\frac{4\pi\mathrm{I}_{\mathrm{SW}}}{4\pi\mathrm{I}_{\mathrm{LW}}}\right). \tag{5}$$

The $\Sigma\mathrm{O}/\mathrm{N}_2$ is a function (f) only of the measured emission rate ratio. Consequently, the uncertainty in $\Sigma\mathrm{O}/\mathrm{N}_2$ is given by the first term in Equation 4 above:

$$\sigma^2_{\Sigma O/N2} = \sigma^2_{SW/LW}\left(\frac{\partial\left(\Sigma\frac{O}{N_2}\right)}{\partial\left(\frac{4\pi\mathrm{I}_{\mathrm{SW}}}{4\pi\mathrm{I}_{\mathrm{LW}}}\right)}\right)^2. \tag{6}$$

In order to increase the statical accuracy of the disk SW/LW measurement, 20 pixels are averaged together. Pixels 15 to 35 were selected for averaging to avoid vignetting of edge pixels. This is justified because the disk emission rates are nearly uniform over the 20 pixels. The variance of the emission rate ratio, $\sigma^2_{SW/LW}$, is given by the square of the standard deviation of the 20 pixels. From the Central Limit Theorem, the distribution of the emission rate ratios over the 20 pixels should be nearly Gaussian.

Details of the disk algorithm are given in Meier (2021). The partial derivatives in Equation 6 above are obtained numerically from the computed dependency of the column density ratio on the column emission rate ratio (Equation 5 above). The standard deviation of the retrieved column density ratio, $\sigma_{\Sigma O/N2}$, is reported in the Level 2.4 database. Note again that the above derivation only accounts for random uncertainties. Systematic uncertainties are currently under study.

Theoretical basis - Nighttime Ionospheric O+ Retrieval. 5.1.4

In this part we describe a comprehensive radiative transfer model of OI 135.6-nm emission, which constitutes the forward model for the nighttime ICON FUV instrument. This model establishes the relation between the nighttime FUV measurements and the O^+ profiles, which allows for the estimation of the O^+ profiles from the measurements. The model includes the two primary production mechanisms of OI 135.6-nm emission in the nighttime ionosphere, namely radiative recombination (RR) of electrons with O^+ and mutual neutralization (MN) of O^+ with O^- (e.g., Hanson 1970; Tinsley et al. 1973):

$$\mathrm{O}^+ + \mathrm{e} \rightarrow \mathrm{O}^* + h\nu \tag{1}$$

$$\mathrm{O}^- + \mathrm{O}^+ \rightarrow \mathrm{O}^* + \mathrm{O} \tag{2}$$

where O^* and $h\nu$ represent the excited oxygen atoms and the direct recombination photons, respectively. Following the above two processes, the excited atoms O^* emit line radiations at 135.6, 130.4, 102.7, 98.9, and the 91.1-nm continuum from recombination into the ground state of O, as well as a variety of visible and infrared wavelengths (Meier 1991; Slanger et al. 2004). The 135.6-nm photons result from the following electric dipole intercombination transition

$$\mathrm{O}(^5\mathrm{S}_2) \rightarrow \mathrm{O}(^3\mathrm{P}) + h\nu_{135.6} \tag{3}$$

that consists of a doublet, ($^5\mathrm{S}_2 \rightarrow {}^3P_2$) and ($^5\mathrm{S}_2 \rightarrow {}^3P_1$). The source volume emission rate, $4\pi\varepsilon_0$, can be calculated as:

$$4\pi\varepsilon_0 = \alpha_{135.6}(T_\mathrm{e})N_\mathrm{e}O^+ + \beta_{135.6}k_1k_2\frac{N_\mathrm{e}[O][O^+]}{k_2[O^+] + k_3[O]} \tag{4}$$

Where ε_0, $\alpha_{135.6}$, N_e, and $[\mathrm{O}^+]$ are the isotropic source volume emissivity, the partial rate coefficient of RR yielding 135.6-nm photons, the electron density, and the O^+ density, respectively, $\beta_{135.6}$ is the proportion of the excited atoms O^* resulting from MN that emit 135.6-nm radiation, and k_1, k_2, and k_3 are the related rate coefficients (Melendez-Alvira et al. 1999).

In its baseline operation mode, the ICON FUV nighttime inversion algorithm includes only the above processes for computational efficiency, since these are the dominant processes contributing to the accuracy of the inferred parameters. In its more comprehensive mode, the forward model incorporates the effects of multiple scattering and absorption, as described below.

The effects of resonant scattering by O and pure absorption by O_2 on the transport of the nighttime OI 135.6-nm emission are taken into account by solving the following time independent radiative transfer equation, assuming a plane parallel atmosphere (Strickland and Donahue 1970; Mihalas 1978):

$$\mu\frac{dI}{dz} = -\chi(x,z)I(x,\mu,z) + \varepsilon(x,\mu,z) \tag{5}$$

where $I(x,\mu,z)$ is the specific intensity in units of photons cm^{-2} s^{-1} hz^{-1} ster^{-1}, $\varepsilon(x,\mu,z)$ is the total volume emissivity defined as the total number of photons emitted cm^{-3} s^{-1} hz^{-1} ster^{-1} at altitude z in the direction μ, and $x = (\nu - \nu_0)/\Delta\nu_D$ is the frequency measured from the line center ν_0 in units of the Doppler width $\Delta\nu_D$. The extinction coefficient $\chi(x,z)$ is given by

$$\chi(x,z) \ = \ k_0(z)\phi(x,z) \ + \ k_{O2}(z) \tag{6}$$

where k_0 is the line center scattering coefficient, and k_{O2} is the pure absorption coefficient. Without external radiation sources, the formal solution to the above radiative transfer equation is

$$I(x,\mu,z) = \int \varepsilon(x,\mu,z')e^{-|\tau_x \ - \tau'_x|/\mu}dz'/\mu \tag{7}$$

where τ_x represents the optical depth $\tau(x, z)$. For the condition of radiative equilibrium, the total volume emissivity is the sum of the source volume emissivity ε_0 and the contributions from multiple resonant scattering

$$\varepsilon(x, \mu, z) = \varepsilon_0(x, \mu, z) + 2\pi \int I(x', \mu', z)\, R(x, x', \mu, \mu', z)\, dx' d\mu' \tag{8}$$

where $R(x, x', \mu, \mu', z)$ is the redistribution function defined as the probability per unit volume that a photon of frequency x' coming from the direction μ' will be absorbed and then reemitted at frequency x in the direction μ (Hummer 1962). Under the assumptions of zero natural width, isotropic scattering, Maxwell-Boltzmann velocity distribution, and complete frequency redistribution, $R(x, x', \mu, \mu', z)$ is given by

$$R = \frac{1}{4\pi} k_0 \phi(x', z) \frac{\phi(x, z)}{\sqrt{\pi}} \tag{9}$$

where $1/4\pi$ is the angular probability for isotropic scattering, $k_0\phi(x', z)$ is the absorption probability of a photon with frequency x' by atomic oxygen at altitude z, and $\phi(x, z)/\sqrt{\pi}$ is the probability of the photon being reemitted with a frequency x. The total volume emissivity ε can be expressed as

$$\varepsilon(x, \mu, z) = \varepsilon(z) \frac{\phi(x, z)}{\sqrt{\pi}} \tag{10}$$

where $\varepsilon(z)$ is the total volume emissivity in photons cm^{-3} s^{-1} ster^{-1}, which is given by the integration of $\varepsilon(x, \mu, z)$ over all frequencies, and $\phi(x, z)$ is the frequency profile given by

$$\phi(x, z) = r(z) e^{-r(z)^2 x^2} \tag{11}$$

where $r(z) = \sqrt{T_0/T(z)}$, and T_0 is the exospheric temperature. After some manipulations, the total volume emissivity can be expressed as

$$\varepsilon(z) = \varepsilon_0(z) + \int \varepsilon(z')\, H(|\tau_x - \tau'_x|) dz' \tag{12}$$

where the Holstein probability is given by

$$H(|\tau_x - \tau'_x|) = \frac{1}{2\sqrt{\pi}} \frac{k_0(z)}{r(z)} \int r e^{-r^2 x^2} r' e^{-r'^2 x^2} e^{-\frac{|\tau_x - \tau'_x|}{\mu}} dx \frac{d\mu}{\mu} \tag{13}$$

which is the probability that a photon emitted in dz' at z' will be resonantly absorbed in dz at z.

Once the total volume emissivity ε is obtained by solving equation (12), the column emission rate of OI 135.6-nm emissions observed at a given location can be calculated by integrating the effective volume emissivity along the line of sight. Expressed in Rayleighs, the brightness $I_{135.6}$ is given by

$$4\pi I_{135.6} = 10^{-6} \int J(s)[B_5 T(\tau'_x) + B_3 T(\tau''_x)]\, ds \tag{14}$$

where $J(s) = 4\pi\varepsilon(s)$ is the total volume excitation rate at location s along the line of sight, τ'_x and τ''_x represent the optical depths of the two lines from the emission location s to the observer. Here the function $T(\tau_x)$ represents the Holstein transmission probability given by

$$T(\tau_x) = \frac{1}{\sqrt{\pi}} \int r e^{-r^2 x^2} e^{-\tau_x} dx \tag{15}$$

which is the probability that a photon will traverse a path with optical depth τ_x without being scattered or absorbed (Strickland 1979; Meier 1991). The radiative transfer problem of the OI 135.6-nm emission in the nighttime ionosphere can be solved numerically by properly discretizing equations (12) and (14).

To construct a matrix form of the radiative transfer equations, the upper atmosphere is divided into N zones with variable width, in which the lower and upper boundaries of the nth zone are represented by z_n and z_{n+1}, respectively, as shown in Figure 5.1. The integral in equations (12) and (14) can then be evaluated zone by zone. Assuming that $\varepsilon(z)$ is constant in each zone, the emissivity equation (12) can be approximated as

$$\varepsilon_n = \varepsilon_{0n} + \sum_{m=1}^{n} G_{nm} \varepsilon_m \tag{16}$$

and the matrix elements G_{nm} are given by

$$G_{nm} = \int_{z_m}^{z_{m+1}} H(|\tau_n - \tau'_x|) dz' \tag{17}$$

where τ_n is the optical depth at the center of the nth zone, and τ'_x represents $\tau_x(z')$. The total volume emissivity ε can be computed numerically by inverting the matrix $(\mathbf{I} - \mathbf{G})$, namely

$$\varepsilon = (\mathbf{I} - \mathbf{G})^{-1} \varepsilon_0 \tag{18}$$

where **I** is the identity matrix. In general, equation (14) can be expressed in the following matrix form

$$I_n = \sum_{m=1}^{N} T_{nm}\varepsilon_m \tag{19}$$

where ε_m is the total volume emissivity in the mth zone that is assumed to be constant inside each zone, and $\mathbf{T}$ is a $N \times N$ square matrix with each element T_{nm} given by

$$T_{nm} = T(\tau_{nm})\Delta s_{nm} \tag{20}$$

where Δs_{nm} represents the distance intersected by the nth line of sight in the mth zone. Combining equation (18) with $I_{135.6} = \mathbf{T}\varepsilon$ leads to

$$\mathbf{b} = \mathbf{Ax} \tag{21}$$

where $\mathbf{b} = 4\pi I_{135.6}$ and $\mathbf{x} = 4\pi\varepsilon_0$ represent the noise-free brightness data and the source volume emission rates, respectively, and the matrix $\mathbf{A} = \mathbf{T}(\mathbf{I} - \mathbf{G})^{-1}$ is constructed based on the important physical processes discussed above, namely the production and transport of the 135.6-nm emission, to relate $\mathbf{x}$ and $\mathbf{b}$.

5.2 Signal Estimates and Geometrical Considerations for Limb Profiles

The responsivity of all imaging instruments is the combination of two major factors (1) the number of photons collected, $P0$ defined by the input aperture area and the solid angle of the field of view (2) ε, the overall conversion efficiency, the efficiency at which input photons are converted into measurable output signal. Measurable signal is defined by the signal to noise ratio (SNR). In an idealized Poissonian system, for example when photo-electrons are emitted by a photocathode, the SNR is equal to the square root of the number of collected photo-electrons. The SNR performance of any system can be characterized by the number of equivalent output photo-electrons which is equal to the square of the SNR at the output. Thus the overall conversion efficiency ε, is the ratio of the equivalent output photoelectrons (SNR squared) divided by the number of input photons. ICON FUV underwent extensive calibration and the conversion efficiency was measured and the responsivity was estimated by combining the efficiency with the geometrically measured FOV and aperture size at the input slit.

To evaluate the ICON FUV imager performance we have defined several relevant spatial bins. A resolution element is an angular bin of 0.093◦ × 0.093◦ and this corresponds to 1 binned pixel on the detector. Note that the geometric distortion does not allow linear transformation of the detector pixels to angular sampling elements. There are 256 × 256 binned pixels on the detector. The vertical dimension of 0.093° is derived from the 24◦ vertical dimension of the FOV divided into 256 binned pixels. The 0.093◦ angle also represents a ~ 4 km altitude step at a tangent height of 155 km, assuming an orbital altitude of 575 km (Table 5.1).

In the following Table we have listed the most significant characteristics of the ICON FUV instrument. For the sensitivity calculations we assumed that the instrument field of view was divided into 6 vertical stripes (line 4 Table 5.1). The science pixel field of view is therefore 3.0° wide and one VRE or 0.093° tall (line 7). Combining this with the measured input slit dimension of 5 × 32 mm provides the etendue per science pixel (Table 5.1 line 11) and the photon collection rate (line 12).

	Parameter	Value	Remarks
1	Orbit	575 km circular 27 degree inclination	Launch from Kwajalein
2	Optic axis	Perpendicular to velocity vector north. 20° below local horizontal.	Steering mirror allows ±30°
3	Field of View	24° × 18° (vertical × horizontal)	
4	Number of science pixels[a] in vertical stripes	~ 256 × 6 (vertical × horizontal)	For limb brightness profile
5	Number of pixels for imaging	256 × 192 (vertical × horizontal)	TDI imaging
6	Maximum altitude coverage	−8° to −32° elevation	−8° = tangent height of 507 km
7	Pixel FOV for vertical stripe	3.0 × 0.093°	6 vertical stripes
8	Pixel FOV for 2di imaging	0.09375° × 0.09375°	TDI imaging
9	Slit area 5 mm × 32 mm	1.6	cm^2
10	Field of view 24° × 18°	0.14 (truncated circle) equivalent F No. = 2.7	sr
11	Étendue per science pixel	1.3e−04 cm^2 sr	$\Omega = 0.093 \times 3.0$ degrees
12	Geometric photon collection rate at input aperture	10.9	Photon/s/science pixel/Rayleigh

[a] Science pixel: $\Omega = 0.093°$ (vertical) ×3.0° (horizontal) → 0.093° corresponds to a Vertical Resolution Element (VRE) of 4 km altitude at tangent height of 155 km = ~1 binned pixel = 4 CCD pixels

Table 5.1: ICON FUV performance summary.

The overall efficiency of ICON FUV was measured directly in the lab during calibrations at CSL. In Table 5.2 we list the various components and their transmissions for each channel. The predicted efficiency of the system, line 5 is the combination of reflectivity of the mirrors and the grating and the photocathode efficiency. The calculated efficiency is somewhat smaller than 1%. Unfortunately the measured value obtained from the calibration (line 6) is smaller than the predicted value. For the SW channel this discrepancy is about a factor of 2 lower but it is substantially more different for the LW channel. The cause for this discrepancy is unknown. In line 7 we tabulated the predicted instrumental counting rates for the two channels and in line 8 the actual measured calibrated counting rates. The science requirement was written in terms of counting rate per altitude bins regardless of the horizontal size of the bin and it is shown in line 9. The counting rate is given here for one stripe out of six and several stripes can be co-added to improve the signal to noise ratio and meet the science requirement with more margin.

The data presented in Table 5.2 shows 97.5 predicted and 49 measured counts/s/kR for the 135.6 nm SW channel per science pixel. There are 6 parallel vertical stripes and the data could be summed up from the six adjacent strips. However the outermost strips have FOV limitations at the top and at the bottom due to the oval shape of the FOV.

It is interesting to compare responsivities with previously flown FUV imagers. IMAGE SI 135.6 nm channel provides a ready example for comparison. A resolution element is defined as a region of 0.093 × 0.093 degree region. There are 192 resolution elements across the 6 channels representing 192/6 = 32 horizontal resolution elements. The counting rate would be 49.0/32 = 1.5 counts/s/kR per single resolution element. The IMAGE SI had a 128 × 128 pixel raster and a counting rate of 3 counts per kR/s in its 135.6 nm channel. If its image were subdivided to a 256 × 256 pixel raster like in ICON then its counting rate would be 0.75 counts/s/kR. We consider that this is in fair agreement with the ICON numbers. We had hoped for better performance because the ICON camera has a larger FOV and therefore larger etendue and it does not have a 1/3rd transmission grill in its entrance slit. Unfortunately the lower grating efficiency and the relatively low detector quantum efficiency cancelled some of the advantages the ICON instrument should have had.

The LW channel measurements do not agree well with predicted performance. The most likely explanation of this is the (difficult) grating efficiency measurement. The grating efficiency in the SW is twice that in the LW; this is difficult to understand on physical grounds given the relatively small difference in wavelength. If we assumed the two grating efficiencies were equal, as would be expected from analytical modeling, then the LW channel efficiency is closer to that predicted and the differences can be attributed to variations in reflectivity optic to optic, which is a particularly important factor in a multi-reflection system like ICON FUV.

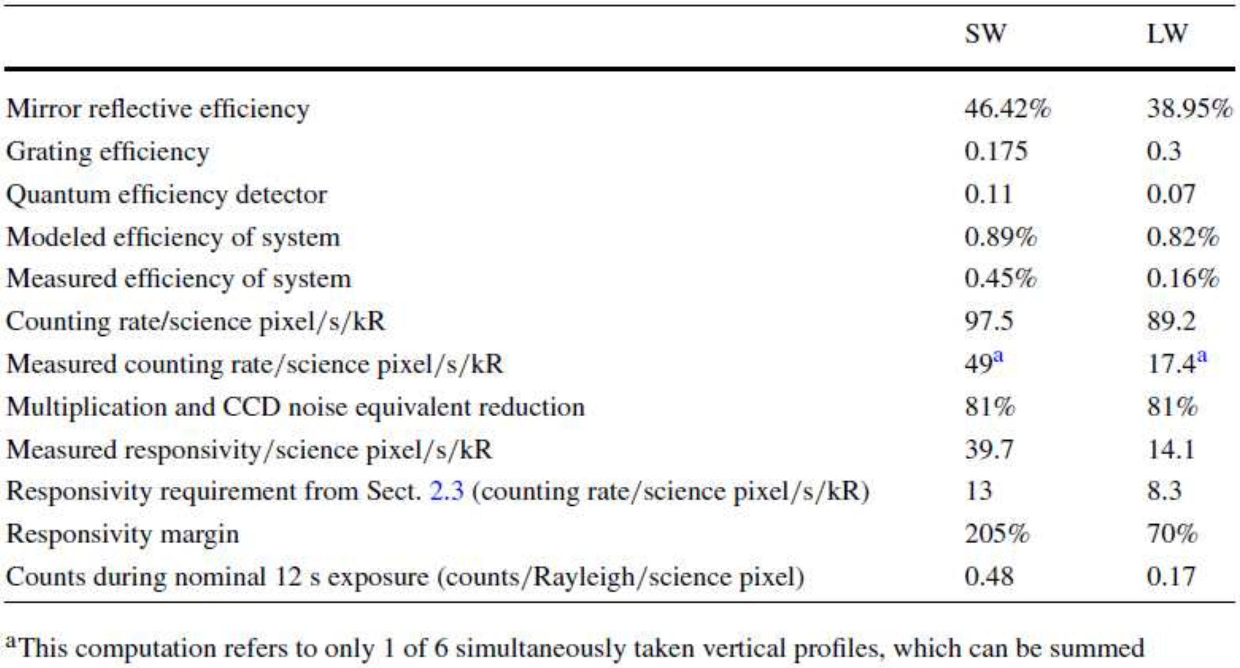

	SW	LW
Mirror reflective efficiency	46.42%	38.95%
Grating efficiency	0.175	0.3
Quantum efficiency detector	0.11	0.07
Modeled efficiency of system	0.89%	0.82%
Measured efficiency of system	0.45%	0.16%
Counting rate/science pixel/s/kR	97.5	89.2
Measured counting rate/science pixel/s/kR	49[a]	17.4[a]
Multiplication and CCD noise equivalent reduction	81%	81%
Measured responsivity/science pixel/s/kR	39.7	14.1
Responsivity requirement from Sect. 2.3 (counting rate/science pixel/s/kR)	13	8.3
Responsivity margin	205%	70%
Counts during nominal 12 s exposure (counts/Rayleigh/science pixel)	0.48	0.17

[a] This computation refers to only 1 of 6 simultaneously taken vertical profiles, which can be summed

Table 5.2: ICON FUV responsivity by channel.

5.3.2 Signal Estimate and Error Analysis for Daytime Disk O/N$_2$

In order to estimate the statistical error in a quantity derived from a measurement of one or more variables, we follow the standard propagation of errors methodology described in Bevington and Robinson (1992) for a normal distribution of counting statistics. For a quantity, x that is a function of two or more variables, u and v, the dependence is described by:

$$x = f(u, v, \ldots) \qquad (3)$$

If u and v are measured quantities, the above equation allows the computation of x. If the standard deviations of the measured quantities are σ_u, σ_v, … Then the variance in the computed value of x is given by the error propagation equation:

$$\sigma_x^2 \cong \sigma_u^2 \left(\frac{\partial x}{\partial u}\right)^2 + \sigma_v^2 \left(\frac{\partial x}{\partial v}\right)^2 + \cdots + 2\sigma_{uv}^2 \left(\frac{\partial x}{\partial u}\right)\left(\frac{\partial x}{\partial v}\right) + \cdots \qquad (4)$$

The column density ratio ($\Sigma\mathrm{O}/\mathrm{N}_2$, equivalent to x above) can be rewritten as a function of the FUV instrument short wavelength (SW) channel column emission rate to long wavelength (LW) channel column emission rate ratio ($\frac{4\pi I_{SW}}{4\pi I_{LW}}$, equivalent to u above):

$$\Sigma O/N_2 = \mathrm{f}\left(\frac{4\pi \mathrm{I_{SW}}}{4\pi \mathrm{I_{LW}}}\right). \qquad (5)$$

The $\Sigma\mathrm{O/N_2}$ is a function (f) only of the measured emission rate ratio. Consequently, the uncertainty in $\Sigma\mathrm{O/N_2}$ is given by the first term in Equation 4 above:

$$\sigma^2_{\Sigma O/N2} = \sigma^2_{SW/LW}\left(\frac{\partial\left(\Sigma\frac{O}{N_2}\right)}{\partial\left(\frac{4\pi \mathrm{I_{SW}}}{4\pi \mathrm{I_{LW}}}\right)}\right)^2. \qquad (6)$$

In order to increase the statical accuracy of the disk SW/LW measurement, 20 pixels are averaged together. Pixels 15 to 35 were selected for averaging to avoid vignetting of edge pixels. This is justified because the disk emission rates are nearly uniform over the 20 pixels. The variance of the emission rate ratio, $\sigma^2_{SW/LW}$, is given by the square of the standard deviation of the 20 pixels. From the Central Limit Theorem, the distribution of the emission rate ratios over the 20 pixels should be nearly Gaussian.

Details of the disk algorithm are given in Meier (2021). The partial derivatives in Equation 6 above are obtained numerically from the computed dependency of the column density ratio on the column emission rate ratio (Equation 5 above). The standard deviation of the retrieved column density ratio, $\sigma_{\Sigma O/N2}$, is reported in the Level 2.4 database. Note again that the above derivation only accounts for random uncertainties. Systematic uncertainties are currently under study, and can be discussed in the systematic offset between the limb and disk column O/N_2.

5.3.3 Signal Estimate and Error Analysis for Daytime Limb O/N$_2$

The retrieval process uses a Levenberg-Marquardt (LM) inversion scheme to find the set of parameters (scalars) that provide the optimal match to the SW and LW radiances. The LM algorithm automatically returns the uncertainty of each scalar based on the uncertainty of the radiance at each tangent altitude for a single limb scan.

Next, the uncertainties in the scalars must be propagated into uncertainties in the number densities and temperatures. Using the standard propagation of errors formula in Equation 4 (Bevington and Robinson, 1992), the variance (square of the uncertainty) in physical quantity, X_i, is:

$$\sigma_i^2 = \sum_j \sum_k \sigma^2_{f_j f_k} \frac{\partial[X_i]}{\partial f_j}\frac{\partial[X_i]}{\partial f_k} \qquad (8)$$

However, as discussed below, there is an unknown source of scattered light in both SW and LW channels. We have developed a complex novel technique to account for this scattered light that involves additional a priori information. The formalism for this technique will be discussed in a future publication. Below is a brief summary of the process.

For a single channel, the Level-1 radiance is given by:

$$4\pi I^{L1} = 4\pi I^{ts} - B, \tag{9}$$

where $4\pi I^{ts}$ is the total signal in Rayleighs and B is the CCD background. This has an uncertainty given in the Level 1 data products, σ^{L1}. This accounts for uncertainties in both $4\pi I^{ts}$and B.

To remove the scattered light and any other issues, this needs to be operated on by a scattered light matrix called the inverse transform matrix T^{inv}. Thus, the data to be inverted are modified in the following way:

$$4\pi I^{d} = T^{inv}\, 4\pi I^{L1} \tag{10}$$

The uncertainty in of T^{inv} , σ^{Tinv} is produced as part of its derivation.

In matrix notation,

$$4\pi I_i^{d} = \sum_{j=1}^{256} T_{ij}^{inv}\, 4\pi I_j^{L1} \tag{11}$$

Using the propagation of errors formalism, the radiance in the Level 1 data base should be:

$$\left(\sigma_i^{d}\right)^2 = \left(\sigma_{i1}^{Tinv}\right)^2 \left(\frac{\partial 4\pi I_i^{d}}{\partial T_{i1}^{inv}}\right)^2 + \left(\sigma_j^{L1}\right)^2 \left(\frac{\partial 4\pi I_i^{d}}{\partial 4\pi I_1^{L1}}\right)^2 + \cdots \tag{12}$$

or,

$$\boxed{\left(\sigma_i^{d}\right)^2 = \left(\sigma_{i1}^{Tinv}\right)^2 (4\pi I_1^{L1})^2 + \left(\sigma_j^{L1}\right)^2 \left(T_{i1}^{inv}\right)^2 + \left(\sigma_{i2}^{Tinv}\right)^2 (4\pi I_2^{L1})^2 + \left(\sigma_j^{L1}\right)^2 \left(T_{i2}^{inv}\right)^2 + \cdots} \tag{13}$$

This is now the uncertainty that must assigned to the Level 1 data products that are used by the LM optimization algorithm.

After a great deal of analysis, we find that the uncertainties described by Equation 11 are unexpectedly large, where using Equation 8 to characterize the uncertainties in the Level 2.4 data products are too small**.** Neither Equation 8 or Equation 11 provide a means to include any systematic errors. As will be seen below, we believe that the temperatures and therefore number densities are too large due to limitations of the scattered light correction.

5.3.4 Comparison of Limb and Disk Thermospheric Data products

Limb vs disk column O/N_2

After syncing and filtering the limb and disk $\Sigma O/N_2$, the two data products can be compared directly by plotting limb vs disk. Figure 5.2 is a plot of this comparison. Both the data and the predictions of NRLMSIS00 are shown. The left panel shows the data plotted on top of the model and the right panel is the opposite.

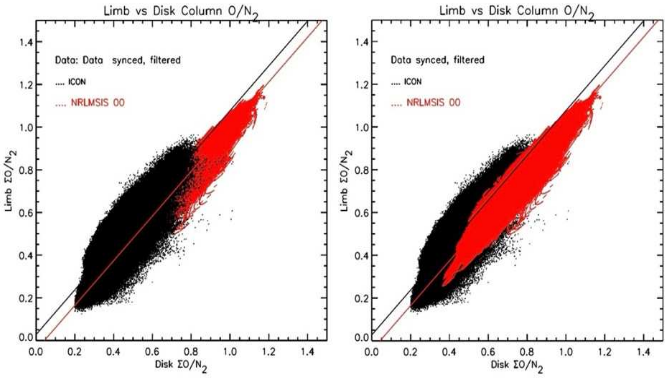

Fig 5.2 – Comparison of column O/N2 retrievals to MSIS, from both the limb and the disk retrievals, over a the full mission, for times when both limb and disk retrievals were available.

The data and the model have virtually identical slopes at 1.05, although their offsets are slightly different. The differences in their magnitudes discussed in the last section are apparent. The broader envelope of data points is a consequence of real variability relative to the climatological model.

FUV limb data products

Intercomparison of data products

Next is a brief look at selected limb data products to check for reasonableness. Because of the presence of unknown scattered light in the FUV instrument, and the complexity of the conversion of incoming dayglow photons into data products, a rigorous error analysis has not been completed. As discussed above, upper and lower limits to the data uncertainties have been derived but are unreliable. The current Level 2.4 database reports only the lower limits to the uncertainties—Equation 8.

In this section, number densities at selected altitudes and temperatures are illustrated and compared with NRLMSIS00 and with GUVI data (Meier et al., 2015) obtained under similar observing conditions as ICON.

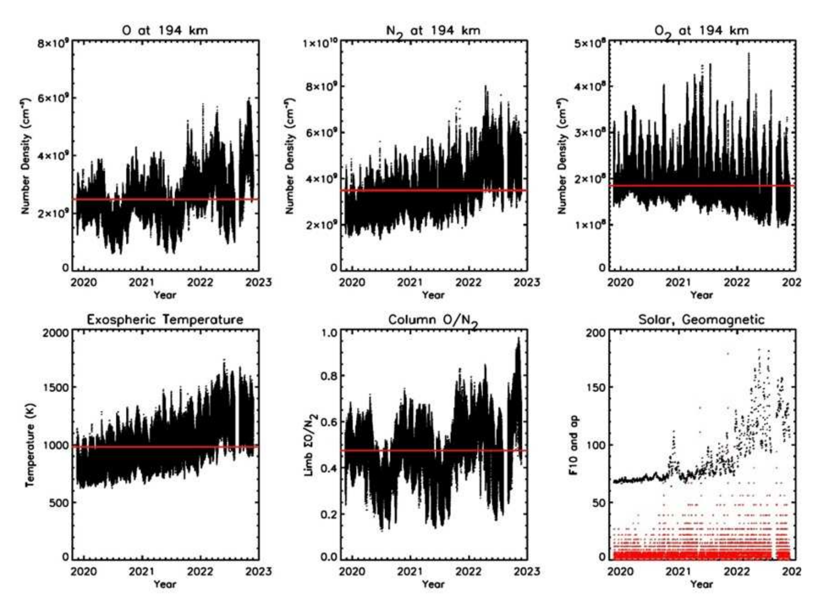

Fig 5.3 Limb products, or samples of those products, from FUV for the full ICON mission.

Figure 5.3 contains time series of the O, N_2 and O_2 number densities at 194 km, the inferred exospheric temperature, the column O/N_2, and the solar/geomagnetic conditions for the database. Red horizontal lines represent the data medians. As before, the data shown have been filtered for warning flags and the limb and disk data have been synchronized in time.

Following extensive testing, the ICON O_2 density scalar was set equal to unity in order to restrict uncertainties in corrections for the unknown scattered light (to be discussed elsewhere). This is supported by the GUVI conclusions that O_2 is well-represented in the lower atmosphere by NRLMSIS00 (Meier et al., 2015). At higher altitudes, O_2 can depart from the model because temperatures are not confined to NRLMSIS00 values. The O_2 number densities should not be considered independent measurements.

Comparing the O and $\Sigma O/N_2$ panels in Figure 5.3 confirms that the seasonal and higher frequency orbital modulations are due mostly to atomic oxygen and not to N_2. The exospheric temperature and the O and N_2 number density rise as expected with increasing solar activity.

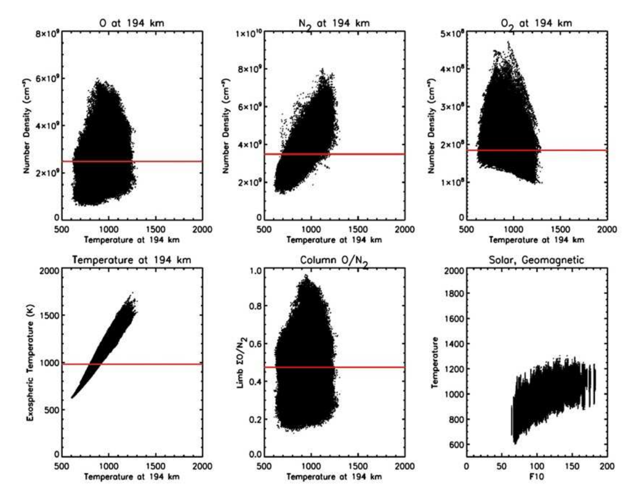

Fig 5.4 – Limb products vs Limb Temperature product @ 194 km altitude.

Figure 5.4 shows the data products in the same format as Figure 5.3, but with the retrieved temperature at 194 km as the abscissae. The lower right panel more clearly displays the rise in temperature with solar activity and the N_2 number density clearly follows the rise in temperature. However, neither O nor O_2 vary as much as N_2 with solar activity, indicating the influence of photochemistry and dynamics at 194 km. Column O/N_2 , also does not correlate with temperature, as expected (it is easy to show that $\Sigma O/N_2$ is independent of temperature in a diffusive equilibrium atmosphere).

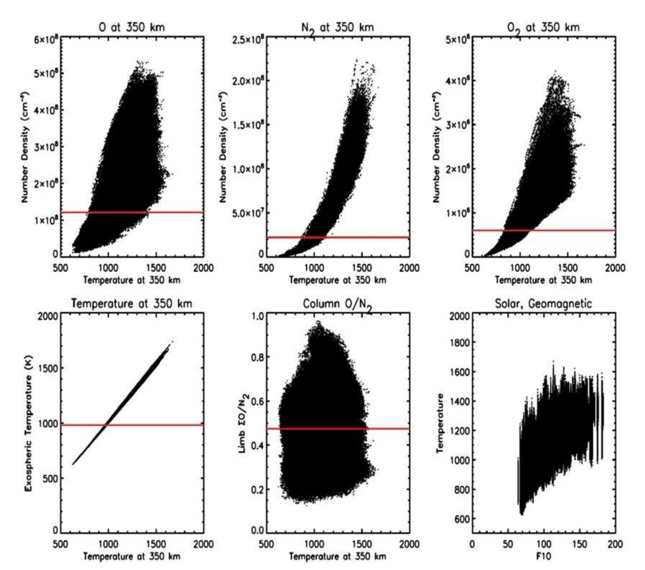

Fig 5.5 Limb products vs Limb temperature at 350 km.

Moving up to 350 km altitude in Figure 5.5, the atmospheric behavior is looking much more like diffusive equilibrium. The broad spread in O and O_2 signifies the continuing influence of chemistry and dynamics. $\Sigma O/N_2$ again does not mimic temperature. And the temperature at 350 km is now much closer to the exospheric temperature (lower left panel) because the ICON mission took place at low solar activity, when the exobase is lower.

Comparison with NRLMSIS00

In order to assess the reasonableness of the ICON FUV data in the previous figures, Figure 5.6, in the same format as Figure 5.4, contains the NRLMSIS00 predictions for the same observing conditions as ICON at 194 km. Red lines are the medians, which are lower than the center of amassed data points, indicating how many points are masked by overplotting. The behavior of NRLMSIS00 is more like diffusive equilibrium at this altitude than are the ICON data in Figure 5.4. This is not particularly surprising because earlier versions of MSIS at least, reached diffusive equilibrium at lower altitudes than did TIEGCM (Figure 4 of Meier et al., 2001).

Note that the spread in points of the data in Figure 5.4 is not much larger than in NRLMSIS00 in Figure 5.6, indicating that the variability is real and not due to counting statistics or data processing.

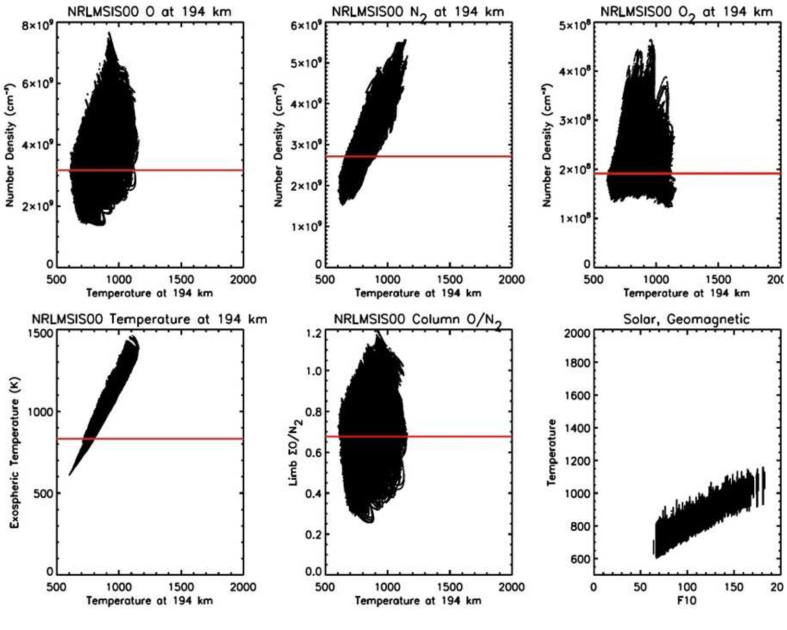

Fig 5.6 NRLMSIS00 outputs vs Limb Data Temperature retrieval at 194 km

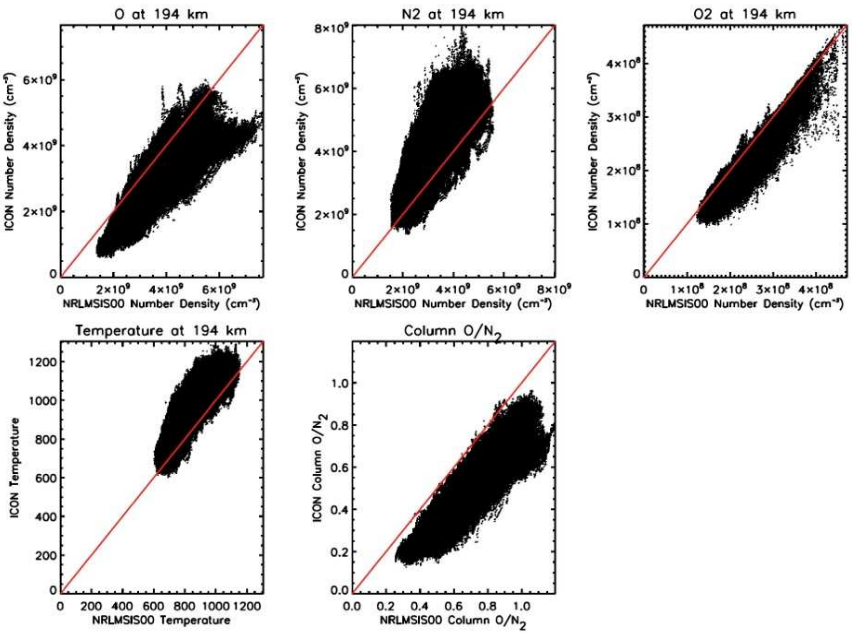

Fig 5.7 NRLMSIS00 vs ICON limb retrievals of same parameters

A point-by-point plotting of the ICON data against the NRLMSIS00 predictions is shown in Figure 5.7. The red lines are the unity slope diagonals. O and N_2 number densities are smaller and larger than NRLMSIS00, accounting for the low column O/N_2.

The higher ICON temperatures may be due the high N_2 values and the low $\Sigma O/N_2$. This may indicate a problem in removing scattered light from the radiance data, especially at higher altitudes, to be evaluated in one final Version 7 product.

Comparison with GUVI

In this section, we compare ICON column O/N_2 number densities and column O/N_2 from the GUVI ***limb*** measurements only.

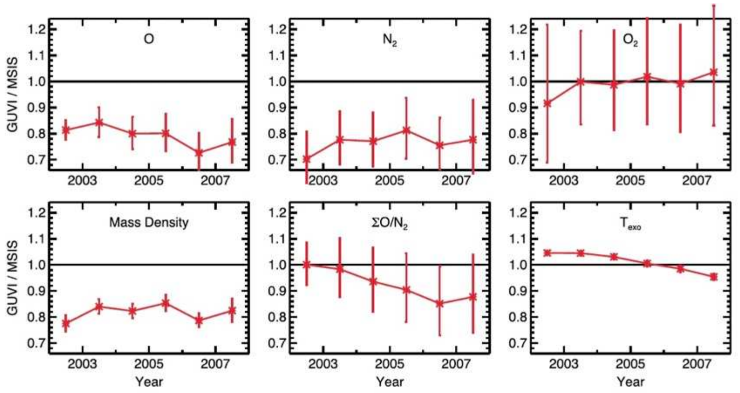

Fig 5.8 General values of GUVI Thermospheric retrievals from over 4 years of the TIMED mission.

The ICON FUV database includes densities and temperatures from NRLMSIS00. Although NRLMSIS 2.0 was published before the ICON limb data products were available (Emmert et al., 2020), the team decided to continue using NRLMSIS00 for continuity in various versions of the database. Precomputed NRLMSIS00 predictions matching the ICON data products also enables ready comparison with the same model included in the GUVI database that was obtained 20 years earlier.

Meier et al. (2015) published yearly averages of GUVI limb data products. Their Figure 20 is reproduced here as Figure 5.8. Higher solar activity occurred in the early GUVI years and low solar activity was in the later years of Figure 5.8. The altitude of comparison is 194 km. GUVI O is lower than NRLMSIS00, consistent with ICON. However, the GUVI N_2 (everywhere) and exospheric temperature (2006 and 2007) are both lower than NRLMSIS00, in contrast to ICON data that shows them higher than NRLMSIS00. This again could be explained by insufficient correction for scattered light in the FUV instrument, especially in the long wavelength channel that measures N_2 exclusively.

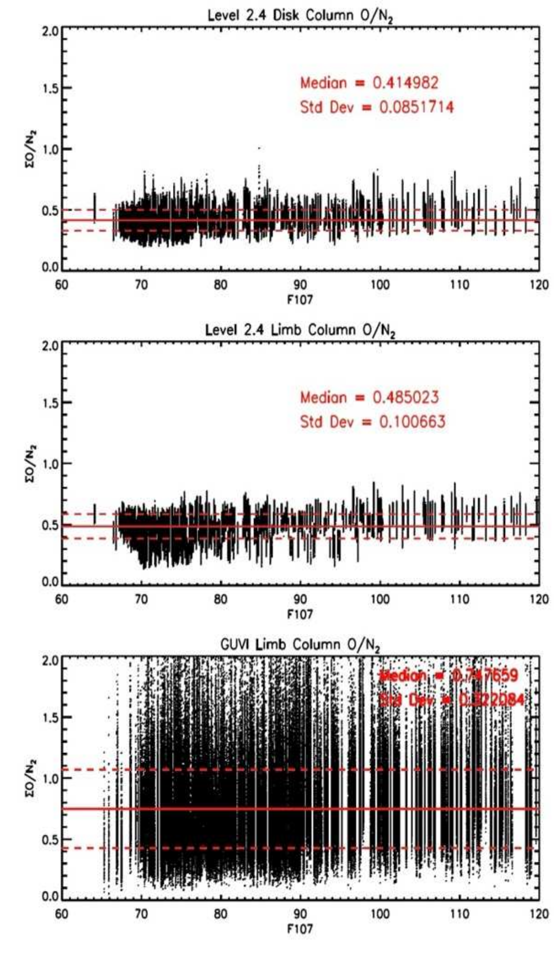

Fig 5.9 Limb and Disk ICON FUV retrievals vs F107

A more straightforward comparison of ICON and GUVI $\Sigma O/N_2$ data is in Figure 5.9. The top panel contains the ICON disk values, the middle panel is the ICON limb values and the bottom panel is GUVI data. All data have been filtered with $F_{10.7} < 120$, Ap < 10, and |latitude| < 38 deg. The median values and the standard deviation from the means are indicated by the solid and dashed red lines, respectively. The GUVI median and standard deviation, which are hard to read in the figure, are 0.75 and 0.32. The large standard deviations for GUVI are due to the much lower instrument responsivity than ICON FUV.

NRLMSIS00 limb median $\Sigma O/N_2$ (not shown) for each of the limb data points in Figure 5.9 are 0.69 and 0.80 for ICON and GUVI, respectively, suggesting differences in the data sampling. The ratios of the median data to median model are:

ICON: 0.48/0.69 = 0.70

GUVI: 0.75/0.80 = 0.94

Exospheric temperature comparisons

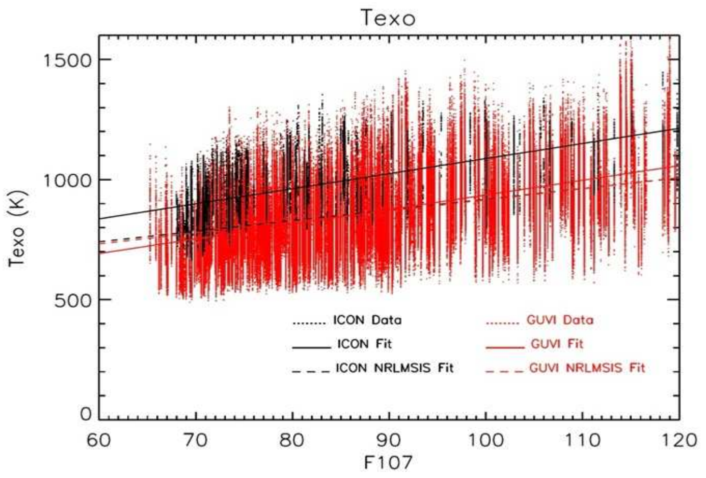

Fig 5.10 GUVI vs ICON FUV Texo vs F10.7.

Figure 5.10 compares ICON and GUVI exospheric temperatures vs F_{10} using the same filtering as in the last section. The solid lines are linear fits to the data and dashed lines are fits to the NRLMSIS00 predictions that are not shown to reduce clutter in the figure. The solid lines show the clear discrepancy of about 150 K between the ICON and GUVI. Remarkably, the slopes of the two are virtually the same. The NRLMSIS00 fits for ICON and GUVI predictions are essentially the same and much closer to GUVI than ICON.

Q_{euv} Comparisons

As discussed in the beginning, the solar energy flux between 0-45 nm that is required to produce the absolute magnitude of the dayglow emissions can be extracted from the magnitudes of either the limb or disk radiances. Figure 5.11 shows a comparison of ICON and GUVI Q_{euv} with SEE solar measurements. Black points are ICON, red points are GUVI, and green are the SEE data that were used in the GUVI limb algorithm. A few outliers in the ICON data can be seen at very low Q_{euv} levels and again at the lowest F_{10} values. These are due to occasional FUV instrument special operations that were not properly filtered out.

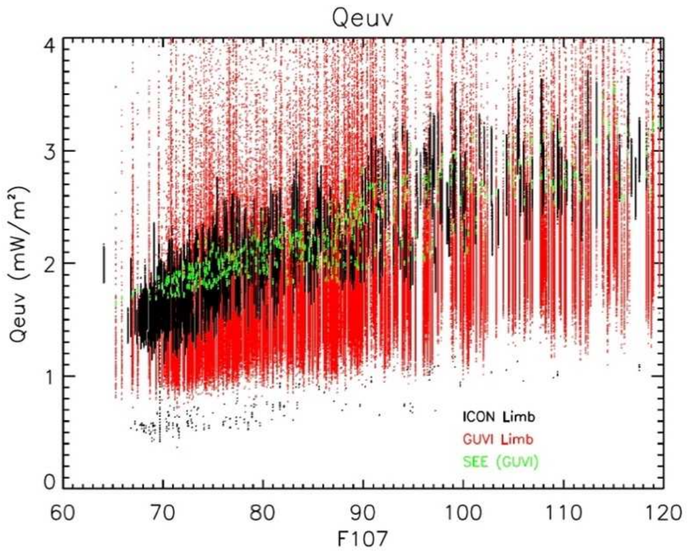

Fig 5.11 – Qeuv retrieved from 3 sources (ICON FUV, GUVI and SEE) vs F107

The medians of the ICON and GUVI data are remarkably similar at 1.88 and 1.86 mW/m^2, respectively. An important implication of these close values is that the absolute calibrations of the two instruments flown 20 years apart are close. The SEE data are higher at a median of 2.38, as was found by Meier et al. (2015). But note that the ICON data are heavily weighted toward $F_{10} < 80$, whereas there are not many SEE points there.

The solar Q_{euv} used as input to the ICON FUV forward model is from an updated version of the Lean et al. (2011) model based on SEE data. Unfortunately, this was not passed through the ICON limb database.

Conclusions

Overall, the variability in both the disk and limb data products obtained by the ICON FUV instrument is remarkably precise and the data can be used in studies of thermospheric behavior. Some discrepancies with the NRLMSIS00 model are present and not unexpected. However, discrepancies with GUVI data also exist and point to the need for further work on the data processing. Detailed conclusions are itemized below. The next Section suggests possible resolution of the differences.

- Flag filtering removes anomalous data points.
  - Syncing and filtering removes 14% of limb points and 18% of disk points.
  - But some of the flagged data are probably good.

- The column O/N_2 retrievals from both the limb and disk FUV emissions vary in similar ways with orbital precession, season, solar activity, and geomagnetic activity (not included in this analysis).

- Because the limb portion of the FUV image generally looks further north than the disk portion of the image, a seasonal modulation is present in the difference between limb and disk $\Sigma O/N_2$.
  - NRLMSIS00 shows a similar modulation, verifying that the source is latitudinal gradients in the thermospheric composition.

- Medians of limb, disk and NRLMSIS00 $\Sigma O/N_2$ over the mission show differences. If the data are filtered with $F_{10} < 120$, ap < 10, and |latitude| < 38 deg, then the ICON data can be compared with GUVI. The median values of each of these are
  - Limb $\Sigma O/N_2$: ICON (0.41) < NRLMSIS00 (0.69) < GUVI (0.75)
  - Disk $\Sigma O/N_2$: ICON (0.47) < NRLMSIS00 (0.68)
  - The nearly equal NRLMSIS00 limb and disk $\Sigma O/N_2$ implies that the offset between ICON limb and disk is due to a data problem.

- Plots of limb vs disk $\Sigma O/N_2$ reveal nearly identical slopes of ICON and NRLMSIS00 with slightly different offsets. More spread in is present in the data due to real variability relative to the climatological model.

- Limb data confirm that the seasonal variations in $\Sigma O/N_2$ are due to O variability.

- O and O_2 at 194 km and $\Sigma O/N_2$ are lower than NRLMSIS00, whereas N_2 and temperature are higher.
    - In contrast, GUVI data filtered for $F_{10} < 120$, $ap < 10$, and $|\text{latitude}| < 38$ deg, have O and N_2 lower than NRLMSIS00. GUVI O_2 is slightly higher and exospheric temperature is slightly lower

- O and O_2 reveal the influence of chemistry and dynamics at 194 km, whereas N_2 behaves more like diffusive equilibrium
    - At 350 km, all three species take on more diffusive-equilibrium-like characteristics.

- ICON exospheric temperatures are high by about 150K compared with NRLMSIS00 and GUVI.
    - This suggests that the correction for scattered light in the FUV instrument is not exact and that the signal needs to be reduced.

- Both ICON and GUVI produce essentially the same Q_{euv} with median values of 1.88 and 1.86 mw/m^2, respectively, for $F_{10} < 120$. The version of SEE data available to Meier et al. (2015) gives 2.38 mW/m^2. Updated solar Q_{euv} for the ICON epoch will be available soon.

Future verification and validation tasks

- Additional work is needed on the methodology for removing scattered light, especially in the LW channel.
    - The focus of this effort is to improve the accuracy of the transform function.
    - This has the potential to resolve the discrepancies itemized above because it could
        - lower the emission scale height and therefore the temperature;
        - decrease the N_2 density at higher altitudes;
        - increase the disk SW/LW ratio and therefore the column O/N_2.

- Other validation tasks are to
    - compare simultaneous ICON and GOLD composition measurements
    - compute ICON total mass densities for comparison with satellite drag measurements

5.3.5 Signal Estimate and Error Analysis for Nighttime O+

In addition to providing estimates of the electron density profile, NmF2, and hmF2, the FUV nighttime data product includes estimated errors in these quantities. The only errors included in this estimate are statistical errors propagated from the brightness data. Systematic errors can be introduced via regularization and inaccurate knowledge of $[\mathrm{O}]$ in the MSIS model, but these are not included in the reported error.

The errors in the measured brightness profile are provided in the Level 1 data product and are dominated by Poisson counting statistics. Errors are propagated through the algorithm described in the previous sections, which comprises three steps: (1) a Tikhonov-regularized inversion to convert a brightness profile $\mathbf{y}$, to a volume emission rate (VER) profile, $\mathbf{x}$, (2) a solution of (22) to obtain an electron density profile, $\mathbf{N}$, and (3) a peak-finding step to extract hmF2 and NmF2. In order to propagate errors through these steps, various assumptions are used, which are described below. These assumptions are then validated by a Monte Carlo simulation.

Step 1 is a regularized inversion with a non-negativity constraint. For the purposes of propagating error, we ignore the non-negativity constraint, which only affects the lowest altitudes, not hmF2 and NmF2. Without this constraint, the inversion is linear, so the covariance matrix of $\mathbf{x}$, denoted $\mathbf{\Sigma_x}$, is simply

$$\mathbf{\Sigma_x} = \mathbf{M}\mathbf{\Sigma}_{\boldsymbol{y}}\mathbf{M}^T \tag{22}$$

where $\mathbf{\Sigma}_{\boldsymbol{y}}$ is the covariance matrix of the measured brightness, assumed to be diagonal (i.e., measurement errors at different angles are uncorrelated), and $\mathbf{M}$ is the inversion matrix from (25):

$$\mathbf{M} = \left(\frac{1}{\sigma_w^2}\mathbf{A^T A} + \gamma^2 \mathbf{L^T L}\right)^{-1} \frac{1}{\sigma_w^2}\mathbf{A}^T \tag{23}$$

Step 2 is nonlinear, involving the solution of a third order polynomial. To propagate error through this step, we assume MN is negligible compared to RR (i.e., [O] = 0), which simplifies the solution of (22) to

$$\mathbf{N} = \sqrt{\frac{4\pi x}{\alpha_{135.6}}} \tag{24}$$

The nonlinearity of (30), which is especially significant for low VER, is too large for linearized error propagation, so actual confidence intervals are calculated, approximating the distribution of $\mathbf{N}$ as a multivariate Gaussian. Thus, the propagated covariance matrix of $\mathbf{N}$ is

$$\mathbf{\Sigma}_{\mathrm{N}}^{ij} = \begin{cases} \frac{4\pi x}{\alpha_{135.6}}\left(\sqrt{x_i + \sigma_x^i} - \sqrt{x_i}\right) & \text{if } i = j \\ \frac{\sigma_N^i \sigma_N^j}{\sigma_x^i \sigma_x^j}\mathbf{\Sigma}_{\boldsymbol{x}}^{ij} & \text{if } i \neq j \end{cases} \tag{25}$$

where σ_x^i and σ_N^j are the uncertainty of VER and electron density at altitude i:

$$\sigma_x^i = \sqrt{\mathbf{\Sigma}_{\mathrm{x}}^{ii}} \tag{26}$$

$$\sigma_N^i = \sqrt{\mathbf{\Sigma}_{\mathrm{N}}^{ii}} \tag{27}$$

Step 3 uses a peak-finder, which is not an analytic function, so errors are propagated using a Monte Carlo method. Many realizations of electron density profiles are calculated by sampling from a multivariate Gaussian distribution with mean $\mathbf{N}$ and covariance matrix $\mathbf{\Sigma}_{\mathrm{N}}$. The parameters hmF2 and NmF2 are estimated from each trial. The standard deviation of the trials provides the final estimated error, σ_{hmF2} and σ_{NmF2} . In practice 100 trials are used.

We validate this error propagation algorithm with an end-to-end Monte Carlo simulation. Using a "true" electron density profile from IRI and neutral oxygen profile from NRL- MSISE00, along with an assumption of spherical symmetry, 1000 brightness profiles are simulated with different shot noise realizations. Each profile is fed through the inversion, resulting in 1000 estimates of hmF2 and NmF2, and 1000 propagated values of σ_{hmF2} andσ_{NmF2}. The mean 68.3% confidence ellipse determined from σ_{hmF2} and σ_{NmF2} agrees well with the sample error ellipse determined from the 1000 values of hmF2 and NmF2, as shown in Figure 5.12. Indeed, 69.6% of the 1000 trials lie within the propagated ellipse, closely matching the expectation of 68.3% for Gaussian statistics. This validates the assumptions used above. A small correlation (ρ = -0.2) is seen

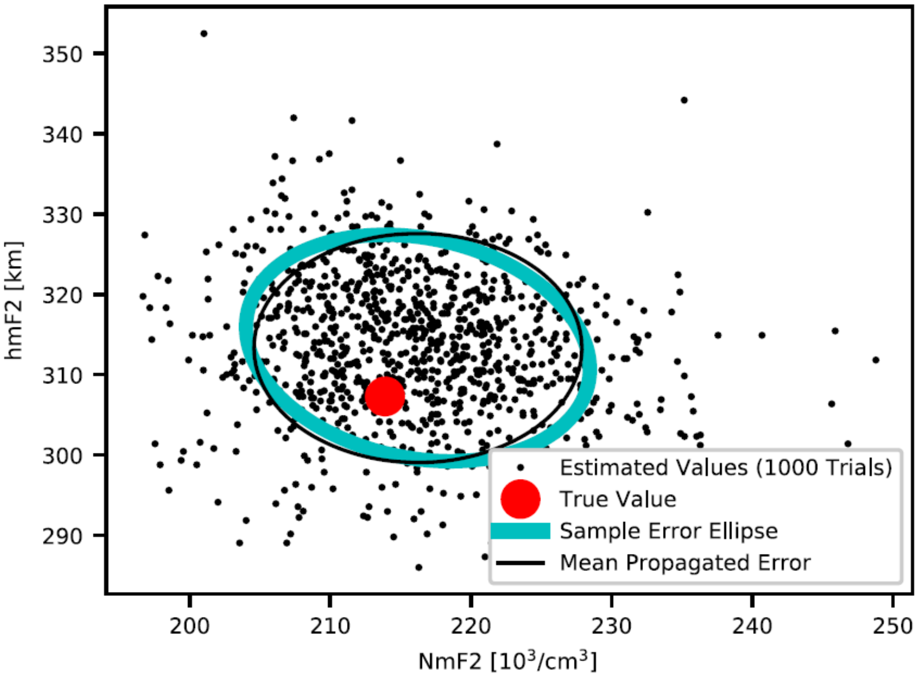

between the samples of hmF2 and NmF2. A small but significant bias exists between the true hmF2 and NmF2 and the mean estimated hmF2 and NmF2. This validation was performed for a low SNR (corresponding to a measured brightness of 10 R on the limb). As SNR increases, the correlation and bias both tend towards zero.

Fig 5.12 The error propagation algorithm is validated with a Monte Carlo simulation. A model electron density profile is used to simulate 1000 noisy measurements, from which 1000 samples of hmF2 and NmF2 are generated. The covariance ellipse of these samples is compared to the mean propagated error

A representative ICON partial orbit and the corresponding set of FUV viewing geometry data were generated and used in combination with the forward model described in the previous sections to create a set of airglow volume emission rates and limb-viewing intensity profiles for the 135.6 nm emission. The simulation spans one nightside orbital pass, from 00:19 to 01:10 UT on 20 Mar 2009 (i.e., solar minimum, F10.7 = 68.2 sfu). For each ICON FUV exposure, the simulations correspond to a single-column ionospheric electron density along the line of sights representing a spherically symmetric, vertically stratified ionosphere described in the forward model of the previous sections. The limb-viewing measurements through these layers are therefore inverted as a single profile for each exposure. Note that while horizontal gradients or structured features caused by ionospheric instabilities may exist in the nighttime ionosphere, ICON FUV is built and operated specifically to reduce the effects of ionospheric instabilities in the estimation of ionospheric state by steering its field of view to always contain the local magnetic meridian. The steered turret mechanism is designed to minimize the effect of horizontal gradients produced by spread-F or other field-aligned irregularities.

The simulated (true) electron density profiles and volume emission rates were generated using IRI and MSIS models, together with the baseline forward model of 135.6 nm emission containing radiative recombination and mutual neutralization. These were then run through an FUV instrument simulator using the pre-flight instrument characterization, e.g., FUV sensitivity of 0.0873 counts/res-cell/sec/R, and 12 second integration (Mende et al., 2017) to generate a full set of FUV viewing images and to create realistic ICON FUV level 1 data profile sets with realistic representation of the anticipated (noisy) input data for level 2 processing.

Figure 5.13 shows an example of a single simulated FUV brightness profile (generated for 10 PM local time at 0 latitude, 0 longitude) and the corresponding reconstructed volume emission rate and electron density profiles based on the inversion of the simulated FUV brightness profile. As can be seen from this figure the entire ionospheric profile, and in particular peak density and height, are reconstructed with high fidelity.

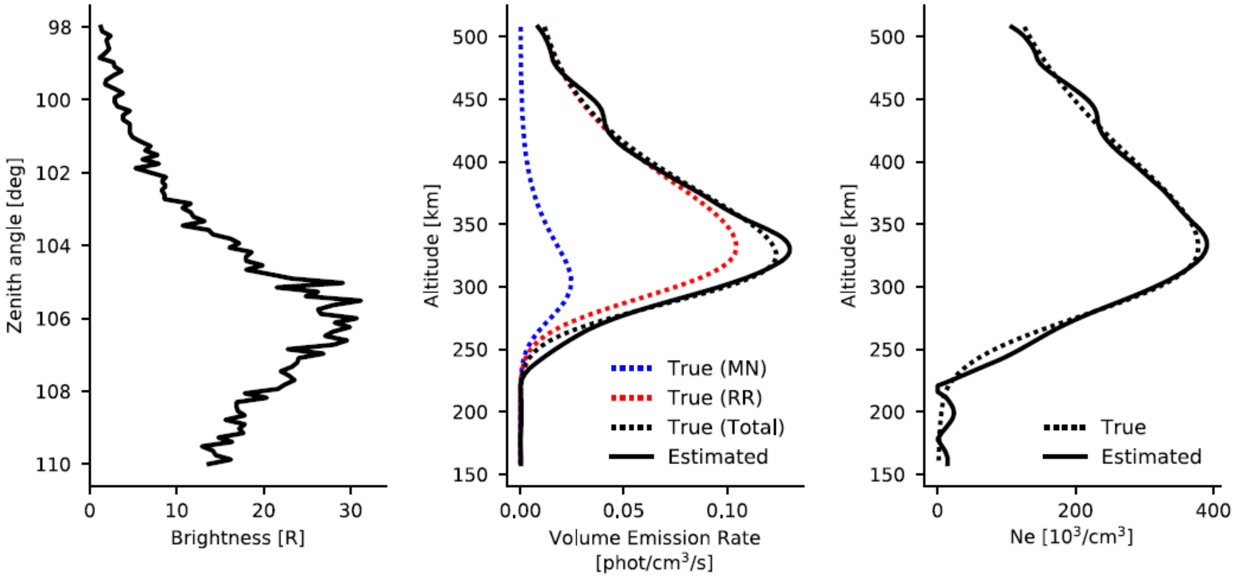

Fig 5.13: Example of an end-to-end ICON FUV inversion corresponding to 10 PM local time at 0 degrees latitude, 0 degrees longitude. Left panel: simulated FUV brightness as a function of zenith angle based on an IRI electron density profile and corresponding volume emission rate using MSIS and 135.6 nm emission containing radiative recombination and mutual neutralization. The simulated brightness was obtained based on ICON FUV viewing geometry and instrument characteristics. Middle panel: solid black curve shows the reconstructed volume emission rate from the simulated brightness of the left panel. Dotted black curve shows the original (simulated) true volume emission rate. The dotted red and blue curves show the contributions from radiative recombination and mutual neutralization processes respectively which in combination result in the total simulated volume emission rate in dotted black curve. Right panel: Solid curve shows the reconstructed electron density profile in comparison with the dotted line which shows the simulated (true) profile

Figure 5.14 shows the result of the simulation described above for an ICON partial orbit containing 255 orbit measurement points obtained from limb images, spanning from −100 to 100 degrees longitude and −20 to 22 degrees latitude. The bottom panel shows the partial orbit path. The green line in the top panel shows the simulated peak brightness level (R) using ICON FUV instrument characteristics (e.g., sensitivity). The volume emission rate is reconstructed from the simulated brightness for each point in the orbit and the electron density is calculated, followed by the extraction of the F2 peak parameters and comparison with the “true” (original) F2 peak parameters of the electron density simulated from the IRI model. The top panels show the resulting errors in NmF2 and hmF2 for each measurement. As can be seen from the figure, the reconstruction errors are within the requirements (20 Km for hmF2, 10% for NmF2, Immel *et al.*, 2018) for time intervals when there is sufficient source signal.

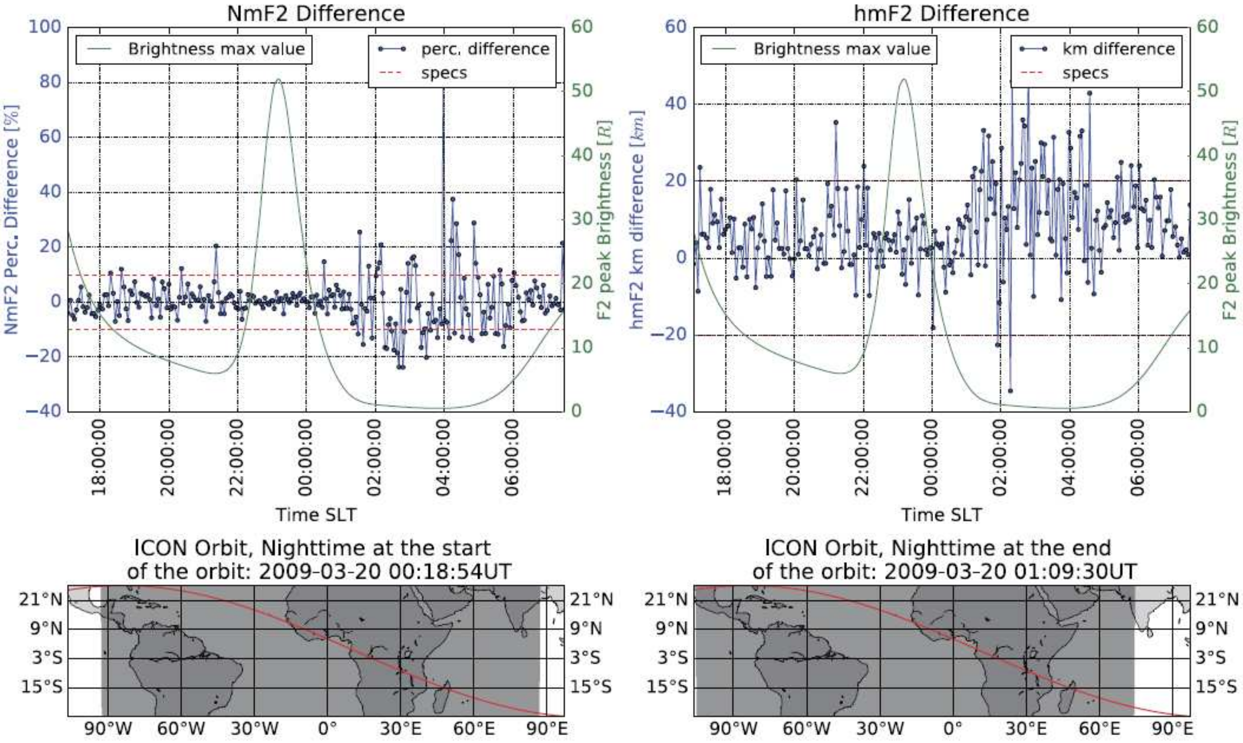

Fig 5.14: An ICON partial orbit containing 255 orbit measurement points, spanning from −100 to 100 degrees longitude and −20 to 22 degrees latitude is shown in the bottom panels. The green line shows the simulated peak brightness (R) using ICON FUV instrument characteristics (sensitivity). The volume emission rate is reconstructed from the simulated brightness for each point in the orbit and the electron density is calculated followed by extraction of the F2 peak parameters and comparison with the "true" (original) F2 peak parameters of the electron density simulated from the IRI model. The top panels show the resulting errors in NmF2 and hmF2 for each measurement (in blue) and the ICON requirements (in red). As can be seen from the figure, the reconstruction errors are within the requirements (20 km for hmF2, 10% for NmF2, Immel et al. (2018) for time intervals when there is sufficient signal

Between 01:00 and 05:00 SLT, the brightness is low due to the low electron density. This causes a significant degradation in the precision of the measurements, but the accuracy is also affected, at least for hmF2, which has a positive bias during this period. This bias arises from the fact that the regularization term penalizes the profile's derivative equally at all altitudes, while real electron density profiles are steeper on the bottom side than the topside. This bias is also apparent in the example in Figure 5.14. In the future, we plan to investigate alternative regularization schemes that do not produce this bias, perhaps using altitude- dependent penalties.

Figure 5.15 shows the errors in NmF2 and hmF2 calculated for each of the 255 points in the orbit, plotted as a function of peak source brightness. Note that for brightness values above 10 R, the reconstruction errors are within the specified specifications of the ICON mission for both NmF2 and hmF2.

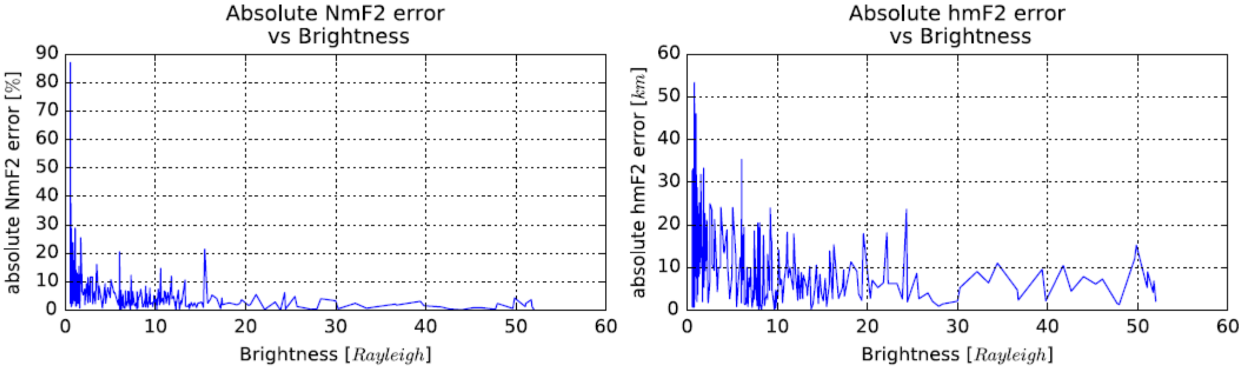

Fig 5.14: NmF2 and hmF2 errors for the 255 orbit points as a function of the simulated brightness. This figure exhibits the correlation between source brightness and reconstruction error. For brightness values above 10 R, the reconstruction errors are within the specified specifications of the ICON mission for both NmF2 and hmF2

Figure 5.16 shows the cumulative distribution function of errors in NmF2 and hmF2 calculated for each of the 255 points in the orbit, whereby the fraction (%) of orbit points within an error range is depicted. Note that 1 standard deviation (1-sigma) value corresponding to a normal distribution is shown with the dashed lines for both NmF2 and hmF2, and both fall well within the requirements.

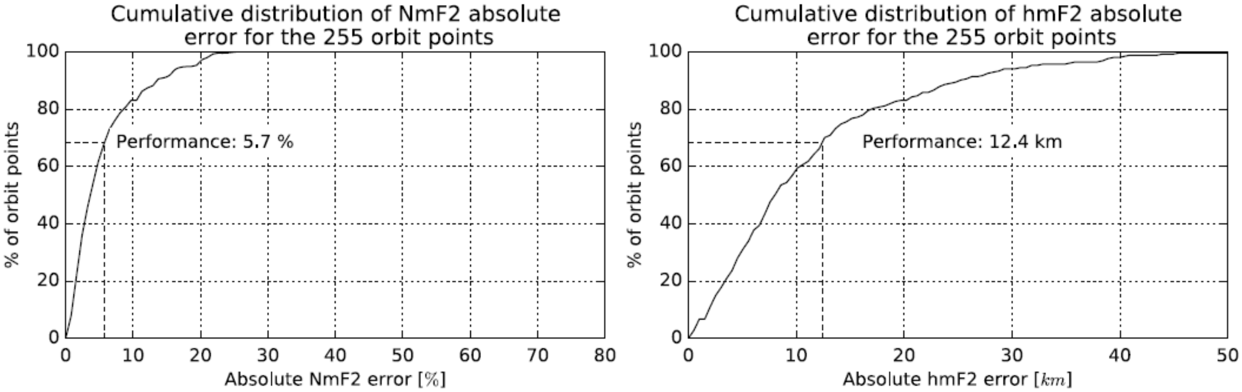

Fig 5.16: Cumulative distribution function of errors in NmF2 and hmF2 calculated for each of the 255 points in the orbit, whereby the fraction (%) of orbit points within an error range is depicted. Note that 1 standard deviation (1-sigma) value corresponding to a normal distribution is shown with the dashed lines for both NmF2 and hmF2, and both fall well within the requirements

5.4 Preflight Calibration Algorithms

Preflight calibration algorithms are completely described in previous sections.

5.5 Retrieval Algorithms

5.5.1 Altitude profile correction

Two additional processing steps are performed on the calibrated FUV altitude profiles, which are the correction of outlier pixels, which is applied only to nighttime data, and the removal of star signals, which is applied to both nighttime and daytime data. The rate of dark current accumulation on the CCD varies from pixel to pixel, and changes with time. Although the CCD background signal is determined and taken out daily for each pixel, shorter term variations in the dark current result in certain pixels being consistently brighter or darker than their neighbors for several orbits.

Although the deviations are usually less than 10 Rayleighs, it becomes significant when the signal level is low, and has a detrimental effect on the nighttime retrievals. The correction is performed on each orbit separately, starting by taking the mean value of each pixel along the orbit. The obtained average altitude profile reveals the outlier pixels since they are consistently larger or smaller than their neighbors along the orbit, hence they appear as sharp peaks or dips in the averaged altitude profile. Passing the per-orbit average profile through a high-pass filter provides these sharp fluctuations due to the outlier pixels. The filter output is then taken out from the entire orbit, resulting in the outlier-free signal.

Stars appear frequently in the FUV observations, reaching brightness values of hundreds of Rayleighs, contaminating the airglow observations and impacting the retrievals, especially in nighttime. Stars can be regarded as point sources; however, they get convolved with the point spread function of the instrument and spread across multiple pixels, making it harder to detect and remove them. Initially, a median filter based detection and removal algorithm was developed, however, it was not able to remove the extended tails of bright stars, leaving a residual signal. Currently a deep learning approach is utilized where a convolutional neural network (CNN) is used for removing the stars. Two separate CNNs have been trained, one for nighttime, and one for daytime data. The CNNs take as input a 6 x 256 altitude profile and output the star-removed version of the input, with the same dimensions. They are only trained once in a supervised fashion with a dataset of (starry, clean) image pairs. Two datasets are created for this task, one for the nighttime and one for the daytime CNN. The datasets are created by first collecting thousands of clean (star-free) profiles from the ICON FUV measurements, where daytime data is used for the daytime dataset, and nighttime data is used for the nighttime dataset, and then synthetically adding stars to generate the starry versions. Synthetic stars are the scaled and shifted versions of the point spread function of the instrument, which itself was estimated from starry images collected during star calibrations. The performance of the approach is satisfactory and can be seen in Figure 5.17, which also demonstrate outlier pixel correction.

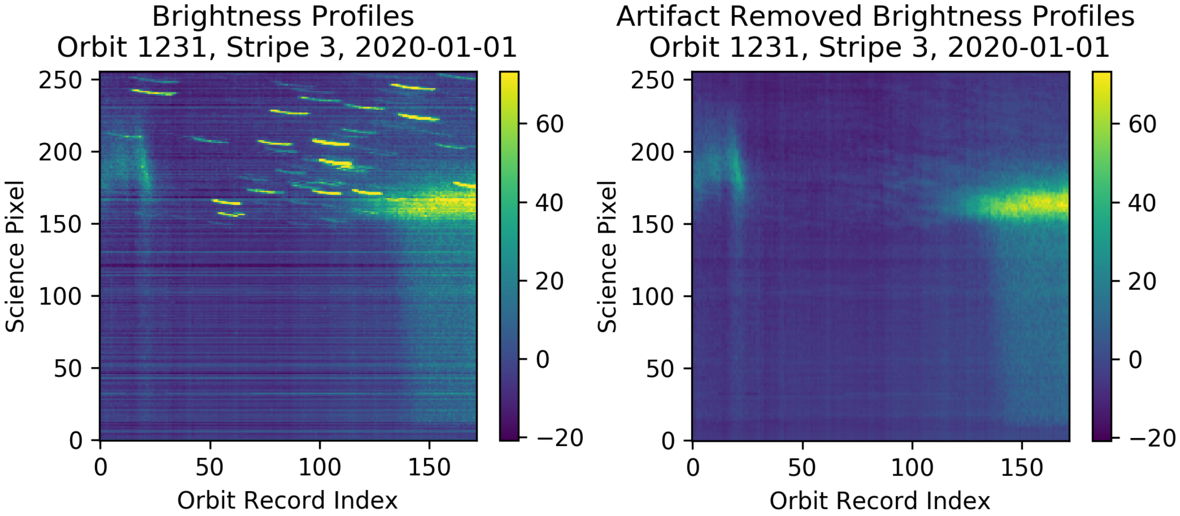

Fig 5.17: Demonstration of stellar track removal applied in the course of FUV Level 1 processing.

5.5.2 Retrieval algorithm for daytime disk O/N_2 (Level 2.4 data product)

The algorithmic approach has a long history dating to the initial proof-of-concept (Strickland et al., 1995). An ICON goal is to obtain thermospheric compositional information along a geographic swath below the ICON orbit.

Strickland et al. (1995) demonstrated a functional relationship between the ratios of observed far ultraviolet airglow emission intensities from the earth disk, which contain no altitude information, and the ratios of the column densities of O and N_2. The latter quantity is designated herein as $\Sigma O/N_2$ to distinguish the ratio of column densities from the volume density ratio, O/N_2. Strickland et al. found minimal ambiguity in the relationship when the vertical column densities are calculated above an altitude, z_{17}, corresponding to an N_2 column (from infinity down to z_{17}) of 10^{17} cm^{-2} (= N_{N2} in Equation 1; N_O is the O column density above z_{17}). $\Sigma O/N_2$ is therefore defined as:

$$\Sigma\frac{\mathbf{O}}{\mathbf{N_2}} \equiv \frac{\int_{z_{17}}^{\infty} n_O \, dz}{\int_{z_{17}}^{\infty} n_{N2} \, dz} = \frac{\int_0^{N_O} dN'_O}{\int_0^{N_{N_2}} dN'_{N_2}} = \frac{N_O}{10^{17} cm^{-2}} \qquad (1)$$

At $N_{N2} = 10^{17}$ cm^{-2}, Strickland et al. found little dependence of the relationship between $\Sigma O/N_2$ and the 135.6 nm / LBH emission ratio on the details of the model atmosphere, although they did find a dependence on solar zenith angle and viewing angle from nadir (Evans et al., 1995). The main point of their discovery is that the column density ratio can be found from the ratio of disk radiances without knowing how O and N_2 are distributed throughout the atmosphere.

A semi-quantitative derivation of the radiance ratio relationship to column density ratio follows. The column emission rate is given by the integration over altitude of the volume emission rate, which is the product of the photoelectron g-factor (excitation rate per sec per atom) and the number density, n at altitude z. Assumed for simplicity is a nadir observing direction from a space-based platform above the atmosphere. Minor multiple scattering effects of the 135.6 nm radiation field are ignored (typically < 10% in the region of peak photon production), as is pure absorption by O_2 that takes place lower in the atmosphere. (The vertical optical depth for O_2 extinction reaches unity at 135.6 nm around 110 km, so it plays little role in affecting the vertical column emission rate which samples much higher altitudes. On the other hand, O_2 extinction for limb viewing takes place at much higher altitudes due to the long slant path through the atmosphere; typically, the atmosphere becomes opaque below tangent altitudes of about 130 km. This allows retrieval of the O_2 concentration from limb scanning data.) The g-factor at each altitude (excitation s^{-1}) is defined as the integration over energy, E of the (isotropic where collisions dominate) photoelectron flux, $\Phi(E)$ (electron cm^{-2} s^{-1} ev^{-1}) times the electron impact excitation cross section, $\sigma(E)$: $g = \int \Phi(E)\, \sigma(E)\, dE$. For LBH bands, the excitation cross section is for the vibrational bands being observed. With these approximations, the ratio of the 135.6/LBH column emission rates (in Rayleighs) is

$$\frac{4\pi I_{1356}}{4\pi I_{LBH}} = \frac{\int_{z_l}^{\infty} g_{1356}(z)\, n_O(z)\, dz/10^6}{\int_{z_l}^{\infty} g_{LBH}(z)\, n_{N_2}(z)\, dz/10^6} \tag{2}$$

Converting more precisely to column density as the independent variable, the emission ratio becomes:

$$\frac{4\pi I_{1356}}{4\pi I_{LBH}} = \frac{\int_0^{N_O^l} g_{1356}(N_O)\, dN_O}{\int_0^{N_{N_2}^l} g_{LBH}(N_{N_2})\, dN_{N_2}} \cong \frac{g_{1356}^{eff}}{g_{LBH}^{eff}} \cdot \frac{N_O^l}{N_{N_2}^l} \tag{3}$$

The lower limit on the integrals, z_l in Equation 2, is the altitude that includes the FUV emitting column (i.e., z_{17}). The right-hand side of Equation 3 assumes that an effective column density exists such that the relationship between intensity ratio and column density ratio is unique. This assumption is not strictly true in a real atmosphere where there is curvature of the slope of the radiance ratio-column density ratio relationship due to the effects mentioned above that this derivation ignores. Nevertheless, it is now clear from Equation 3 why Strickland et al. (1995) were able to obtain a definitive relationship between the radiance and column density ratios.

The proportionality between the column emission rate ratio and the column density ratio can be represented generally by defining S as the slope of the relationship:

$$\frac{4\pi I_{1356}}{4\pi I_{LBH}} = S(\Sigma O/N_2, \boldsymbol{X}) \cdot \Sigma O/N_2 \tag{4}$$

where **X** is a vector representing four parameters of the model that determine the O, N2, O2 composition and temperature.

Traditionally the functionality of S is synthesized numerically from forward modeling and organized into a lookup table. For ICON, a new and more concise technique for extracting $\Sigma O/N_2$ from the disk 135.6 nm to LBH band ratio was developed. It is new because all previous algorithmic approaches have employed lookup tables. Although the table lookup method uses first principles models to populate the table, the new methodology employs the first principles model directly. The process consists of the following steps:

1) Compute the 135.6 nm and LBH band emissions with a forward model that incorporates the viewing geometry, the best prediction of the solar EUV irradiance and model atmosphere, and a representation of the instrument characteristics.

2) Compute the predicted vertical column density ratio, $\Sigma O/N_2$ at a standard location, such as the pierce point, where the line of sight passes through the 150 km level.

3) Scale the predicted $\Sigma O/N_2$ up and down by a specified increment (e.g., multiply the O concentration by 0.5 and 1.5) and recompute the 135.6 nm/LBH radiance ratios for the higher and lower column density ratios to create three emission rate ratios.

4) Fit the three column density ratios vs radiance ratios with a simple polynomial or interpolate to find the value of $\Sigma O/N_2$ for the observed radiance ratio.

Step 1) of the procedure accounts for four of the parameters that determine $\Sigma O/N_2$. It includes physical effects, such as multiple scattering of 135.6 nm photons, production of O (^5S) from dissociative excitation of O_2 by energetic photoelectrons, O_2 extinction and an instrument model.

5.5.3 Retrieval algorithm for nighttime O+ (Level 2.5 data product)

The inversion task amounts to estimating the vector $\mathbf{x}$ given the vector of measurements $\mathbf{y}$, the forward model matrix $\mathbf{A}$, and all known information, statistical or otherwise, regarding the measurement noise vector $\mathbf{w}$.

The ill-conditioned nature of $\mathbf{A}$ implies that a systematic approach to the incorporation of additional constraints in the solution space is required. In other words, it becomes necessary to replace the original ill-conditioned problem with another inverse problem with better conditioning that is close to the original one.

A formal mechanism for addressing this requirement is through regularization which leads to the minimization of an appropriately formulated cost function (Hansen 2010). This approach incorporates prior knowledge concerning the unknown solution in a least squares setting. The prior information can be introduced in a deterministic way (Tikhonov and Arsenin 1977; Engl et al. 1996; Bertero and Boccacci 1998), or in a statistical setting (Kaipio and Somersalo 2005), which is related to the Bayes paradigm of Geman and Geman (1984).

A general formulation for the cost function (the objective function) can be expressed as (Kamalabadi 2010):

$$\Phi(\mathbf{x}) = \|\mathbf{y} - \mathbf{Ax}\|_{\mathcal{W}}^2 + \sum_i \gamma_i \, C_i(\mathbf{x}) \tag{28}$$

where $\|\mathbf{y} - \mathbf{Ax}\|_{\mathcal{W}}^2$ denotes the weighted residual norm, i.e., $(\mathbf{y} - \mathbf{Ax})^T \, \mathcal{W}(\mathbf{y} - \mathbf{Ax})$, C_i and γ_i are the i-th regularization functional and regularization parameters respectively, and $\mathcal{W}$ is an appropriate weight, all to be chosen according to the specifics of the problem. The first term controls data fidelity (i.e., how faithful the reconstruction is to the data), whereas the second term (the regularization term) controls how well the reconstruction matches our prior knowledge of the solution.

Tikhonov (quadratic) regularization (Tikhonov 1963) is perhaps the most common technique used for regularization and is equivalent to maximum a posteriori (MAP) estimation, assuming Gaussian statistics for both the unknown image and noise (Karl 2000). Assuming $\mathbf{w} \sim \mathcal{N}(\mathbf{0}, \mathbf{\Sigma_w})$ and $\mathbf{x} \sim \mathcal{N}(\mathbf{x_0}, \mathbf{\Sigma}_x)$, where $\mathcal{N}(\boldsymbol{\mu}, \mathbf{\Sigma})$ represents the normal distribution with mean $\boldsymbol{\mu}$ and covariance $\mathbf{\Sigma}$, the MAP estimate is:

$$\begin{aligned} \hat{\mathbf{x}}_{\mathrm{MAP}} &= \arg\min_{x \in \mathbb{R}^N} \left[-\log p(\mathbf{y}|\mathbf{x}) - log\, p(\mathbf{x})\right] \\ &= \arg\min_{x \in \mathbb{R}^N} \left[\|\mathbf{y} - \mathbf{Ax}\|^2_{\mathbf{\Sigma_w^{-1}}} + \|\mathbf{x} - \mathbf{x_0}\|^2_{\mathbf{\Sigma_w^{-1}}}\right] \\ &= \mathbf{x_0} + (\mathbf{A^T \Sigma_w^{-1} A} + \mathbf{\Sigma}_x^{-1})^{-1} \mathbf{A^T \Sigma_w^{-1}} (\mathbf{y} - \mathbf{A x_0}) \end{aligned} \qquad (29)$$

The connection between this MAP formulation of Tikhonov regularization and the variational form just discussed becomes apparent by assuming independent identically distributed (IID) Gaussian noise and taking $\mathbf{\Sigma_x} = \frac{1}{\gamma^2}(\mathbf{L^T L})^{-1}$ and $\mathbf{x_0} = \mathbf{0}$, hence arriving at the well known Tikhonov regularization functional:

$$\begin{aligned} \hat{\mathbf{x}}_{\mathrm{Tik}} &= \arg\min_{x \in \mathbb{R}^N} \left[\frac{1}{\sigma_W^2} \|\mathbf{y} - \mathbf{Ax}\|_2^2 + \gamma^2 \|\mathbf{L}(\mathbf{x} - \mathbf{x_0})\|_2^2\right] \\ &= \arg\min_{x \in \mathbb{R}^N} \left[\|\mathbf{y} - \mathbf{Ax}\|_2^2 + \lambda \|\mathbf{Lx}\|_2^2\right] \\ &= \left(\frac{1}{\sigma_w^2} \mathbf{A^T A} + \gamma^2 \mathbf{L^T L}\right)^{-1} \frac{1}{\sigma_w^2} \mathbf{A}^T \mathbf{y} \end{aligned} \qquad (30)$$

where $\mathbf{L}$ is a positive definite regularization matrix (often a derivative operator) and $\lambda = (\gamma \sigma_w)^2$ where σ_w^2 is the variance of the noise samples. A special case is when $\mathbf{L} = \mathbf{I}$, which results in λ being inverse of the signal-to-noise ratio. Although we assumed IID noise, more general forms of noise covariance have also been applied in different imaging applications.

References

J.M. Ajello, D.E. Shemansky, A reexamination of important N2 cross sections by electron impact with application to the dayglow: the Lyman–Birge–Hopfield band system and NI (119.99 nm). J. Geophys. Res. **90**(A10), 9845–9861 (1985). 10.1029/JA090iA10p09845

Bevington, P. R., and D. K. Robinson (1992), Data Reduction and Error Analysis for the Physical Sciences, 2nd ed., McGraw-Hill, New York.

Frey, H.U., Mende, S.B., Meier, R.R., Kamaci, U., Urco, J.M., Kamalabadi, F., England, S.L. and Immel, T.J., 2023. In flight performance of the Far Ultraviolet instrument (FUV) on ICON. *Space Science Reviews, 219(3)*, 23. 10.1007/s11214-023-00969-9

S.T. Gibson, B.R. Lewis, Understanding diatomic photodissociation with a coupled-channel Schrodinger equation model. J. Electron Spectrosc. Relat. Phenom. **80**, 9–12 (1996). https://doi.org/10.1016/0368-2048(96)02910-6

S.T. Gibson, H.P.F. Gies, A.J. Blake, D.G. McCoy, P.J. Rogers, Temperature dependence in the Schumann-Runge photoabsorption continuum of oxygen. J. Quant. Spectrosc. Radiat. Transf. **30**, 385–393 (1983). 10.1016/0022-4073(83)90101-2

Geman S, Geman D (1984) Stochastic relaxation, gibbs distributions, and the bayesian restoration of images. IEEE Trans Pattern Anal Mach Intell 6:721–741 [PubMed: 22499653]

H W Engl MH, Neubauer A (1996) Regularization of Inverse Problems. Kluwer

Hansen PC (2010) Discrete Inverse Problems: Insight and Algorithms, vol 7. SIAM

Hanson WB (1970) A Comparison of Oxygen Ion-Ion Neutralization and Radiative Recombination Mechanisms for Producing Ultraviolet Nightglow. J Geophys Res 75(22):4343–4346, 10.1029/ JA075i022p04343

Hummer DG (1962) Non-Coherent Scattering 1. the Redistribution Functions with Doppler Broadening. Mon Not Roy Astron Soc 125(1):21–37

Kaipio J, Somersalo E (2005) Statistical and Computational Inverse Problems. Springer

Karl WC (2000) Handbook of Image and Video Processing, Plenum Press, chap Regularization in image restoration and reconstruction

D.W. Marquardt, An algorithm for least-squares estimation of nonlinear parameters. J. Soc. Ind. Appl. Math. **II**(2), 431–441 (1963). 10.1137/0111030

M MB, P PB (1998) Introduction to Inverse Problems in Imaging. IOP Publishing

Meier RR (1991) Ultraviolet Spectroscopy and Remote-Sensing of the Upper-Atmosphere. Space Sci Rev 58(1–2):1–185, 10.1007/BF01206000

Meier, R. R. (2021). The thermospheric column O/N2 ratio. *Journal of Geophysical Research: Space Physics*, *126*, e2020JA029059. 10.1029/2020JA029059

Meier, R. R., J. M. Picone, D. Drob, J. Bishop, J. T. Emmert, J. L. Lean, A. W. Stephan, D. J. Strickland, A. B. Christensen, L. J. Paxton, D. Morrison, H. Kil, B. Wolven, T. N. Woods, G. Crowley, and S. T. Gibson (2015), Remote Sensing of Earth’s Limb by TIMED/GUVI: Retrieval of thermospheric composition and temperature, Earth and Space Science, 2, 1–37, 10.1002/2014EA000035.

R.R. Meier et al., Remote sensing of Earth's limb by TIMED/GUVI: retrieval of thermospheric composition and temperature. Earth Space Sci. **2**, 1–37 (2015), 10.1002/2014EA000035

R.R. Meier, J.M. Picone, Retrieval of absolute thermospheric concentrations from the far UV dayglow: an application of discrete inverse theory. J. Geophys. Res. **99**(A4), 6307–6320 (1994). 10.1029/93JA02775

Melendez-Alvira DJ, Meier RR, Picone JM, Feldman PD, McLaughlin BM (1999) Analysis of the oxygen nightglow measured by the Hopkins Ultraviolet Telescope: Implications for ionospheric partial radiative recombination rate coefficients. J Geophys Res 104(A7):14,901–14,913, 10.1029/1999JA900136

Mende, S.B., Frey, H.U., Rider, K., Chou, C., Harris, S.E., Siegmund, O.H.W., England, S.L., Wilkins, C., Craig, W., Immel, T.J. and Turin, P., 2017. The far ultra-violet Imager on the ICON mission. Space Science Reviews, 212(1-2), 655-696, 10.1007/s11214-017-0386-0.

W. Menke, *Geophysical Data Analysis: Discrete Inverse Theory*. Int. Geophys. Ser., vol. 45 (Academic Press, San Diego, 1989). 289 pp.

Mihalas D (1978) Stellar Atmospheres. W. H. Freeman and Co., San Francisco

J.M. Picone, A.E. Hedin, D.P. Drob, A.C. Aikin, NRLMSISE00 empirical model of the atmosphere: statistical comparisons and scientific issues. J. Geophys. Res. **107**(A12), 1468 (2002). 10.1029/2002JA009430

Qin J, Makela JJ, Kamalabadi F, Meier RR (2015) Radiative transfer modeling of the OI 135.6-nm emission in the nighttime ionosphere. J Geophys Res 120:10,116–10,135, 10.1002/2015JA021687

Qin J, Kamalabadi F, Makela JJ (2016) Quantifying the inversion accuracy of simplified physical models for the nighttime OI 135.6 nm emission. J Geophys Res 121:5805–5814, 10.1002/2016JA022720

Slanger TG, Cosby PC, Huestis DL, Meier RR (2004) Oxygen atom Rydberg emission in the equatorial ionosphere from radiative recombination. J Geophys Res 109:A10, 309

Strickland, D. J., J. S. Evans, and L. J. Paxton, Satellite remote sensing of thermospheric O/N_2 and solar EUV: 1. Theory, *J. Geophys. Res., 100*, 12,217, 1995.

Strickland DJ (1979) Transport of Resonance Radiation in a Nonisothermal Medium - Effect of a Varying Doppler Width. J Geophys Res 84(NA10):5890–5896, 10.1029/JA084iA10p05890

Strickland DJ, Donahue TM (1970) Excitation and Radiative Transport of OI 1304 A Resonance Radiation I. the Dayglow. Planet Space Sci 18(5):661–689, 10.1016/0032-0633(70)90049-8

Tikhonov AIN, Arsenin VY (1977) Solutions of Ill-Posed Problems. Winston, Washington, D.C.

Tikhonov AN (1963) Solution of incorrectly formulated problems and the regularization method. Soviet Mathematics 4:1035–1038

Tinsley BA, Christen AB, Bittenco J, Gouveia H, Angreji PD, Takahashi H (1973) Excitation of oxygen permitted line emissions in the tropical nightglow. J Geophys Res 78(7):1174–1186, 10.1029/JA078i007p01174